E-706

NUB 2980

PARTICLES PRODUCED IN ASSOCIATION WITH HIGH TRANSVERSE MOMENTUM SINGLE PHOTONS AND π°s IN HADRONIC COLLISIONS*

A Dissertation Presented

by

Alexandros Pericles Sinanidis

to

The Department of Physics

in partial fulfillment of the requirements

for the degree of

Doctor of Philosophy

in the field of

Physics

Northeastern University

Boston, Massachusetts

October 1989

* Work supported in part by the National Science Foundation

AAB1952

NORTHEASTERN UNIVERSITY

Graduate School of Arts and Sciences

Dissertation Title: Particles produced in association with high transverse momentum single photons and π^0s in hadronic collisions

Author: Alexandros Pericles Sinanidis

Department: Physics

Approved for Thesis Requirements of Doctor of Philosophy Degree

David Hartlick — 11/10/89

William P Fausler — 11/10/89

Yogendra N Srivastava — 11/10/89.

George Alverson — 10-Nov-89

Thesis Commitee — Date

S. Rencuse — 10 November 1989.

Head of Department — Date

Graduate School Notified of Acceptance

K Cuan — 15 November 89

Dean — Date

Copy Deposited in Library

Signed — Date

NORTHEASTERN UNIVERSITY

Graduate School of Arts and Sciences

Dissertation Title: Particles produced in association with high transverse momentum single photons and π°s in hadronic collisions

Author: Alexandros Pericles Sinanidis

Department: Physics

Approved for Thesis Requirements of Doctor of Philosophy Degree

David Gaelick 11/10/89

William J Faissler 11/10/89

Yogendra N Srivastava 11/10/89

George Alverson 10-Nov-89

Thesis Commitee — Date

S. Reucroft 10 November 1989.

Head of Department — Date

FERMILAB LIBRARY

ABSTRACT

The charged and neutral particles produced in association with high transverse momentum ($p_T > 5.0$ GeV/c) photons (γ) and neutral pions (π^0) in p(Cu+Be) and π^-(Cu+Be) collisions at $\sqrt{s} = 31.5$ GeV are studied in this thesis. It was observed that **1)** The relative rapidity of the two highest p_T recoiling particles in the events have a jet - like structure. **2)** The relative rapidity of the single γ (or π^0) and the highest p_T charged particle accompanying the single γ (or π^0) show that the high p_T π^0 events have a jet - like structure in the trigger hemisphere whereas the high p_T single γ events do not. **3)** The angular distributions of the particles produced in the reactions show that high p_T π^0s are accompanied by other particles, whereas high p_T single photons are relatively isolated. **4)** The fragmentation distributions of the recoiling particles from the high p_T single photons and π^0s are consistent with the measurements of other experiments. **5)** The recoiling particles are consistent with the fragmentation of either a quark or a gluon according to the QCD (Quantum Chromodynamics).

In summary, particles produced in association with high transverse momentum single photons and π^0s in hadronic collisions have been measured and their properties are in good agreement with the predictions of the parton model and those of QCD.

This Thesis is dedicated to

the memory of my father,

Pericles G. Sinanidis

Acknowledgment

To sucessfully complete an experiment as large as E-706 requires the combined efforts of a large number of people. The work described in this thesis has to be credited not only to the author but also to the great majority of the E-706 collaborators. I want to take this opportunity to thank them.

First, I would like to express my very special thanks to two E-706 postdocs with whom I worked closely and whom I value both as physicsists and as friends. I thank Takahiro Yasuda for his guidance, advice and corrections on my thesis. Without Taka the completion of this thesis would be more difficult. I also thank George Ginther for his comments and suggestions on my thesis, and his advice and friendship during all these years. I am greatly indebted to them.

I would like to thank my advisor Professor David Garelick for his continuous support and encouragement throughout my stay at Fermilab and Northeastern. His suggestions and comments on my thesis were very valuable to me. I also would like to thank Professor Mike Glaubman who has given me much support, good advice, and friendship during my graduate studies. In addition I thank the Northeastern University Professors William Faissler, and George Alverson for their support and comments on my thesis.

I thank my fellow graduate students Ioanis Kourbanis, Casey Hartman, Carlos Yosef, Giussepe Ballocchi, Dhammika Weerasundara, Sajan Easo, Vijay Kapoor, David Brown, B. C. Choudhary, John Mansour, Bill DeSoi, Chris Lirakis, Dane Skow, Eric Prebys, Richard Benson, and Armando Lanaro for their help, their participation in this experiment, and for their friendship. Thanks also to the new E-706 members, Nikos Varelas, Jim Dunlea, and Rob Roser.

I also would like to thank my senior collaborators, Phil Gutierrez, Joey Huston, Carl Bromberg, Marek Zielinski, S. Mani, and George

Fanourakis for their help, guidance, patience and advice during my studies at Fermilab. Their excellent knowledge of physics research was most helpful in my work.

Additional thanks are due to the E-706 people, not mentioned above, P. Slattery., T. Ferbel, F. Lobkowicz, Guan H. Wu, Bud Dickerson, Ed Pothier, Clark Chandlee, G. Glass, R. Shivpuri, W. Baker, C. Johnstone, P. Lukens, E. Engels, and P.F. Shepard.

I gratefully acknowledge the valuable assistance of the Fermilab technical personnel, and particularly the people of LAB 6, Bud Koecher, Jerry Sasek, Dave Cosgrove, Kevin Jengins and Geno Olsen who helped us during the building of the E-706 Photon Detector. I also thank Dinesh Kaul, B. M. Rajaram and Tara Chand from the University of Delhi who also helped us in this difficult task.

Finally, I extend special thanks to my mother, Margarita Sinanidis, and my wife, Eleni Buduri - Vuduri, for their support and encouragement throughout my studies. I also thank Eleni for her patience and love throughout our difficult years in this friendly but foreign country.

Ο ανθρωπος τη φυσει του ειδεναι ορεγεται

Table of Contents

1. INTRODUCTION 1
2. PHYSICS MOTIVATION 4
   2.1 Kinematics 4
   2.2 High p_T Phenomenology 8
   2.3 Direct Photon Production 13
   2.4 π^o Production 18
   2.5 Jet Production 20
   2.6 Experimental Methods 23
   2.7 Results from Previous Experiments 28
   2.8 Physics Goals of Experiment E-706 32
   2.9 Goals of this Thesis 36
3. THE EXPERIMENT 40
   3.1 Experimental Design and Components 40
   3.2 The Beam Line 42
   3.3 Targets 46
   3.4 Magnet 48
   3.5 Silicon Strip Detector 48
   3.6 Proportional Wire Chambers 51
   3.7 Liquid Argon Calorimeter 52
   3.8 Forward Calorimeter 78
   3.9 Trigger 80
   3.10 On-Line Data Acquisition and Monitoring 89
4. LAC CALIBRATION 93
   4.1 Introduction 93
   4.2 Charge Collection & High Voltage Response 98
   4.3 Timing Tests 101
   4.4 The Zero Suppression Window 103
   4.5 Energy Calibration 107
   4.6 Energy Resolution 110

4.7 Detector Uniformity 141
4.8 Pedestal Corrections 143
4.9 Conclusions 144
5. OFFLINE DATA ANALYSIS 146
5.1 Introduction 146
5.2 Charged Particle Tracking 148
5.3 Alignment of PWCs and SSDs 159
5.4 Performance of PWCs and SSDs 159
5.5 Data Bank Structures for the EMLAC and the HALAC 166
5.6 Electromagnetic Shower Reconstruction (EMREC) . . 173
5.7 Alignment of the LAC 177
5.8 Performance of the EMLAC 179
5.9 Hadron Shower Reconstruction (HCREC) 182
5.10 Performance of Hadron Shower Reconstructor . . . 196
6. HIGHER LEVEL DATA ANALYSIS 207
6.1 Pre-selection of Events 207
6.2 Event Selection 208
6.3 Event Classification 221
6.4 Particle Selection and Classification 232
6.5 Event Structure 239
6.6 Total p_T 247
6.7 The Backgrounds for Direct Photons Due to $\pi^o \rightarrow \gamma\gamma$. 253
7. RESULTS AND CONCLUSIONS 257
7.1 Particle Distributions 257
7.2 Rapidity Correlations 264
7.3 Fragmentation Fraction 273
7.4 Charge Ratio 288
7.5 Discussion 290
7.6 Summary 292

LIST OF FIGURES

1) The hadronic interaction $AB \rightarrow CD$+other particles at large p_T in terms of the parton sub-process $ab \rightarrow cd$. (5)

2) a) Q^2 behavior of the strong and electromagnetic coupling constants. b) Gluon and quark distribution functions in the proton for Q^2 =4 GeV/c^2. c) The u quark and gluon fragmentation functions (solid curves) calculated by the Lund group (see Ref. [10]). The dotted curve is the gluon fragmentation distribution when the events with $z \leq 0.05$ have been discarded. Plot b) is taken from R. Rusack (Rockefeller University) IX International Conference on Physics in Collisions, Israel, and plot c) from Reference [10]. (9)

3) Dominant Feynman diagrams for direct photon production. (13)

4) Ratio of the two components contributing to the direct photon cross section in pp collisions. The plot is taken from Reference [8]. (17)

5) A comparison to γ/π^o production ratios. The plot is taken from Reference [7]. (19)

6) (top): Simplified picture of a pp collision. (bottom): Illustration of hard scattering event which consists of four jets. The latter graph is taken from Reference [19]. (21)

7) π^o decay. (26)

8) Distribution in the average transverse momentum of charged particles as a function of azimuth with respect to the trigger particle, from experiment a) R806/R807 and b) UA2. The plots are taken from the References listed at the end of Chapter 2. (29)

The page where the figure can be found in the text is indicated in parenthesis at the end of the figure listings.

9) The relative density of positive to negative particles in the awayside (opposite the trigger) hemisphere as a function of z. The curves shown in the bottom graph are from the calculation in Ref. [42] for $p_T = 6.0$ GeV/c. The plots are taken from the References [25] (top plot), and [22] (bottom plot). (30)

10) Density of recoiling particles ($\Delta\phi > 90°$ versus z from experiments R806, R807 (top) and WA-70 (bottom). The plots are taken from the References [7] and [24]. (31)

11) (top): Difference in rapidity between the two tracks with the highest p_T opposite the trigger. (bottom): z distribution of the highest p_T and second highest p_T particles in the kinematic region $2 < Q^2 < 6\ GeV^2$, from a deep inelastic electron scattering experiment in DESY. The plots are taken from the References [23] and [43]. (33)

12) E-706 experimental layout. (41)

13) MW Beamline components plotted in horizontal position x vs. longitudinal position. (43)

14) Pressure curves of Cherenkov counter using negative (right graph) and positive (left graph) beams. (44)

15) (top): Veto walls. (bottom): z-coord distribution of reconstructed vertices in the target region. (46)

16) The Silicon Strip Detectors (SSD) and the segmented target. The plot is taken from Reference [47]. (49)

17) Blowup of the Electromagnetic Calorimeter. The plot is taken from Reference 50. (61)

18) Blowup of the Electromagnetic Calorimeter. The figure is taken from Reference 47. (63)

19) A single hadron calorimeter readout board (left) and detail of the readout scheme (right). The plots are taken from Reference 50. (66)

20) The assembly of the hadron calorimeter (top) and an exploded view of one readout layer (bottom). The plots are taken from Reference 50. (67)

21) The overall gantry and cryostat of the LAC. The plot is taken from Reference 47. (69)

22) The LAC data acquisition system. The plot is taken from Reference 47. (72)

23) Electromagnetic Calorimeter (EMLAC) readout schematic (top) and the EMLAC high voltage schematic (bottom). The bottom plot is taken from Reference 47. (74)

24) Pedestal distributions from four classes of channels. (76)

25) Pulse distribution of each channel of the front/back HALAC sections. (77)

26) The forward calorimeter. The figure is taken from Reference 47. (79)

27) Triggering scheme of one quadrant. The plot is taken from E. Prebys, E-706 internal memo. (82)

28) Octant summing scheme of the LAC trigger. The plot is taken from E. Prebys, E-706 internal memo. (83)

29) (top):Schematic of the counters used to form the logic of the triggers. (bottom): The "two gamma trigger" octant combination. (86)

30) LAC pretrigger efficiency curves. (89)

31) SINGLE LOCAL trigger efficiency curves (90).

86) The asymmetry distributions of the π^0 sample used for this analysis ($p_T \geq 5.0$ GeV/c) for both positive and negative data. Only a fraction of the total data is shown. The distributions have not been corrected for trigger efficiency or detector acceptance. (228)

87) The p_T and energy distributions of the π^0 sample used for this analysis ($p_T \geq 5.0$ GeV/c) for both positive and negative data. Only a fraction of the total data is shown. The distributions have not been corrected for trigger efficiency or detector acceptance. (229)

88) The trigger efficiency as a function of the π^0 p_T. (230)

89) The rapidity distributions of high p_T single photon candidates. Only a fraction of the total data is shown. The distributions have not been corrected for trigger efficiency or detector acceptance. (232)

90) The p_T and energy distributions of high p_T single photon candidates. Only a fraction of the total data is shown. The distributions have not been corrected for trigger efficiency or detector acceptance. (233)

91) The minimum radial distance between the tracks and all showers in the EMLAC (top graph) and the HALAC (bottom graph). (236)

92) The mass spectrum of the awayside 2γs for various p_T and asymmetry cuts. Only a fraction of the total data is shown. The distributions have not been corrected for trigger efficiency or detector acceptance. (237)

93) The rapidity distributions of the awayside π^0s for three p_T cuts. Only a fraction of the total data is shown. The distributions have not been corrected for trigger efficiency or detector acceptance. (238)

94) The particle multiplicity distributions in the LAC and magnetic spectrom-

eter. The events with no particles reconstructed are not shown. Only a fraction of the total data is shown. The distributions have not been corrected for trigger efficiency or detector acceptance. (240)

95) p_T distributions of all particles (see text). Only a fraction of the total data is shown. The distributions have not been corrected for trigger efficiency or detector acceptance. (241)

96) Energy distributions of all particles (see text). Only a fraction of the total data is shown. The distributions have not been corrected for trigger efficiency or detector acceptance. (242)

97) The transverse momentum distributions of the tracks with $|y| < 0.9$ and energy greater than 10.0 GeV are are normalized to be equal in the region 2 to 4 GeV/c with the neutral hadron p_T distribution. Only a fraction of the total data is shown. The distributions have not been corrected for trigger efficiency or detector acceptance. (243)

98) An event where particles that survived the cuts described in the text are projected on the p_T plane. (245)

99) An event where particles that survived the cuts described in the text are projected on the p_T plane. (246)

100) The ${p_T}^{total}$ distributions for all events (i.e., π^o and single γ triggers with $p_T > 5.0$ GeV/c). Only a fraction of the total data is shown. The distributions have not been corrected for trigger efficiency or detector acceptance. (248)

101) ${p_T}^{total}$ as a function of the rapidity. (250)

102) Mean $|\sum x_e|$ as a function of the p_T of the neutral trigger. (251)

103) (top): p_T of the beam. (bottom): The beam slope correction calculation. (253)

104) (top): R_{fake} for the negative and positive beam data. The average R_{fake} value for p_T higher than 5.0 GeV/c is 16% for both beam polarities (see text). (bottom): R_{fake} as a function of rapidity. (255)

105) The angular distributions of charged and neutral particle multiplicities with respect to the high p_T photon or π^o. Trigger $5.0 < p_T < 5.5$ GeV/c. Only particles with p_T greater than 0.5 GeV/c are counted. (258)

106) The angular distributions of charged and neutral particle multiplicities with respect to the high p_T photon or π^o. Trigger $5.5 < p_T$ GeV/c. Only particles with p_T greater than 0.5 GeV/c are counted. (259)

107) The angular distributions of charged and neutral particle p_T densities with respect to the high p_T photon or π^o. Trigger $5.0 < p_T < 5.5$ GeV/c. Only particles with p_T greater than 0.5 GeV/c are counted. (260)

108) The angular distributions of charged and neutral particle p_T densities with respect to the high p_T photon or π^o. Trigger $5.5 < p_T$ GeV/c. Only particles with p_T greater than 0.5 GeV/c are counted. (261)

109) The distribution of the mean value of the sum $\sum |q_T|_i$ for negative beam (left plot) and positive (right plot) in intervals of $\Delta\phi$. (263)

110) The particle density as a function of the difference in $\Delta\phi$ between the particles and the trigger, for different cuts on the particle transverse momentum. (265)

111) The particle p_T density as a function of the difference in $\Delta\phi$ between the particles and the trigger, for different cuts on the particle transverse momentum.

(266)

112) Distribution in $|\Delta y|$, the difference between the rapidity of the trigger particle and the fastest charged track in the event for ${p_T}^{trig} > 5.0 GeV/c$. (267)

113) The rapidity difference between the two fastest charged tracks opposite to the high p_T photon (or π^o). (269)

114) The rapidity difference between the two fastest particles opposite to the neutral trigger, for the same p_T ranges of the trigger when one of the two fastest particles is a neutral hadron (reconstructed in the HALAC and the EMLAC) and the other one is a charged track. (270)

115) The rapidity difference between the two fastest particles opposite to the neutral trigger, for the same p_T ranges of the trigger when one of the two fastest particles is a π^o (reconstructed in the EMLAC) and the other one is a charged track. (271)

116) The distribution of the difference between the rapidity of the high p_T photon (or π^o) and the rapidity of the leading track on the same side with the high p_T photon or π^o (i.e., $\Delta\phi < \pi/2$) for four ${p_T}^{track}$ cuts. (273)

117) The distribution of the mean value of the sum $\sum[x_e]_i$ for both charged and neutral particles in intervals of $\Delta\phi$, for the high p_T single photon and π^o events. (275)

118) The x_e distributions of the fastest and second-fastest charged particles for the π^o data. (276)

119) The x_e distributions of the fastest and second-fastest charged particles for the single photon data. (277)

120) The x_e distribution when the fastest particle in the event is a neutral hadron ($E^{HAD} \geq 10.0$ GeV in the HALAC). (279)

121) The x_e distribution when the fastest particle in the event is a π^o. The x_e distribution of the π^o background was subtracted from the x_e distribution of the raw π^o signal. (280)

122) The x_e distributions for all particles in the event for proton/π^- beam and single photon/π^o data. p_T (trigger) > 5.0 GeV/c. (281)

123) The x_e distributions for the charged particles in the events. (282)

124) The x_e distributions for the neutral particles in the events. (283)

125) Ratio of the numbers of positive and negative particles as function of x_e. The single photon events are compared with the π^o events for the p(Be+Cu) and π^-(Be+Cu) data. The π^o background in the single photon events has not been subtracted. (289)

LIST OF TABLES

1: List of direct-photon experiments at CERN and at Fermilab. (34)

2: Targets for E-706 1988 Data Run. (47)

3: The active areas and z-positions of the PWC modules. (51)

4: LAC cell structures and depths in interaction lengths (λ_o), radiation lengths (X_o) and cm. (59)

5: Trigger Characteristics for E-706 1988 Data Run. (81)

6: Average trigger thresholds for 1988 E-706 Data Run. (85)

7: Summary of the E-706 1987 - 1988 data run. (91)

8: Particle compositions for the LAC calibration beam. (94)

9: Charge response of LAC at various times during the experimental run. (100)

10: Characteristics of SSD and PWC view tracks. (161)

11: Efficiency of PWC tracks. (164)

12: Number of events surviving various cuts. (209)

13: The percentage of events where the highest p_T particle residing in the hemisphere away from the high p_T photon, was a neutral hadron a π^o or charged hadron. The measurements have not been corrected for reconstruction inefficiencies and detector acceptance. (244)

14: Fraction of the momentum of the high p_T photon or π^o carried by the fastest and second-fastest charged particles. (183)

15: Fragmentation fraction D(x_e) for $p_T > 5.0$ GeV/c. Both charged and neutral particles are counted. (285)

The page where the table can be found in the text is indicated in parenthesis at the end of the table listings.

16: Fragmentation fraction $D(x_e)$ for $p_T > 5.0$ GeV/c. Only charged particles are counted. (286)

17: Results of the $D(x_e)$ fits. The data in the range $0.1 < x_e < 0.9$ were used in the fit. (287)

1. INTRODUCTION

During the last fifteen years a theory was developed to describe the strong interactions of the constituents of elementary particles called "partons". This theory is called Quantum Chromodynamics (QCD), in analogy to the theory which describes the electromagnetic interactions between charged particles, called Quantum Electrodynamics (QED). There are many analogies between QED and QCD as well as many differences. For example, in QED the mediator in the particle interactions is the photon, and the coupling between charged particles and photons is given by the fine structure constant $\alpha \sim 1/137$. In QCD the partons interact through particles called "gluons". The gluons are the field carriers of the strong interactions and, unlike the photons they can also interact with themselves. The coupling constant in QCD, α_s, becomes weaker as the relative energies of the particles increase. It takes the value of ~ 0.2 at energies around 1 GeV.

There are three kinds of partons; the quarks (q), antiquarks ($\bar{q}$) and gluons[5]. All hadrons are composed of either three quarks (called baryons) or a quark and an antiquark (called mesons). These quarks are called valence quarks. In addition to the valence quarks there is a "sea" of gluons and $q\bar{q}$ pairs inside hadrons. The partons are very strongly bound inside the hadron and cannot exist as free particles. This property is called asymptotic freedom. In interactions involving high momentum transfer (i.e., high compared with the hadron mass) partons can be regarded as being independent. This theoretical model is referred as "parton model" (Ref. [1], [2], [3], [4]).

The parton model, and consequently QCD, have been tested by various experiments. There are three kinds of processes studied by experimenters which have

been successfully interpreted by the parton model.

a) Deep Inelastic lepton Scattering (DIS) where the underlying process is the scattering of the incident lepton on nucleons.

b) e^+e^- annihilation where $q\bar{q}$ pairs are produced and decay into hadrons. This quark decay into hadrons is called fragmentation or hadronization.

c) High transverse momentum hadron-hadron (h-h) interactions where QCD predicts that the particles produced with high transverse momentum (p_T) result from the hard scattering between the constituents of the hadrons, i.e, the partons[6].

An example of high p_T h-h interactions is photons at large p_T. QCD predicts a significant yield of photons at high p_T. A photon which comes directly from the interaction of the constituents of the colliding hadrons, rather than from the decay of π^0s, is called a direct photon. The experiment described in this thesis studies the characteristics of events with large p_T direct photons produced by 530 GeV proton and pion beams on nuclear targets.

The thesis is divided into the following chapters:

Chapter 1: INTRODUCTION.

Chapter 2: PHYSICS MOTIVATION. Describes the physics motivation of the experiment.

Chapter 3: THE EXPERIMENT. Describes the experimental apparatus.

Chapter 4: LAC CALIBRATION. Describes the Liquid Argon Calorimeter (LAC) Calibration.

Chapter 5: OFFLINE DATA ANALYSIS. Describes the data reconstruction

programs and their performance.

Chapter 6: HIGHER LEVEL DATA ANALYSIS. Describes the cuts used to reduce the reconstructed data to the sample used for the final analysis.

Chapter 7: RESULTS AND CONCLUSIONS. Presents the physics results and final conclusions.

The projects in which the author of this thesis was most intensively involved include: a) Construction of the large Liquid Argon Calorimeter (LAC); b) Calibration of the LAC; c) Shakedown of the spectrometer; d) Acquisition of the data employed in this thesis; e) Development of the computer code used to reconstruct hadrons from the data obtained from the LAC; and f) The analysis of the data presented in this thesis.

2. PHYSICS MOTIVATION

In this chapter the theoretical background and overall motivation for E-706 experiment and this Thesis are described. In the first section of this chapter some frequently used kinematic variables are defined. The second section is an introduction to the phenomenology of high p_T processes. The next three sections briefly describe the production of direct photons, π^0s and jets. The sixth section describes experimental methods used in this thesis. The next section presents results from other experiments which are relevant to the physics presented in this thesis. Finally the last two sections describe the physics goals of E-706 and the physics goals of this thesis.

2.1. Kinematics

A short review of the variables which are commonly used to describe high energy particle collisions follows. Consider the inclusive single particle reaction (Figure 1),

$$A + B \rightarrow C + D \tag{2.1}$$

The kinematics of the above reaction can be expressed through the Mandelstam variables. If p_A, p_B, and p_C are the four vectors of the initial state hadrons (A and B) and the final state hadron (C), respectively, the Mandelstam variables are defined as,

$$s = -(p_A + p_B)^2, \;\; t = -(p_A - p_C)^2, \;\; and \;\; u = -(p_B - p_C)^2 \tag{2.2}$$

When particles A, B, C and D are hadrons they consist of quarks, antiquarks and gluons. The constituents of particles A, B, C, and D will be labeled as a,

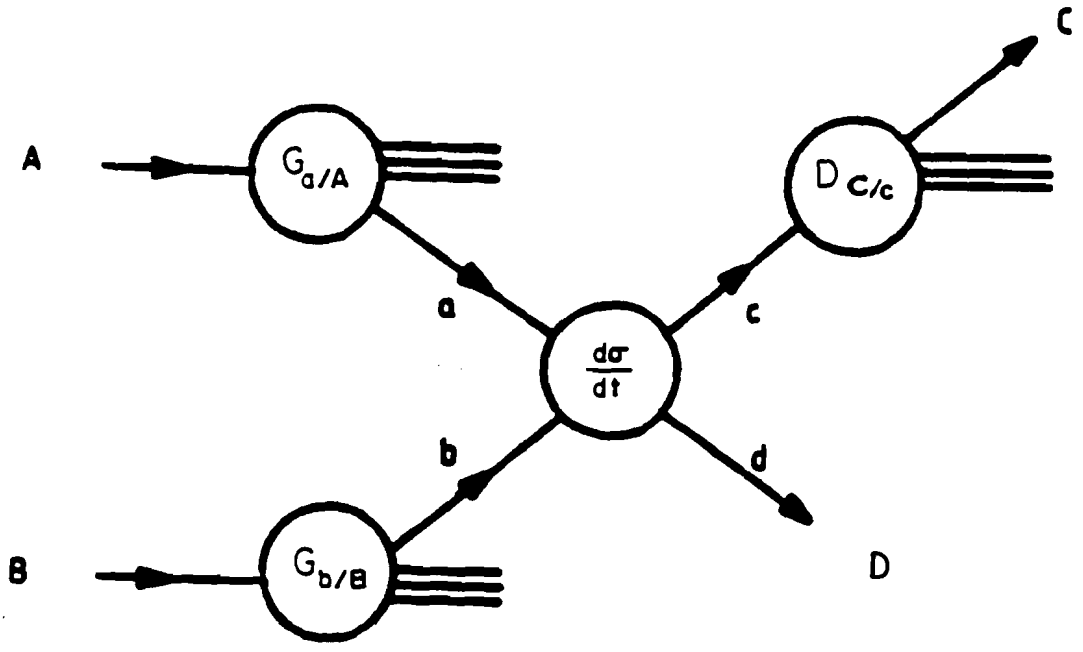

Figure 1: The hadronic interaction $AB \to CD+$ other particles at large p_T in terms of the parton sub-process $ab \to cd$.

b, c, and d respectively.* A set of Mandelstam variables can be defined for the hadron constituent scattering subprocess $a + b \rightarrow c + d$. Here we neglect any momentum the partons a and b may have in directions transverse to the beam direction, and also neglect the masses of both the hadrons and partons since they are small compared to the momenta. The hadron A contains a parton carrying a fraction $x_a = q_a/p_A$ of its momentum, where $0 \leq x_a \leq 1$ and q_a refers to the colliding hadron constituent's momentum. The outgoing parton c fragments to many particles, one of them being hadron C which carries parton c's momentum fraction $z_c = p_C/q_c$, where $0 \leq z_c \leq 1$. The corresponding Mandelstam variables for the parton subprocess, $ab \rightarrow cd$, are

$$\hat{s} = -(q_a + q_b)^2 = x_a x_b s \tag{2.3a}$$

$$\hat{t} = -(q_a - q_c)^2 = x_a t/z_c \tag{2.3b}$$

$$\hat{u} = -(q_b - q_c)^2 = -(\hat{s} + \hat{t}) \tag{2.3c}$$

Since the particles are considered to be massless, Mandelstam variables satisfy the equation $\hat{s} + \hat{t} + \hat{u} = 0$.

The momentum of each particle has a transverse component (p_T) and a longitudinal component (p_L) with respect to the beam direction. When p_T and p_L are normalized by the maximum momentum that a particle can carry after the interaction, they are called x_T and x_F respectively. If the masses of the particles

* The notation of reference [8] is employed throughout this chapter.

are neglected we can write

$$x_T \equiv \frac{p_T}{p^*_{max}} = \frac{2p_T}{\sqrt{s}} \tag{2.4}$$

$$x_F \equiv \frac{p^*_L}{p^*_{max}} = \frac{2p^*_L}{\sqrt{s}} \tag{2.5}$$

where $\sqrt{s}$ is the available energy in the center of mass frame, and the asterisk indicates that the variable refers to the center of mass reference frame. The allowed range of x_T is (0,1) and the range of x_F is (-1,1).

The rapidity, y, of a particle with energy E, is defined by the following formula

$$y \equiv \frac{1}{2}\ln\frac{E+p_L}{E-p_L} \xrightarrow{(for\ p_T>>m)} -\ln[\tan(\theta/2)] \tag{2.6}$$

The rapidity is analogous to the production angle of a particle (θ). Under a boost in the beam direction from the center of mass frame to the laboratory frame with velocity β the rapidity becomes,

$$y_{LAB} \rightarrow y_{CM} + \tanh^{-1}\beta \tag{2.7}$$

Hence the rapidity distribution dN/dy is invariant. In scattering processes where particles are produced with high p_T, the rapidity takes values close to zero in the center of mass system (CM). The particles produced at y_{CM}=0 are moving in directions perpendicular to the direction of the colliding particles.

2.2. High p_T Phenomenology

Hadrons are regarded as clusters of confined partons, i.e., quarks (q), antiquarks ($\bar{q}$) and gluons (g). Figure 1 shows the interaction of hadrons A and B. The transverse momentum, p_T, is the conjugate variable to the impact parameter of the collision. Large p_T implies that the basic scattering process has occurred at a small impact parameter. In the parton picture this means that two of the partons have passed very close to each other and have scattered at wide angles. Thus the parton - parton interaction $ab \rightarrow cd$ leads to a large p_T event $AB \rightarrow CD$ + other particles. This type of event is rare but reveals the fundamental parton interaction.

The theoretical framework for hadronic interactions is the parton model, using QCD to describe interactions between the partons. There are many publications describing the parton model, the inclusive production of particles and QCD. In the following the theoretical framework for describing the production of high p_T particles in hadronic collisions is reviewed. The p_T component is directly related to the invariant mass of an appropriate momentum transfer (Q^2) which characterizes the collision and it is invariant under Lorentz transformations. In the parton subprocess $ab \rightarrow cd$, Q^2 is the momentum exchanged in the interaction between primary partons a and c. When Q^2 is large the angle (θ) between the emerging parton's direction and the collision axis is large.* In high p_T interactions most of the primary quark momentum after the collision is transverse to the collision axis and $Q^2 \propto 2{p_T}^2$. Therefore large p_T implies[9] large Q^2.

* Neglecting the masses $Q^2 = 2E_aE_c(1 - \cos\theta)$.

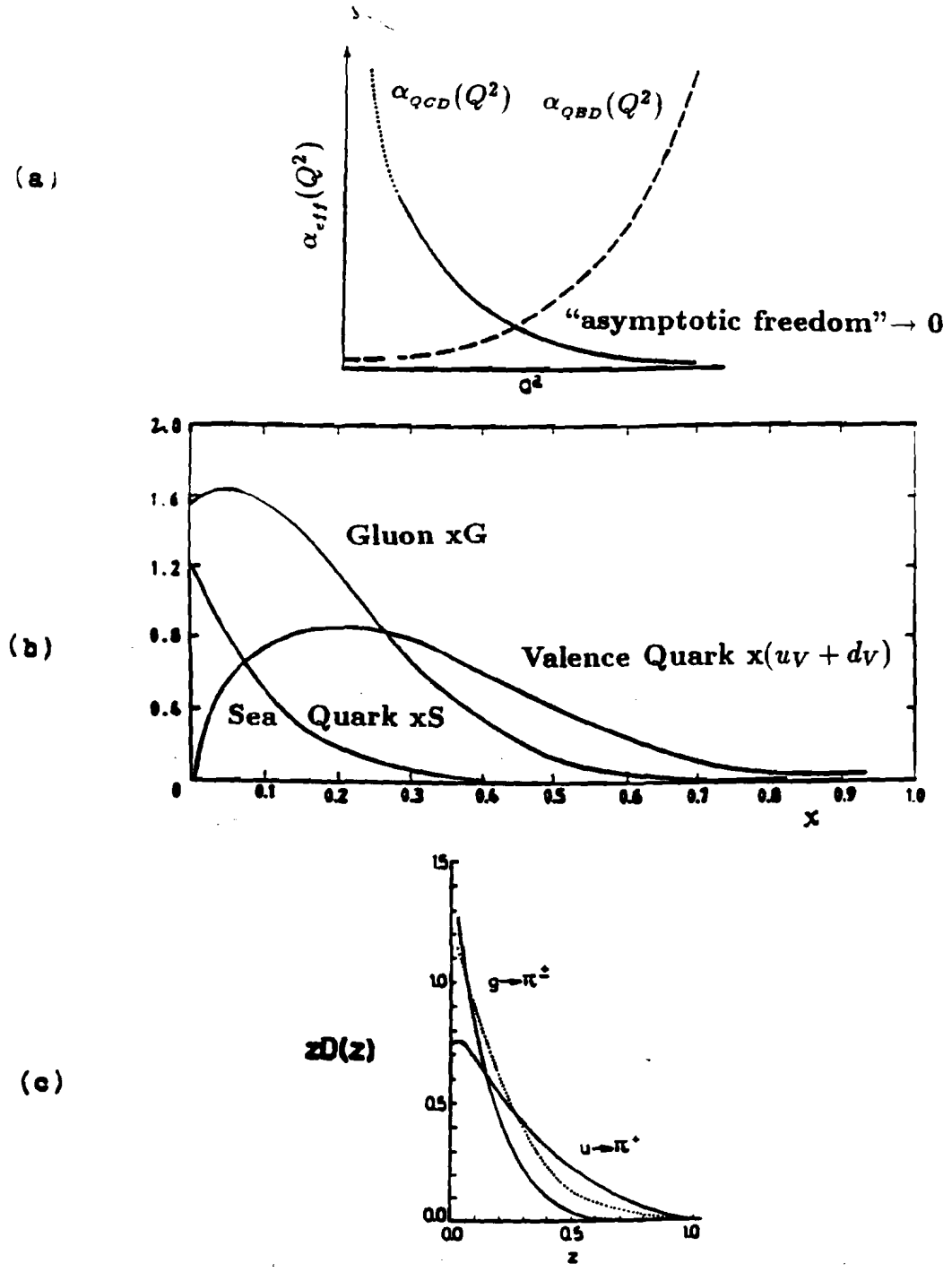

Figure 2: a) Q^2 behavior of the strong and electromagnetic coupling constants. b) Gluon and quark distribution functions in proton for $Q^2 = 4\ GeV/c^2$. c) The u quark and gluon fragmentation functions (solid curves) as they were calculated by the Lund group (see Ref. [9]). The dotted curve is the gluon fragmentation distribution if the events with $z \leq 0.05$ have been discarded.

In high p_T hadronic processes the interaction is governed by the strong interaction force. The strong interaction is the result of the exchange of colored massless vector gluons between colored quarks. One of the key features of the strong interactions is the property of asymptotic freedom (AF). AF predicts the weakening of the effective quark - gluon coupling constant at short distances (or large Q^2). AF allows the application of perturbative techniques calculating cross sections for strong interaction processes. The behavior of the strong coupling constant is given by

$$\alpha_s(Q^2) = \frac{12\pi}{(33 - 2f)\ln(Q^2/\Lambda^2)} \tag{2.8}$$

with f denoting the number of quark flavors that can contribute to the interaction and the constant Λ sets the scale for the Q^2 dependence. The value of α_s can be estimated from the detailed measurements of the quark distributions in nucleus, and then from Equation 2.8 the value of the scale parameter Λ is derived. Measurements[11] of Λ give values in the range 0.1 to 0.5 GeV. Equation 2.8 is valid when $Q^2 \gg \Lambda^2$. As $Q^2 \rightarrow \infty$, then $\alpha_s \rightarrow 0$, which makes the application of perturbation theory possible. Figure 2a shows the Q^2 behavior of the strong coupling constant. For comparison the electromagnetic coupling constant is also shown.

Figure 1 shows a schematic representation of the hadronic scattering process $AB \rightarrow CD$ + other particles. This interaction can be characterized by the following three quantities:

i) The distribution function $G_{a/A}(x)$ is the probability of finding a parton a in hadron A with a momentum fraction, $x = p_a/P_A$, lying between x and x+dx.

ii) The distribution function $G_{b/B}(x)$ is the probability of finding a parton b in a hadron B with a momentum fraction, $x = p_b/P_B$, lying between x and x+dx.

iii) The fragmentation function $D_{C/c}(z)$ is the probability of obtaining a hadron C with momentum fraction, $z = P_C/p_c$, between z and z+dz from parton c.

iv) The scattering cross section for the constituents a and b is denoted by $d\sigma/dt$.

In the parton model hard scattering is described by the lowest order subprocesses which are two-body scatterings. If the calculations are made to all orders of perturbation theory, and only the leading logarithmic contribution from each order is retained, this is called the leading logarithmic approximation.

The total invariant cross section for the reaction shown in Figure 1 in the leading logarithmic approximation is:

$$E_C \frac{d\sigma}{d^3 p_C}(AB \to C + X) = \sum_{abcd} \int dx_a dx_b dz_c G_{a/A}(x_a, Q^2) \tag{2.9}$$

$$\cdot G_{b/B}(x_b, Q^2) D_{C/c}(z_c, Q^2) \frac{\hat{s}}{z_c^2 \pi} \frac{d\sigma}{d\hat{t}}(ab \to cd) \delta(\hat{s} + \hat{t} + \hat{u})$$

with the subprocess calculated using the strong coupling constant of Equation 2.8. The particles D in Figure 1 were replaced by X to emphasize that the above cross section is summed over all particles X. The delta function insures the constraint $\hat{s} + \hat{t} + \hat{u} = 0$. The initial and final partons have been assumed to be collinear with the corresponding initial and final hadrons, i.e., no parton transverse momentum (k_T) smearing has been included.

The single hadron inclusive invariant cross section can be calculated from Eq. 2.9. The arguments of the delta function can be substituted by the parton kinematic variables of Equations 2.3, and the z_c integration carried out. The single

hadron cross section reads[8]

$$E_C \frac{d\sigma}{d^3p_C}(AB \to h + X) = \sum_{abcd} \int_{x_{amin}}^{1} dx_a \int_{x_{bmin}}^{1} dx_b G_{a/A}(x_a) \cdot$$

$$\cdot G_{b/B}(x_b) D_{h/c}(z_c) \frac{1}{z_c \pi} \frac{d\sigma}{d\hat{t}}(ab \to cd)$$

where

$$z_c = \frac{x_T}{2x_b} e^{-y} + \frac{x_T}{2x_a} e^{y}$$

$$x_{bmin} = \frac{x_a x_T e^{-y}}{2x_a - x_T e^{y}} \quad and$$

$$x_{amin} = \frac{x_T e^{y}}{2 - x_T e^{-y}}$$

At present the fragmentation and distribution functions cannot be obtained using perturbation theory and are obtained from various types of hard scattering processes. The quark distribution functions for the proton have been measured in Deep Inelastic lepton - nucleon Scattering experiments (DIS), [12] i.e., in processes such as $eA \to eX$, $\mu A \to \mu X$, $\nu_\mu A \to \mu^- X$, and $\hat{\nu}_\mu A \to \mu^+ X$ with a large momentum transfer between the leptons and the nucleon. Gluon distributions have been studied with DIS data and J/Ψ production experiments[13]. These measurements are not very precise, making comparisons between experiment and theory difficult. The fragmentation function $D_{C/c}(z_c, Q^2)$ has been measured directly in the process $e^+e^- \to CX$. In such reactions, the initial state has no hadrons which makes these reactions simpler to interprete. Gluons are not produced directly in e^+e^- annihilation or in DIS since they do not carry weak or electromagnetic charge.

Figure 2b shows the gluon and quark[14] (both sea and valence) distribution functions for $Q^2 = 4\,(GeV/c)^2$. Figure 2c shows the u quark and gluon fragmentation functions (solid curves) as they were calculated by the Lund group (see Ref. [10]). The gluon fragmentation function comes out to be softer than that of the quark.*

2.3. Direct Photon Production

In this subsection the QCD subprocesses for the direct photon production are discussed.

There are advantages in studying high p_T direct photons produced in the hard scattering of hadron constituents. The most important are[15]:

1) The are only two first order parton processes: $gq \rightarrow g\gamma$ and $\bar{q}q \rightarrow g\gamma$.

2) The coupling of the photons to quarks is well understood.

3) The photons which are produced in the hard scattering are directly detectable. The measurements can be directly compared to theory with no need of a fragmentation model. This is in contrast to partons whish cannot be detected directly. Partons are observed only through their fragmentation into hadrons.

4) The kinematics (i.e., energy and angle) of the direct photon can be measured with good precision.

On the other hand there is a difficulty in the direct photon experiments relative to DIS experiments or e^+e^- experiments or hadron - hadron experiments all which study partons. The yield of direct photons relative to jets of the other experiments

* The dotted curve is the gluon fragmentation distribution if the events with $z \leq 0.05$ have been discarded. This cut was was used by UA-2 experiment in CERN (other experiments used similar cuts) and reduces the difference between quark and gluon distributions.

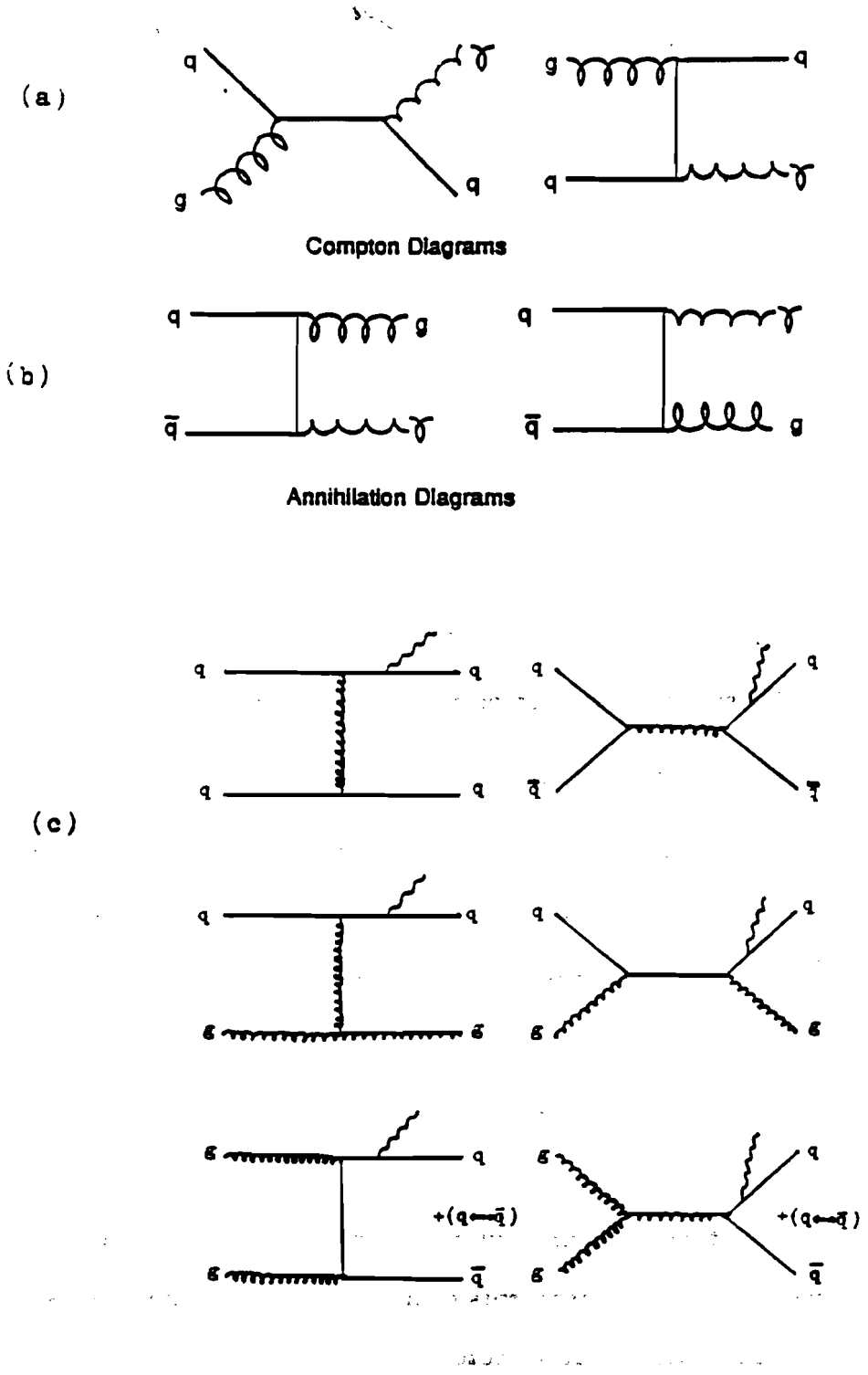

Figure 3: Dominant Feynman diagrams for direct photon production.

is smaller by $\sim 10^{-2}$ because the photon production is reduced by a factor α/α_s compared to jets. Also many more graphs and color factors enhance to the jet yield relative to the direct photon yield.

High p_T photons are produced through several mechanisms. The main sources of high p_T photons are the following:

i) From subprocesses where the photon is produced without any intermediate fragmenting quark or gluon. To lowest order in $\alpha_s(Q^2)$ the two subprocesses (Figure 3a and 3b) predicted by QCD are

$$\bar{q}\, q \;\rightarrow\; g\, \gamma \qquad (\textit{Annihilation process})$$

$$g\, q \;\rightarrow\; q\, \gamma \qquad (\textit{Compton process})$$

The cross section expressions for these two subprocesses (after performing color sums and spin averages) are

$$\frac{d\sigma}{dt}(q\bar{q} \rightarrow g\gamma) \;=\; \frac{-8\pi\alpha\alpha_s}{9s^2} e_i{}^2 (\frac{\hat{u}}{\hat{t}} + \frac{\hat{t}}{\hat{u}}) \tag{2.10}$$

$$\frac{d\sigma}{dt}(gq \rightarrow q\gamma) \;=\; \frac{-\pi\alpha\alpha_s}{3s^2} e_i{}^2 (\frac{\hat{u}}{\hat{s}} + \frac{\hat{s}}{\hat{t}}) \tag{2.11}$$

where e_i is the fractional charge of the ith quark and $\hat{s}$, $\hat{t}$, and $\hat{u}$ are the Mandelstam variables for the parton subprocess defined in section 2.

ii) The quark fragmentation into a photon (by bremsstrahlung). In this case the photon takes only a fraction of the parton's momentum to create a high p_T photon (Figure 3c). Here the photon is also accompanied by additional hadrons from the fragmenting quark. This mechanism is of the order of $\alpha\alpha_s{}^2$. Calculations indicate that the $qq \rightarrow qq\gamma$ process contributes, for moderate x_T ($0.1 \leq x_T \leq 0.3$), at about

30% of the Born term of the Compton graph[16]. The ratio of the components contributing to the direct photon cross section in pp collisions at $\sqrt{s}$=63 GeV, of the two first order diagrams and the bremsstrahlung diagrams[17],[8] is shown in Figure 4a. The two curves, referred as Set 1 and Set 2, are calculated by using nucleon parton distributions obtained from the analysis of data from different experiments[8]. In Set 1 the data comes from J/ψ, Υ, and high - mass dilepton production experiments, and in Set 2 the data comes from deep inelastic lepton scattering experiments. The curves show that the bremsstrahlung contribution is not very large at $5 < p_T < 9$ GeV/c and the fall-off with p_T is slow.

The relative importance of the Annihilation and Compton subprocess in hadron - hadron collisions is determined by two factors:

a) Type of incident particle: For p_T higher than 6 GeV/c the Annihilation subprocess dominates the Compton one in the $\bar{p}p$, and $\pi^- p$ interactions. The Compton subprocess dominates[9] in the pp collisions due to the smallness of the antiquark content of the interacting partons. The presence of a valence $\bar{u}$ quark (q= -2/3) in the π^- and a valence $\bar{d}$ quark (q= 1/3) in the π^+ causes the annihilation subprocesses to make a relatively large contribution in the π interactions compared to the p interactions. The Annihilation contribution in the π^+ case is reduced by a factor of 4 compared to the π^- reaction because of the charge difference in the valence antiquarks. The Compton subprocess dominates for all p_T in the π^+ reactions.

b) Kinematic region: For the $\bar{p}p$, $\pi^- p$ collisions at values of $x_T < 0.5$ the Compton subprocess dominates while at $x_T > 0.4$ the Annihilation subprocess is the dominant one. The dominance of $gq \rightarrow q\gamma$ subprocess[9] stems from the fact

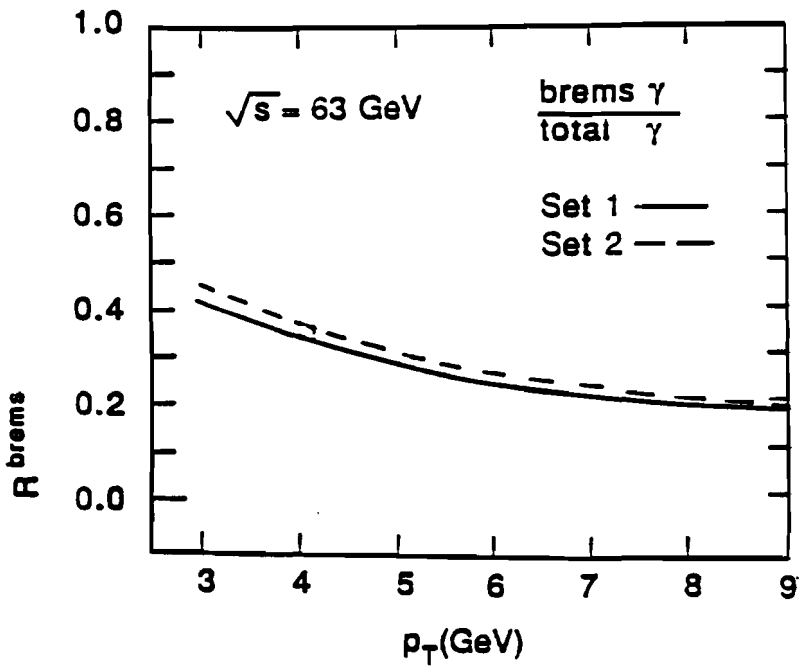

Figure 4: Ratio of the two components contributing to the direct photon cross section in pp collisions.

that for both pions and protons the gluon distribution is larger than the $\bar{u}$ or $\bar{d}$ quark distributions in the region $x_T \leq 0.3$.

2.4. π^o Production

π^os decay into two photons with branching ratio of 98.8%. Since the mean lifetime[18] of π^o is 8.4×10^{-17} sec, it decays immediately after its production in the target. It is very important to understand π^o production and decay in order to estimate precisely their contribution to the background to single photon events.

There is another advantage in studying π^o events. The π^o is produced with various mechanisms. It is produced as a "decay product" of the quarks and gluons from the lowest order subprocesses $qq \rightarrow qq$, $q\bar{q} \rightarrow q\bar{q}$, $gq \rightarrow gq$, $q\bar{q} \rightarrow gg$, $gg \rightarrow q\bar{q}$, and $gg \rightarrow gg$.

Since the π^o and η are produced through parton fragmentation (see next section) in contrast to direct photons[15], we expect the ratio of number of direct photons to the number of π^os (γ/π^o) to increase with increasing p_T (at the same $\sqrt{s}$). Here we list several effects that contribute to the increase of γ/π^o with p_T:

1) The fragmentation function becomes smaller as the z of the hadrons increases (i.e., at higher p_T).

2) The gluon distributions become small at high gluon x values reducing the contribution of graphs like $gg \rightarrow gg$ or $qg \rightarrow qg$ to π^o jet yields.

3) When the Q^2 of the parton process increases, the strong coupling constant decreases thus favoring the direct photon production relative to jet production (i.e., π^os).

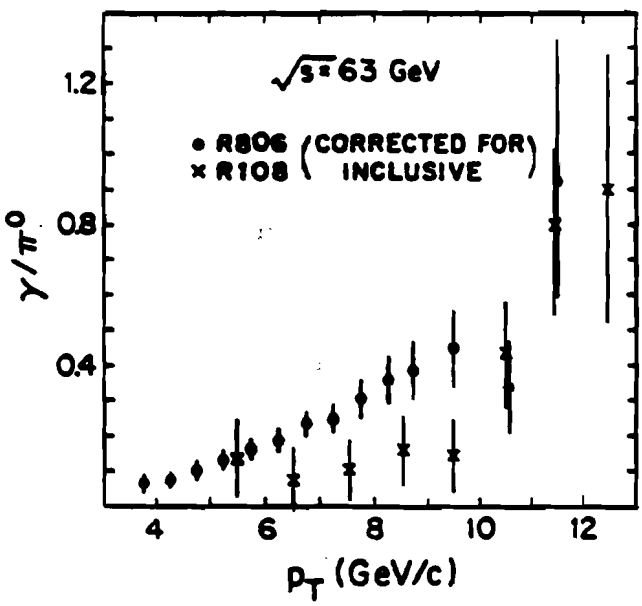

Figure 5 : A comparison to γ/π^o production ratios.

Figure 5 shows the γ/π^{o} ratio from the experiments R806 and R108 at the CERN - ISR, for pp collisions at $\sqrt{s}$= 63 GeV. The data have been corrected for the expected sources of background to the direct photon signal. For the p_T range 5 to 9 GeV/c the ratio increases about 30%.

2.5. Jet Production

A Jet is the hadronic materialization of a parton. Experimentally, a jet appears as clusters of particles traveling approximately in the direction of the parent parton. The mean transverse momentum of particles in the jet with respect to the parton momentum vector is rather small (around 300 MeV/c). In hadronic collisions (such as pp collisions) the scattered partons evolve into the "trigger" jet and the "away" jet and the non-interacting partons which evolve into the beam and target jets, all jets fragmenting independently. The existence of the jets originating from the non - interacting partons (i.e., the spectators) is the most obvious difference between a hadron - hadron collisions and e^+e^- annihilations. Thus the task to understand jets in hadronic collisions is more complex than for e^+e^- annihilations.

Consider the simplified interaction indicated in Figure 6 (top graph). Two hadrons are moving along the z-axis towards each other with momenta $P_1 = P_{1z}$ and $P_2 = P_{2z}$ in the CM system of the hadrons. Each parton, i, of hadron 1 carries a momentum P_1, similarly for hadron 2. From the interaction of one parton from each hadron 2 a photon and a quark (or gluon) are produced back to back in the parton rest frame. The quark or gluon fragments to a jet and carries momentum $P_{jet} = \sum_i P_i$ where the summation runs over all particles in the jet.

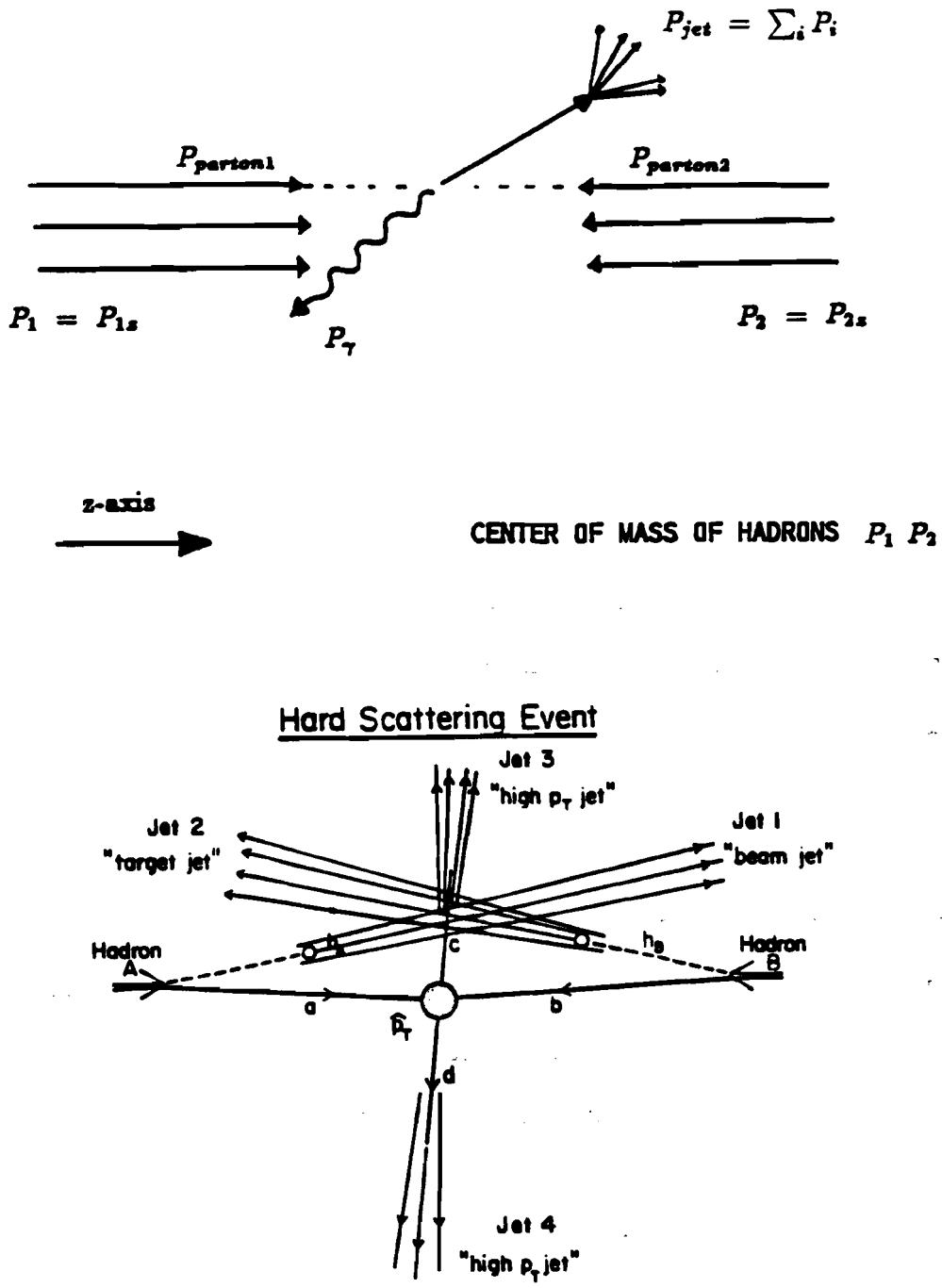

Figure 6: (top): Simplified picture of a pp collision. (bottom): Illustration of hard scattering event which consists of four jets.

The photon's momentum is P_γ. If it is assumed that the partons are massless and their intrinsic transverse momentum (k_T) is zero, then in the parton-parton CM system the momentum of the jet equals the photon momentum and the jet axis makes an azimuthal angle of 180 degrees relative to the photon direction.

Some of the partons are not as significantly affected by the collision of the two hadrons. These partons, called spectators, continue to travel along the initial direction of the hadrons. After the collision they may carry a significant fraction of the parent hadron's momentum and appear at values of $|x|$ close to 1. These partons may be so little influenced that they combine to reform the parent hadron. In this case one finds in the final state a "leading particle" with $|x|$ close to 1 which is basically the incident hadron with slightly reduced momentum. Those partons which travel slowly in the center of mass at the moment of collision, produce new hadrons, nearly at rest. It is this central particle production (at $x \simeq 0$, $y_{CM} \simeq 0$) which populates the center of mass rapidity distribution in the region around zero. This region is also called the "central region". Most high energy hadron interactions, low p_T, result in two groups of particles. One group contains fragments of the hadron with momenta close to the initial parent hadron momenta, and the other group contains fragments of the hadron with low momenta in the h-h CM system. Figure 6 (bottom graph) pictures the rare production of high p_T particles when partons from the beam and target hadrons interact with a hard large - angle elastic scattering. These events consist of four jets. Jet 3 and Jet 4 have large p_T and they result from the fragmentation of the outgoing partons. Jet 1 and Jet 2, the spectator jets, have small p_T and they result from the residual of the beam and target hadrons.

Collider experiments at CERN (UA1, UA2) have seen very clear evidence for jets in hadronic collisions at CM energies above $\sqrt{s} = 500$ GeV. One of the major tasks of a direct photon experiment, which is capable of identifying jets, is the reconstruction of the jet recoiling against the single photon. As stated in Reference [20], the simultaneous measurement of the four-vectors of the high p_T photon and the recoiling awayside jet allow the parton-level kinematics to be tightly constrained. Thus, the parton distributions and fragmentation functions can be directly determined. Without the away side jet measurements, only the integrals of the parton distributions can be determined.

2.6. Experimental Methods

This section describes several experimental methods, and techniques used in the measurement of direct photons and π^os. The advantages and disadvantages of these methods are also discussed.

A) Direct photons

In general, two different techniques have been employed by various experiments to extract the direct photon signal; the direct method and the conversion method. A brief explanation of the two techniques follows:

1. Direct method. The direct photons are defined as photons that do not come from decays (i.e., $\pi^o \rightarrow \gamma\gamma$,$\eta \rightarrow \gamma\gamma$). The single photon signal is measured from the excess of observed photons over the calculated backgrounds from the π^o, η and other decays. The main disadvantage of this method is that at high p_T the two photon spatial separation is small (sometimes comparable to the detector granularity), and some of the decays cannot be resolved. Also, in highly asymmetric

decays the low energy photon is not always detected. There are three different methods that have been used to extract the direct photon signal:

1a) Reconstruction method. The π° and η decays are identified by calculating the invariant mass of two photon combinations.

1b) Shower Profile method. The longitudinal and lateral shower profiles are measured. The direct photon shower widths are known (from calibrations and Monte Carlo studies) and very wide showers are rejected from the direct photon sample. Usually the wide showers are due to two coalesced photons from π°/η decays.

1c) Isolation method. The π° and η are usually part of a jet (i.e., they are accompanied by other particles) and the direct photons are usually unaccompanied (except for bremsstrahlung photons) by other particles. Thus, the direct photon events can be identified by employing isolation criteria.

2. Conversion method. This method is based on the fact that the π° and η decay into two photon final states. Thus π°s and ηs are twice as likely to convert in material as are the direct photons. In this method the fraction of direct photons is determined statistically by measuring the conversion rate.

There are two difficulties in the isolation of the direct photon signal in experiments which employ hadron beams and trigger on the direct photons:

1) Large backgrounds resulting from π° and η decays into $\gamma\gamma$. The main reasons for missidentifying the photons coming from meson decays are:

1a) One photon carries low momentum, and is not detected.

1b) At high momentum the $\gamma\gamma$ pair has too small a spacial separation to be

resolved in the detector.

1c) One of the two photons misses the detector.

2) In a fixed target experiment beam halo or μ bremsstrahlung fake the direct photon signal.

B) π^os

The electromagnetic decays of neutral hadrons ($\pi^o \rightarrow \gamma\gamma$, $\eta \rightarrow \gamma\gamma$, $\eta' \rightarrow \gamma\gamma$, $\Sigma^o \rightarrow \Lambda\gamma$, etc.) constitute the dominant source of background to the direct photon signal. The main source of such background photons from these decays is the π^o decay. Here we present the kinematical characteristics of π^o decays.

Both π^os and ηs are spin 0 particles, and thus decay isotropically in their rest (0r CM) frame. In the following discussion we will refer only to the π^o for simplicity. The same conclusions can be applied to η or any other spin 0 meson that decays into two photons. The two photons have energies $E_{CM} = m_{\pi^o}/2$ in the π^o center of mass frame. The photon energies in the laboratory frame are given (Figure 7) by

$$E_1 = \gamma(E_{CM} + \beta\, E_{CM} \cos\theta_{CM}) \tag{2.12a}$$

$$E_2 = \gamma(E_{CM} - \beta\, E_{CM} \cos\theta_{CM}) \tag{2.12b}$$

where θ_{CM} is the angle between the daughter photons and the line of flight of π^o, and γ and β are the Lorentz factors connecting the two frames. Obviously, $E_1 + E_2 = E$, where E is the π^o energy in the laboratory frame.

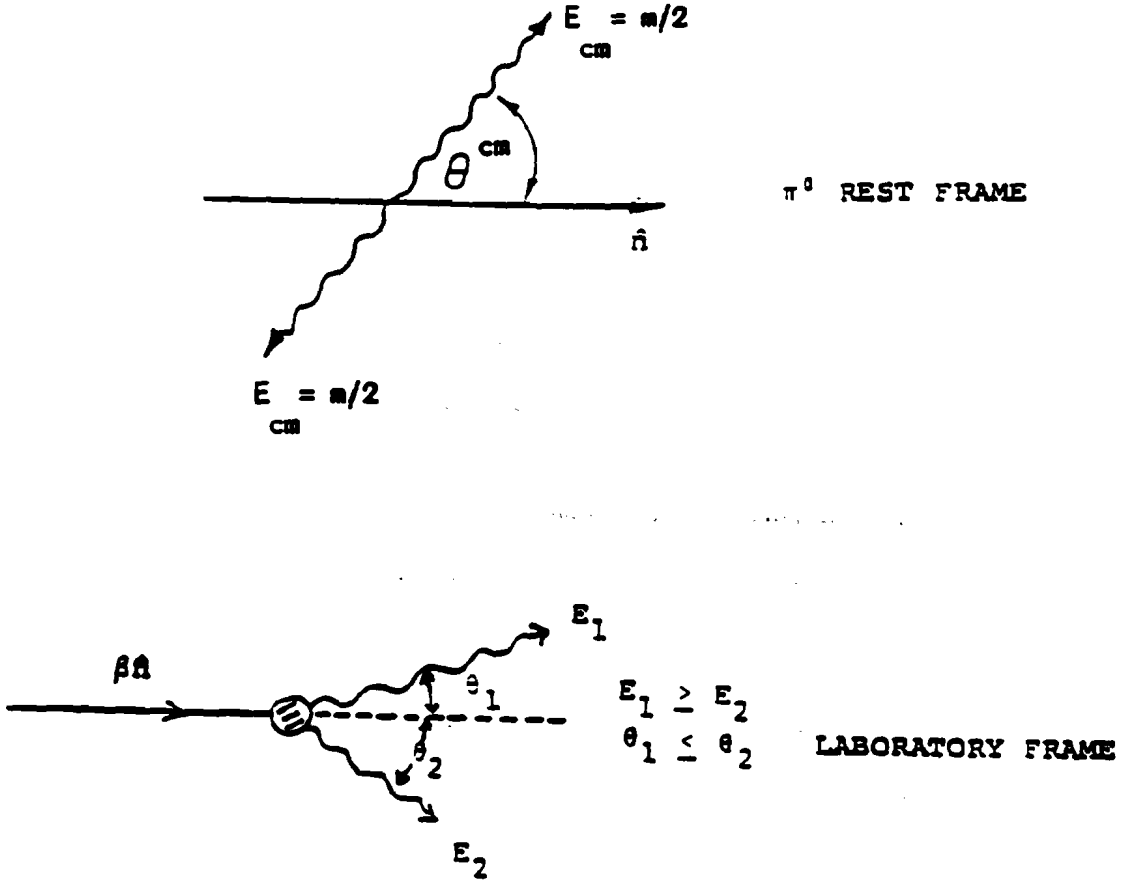

$$\text{Asymmetry} = \frac{|E_1 - E_2|}{(E_1 + E_2)} = \beta\,|\cos\theta_1^{cm}|$$

Figure 7: π° decay.

The energy asymmetry, A, is defined by

$$A \equiv \frac{|E_1 - E_2|}{(E_1 + E_2)} = \beta|\cos\theta_{CM}| \tag{2.13}$$

The opening angle in the laboratory frame as a function of asymmetry is

$$\cos\theta = 1 - \frac{2m_{\pi^\circ}{}^2}{(E_1 + E_2)^2 \cdot (1 - A^2)} \tag{2.14}$$

Since the π° decays isotropically, the distribution in $\cos\theta_{CM}$ is flat over the range (-1,1). Consequently, the asymmetry distribution is also going to be flat over the range (0,1). Two kinematic limits of particular interest are:

a) $\theta_{CM} = 0$. Then the Equations 2.12 become

$E_1 \simeq \gamma m_{\pi^\circ} = E$ *and* $E_2 \simeq 0$

b) $\theta_{CM} = 90°$. Then the Equations 2.12 become

$E_1 = E_2 = \gamma E_{CM} = E/2$

In the second case, $A = 0$, and it corresponds to the minimum opening angle (θ) in the laboratory frame

$$\theta^{min} \simeq 2\frac{m_{\pi^\circ}}{E} \tag{2.15}$$

A→1 corresponds to large opening angles. The detection efficiency of the lowest energy photons is small but improves as the photon energy increases. This is the main reason the experimentally measured asymmetry distribution falls off at asymmetries close to one. Values of A close to one give the largest background to the single photon signal.

2.7. Results from Previous Experiments

Eight experiments conducted at CERN performed measurements relevant to the ones presented in this thesis. Experiments R806/R807[22], R808[21], and experiment R108[26] at CERN ISR, experiments UA1/UA2[27],[34],[35],[36],[37],[38] at CERN $p\bar{p}$ collider, experiment WA-70[25],[24] at CERN SPS, experiment NA-24[40] at CERN SPS, and experiment UA-6[39] at CERN SPS. Experiments R806/R807, WA70, UA6 and NA24 used the direct method, experiment R108 used the conversion method, experiment UA1 used the longitudinal shape and isolation method, and experiment UA2 used the conversion and isolation method. Various experiments at PETRA (W. Germany) and SLAC (California) studied in detail the properties of jets produced in e^+e^- annihilation. In particular, the fragmentation characteristics of jets have been studied with charged particles at various CM energies by the TASSO[29],[30] and JADE[28] Collaborations.

Figures 8a and 8b show the distribution in the average of the sum of the transverse momentum of charged particles as a function of azimuth with respect to the trigger particle, from experiments R806/R807 and UA2 respectively.

Experiments R108, R806/R807, and WA-70 have investigated the charge distribution of recoiling particles. The relative density of positive to negative particles in the awayside (opposite to the trigger) hemisphere as a function of z is plotted in Figure 9. Since it was not possible to detect the entire jet, variables like, z_T or $z_{||}$, that are approximately equal to z, are employed. For a definition of the above variables see Ref. [7].

Figure 10 shows the density of recoiling particles ($\Delta\phi > 90°$ versus z) from ex-

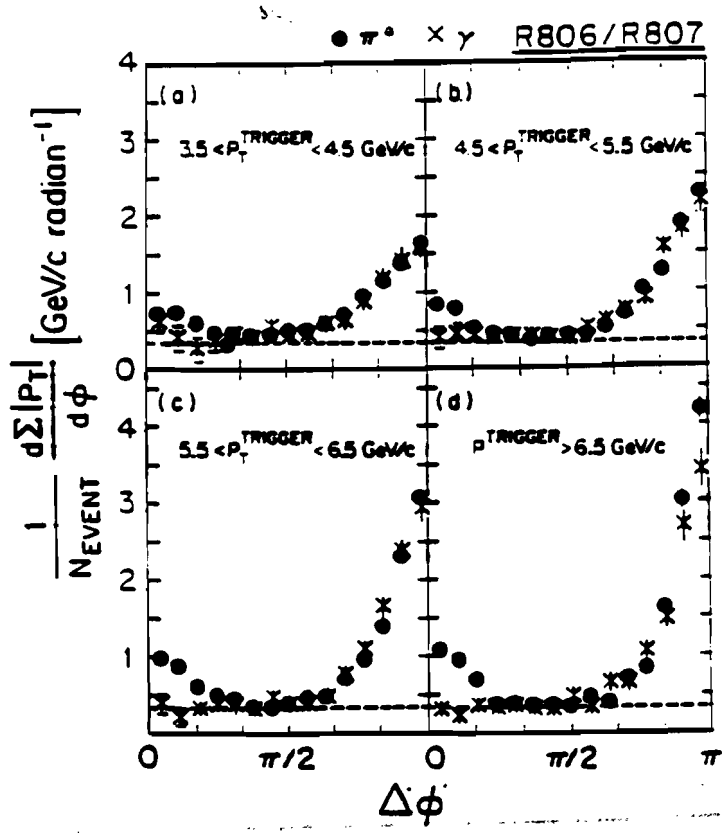

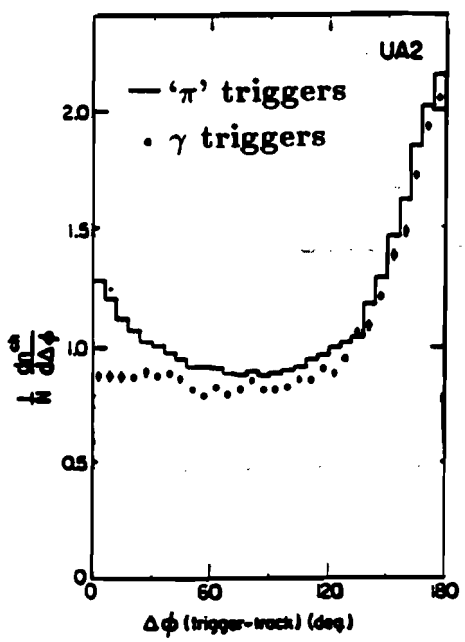

Figure 8: Distribution in the average transverse momentum of charged particles as a function of azimuth with respect to the trigger particle, from experiment a) R806/R807 and b) UA2.

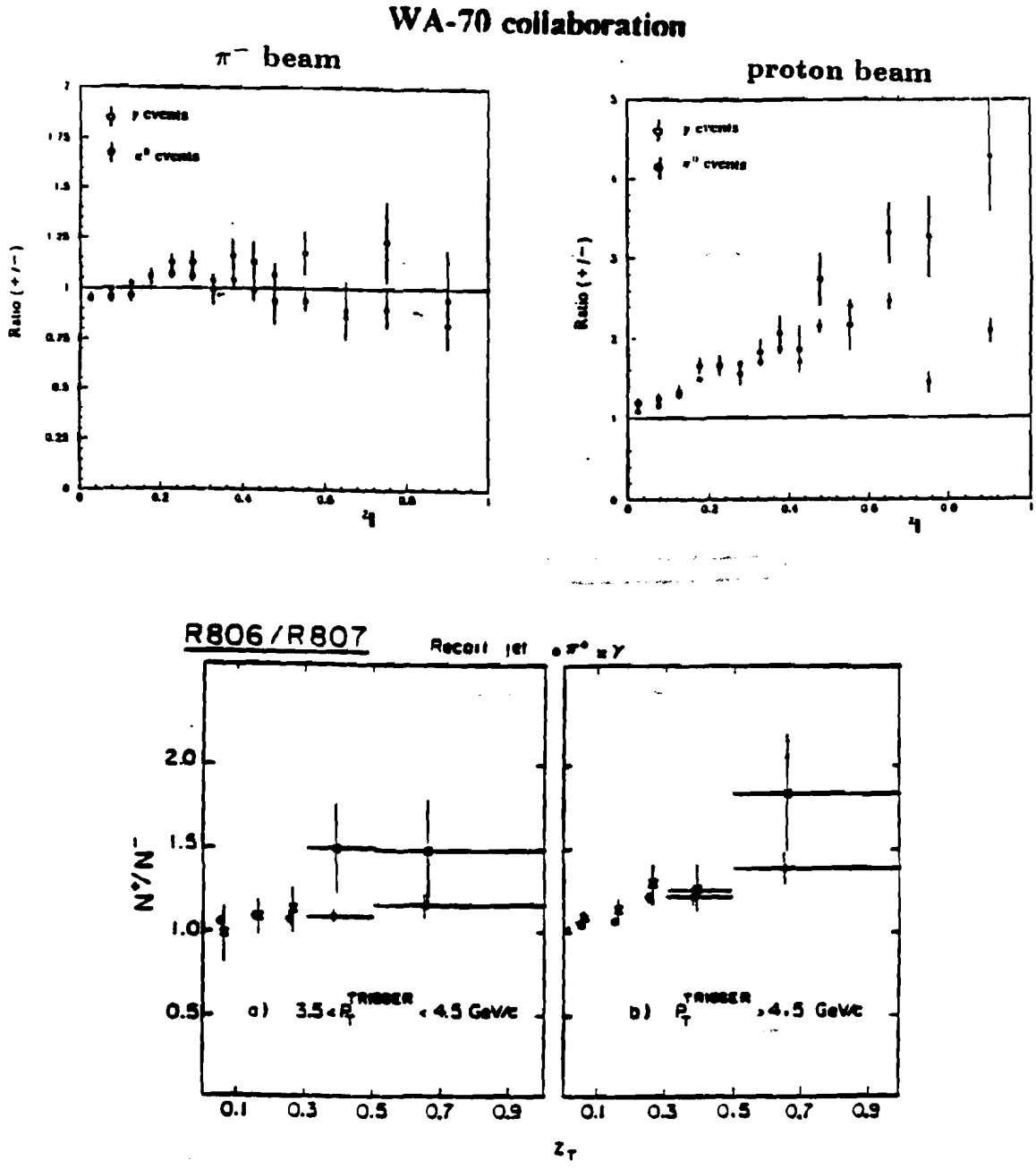

Figure 9: The relative density of positive to negative particles in the awayside (opposite the trigger) hemisphere as a function of z.

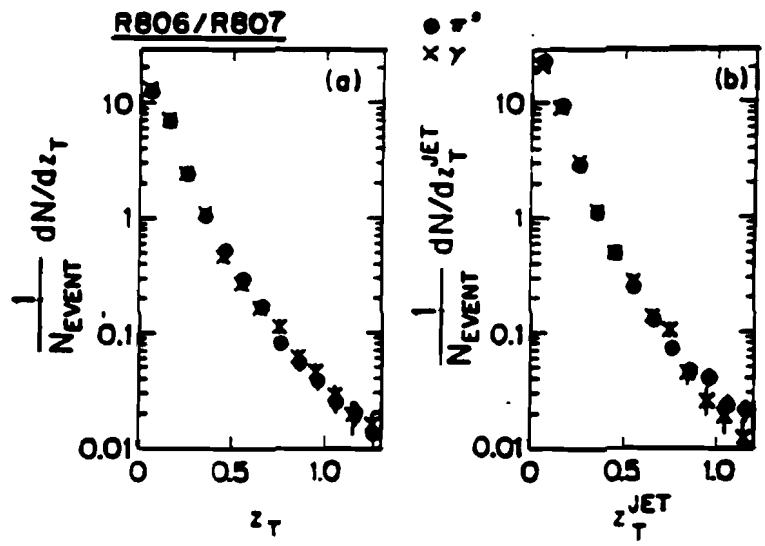

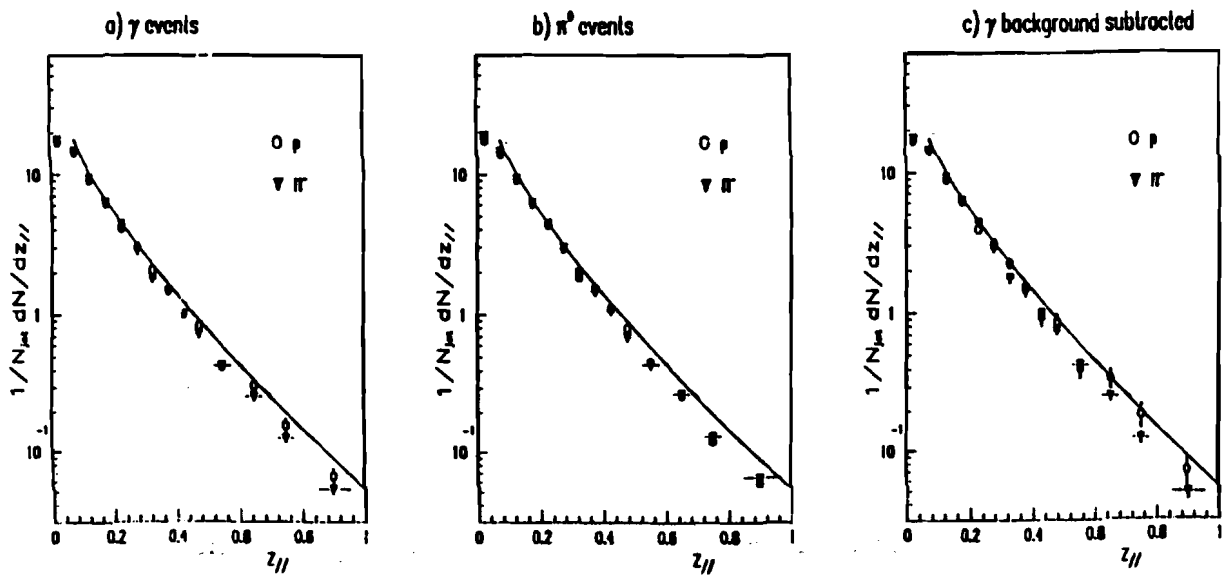

Figure 10: Density of recoiling particles ($\Delta\phi > 90°$ versus z from experiments R806, R807 (top) and WA-70 (bottom).

periments R806/R807 and WA-70. In the upper right hand plot of the R806/R807 results, the $z_T{}^{jet}$ was calculated by adding the momenta of all charged particles within a cone 45° around the trigger particle direction.

Figure 11 (top graph) shows the difference in rapidity between the two tracks with the highest p_T opposite the trigger, from experiments R806/R807. The dashed line corresponds to the estimated background. It was calculated by mixing particles from different events. The number of events is normalized to the number of single photons.

Figure 11 (bottom graph) shows the z distribution of the fastest and second fastest particles in the kinematic region $2 < Q^2 < 6\ GeV^2$, from a deep inelastic electron scattering experiment of DESY[43].

2.8. Physics Goals of Experiment E-706

Experiment E-706 was designed to measure single photon production cross section for p_Ts greater than 4 GeV/c, as well as to study the associated jets produced along with the single photon, using $\pi^+/\pi^-/K^+/K^-/p$ beams with incident energies up to 1 TeV. The E-706 apparatus covers the kinematical range $0.2 < x_T < 0.7$. The acceptance of the E-706 apparatus, for 530 GeV energy incident hadrons, is $-1.0 \leq y_{CM} \leq 1.0$ for photons and neutral hadrons, and $-1.0 \leq y_{CM} \leq 2.5$ for charged hadrons.

For comparison, Table 1 lists the kinematic regions explored by the previous experiments.

E-706 is a second generation experiment for the single photon production study. The primary physics goals of E-706 experiment are,

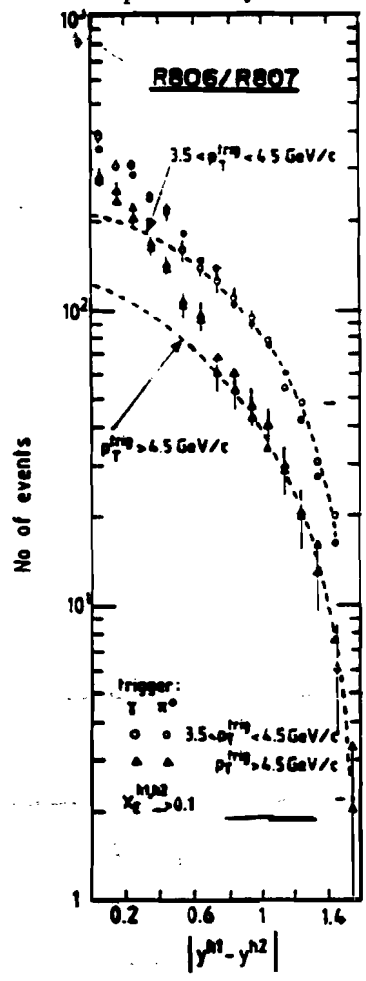

DESY deep-inelastic electron scattering.

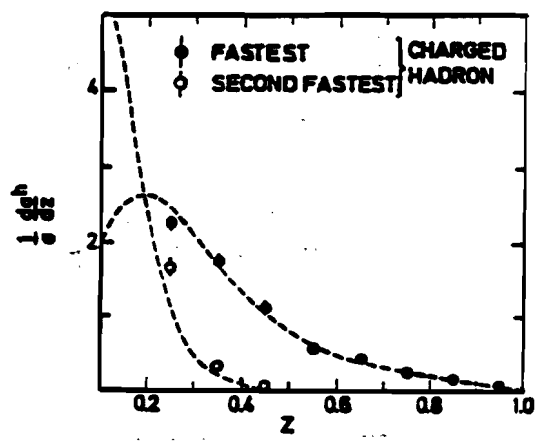

Figure 11: (top): Difference in rapidity between the two tracks with the highest p_T opposite the trigger, (bottom): z distribution of the highest p_T and second highest p_T particles in the kinematic region $2 < Q^2 < 6\ GeV^2$, from a deep inelastic electron scattering experiment in DESY.

	Machine	Experiment	$\sqrt{s}$ GeV	Reaction ($\int Ldt$ pb^{-1})	P_T GeV/c	x_T	$\sigma(M_{\pi^0}$ MeV)	Method	Photon Detection	Hadron Measurement	γ Energy Res. ($\sigma(E)/E$)
1	CERN ISR	R806	63.0	pp, (.17)	4-12	.13-.38	~ 15	Reconstruct	Liquid Argon Cal.	LAr Cal., Magnet Spectr.	$.14/\sqrt{E}$
2	CERN ISR	R807	63.0	pp, (.17)	4-10	.13-.32	~ 15	Reconstruct	Liquid Argon Cal.	LAr Cal., Magnet Spectr.	$.14/\sqrt{E}$
3	CERN ISR	R808	63.0	pp	4-10	.13-.32	20 - 50	Reconstruct	NaI and U Cal.	Calorim. and Magnet Spectr.	$(.16)/\sqrt{E}$
4	CERN ISR	R108	63.0/44.	pp	3.5-12	.13-.38		Conversion	Lead glass & PWC's	Magnet spectr.	
5	CERN ISR	R110	63.0	pp, (65.)	4-6	.13-.29		Profile	Lead glass & PWC's	Magnet spectr.	$.05/\sqrt{E}$
6	CERN SPS	WA-70	22.9	$\pi^{\pm}p, pp$, (.03,.5,.5)	4-7	.33-.60	12	Reconstruct	Liquid scintillator/lead	Ω spect.,RICH counter	$.10/\sqrt{E}$
7	CERN SPS	UA-6	24.3	$\bar{p}p, pp$, (3.6, 5.5)	4-7	.33-.58		Reconstruct	Proportional tube/lead	Mag. spect., $\frac{dE}{dx}$, transition rad.	$.23/\sqrt{E}$
8	CERN SPS	NA-24	23.7	$\pi^{\pm}p, pp$, (.19,1.,.45)	4-7	.33-.58	15	Reconstruct	Propor. tube/lead, scintil./lead	Hadron Calorimeter	$.34/\sqrt{E}$
9	CERN SPS	NA-3	19.4	$\pi^{\pm}p, pp$	4-8	.33-.5		Reconstruct	Scintillator/lead, shower chamber	Magnet spectr., Cherenkov	$.21/\sqrt{E}$
10	CERN Coll.	UA-1	540,630	$\bar{p}p$, (.7)	15-40	.05-.13		Profile,Isolation	Scintillator/lead	Magnetic spectr., calorim.	$.15/\sqrt{E}$
11	CERN Coll.	UA-2	540,630	$\bar{p}p$, (7.)	15-80	.05-.26		Conversion,Isolation	Proportional tube/lead calor.	Magnet spectr., Calor.	$.15/\sqrt{E}$
12	FNAL Coll.	CDF	1800	$\bar{p}p$, (4.0)	14-40	.05-.13		Profile,Isolation	Calor./strip/wire chambers	Magnetic spectr., strip chambers	
13	FNAL Proton	E-705	23.7	$\pi^{\pm}p, pp, \bar{p}p$, (7.4, 6.8, 4.2, .16)	4-9	.33-.6	~ 20	Reconstruct	Scintillating barium glass	magnet spectr., Cherenkov	$.06/\sqrt{E}$
14	FNAL Meson	E-629	19.4	$\pi^{+}p, pp$	2-5	.2-.5	6.5	Reconstruct	Liquid argon/lead	PWC's,calorimeter	$.15/\sqrt{E}$
15	FNAL Meson	E-515	24.	pp	2-6	.2-.5	15.7	Reconstruct	Liquid argon/lead	PWC's,calorim., Cherenkov	$.157/\sqrt{E}$
16	FNAL Meson	E-706	31.5	$\pi^{\pm}p, pp, K^{\pm}p$, (.03, .5, .5, >.01, >.01)	4-11	.22-.68	8	Reconstruct	Liquid argon/lead	mag. spectr.,calorim., silicon pstripe	$.20/\sqrt{E}$

Table 1: List of direct-photon experiments at CERN and at Fermilab.

a) Measure the single photon cross section for incident π^+ and π^- beams over a large p_T range.

b) Determine the gluon structure functions of the π^+ and π^-.

c) Determine the gluon fragmentation functions from the π^+, π^- and p beam data.

d) Measure the quark and gluon fragmentation functions.

e) Measure the four-vectors of (and consequently study) the jets produced in association with the direct photons and the π^os.

f) As a test of QCD, E-706 will study the reaction $q\bar{q} \rightarrow \gamma\gamma$ and compare it to Drell - Yan production $q\bar{q} \rightarrow l\bar{l}$.

In particular, regarding the jet physics, the ultimate goal of E-706 is to go beyond the particle "correlation studies" and measure the fragmentation and distribution functions. In order to do this it is important to reconstruct the awayside jet and thus determine the four vectors of the scattered partons.

2.9. Goals of this Thesis

In this thesis, I study the particles associated with the high p_T single photons and π^0s for incident proton and π^- beams. These studies are referred to in the relevant literature as "correlation studies". The following correlation studies are addressed in this experiment:

A) Particles accompanying the triggering γ or π^0

The first goal is to study the particle density and energy density of both charged and neutral particles accompanying (i.e., the same side) the single photons and the π^0s.* This analysis focuses on differentiating among specific mechanisms for photon production. Three mechanisms of photon production are considered [7] [8] [22] [23]: a) Compton scattering ($gq \rightarrow q\gamma$), b) Annihilation scattering ($\bar{q}q \rightarrow g\gamma$), and c) the bremsstrahlung production of a photon from a scattered quark. In the Compton and Annihilation production, the single photon is produced unaccompanied by other particles. In the bremsstrahlung production, the single photon is accompanied by other particles because it is a fragment of a jet from a scattered parton. In principle, the direct and bremsstrahlung components can be separated by grouping the events into two classes, i.e., the ones with accompanying hadrons and the ones without accompanying hadrons.

B) Particles recoiling against the single γs

I also study the particle density and energy density of both charged and neutral particles recoiling against single photon and π^0s. The purpose of this study is twofold; first, to study the kinematical correlation between the awayside particles

* In π^0 events the highest p_T particle identified in the electromagnetic calorimeter is a π^0. For a detailed discussion on the definition of the π^0 events see Chapter 6.

(in order to demonstrate that the high p_T events have a jet - like structure), and second, to study the properties of the recoiling particles which originate from quarks and gluons. The nature of the recoiling parton from either the direct photon or the π^o events varies according to the kinematic region and the type of the interaction. By looking at different kinematic regions for π^+p or π^-p collisions it is possible to study the accompanying particles originating from different first order subprocesses. The arguments here are similar to the ones used before, when the "same side" correlations were described. In the case of the Compton process, the recoiling jet results from the fragmentation of the recoiling quark. In the Annihilation process, the jet originates from the fragmentation of a gluon. Thus, by choosing the appropriate type of beam particles and kinematic region, we can select event samples which are dominated by either gluon or quark jets. The jets recoiling from the high p_T π^os are from a combination of gluons and quarks. In order to attribute the differences observed between the direct photon and the π^o samples to differences in the fragmentation of quark and gluon jet, it is important to know the ratio of quark to gluon jets in π^o events[44].

C) Charge Ratio

In pp collisions the recoiling jet from single photons originate mostly from u quarks rather than d quarks. This is because the proton is composed of two valence u quarks and one valence d quark, and the differential cross section at the parton level is proportional to the charge of the quark squared:

$$\frac{u}{d}(pp\ collisions) \;=\; 2 \times \frac{(4/9)e^2}{(1/9)e^2} \;=\; \frac{8}{1}$$

In this experiment most of the data were taken with a Beryllium (Be) target. Be is not isoscalar. Its nucleus consists of four protons (valence quarks, uud) and

five neutrons (valence quarks, udd). The contributions to the differential cross sections for obtaining a u-quark in the awayside jet in pp and pn collisions are proportional to:

$$u^{pp} = 4 \times 4u^2 = 7.10e^2 \quad and \quad u^{pn} = 5 \times 3u^2 = 6.67e^2$$

and similarly for d-quark jet,

$$d^{pp} = 4 \times 2d^2 = 0.89e^2 \quad and \quad d^{pn} = 5 \times 3d^2 = 1.67e^2$$

The ratio of u- quarks d- quarks in the recoiling jet is

$$\frac{u}{d}(pBe\ collisions) = \frac{u^{pp} + u^{pn}}{d^{pp} + d^{pn}} = \frac{7.10 + 6.67}{0.89 + 1.67} \simeq 5.4$$

Thus, there should be a substantially larger fraction of positive hadrons in the direct photon sample from pBe collisions than in π^+Be or π^-Be collisions at high p_T. Moreover, for a fixed value of the photon p_T, this fraction should increase with the awayside p_T because the average value of the z in the fragmentation function increases, and this increases the correlation between the charge of the jet and the charge of the parent quark.

D) Fragmentation Function of Quark and Gluon

We expect the fragmentation patterns of quark and gluon jets to be rather different[45],[28]. Experiments that have studied the differences in quark and gluon jets were performed at CERN SPS, CERN ISR, CERN collider, SLAC, and DESY (see References [31], [32], [28], [33] and [41]). In this thesis I study the quark - gluon fragmentation properties qualitatively or quantitatively , by studying the

jets recoiling from single photons and π^os. The gluon structure function peaks at considerably smaller values of x than the corresponding quark structure function. Therefore we can study differences between quark and gluon jet fragmentation by studying the fragmentation distributions from the events dominated by the Annihilation diagram and the Compton diagram. The fragmentation distributions obtained are compared with the fragmentation functions found in e^+e^- experiments[29].

3. THE EXPERIMENT

3.1. Experimental Design and Components

This chapter describes the apparatus employed in this experiment. The experiment, Fermilab experiment E-706, was performed by a collaboration of physicists from Northeastern University, University of Rochester, Fermilab, Michigan State University, University of Minnesota, Pennsylvania State University, University of Pittsburgh and University of Delhi (India). The first physics run of E-706 was conducted in the MW beam line at Fermilab from July 1987 through February 1988.

The experiment used a beam Cherenkov counter, a Silicon Strip Detector (SSD), sixteen Proportional Wire Chamber (PWC) planes, a Large Liquid Argon Calorimeter (LAC), and a steel acrylic scintillator Forward Calorimeter (FCAL). The analysis magnet was provided by Fermilab. For the online Data Acquisition and Monitoring as well as for part of the offline analysis, the experiment used four PDP-11 computers and a cluster of three VAX computers (a VAX-780, and two Micro Vaxes). These computers were provided by Northeastern University, University of Rochester, and Fermilab.

Figure 12 shows the E-706 experimental apparatus. A right handed coordinate system is used. The z-coordinate points along the direction of the beam, the positive x-coordinate points in the horizontal direction to the left, looking downstream along the beam, and the positive y-coordinate points upward. The origin of the coordinate system is placed 9 meters upstream of the front face of the LAC, which is near at the midpoint of the experimental target. The details of the components

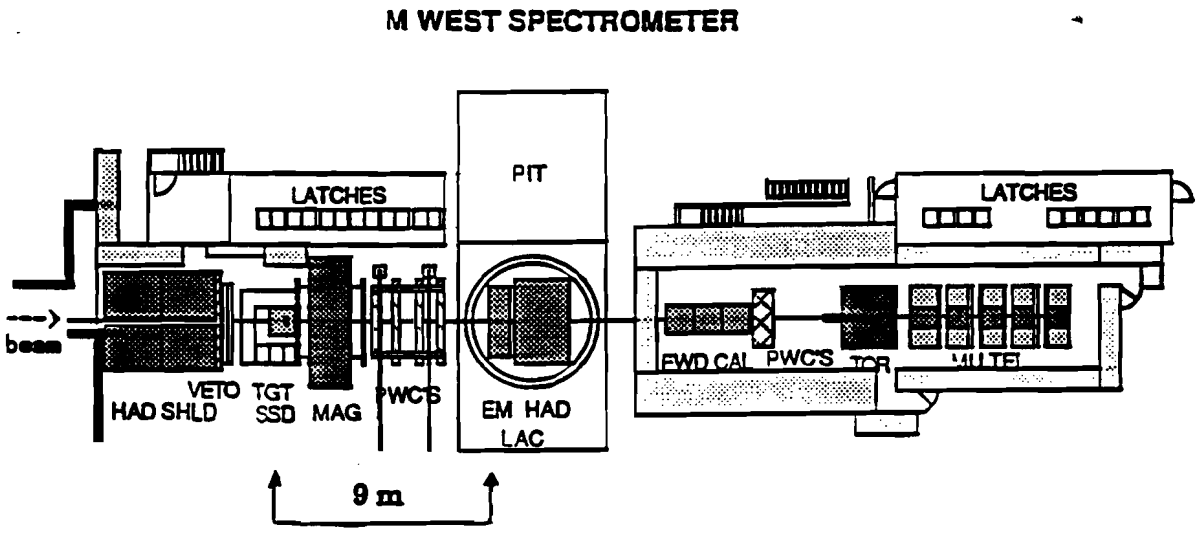

• Beamline	muon spoilers 43 m differential Cherenkov counter hadron shield 2 veto walls	
• Target	0.1 λ Be (0.1 X_0) 0.01 λ Cu (0.1 X_0) 0.1 λ C (0.2 X_0)	97% of data 42% of data 3% of data
• SSD's	3X + 3Y planes upstream of target 4X + 4Y planes downstream of target 50 μm pitch	7120 active channels
• Analyzing Magnet	450 MeV/c p_T^{kick}	
• PWC's	4 modules of X,Y,U,V planes 2.54 mm wire spacing	~ 13,000 channels
• EM Calorimeter	Segmentation: 10 X_0|20 X_0 : front|back Geometry: $r - \phi$, ~ 6000 channels	
• Hadron Calorimeter	Segmentation: 2 λ|6 λ : front|back Geometry: triangular pads, ~ 2000 channels	
• Forward Calorimeter	Segmentation: 3 longitudinal segments Fe & scintillator, 10 λ total	

Figure 12: E-706 experimental layout.

and their relationship to the experiment are described in the following sections.

3.2. The Beam Line

The experiment was performed in the west branch of the Meson Laboratory's secondary beam line [46] in the Meson West building at Fermilab. This beam line is one of the newest fixed target beamlines at Fermilab and it was designed to operate in two modes: the positive and the negative charged beam modes. In the positive mode it transported 530 GeV/c secondary positive particles, mainly protons (92.0%) and positive pions (7.5%). In the negative mode it transported mainly negative pions (97.5%) and negative kaons (2.5%). The beam line elements are shown in Figure 13. A primary proton beam of 800 GeV/c, with an average intensity of 2×10^{12} particles/spill, hit the primary upstream target and the secondaries were extracted through the aperture of dipole magnet MW6W. The production angles were chosen to be 0 mrad for the negative beam mode and 1.4 mrad for the positive beam mode. The non-zero production angle was required for the positive beam mode to avoid the possibility of transporting the full primary beam into the E-706 detector area. By adjusting the magnetic field and the polarity of the MW6W magnet, the beam of the desired momentum was directed through the collimators to the MW secondary beam line. The positive beam had an intensity of up to 7×10^7 particles/spill and the negative beam had an intensity of up to 4×10^7 particles/spill. The intensity of the beam was controlled by a set of collimators, and its profile was monitored by segmented wire ionization chambers (SWIC) positioned throughout the beamline. The beam spills were ~23 sec long,

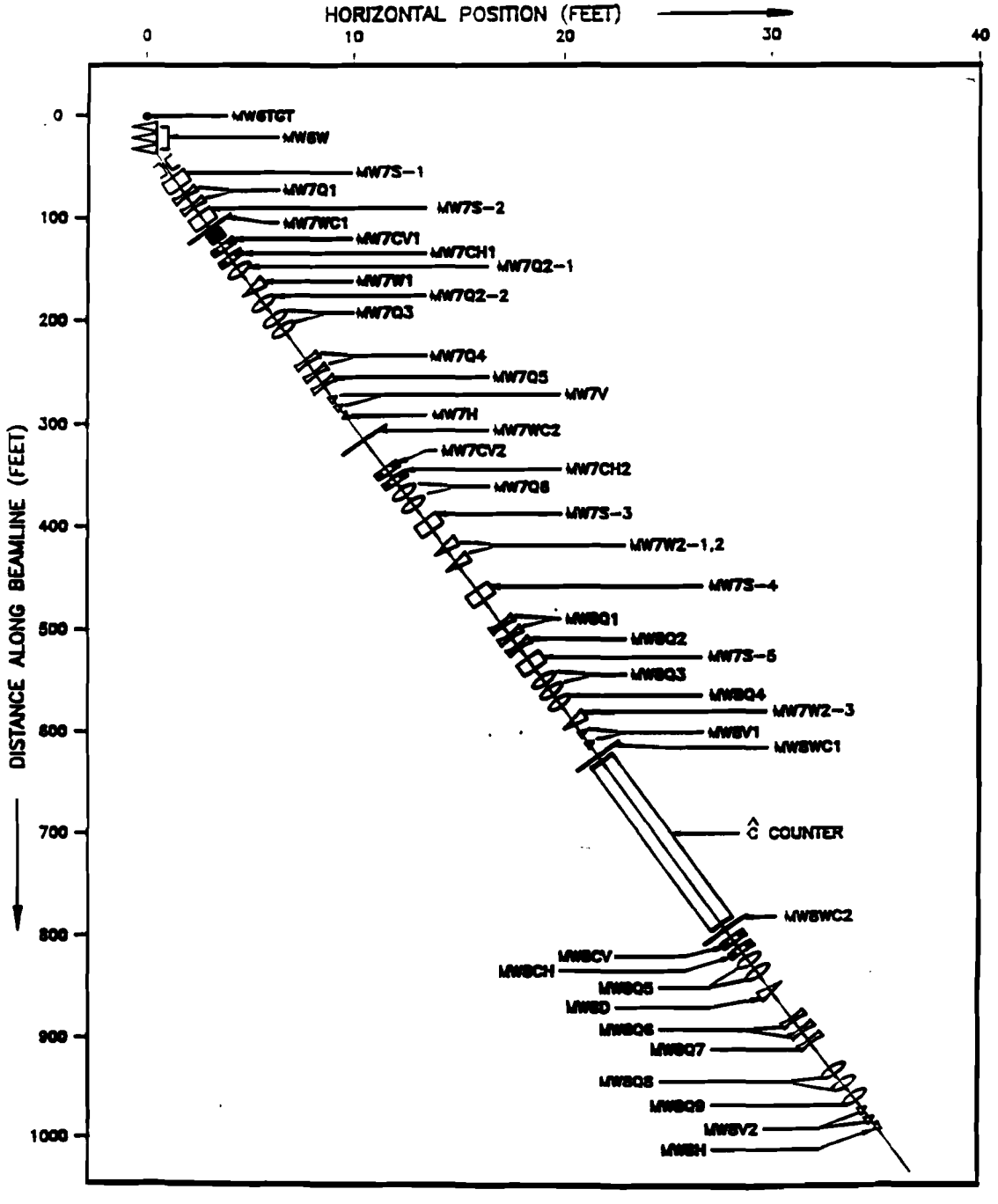

Figure 13: MW Beamline components plotted in horizontal position x vs. longitudinal position.

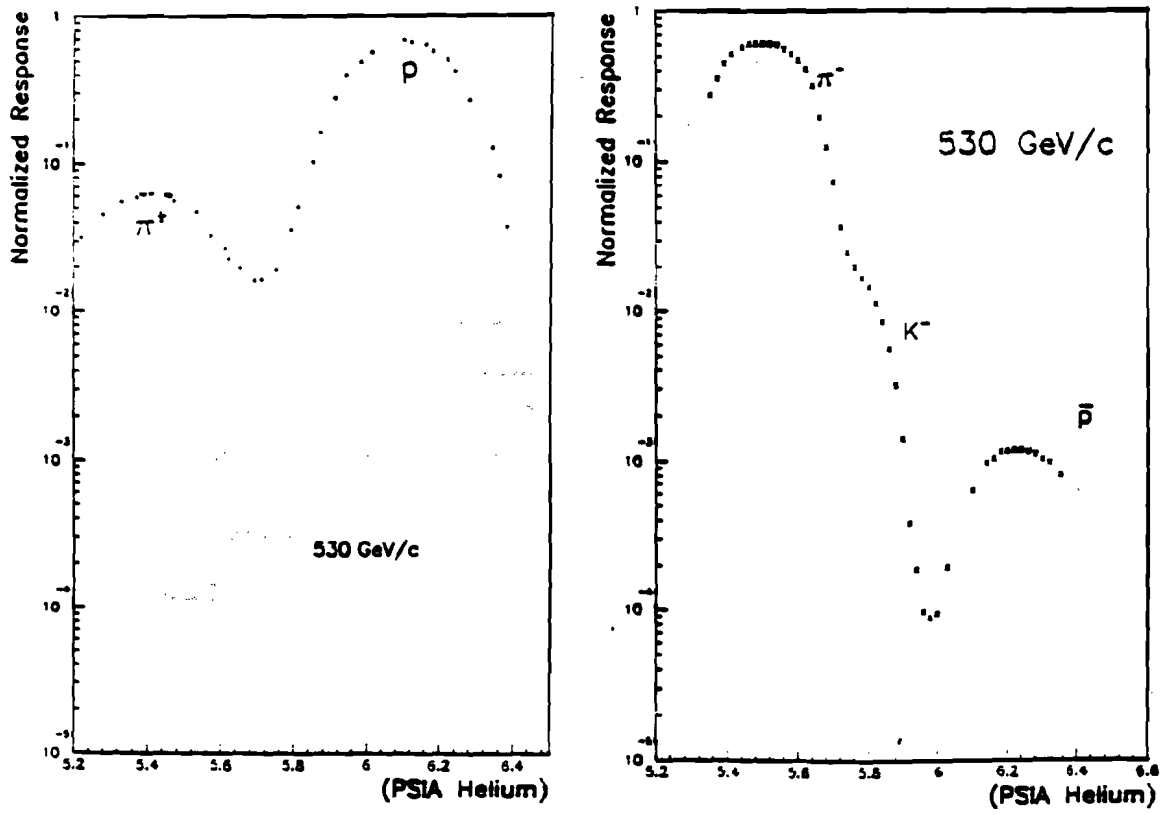

Figure 14: Pressure curves of Cherenkov counter using negative (right graph) and positive (left graph) beams.

separated by 38 sec.*

About 100 meters upstream of the experimental setup, the beam passed through a differential gas Cherenkov counter which was used to identify the incident beam particles. The counter was 42.1 m long with a focal length for Cherenkov light of 32.3 m, had a radius of 24.4 cm and used helium gas in the pressure range of 4 to 7 psia, as the radiator. It had one coincidence and one anti-coincidence ring, each containing six phototubes. The Cherenkov angle for the coincidence ring was 5 mrad. The typical efficiency for twofold coincidences in the coincidence ring was 95%. Figure 14 shows the pressure curves for 530 GeV/c positive beam and negative beam, respectively. The vertical axis is the normalized number of hits for a coincidence level requiring three or more hits for the positive beam (four or more hits for the negative beam) in the coincidence ring, and less than two hits were allowed in the anticoincidence ring.

The background muon flux along the beam line was reduced by spoiler magnets in the beam line. The hadronic halo was attenuated by a 3 meter long iron shield in front of the spectrometer. The spectrometer was shadowed by two scintillation counter veto walls which further reduced the contamination of the triggers by halo muons. Each wall was made from 32 scintillation counters with a square hole at the center for the beamline. Figure 15 shows the two veto walls.

* The time structure of the beam consisted of 23 second spills followed by 38 seconds of time when beam was being accelerated. Within each of these spills, the beam particles came in 2 nsec bunches, separated by 19 nsec intervals.

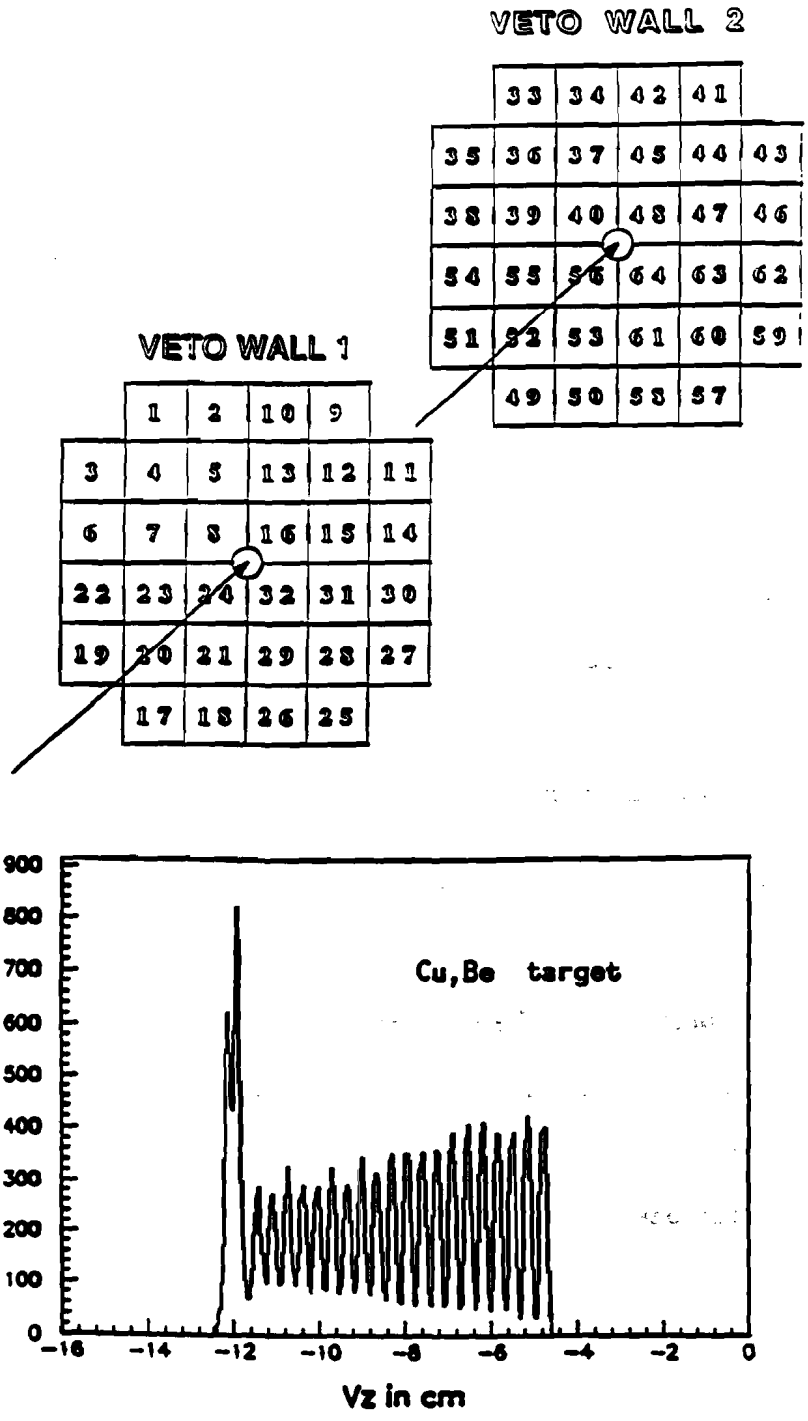

Figure 15: (top): Veto walls. (bottom): z-coord distribution of reconstructed verticies in the target region.

3.3. TARGETS

The target design was based on considerations of the radiation lengths and interaction lengths of the materials used. A low Z (atomic number) material was selected for the target to reduce the conversion rate of photons into e^+e^- pairs. The overall thickness of the target and the spacing between target segments were determined by the position resolution of the z coordinate of the vertex measured by the SSD system. Total thickness of the targets was chosen to be 10% of a nuclear interaction length. For most of the data (see Table 2) the target consisted of twenty 2 mm thick beryllium segments separated by 1.6 mm gaps. For a portion of the run, two 0.8 mm thick copper segments separated by a 1.6 mm gap followed by a 3.2 mm gap were positioned upstream of the beryllium (Be) target to measure the A dependence of the cross sections. This segmentation was intended to aid in separating vertices originating in different target segments. Figure 15(bottom graph) shows the z-distribution of the reconstructed interaction vertices.

PARAMETERS/Targets	C	Be	Cu/Be
No. of triggers (K)	160	2740	2090
Length (cm)	4.0	4.0	4.+ 0.16 (Be+Cu)
Density (g/cm^3)	2.26	1.85	1.85(Be),8.96(Cu)
Total Radiation length (%)	21.3	11.3	22.4
Total Interaction length (%)	10.5	9.85	10.0

Table 2: Targets for E-706 1988 Data Run.

3.4. Magnet

The dipole magnet (referred to as MW9AN), along with the silicon strip detectors and proportional wire chambers, was used to determine the momenta of charged particles. Its center was located 2 meters downstream of the target. It had an aperture of 122 cm horizontally and 91.5 cm vertically. The length through which the charged particles were deflected was ~70 cm. The data was taken with the current set to 1050 Ampere and the magnetic field was predominantly along the y axis. This current corresponded to an integrated field length ($\int B \times dl$) of 1.5 T-m or a transverse momentum kick of 0.45 GeV/c. This current produced a large amount of heat in the magnet coil. To prevent overheating, cold water was circulated through the coil. To reduce the fringe field, two magnetic mirror plates were placed on the ends of the magnet.

3.5. Silicon Strip Detector

The Silicon Strip Detectors(SSDs)[48] , along with the target, were positioned directly upstream of the analyzing magnet. The SSDs together with the Proportional Wire Chambers (PWCs) downstream of the magnet, and the magnet, determined the charged particle momenta. The SSDs also served as a vertex detector for locating the primary interaction in the target and in separating the primary interaction from secondary interactions in the target.

Figure 16 shows the SSD segmented target region. There were 7 X-Y modules (14 SSD planes) with a total of 7,120 active strips. All of the SSDs had a 50 μm pitch and a thicknesses of 250 or 300 μm. The two X-Y modules both upstream and downstream of the target were 3×3 cm^2. In order not to limit the acceptance,

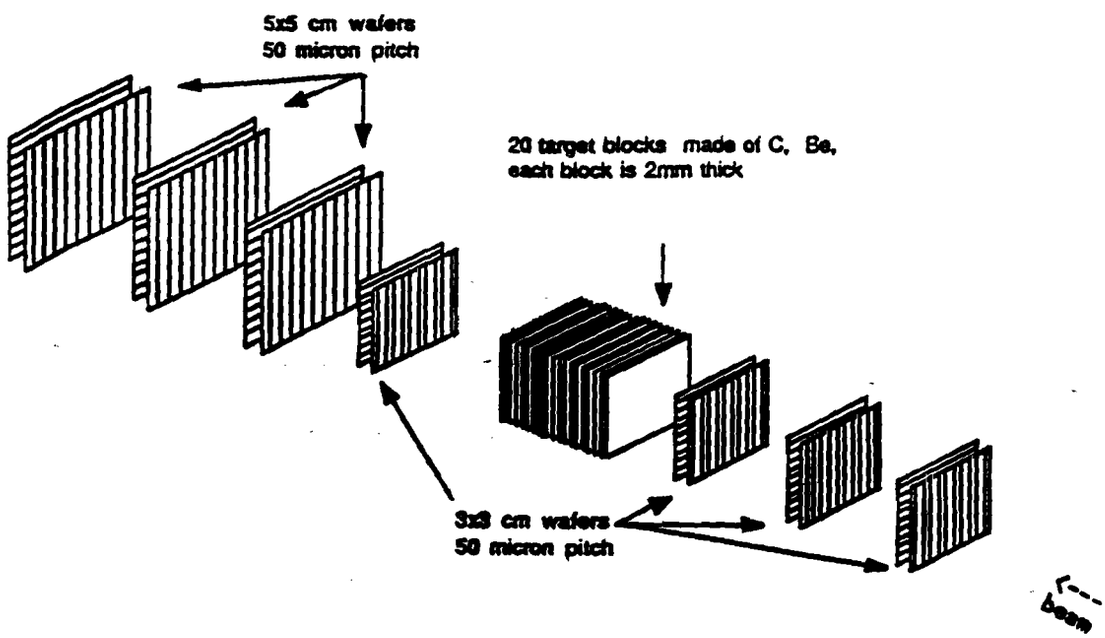

Figure 16: The Silicon Strip Detectors (SSD) and the segmented target.

the last two X-Y modules were 5×5 cm^2. The design requirements of the SSD system were:

1. The detector upstream of the spectrometer magnet must be compact in size along the longitudinal direction and be matched to the magnet and Liquid Argon Calorimeter apertures.

2. The angular resolution of the detectors upstream of the magnet must match the angular resolution of the detectors(PWCs) immediately downstream of the magnet.

3. The detector system before the magnet must have a high position resolution in the X-Y plane to resolve track reconstruction ambiguities in the downstream PWC system resulting from large track densities entering the PWCs.

4. The detector system is required to have a good position resolution in the z coordinate to reconstruct primary and secondary vertices and discriminate between them.

The SSD readout system had high efficiency and a small dead time for minimum-ionizing particles. The readout system used was manufactured by Nanometrics Systems. A minimum ionizing particle traversing the detector produces electron-hole pairs and the charge is collected in about 20 nsec. This charge is fed to a charge sensitive preamplifier. The output from the preamplifier is further amplified, discriminated, and finally converted to logic signals for storage as digital data.

3.6. Proportional Wire Chambers

Downstream of the analyzing magnet a system of 16 proportional chambers was employed. These chambers, in conjunction with the upstream SSDs, determine the momenta and directions of the charged particles. By determining the path of the charged particles before and after they were deflected by the magnet, their momenta were determined. The chambers had a high rate capability (>1 MHz interaction rate in the target) and a small angular segmentation(<1 mr) in order to separate the fragmentation products of gluon and quark jets which accompany direct photons. The PWCs[49] were packed into four modules each in an x, y, u(+37°), and v(−53°) configuration with a 1.7 cm spacing between planes. The active areas and (x-planes) z-positions, relative to the center of the target, of these modules were:

Module	Area(cm^2)	z-coord(cm)
I	122 × 163	380
II	203 × 208	473
III	203 × 208	568
IV	244 × 244	660

Table 3 :The active areas and z-positions of the PWC modules.

The sense wire spacing was 2.54 mm and the resultant angular resolution was <1 mrad. Mylar (0.00254 cm thick), painted with graphite, was used for the cathodes of all chambers. The graphite paint was masked into segments on which the high voltage could be independently set. This allowed the regions near the beam to be selectively deadened during high intensity running. The total number

of instrumented channels was 13,400.

3.7. Liquid Argon Calorimeter

A large Liquid Argon sampling Calorimeter (LAC) was placed 9 m downstream from the target behind the tracking system. Its purpose was to measure the energies and positions of photons, electrons and hadrons, and to trigger on the events with high p_T electromagnetic showers. It consisted of two sections, the Electromagnetic Calorimeter section (EMLAC) and the Hadron Calorimeter section (HALAC). Both sections shared a common cryogenic enclosure. In the following sections, we will describe the design criteria, calorimetric properties, structure, and finally the readout system of the LAC.

3.7.1. LAC Design Criteria

The design requirements for the LAC were[50]:

i) Nearly complete coverage at rapidity $-1 < y < 1$. At an incident beam momentum of 530 GeV/c, this corresponds to an angular range of 22 mrad $< \theta_{lab} <$ 160 mrad in the laboratory coordinate system and an angular range of $40° < \theta_{CM} < 138°$ in the center of mass(CM) system. The calorimeter covers 77% of the total 4π solid angle in the CM system.

ii) Ability to resolve the two photons from π^0 decay.

iii) Energy resolution of $< 15\%/E^{1/2}$, and a position resolution of $< 0.1cm$ for photons and electrons.

iv) Hadron energy resolution of $\leq 100\%/E^{1/2}$ with a position resolution of < 2.5 cm.

v) Electron/hadron separation at the 10^{-4} level.

vi) Ability to sustain an interaction rate of 10^6 Hz in the target.

The requirements for the electromagnetic calorimeter are discussed in more detail below and elsewhere[7]. To be able to measure single photon production the EMLAC must be able to discriminate photons coming from direct production from photons coming from π^o decays. This was achieved by selecting the lateral segmentation of the electromagnetic calorimeter section to be comparable to the lateral width of the electromagnetic shower. A useful unit of length for transverse shower distributions is the Moliere unit,

$$R_M = 21(\text{MeV}) \times \frac{X_o}{E_o}$$

where X_o is the radiation length and $E_o \sim (580\ MeV)/Z$ is the critical energy.* For lead (Pb) the Moliere unit is 1.65 cm. 99% of the energy of the shower is contained[51] inside a radius $3R_M \sim 5$ cm. The average channel width of the electromagnetic calorimeter section was 0.5 cm.

For energies above a few GeV, the opening angle between the two photons from π^o decay is $\Theta \sim M_\pi/\sqrt{(E_1 \times E_2)}$, where E_1 and E_2 are the photon energies. The minimum opening angle (Θ_{min}) occurs when the two photon energies are equal in the laboratory frame. For a π^o the corresponding lab energy at x_f=0 is $E_{\pi^o} = \gamma p_T$. For our experiment, p_T range of 5-10 GeV/c, γ= 16.3 (530 GeV beam energy)

* The interactions of photons and electrons in the EMLAC (at energies above 100 MeV) are dominated by the creation of e^--e^+ pairs and by bremsstrahlung radiation. This leads to a cascade of e^-, e^+ and γ's which stops when the energy of these particles reaches the critical energy E_o. When a primary photon of energy E enters the detector it produces e^--e^+ pairs. The electrons on average have energy E/2. If $E > E_o$, the e^- and e^+ lose their energy predominantly by bremsstrahlung. In a layer of thickness X_o, the charged particle energy decreases to $E_o/2e$. The radiated photon produces e^--e^+ pairs again, such that after n generations a shower is formed. The cascade process stops when the energy loss of electrons by ionisation equals that by bremsstrahlung.

and for these p_Ts a typical minimum opening angle is $\Theta_{min} \sim 5$ *mrad*. The lateral segmentation of our detector should allow it to resolve two photons with this opening angle, or at distances $L \times \Theta$, where L is the distance of the detector from the target. Since L= 9 m the separation of these photons is typically ~4.5 cm.

In order to detect π^o decays into highly asymmetric photons, the detector must be able to detect low energy photons. For a detector with an energy threshold of 2 GeV, the detection efficiency of π^o of a 20 GeV is 75%. The rest of π^os give the same signature as do direct photons.

The detector acceptance should be large to minimize the number of events in which one of the photons from a π^o misses the detector. The opening angle between the two π^o decay photons increases slowly as the energy asymmetry of the π^o increases. Even if one of the two photon's energies is an order of magnitude higher than the energy of the other photon, the opening angle is still less than twice of its minimum value. This actually means that a large calorimeter can have good acceptance for π^o decays up to large asymmetries. Note that this is not the same for η decay photons because their minimum opening angle is about 4 times that of the π^o to start with. The detector should also have the smallest possible dead.

The detector should be able to distinguish between electromagnetic and hadronic showers to reduce the possibility of missidentifying charged or neutral hadrons as photons. The LAC can make this separation using three different methods:

1) By fitting the transverse energy distribution using the shower shape of electromagnetic showers expected in the EMLAC and identify as hadrons the

showers with a large chi-square for the electromagnetic shower hypothesis.

2) The fraction of energy deposited in the front section of the EMLAC (called E_{FRONT}/E_{TOTAL} ratio) is a very good tool for separating electromagnetic showers from hadronic showers since almost all of the incident electrons and photons deposit most of their energy in the front section of the EMLAC.

3) All particles that deposit energy in the HALAC are hadrons. When the position of a reconstructed shower in the EMLAC overlaps with the imaginary line that connects a reconstructed shower in the HALAC and the target, then the EMLAC shower can be identified as part of the same hadronic shower that started showering in the EMLAC.

The detector should have sufficient length (in terms of radiation and absorption lengths) in order to fully contain the highest energy showers. It should also have a linear energy response to minimize corrections in the measurements of the single photon energies or in the measurements of π^o energies relative to single photon energies.

The requirements for the hadron calorimeter are discussed below. The lateral hadronic shower spread is much wider than the electromagnetic one, making the hadron shower shape less well defined; this means that a very fine lateral segmentation is not as useful as in the EMLAC. The average area of each readout channel is 65 cm^2 (equilateral triangle), enough to contain about 50% of the energy deposited by a single hadron shower located at the center of the triangle. The HALAC was the only apparatus available to measure neutral hadrons.

The basic design considerations for the HALAC were:

i) Good hadron energy and position resolution.

ii) Enough longitudinal length to fully contain the hadronic showers.

iii) Sufficient lateral segmentation to resolve neighboring hadrons.

iv) The acceptance should be at least as large as the EMLAC to detect the hadrons opposite high p_T π^os and photons.

3.7.2 Calorimeter Properties of Liquid Argon

Calorimeters can be used to determine the energy, position and direction of particles. The total particle energy is absorbed in the calorimeter materials by atomic ionization and excitation. In general we distinguish between an electromagnetic calorimeter and a hadronic calorimeter. In the former the energy is converted through an electron - photon cascade and in the latter through a hadronic cascade. In the electromagnetic cascade most of the energy is converted into ionization mainly by e^+s and e^-s. In a hadronic cascade a smaller part of the incoming energy is seen as ionization and excitation due to the fact that the nuclear binding energy is much larger than the critical energy (E_o). Also, some of the produced particles (like muons, neutrons and neutrinos) do not interact in the detector. This undetected energy causes large fluctuations in the energy measurements. In most calorimeters only part of the deposited energy is detected by scintillators, liquid argon, wire chambers or other detectors. The ionization detectors are usually sandwiched between absorber plates. The detector and absorber plates are called 'active' and 'inactive' parts, respectively. Many different types of calorimeters have been built and tested using different materials for the active and inactive parts of the detector.

The main advantages of using liquid argon are the following:

i) Uniform response over the detector,

ii) Relatively fine segmentation (compared with scintillator or lead glass calorimeters)

Some other benefits of using liquid argon are the following:[52]

i) Liquid argon is dense (1.4 g/cm^3).

ii) It produces large charge output (about 4e$^-$/100 eV).

iii) The collected charge saturates with increasing high voltage.

iv) It has relatively high mobility (about 200 nsec/mm).

v) Liquid argon is relatively inexpensive (about 4 dollars/gallon).

vi) It is relatively easy to purify.

vii) Many of the impurities are not soluble in liquid argon.

The main disadvantage of this type of calorimeter is that liquid argon requires expensive and complicated cryogenic systems.

In the following the calorimetric properties of the EMLAC and the HALAC will be presented. More information can be found in numerous publications (References [53], [54], [55], [56], [57] and [58]).

Due to the fact that nearly all the energy in an electromagnetic shower results in ionization, the uncertainties in the energy measurement should be very small. However detector limitations do limit the energy resolution. These limitations are the cut-off energy E_0, below which the detector is insensitive to traversing particles, non-containment due to limited detector size, instrument noise, dead channels, and liquid argon impurities. The EMLAC limitations due to detector imperfections

become very small with respect to the fluctuations caused by the limited shower sampling. The sampling has been optimized, based on the considerations about cost, size, noise from capacitance, availability of materials and energy resolution.

Table 4 lists the most important detector properties that contribute to the shower development characteristics in the EMLAC. These data were put in the Monte Carlo program used to simulate the detector.

Hadronic calorimeters are in general much more massive than the electromagnetic ones since reasonable longitudinal shower containment requires a thickness of typically 1200 g/cm^2. Sampling fluctuations in this case give only a relatively small contribution to the resolution. The main contributions to the resolution are the shower fluctuations which can be attributed to two facts:

i) In a nuclear cascade, part of the incoming particle energy is not detected and this part fluctuates from one cascade to the other. In the HALAC, where the inactive material is 405 steel, a 5 GeV pion gives[57]:

Detectable energy:

Charged pions and protons 40%

Electromagnetic from π^o 17%

Nuclear fragments 8%

Undetectable energy:

Neutrinos 18%

Neutrons and other leakage 17%

ii) The average number of pions in the first interaction is small and the ratio of

	Material	Thickness (cm)	X_o	Density (g/cm^3)	Z	A	λ_o	ΔE(MeV)
				EMLAC				
A:	G-10[1]	4.2	.22	1.7	-	-	.08	11.3
	LAr	2.4	.17	1.4	18	39.95	.029	5.3
	Cu[2]	0.735	.51	8.96	29	63.54	.05	8.7
	Total	7.33	.9		1.7		.16	25.3
B:	G-10[3]	4.8	.25	1.7	-	-	.09	13.
	LAr	3.7	.26	1.4	18	39.95	.044	8.1
	Cu[4]	.715	.5	8.96	29	63.54	.047	8.4
	Total	9.23	1.01	1.64			.18	29.5
C:	Pb	0.2	.36	11.35	82	207.19	.012	2.34
	G-10	.16	.0082	1.7	-	-	.003	.43
	LAr	0.5	.036	1.4	18	39.95	.006	1.1
	Cu	0.013	.0091	8.96	29	63.54	.0009	.15
	Total	.87	.41	3.58			.022	4.
	EMLAC	74.	29.	3.2			1.76	320.
				HALAC				
D:	Fe[5]	2.54	1.44	7.87	26	55.85	.15	27.2
	G-10	1.6	.083	1.7	-	-	.03	4.3
	LAr	1.6	.11	1.4	18	39.95	.019	3.5
	Cu	0.08	.056	8.96	29	63.54	.0053	.95
	Total	5.8	1.7	4.41			.21	36.
	HALAC	293.	88.4	4.41			10.5	1850.
	LAC	367.	117.4	4.17			12.26	2170.

X_o: Number of Radiation Lengths; λ_o Number of Interaction Lengths; ΔE: Ionization Loss of minimum ionizing particle.

A: Material in front of active volume of EMLAC (after excluder vessel).

B: Material between active volume of EMLAC and HALAC.

C: EMLAC cell.

D: HALAC cell.

Table 4: LAC cell structures and depths in absorption lengths (λ), radiation lengths (X_o) and cm.*

π°s to charged pions has large fluctuations. This causes fluctuations in the energy deposition, because a π° releases all its energy in the form of an electromagnetic shower which contains a large amount of detectable ionization whereas the charged pions continue as hadronic particles. This phenomenon plays a very important role in the hadronic calorimeter. In Table 4, the most important characteristics of the detector that contribute to the shower development and confinement in the HALAC are listed.

3.7.3 Structure and Operation of the EMLAC

The electromagnetic calorimeter was subdivided into four mechanically independent quadrants, held together by the overall support structure. Figure 17 shows a blowup of the photon detector along with a summary list of the most important geometric characteristics of the detector. The following description of the detector is taken from Reference [50].

Each quadrant consisted of 66 layers in which 2.0 mm lead plates were separated by 2.5 mm gaps of liquid argon and G_{10} readout boards. About 20% of the incident particle energy was sampled by the EMLAC:

$$\frac{\Delta E(LAr)}{\Delta E(LAr + Pb + Cu + G_{10})} = 20\%$$

where $\Delta E = \frac{dE}{dz} \times \Delta l$ where $\frac{dE}{dz}$ is the ionization energy loss and Δl is the length of the material.

Interleaved boards are used to read out the r coordinate and the ϕ coordinate in a polar coordinate system. The r coordinate readout consists, in each octant, of 254 concentric radial strips in the front section of the detector, and 240 strips in

Electromagnetic Calorimeter

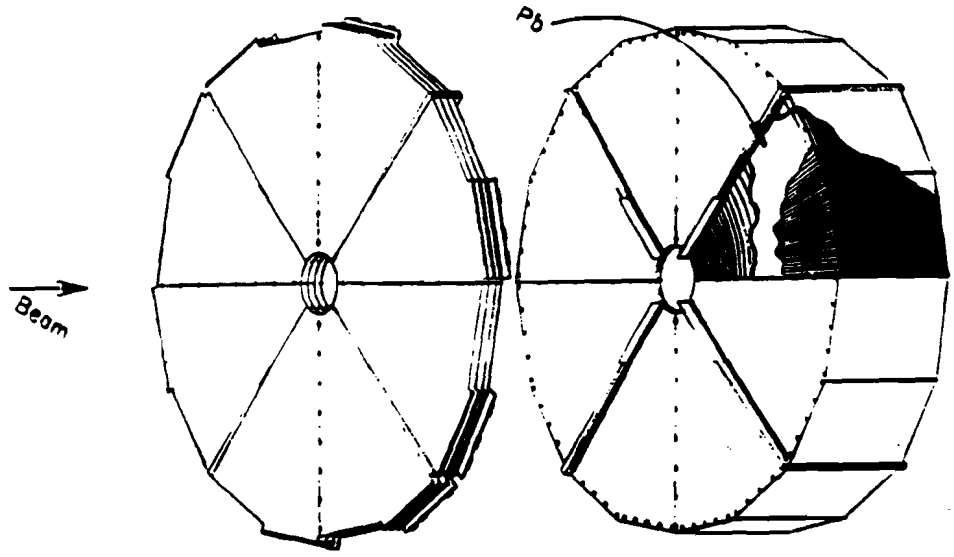

- Pb-Argon Electromagnetic Calorimetry
  - 2 mm Pb plates with 2.5 mm Ar gaps
  - Rapidity Coverage: (-1,1)
  - r Segmentation: 254 strips/octant

    5.5 mm wide, $\Rightarrow \Delta\theta = 0.6$mrad
  - ϕ Segmentation:

    Inner r: 21 mrad $< \theta <$ 44 mrad, $\Delta\phi = 16.4$ mrad

    Outer r: 44 mrad $< \theta <$ 173 mrad, $\Delta\phi = 8.2$ mrad

Figure 17: Blowup of the Electromagnetic Calorimeter.

the back section. The width of the r strips in each layer increased as the distance between the target and the layer increased, making a tower structure focused on the target 9.0 m upstream of the front face of the EMLAC. The width of the r strips is 0.55 cm at the first readout board. Because of the space limitation the two inner strips as well as the two outer strips were omitted in the back section of the calorimeter.

The ϕ coordinate strips were subdivided into inner and outer segments. Each inner strip subtends an azimuthal angle of 16.4 mrad, while each outer strip covers an angular range of 8.2 mrad. The ϕ coordinate readout consists of 48 strips in each octant in the inner section of the detector, and 92 strips in the outer section. The transition between the inner and outer ϕ-strips corresponds to a laboratory polar angle of 56 mrad from the target, or a center of mass angle of 85° at an incident beam momentum of 530 GeV/c. Figure 18 shows the physical boundaries of one quadrant.

Each lead plate was connected to two 1.0 μF capacitors in parallel. The capacitors had a leakage current of $< 10^{-10}A$ at 9 kV, both at room and at cryogenic temperatures. When a particle hits the calorimeter it produces a shower of particles which lose part of their energy in the liquid argon. This energy loss goes into ionizing the argon atoms with the ionization electrons drifting toward the anode plane under the influence of the applied electric field between the lead plates and the anode boards. The ionization electrons suppress the electric field thus altering the drift characteristics of the detector. Ballast capacitors of 1.0 μF were connected to each lead plate to act as a "reservoir" of charge to compensate for the field suppression due to drifting electrons. Figure 23 (bottom) shows the EMLAC

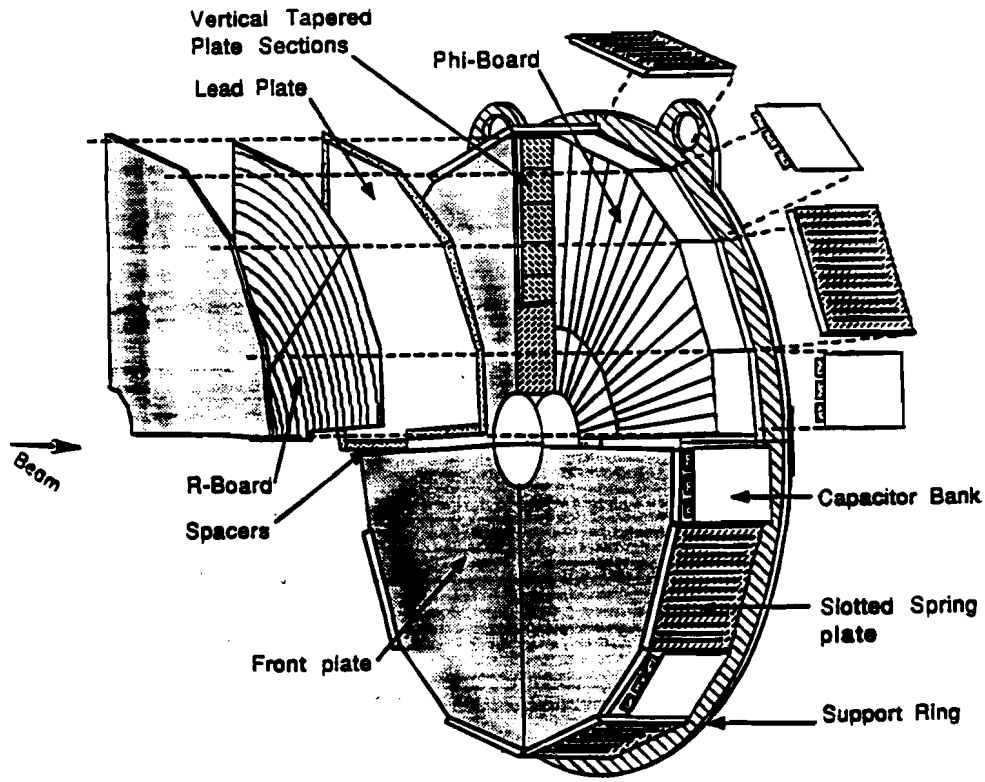

Figure 18: Blowup of the Electromagnetic Calorimeter.

high voltage arrangement. The 5.6 Ω and 5.0 Ω resistors were used to damp Mhz oscillations that would interfer with the electronic readout system.

The support structure of each quadrant, as well as the additional space needed for readout connectors and G_{10} spacers (to separate the boards from each other and from the lead), introduced dead areas in the detector. There were two sets of special "readout boards", one in front and one in the back of the photon detector assembly. These provided leads from the inner ϕ strips as well as from the r strips to the outer edge of the detector where external cables were connected. Only one side of these boards had leads routed on them and the other side was a ground plane in order to prevent cross talk. Between the front special readout boards and the rest of the stack a ground board was placed in order to further isolate these boards from noise induced from the rest of the detector. Each strip of the first 22 layers (10 radiation lengths) was ganged and read out via the other front readout boards, and the 44 layers (20 radiation lengths) were read out via the back readout planes. Figure 18 shows an exploded view of the EMLAC.

Each quadrant was assembled on the same specially built frame. Then the four quadrants were put together. First the two bottom quadrants were joined together by means of the tapered stainless steel plates which they shared. These plates were bolted on the horizontal and vertical radial sides of the quadrants. A pair of stainless steel rings was attached on the front and rear outer edges of each quadrant and were joined together by stainless steel bars. A special structure was used to support the two quadrants. The two top quadrants were joined to the bottom ones. Then the rings of the two halves were bolted together by means of four joiner plates. Finally the assembled detector was suspended from a gantry

by the rings.

3.7.4 Structure and Operation of the HALAC

The hadron calorimeter also has a tower readout structure. Each tower consists of a series of equilateral triangle readout pads as illustrated in Figure 19. All pads were focused in tower-like fashion towards the target 9.83 m from the front of the HALAC. Because of the pad focusing, the pad size changed with the detector depth. The average area of a pad was 65 cm^2 and the total number of readout channels was 2340. The following description of this detector is taken from Reference [50].

To have electrical connections from each pad to the edge of the detector, readout planes were subdivided into pairs, one of which is shown in the Figure 19. Each of the readout planes covered one-half of the area with pads, leaving the space between two rows for the readout lines. As illustrated in Figure 20, during assembly, the readout lines were covered with horizontal spacer strips which were glued to the readout boards and provided mechanical stability. Each plane consisted of three 1.2 m $\times$ 3.6 m G_{10} boards. Vertical ribs held the individual boards together and added to the rigidity of the whole assembly. Each layer (Figure 20 bottom graph) had in sequence a high voltage board, a layer of horizontal strips that define the 3 mm argon gap, one readout board, a layer of vertical ribs, the second readout, another layer of horizontal strips, and finally a second high voltage board. Each high voltage board consisted of three double-sided 1/32 in (0.08 cm) thick copper-clad G_{10} boards, with the perimeter grounded. The double sided boards were used to place the ballast capacitance next to the high voltage plane.

Hadron Calorimeter

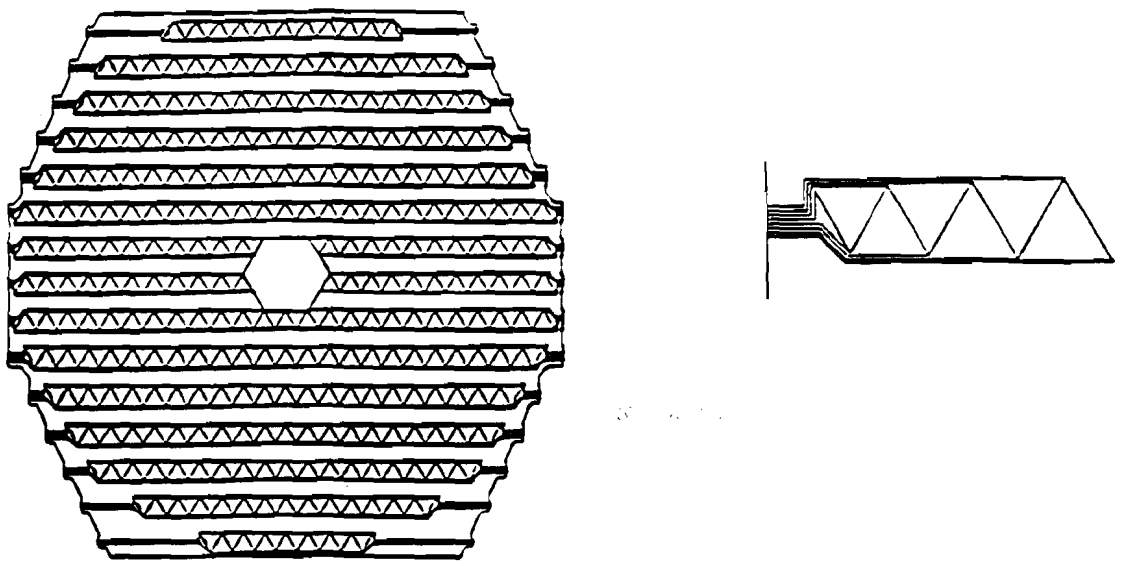

- Fe-Argon Hadronic Calorimetry
  - 2.5 cm Fe plates with 3 mm Ar gaps
  - Pad Geometry:

    Triangular Pads, towered, $\sim$ 12.5 cm per side

Figure 19: A single hadron calorimeter readout board (left) and detail of the readout scheme (right).

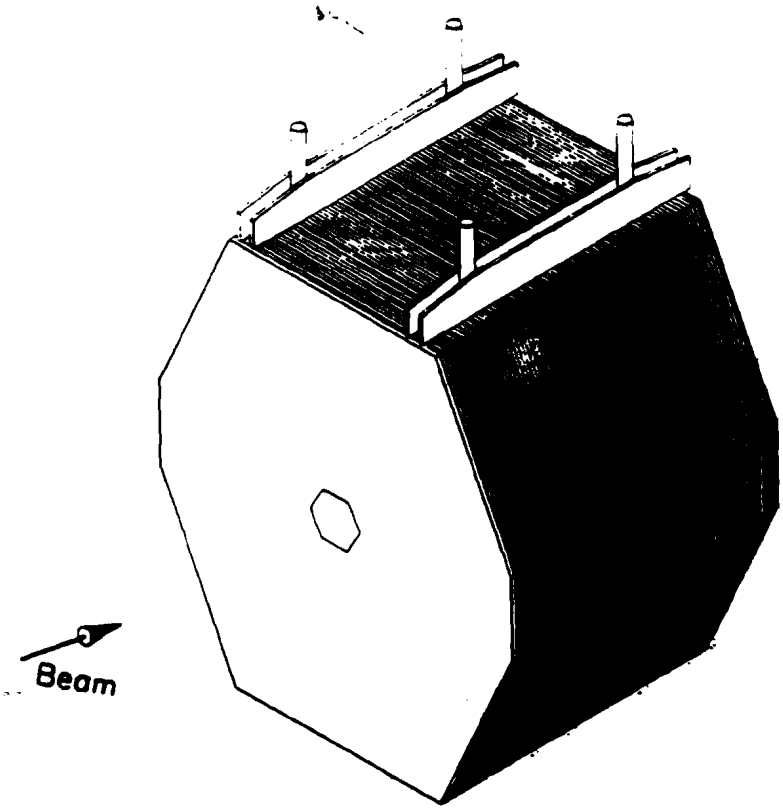

The assembly of the hadron calorimeter.

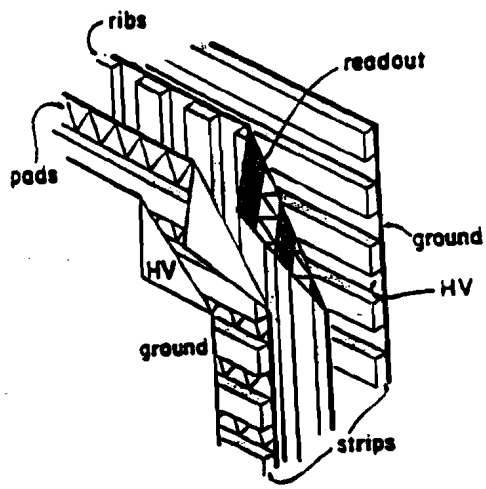

exploded view of one readout layer.

Figure 20: The assembly of the hadron calorimeter (top) and an exploded view of one readout layer (bottom).

There were 53 layers of readout assembly and 52 steel plates, 2.54 cm thick, in the hadron calorimeter, for a total of ~10 interaction lengths. The readout planes were grouped into two sections longitudinally. The front section consisted of the first 14 layers (1206 readout pads) and the back section consisted of 39 layers (1134 readout pads).

For a shower that originated in the HALAC about 1.4% of the incident hadron energy was sampled:

$$\frac{\Delta E(LAr)}{\Delta E(LAr + Fe + Cu + G_{10})} = 1.4\%$$

Almost all the hadronic cascades were contained within the two calorimeter sections.

3.7.5 LAC Support System and Cryogenics

Both the electromagnetic calorimeter and the hadron calorimeter were suspended from the cover plate, 5 m diameter, of the 9 m hight upright cylindrical cryostat as shown in Figure 21. The cryostat consisted of the cover plate, composed of carbon steel, and the stainless steel can. Eight steel rods, attached to the cover plate, provided support for the EMLAC and the HALAC. The cover plate was attached to the top of a gantry structure. The gantry could be moved on rails perpendicular to the beam direction. The horizontal motion, together with a vertical steering magnet in the beam line, allowed the beam to be swept across the face of the calorimeter for calibration and testing. The cryostat was made of 9/16 inch (1.43 cm) stainless steel and was covered on the outside with ~25 cm of fiberglass and foam insulation. On the upstream side of the cryostat

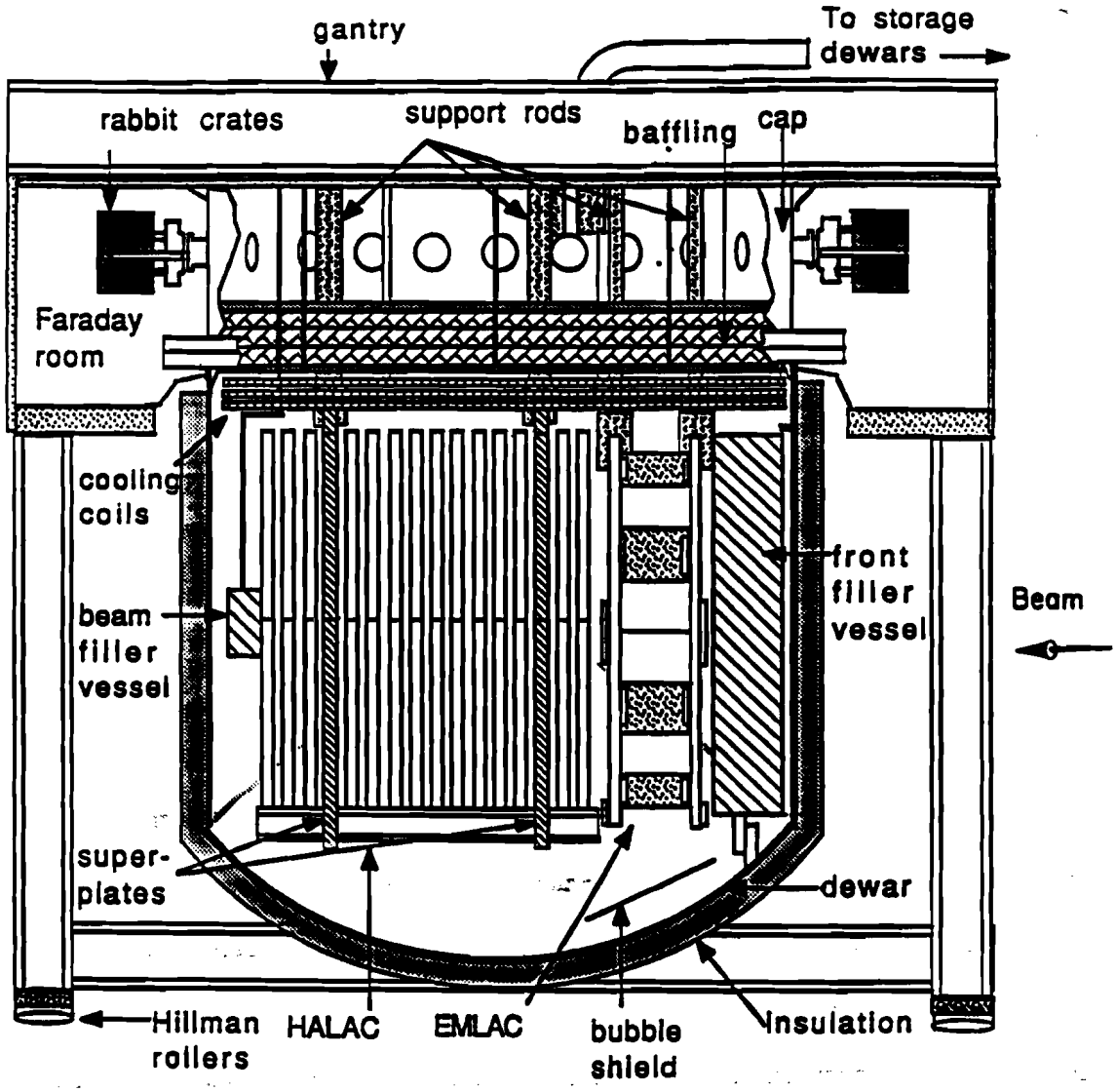

Figure 21: The overall gantry and cryostat of the LAC.

there was a 5.08 cm diameter beam hole covered with two thin layers of stainless steel sheets with a small gap between them. Prior to the beginning of the physics run the beam was adjusted so that it pointed directly into this beam window of the cryostat. The purpose of the beam window was to reduce the material placed in the beam. Two additional vessels were placed inside the cryostat along with the calorimeters. The first one was attached directly upstream of the EMLAC. It was an argon excluder vessel filled with low density foam. Its purpose was to reduce the energy loss of the incident particles caused by the material in front of the readout sections of the LAC. The second vessel had a cutoff conical shape. It was made of stainless steel and filled with helium. This vessel was inserted into the beam holes of the two calorimeters and served the same purpose as the beam window, i.e., to reduce the amount of material placed in the path of the beam.

The calorimeters were cooled down from room temperature to liquid argon temperature in two phases; the pre-cooling phase and the cool down phase. First, after the cryostat was sealed, the vessel was pumped down to a few microns. This procedure lasted about one month because of the detectors' outgassing and small leaks. The cryostat and its contents were thoroughly degassed by an elaborate pumping and purging system. By using a mass spectrometer (tuned to identify helium gas) and spraying helium gas on the outside surface of the vessel, most of the small leaks were detected and fixed. Most of the leaks were found in the cable feedthroughs, i.e., the joints between the external cabling and the cables inside the cryostat.

In the second phase, argon gas was admitted in the cryostat. The argon gas was cooled by boiling liquid nitrogen in the copper coils, attached to the cover

plate. Approximately 170 thermocouples were attached to the EMLAC and the HALAC (and to the support rods, cryostat walls and argon excluder vessels) to monitor temperature changes and variations. The calorimeters, the electromagnetic calorimeter in particular, were expected to be sensitive to large temperature gradients.

Once the detector was cooled to 95°K, 17,800 gallons of liquid argon were transferred filling the cryostat. The liquid argon used was the best commercial grade produced in the USA, with an oxygen content measured to be less than 0.2 ppm. The cooldown and fill operation lasted several weeks, with the maximum temperature gradient between any two points of the calorimeter never exceeding 30°C.

3.7.6 LAC Readout System

Cables, approximately 10 meter long, carry the signals from the calorimeter sections to amplifiers mounted in crates on the outside of the top (cap) of the cryostat. All the electronic crates were attached directly to the cryostat cap. To reduce the effect of the electronic noise on the charge amplifiers, a Faraday room was built to shield all the crates. Digitized signals were sent to the counting room through optical couplers.

The 8,604 readout channels (6,264 for the EMLAC and 2,340 for the HALAC) were read using the RABBIT[59] (Redundant Analog Bus Based Information Transfer) system developed at Fermilab. The RABBIT system consisted of crate controllers called EWEs, Before After Timers (BATs), and Front End Electronic Devices (FEED) as the LAC amplifiers (LACAMP)[60]. The EWEs were controlled through hard wired ECL processors (called MXs). The MXs are dedicated com-

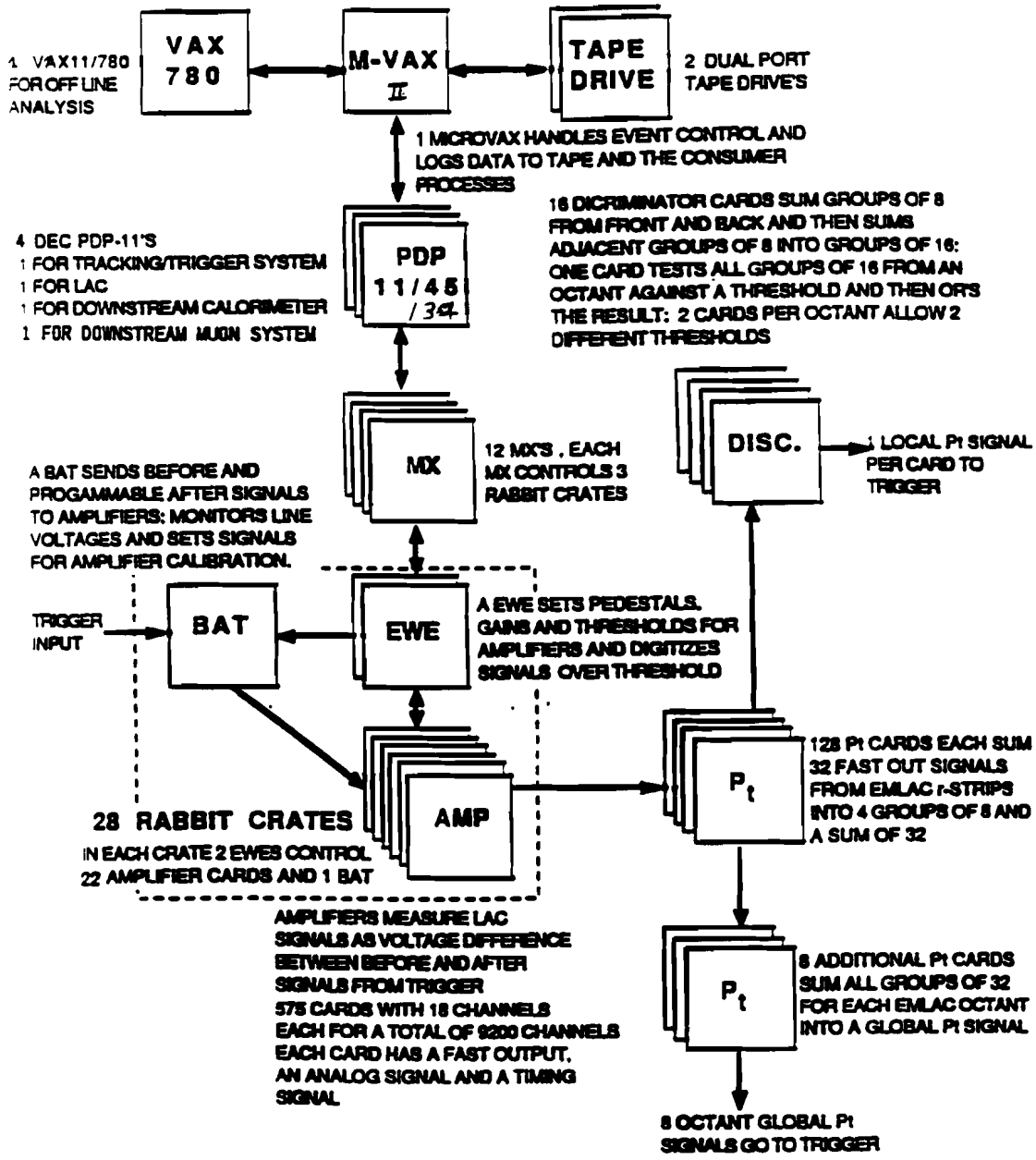

Figure 22: The LAC data acquisition system.

puters developed at Fermilab for use with the RABBIT system. It was used both as an event buffer for the LAC data and to run calibration and correction programs for the online data. The MXs were controlled by a PDP-11/45 computer. This computer was connected to the event process controller (μVax II) which performed all the data aquisition tasks for E-706. Figure 22 shows the LAC data acquisition system. The components shown in this figure will be discussed below.

Each crate has two EWEs each reading half of the amplifier cards in the crate, one BAT and up to 22 amplifier cards. Each amplifier card has 16 channels. The total number of crates used was 27 and they were readout by 10 MXs.

Figure 23(top diagram) shows the block diagram of the LACAMPs. The output of each amplifier was routed to three separate areas: the fast output, the TVC (Time to Voltage Converter), and the sample and hold. The output of each amplifier was delayed 800 nsec to allow time to determine if the trigger conditions had been satisfied. If the trigger was satisfied, the BAT received a front panel "event" signal instructing it to generate a BEFORE signal and (500 nsec later) an AFTER signal on the RABBIT backplane. The delay between the BEFORE and the AFTER was programmable via an 8 bit DAC (Digital to Analog Converter) on the BAT. The EWE digitized the difference between these two levels or either one and ground. The fast outputs were derived from the delay line taps at 180 nsec. They were directed to the LAC trigger electronics for trigger purposes. The TVCs received the sum of the outputs of four adjacent amplifiers. Their function was to produce a voltage proportional to the time between the beginning of a LAC pulse and the BEFORE pulse. An onboard calibrator was provided for remote calibration and testing of the LACAMP modules. The calibrator produced pulses

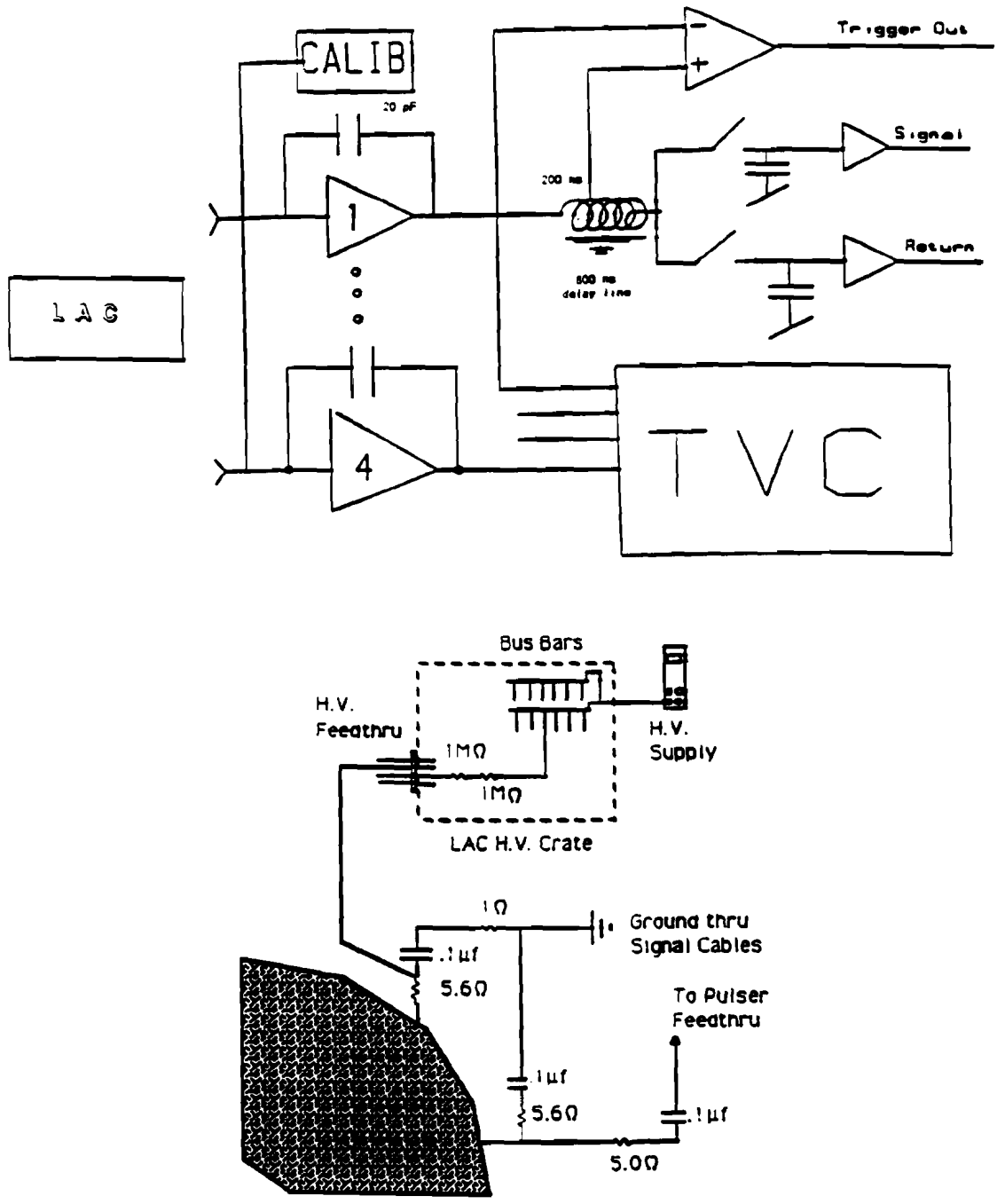

Figure 23: Electromagnetic Calorimeter (EMLAC) readout schematic (top) and the EMLAC high voltage schematic (bottom).

of preset amplitude to any preselected amplifier channels. This allowed for checks of amplifier performance and calibrations. The total time for reading out the LAC was ~17 msec.

The amplifier gains and the pedestals were measured by injecting charge into the amplifiers using the onboard calibrators. This procedure was performed every several runs during the data aquisition and the data were stored in a data base to be accessed by the off-line reconstruction programs.

A zero suppression threshold was applied by the EWE circuitry to every channel to reduce the number of channels to be readout. This threshold turned out to be wider and often shifted from the set value. The consequence of this was that the pedestal values recorded from the electronic calibration procedure had to be determined more accuretly. A procedure was established to determine the pedestal value of each channel by studying the pulse distributions. Figure 24 shows the pedestal distributions from four classes of channels. Figure 25 shows the pulse distribution of each channel of the two HALAC sections from a rather noisy run (10K events). The letter C points to a EWE where the zero suppression window did not work. The area pointed to by A shows several channels where the zero suppression window malfunctioned. Most of the spikes above zero indicate very active channels around the beam hole. The channels at B did not have a stable pedestal value, thus they were giving unreliable output and they were called "noisy" channels. Noisy channels were suppressed either before the data reconstruction, if they were not run dependent, or after the data reconstruction, if they were run dependent. About 2% of all HALAC channels and less than 1% of the EMLAC channels were suppressed.

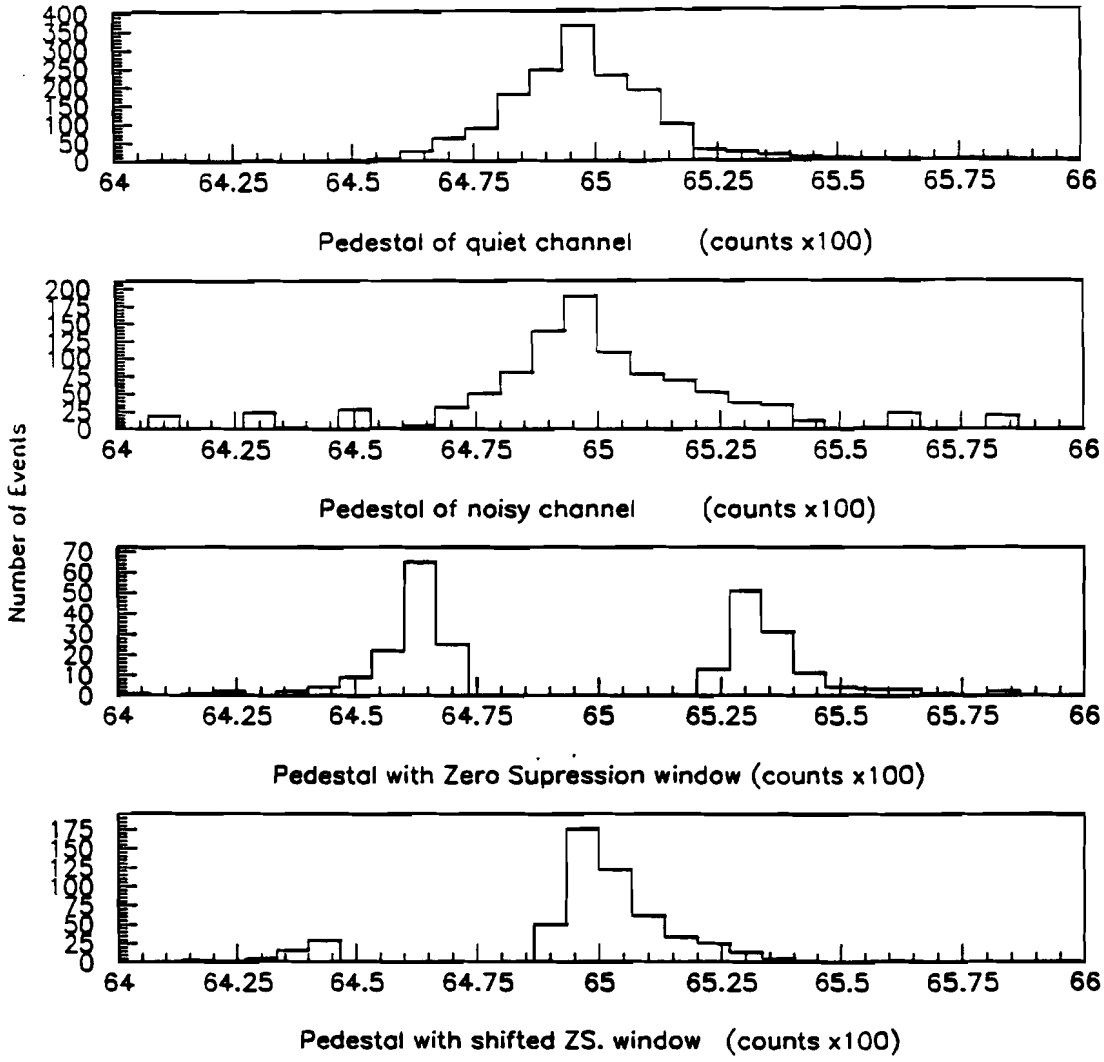

Figure 24: Pedestal distributions from four classes of channels.

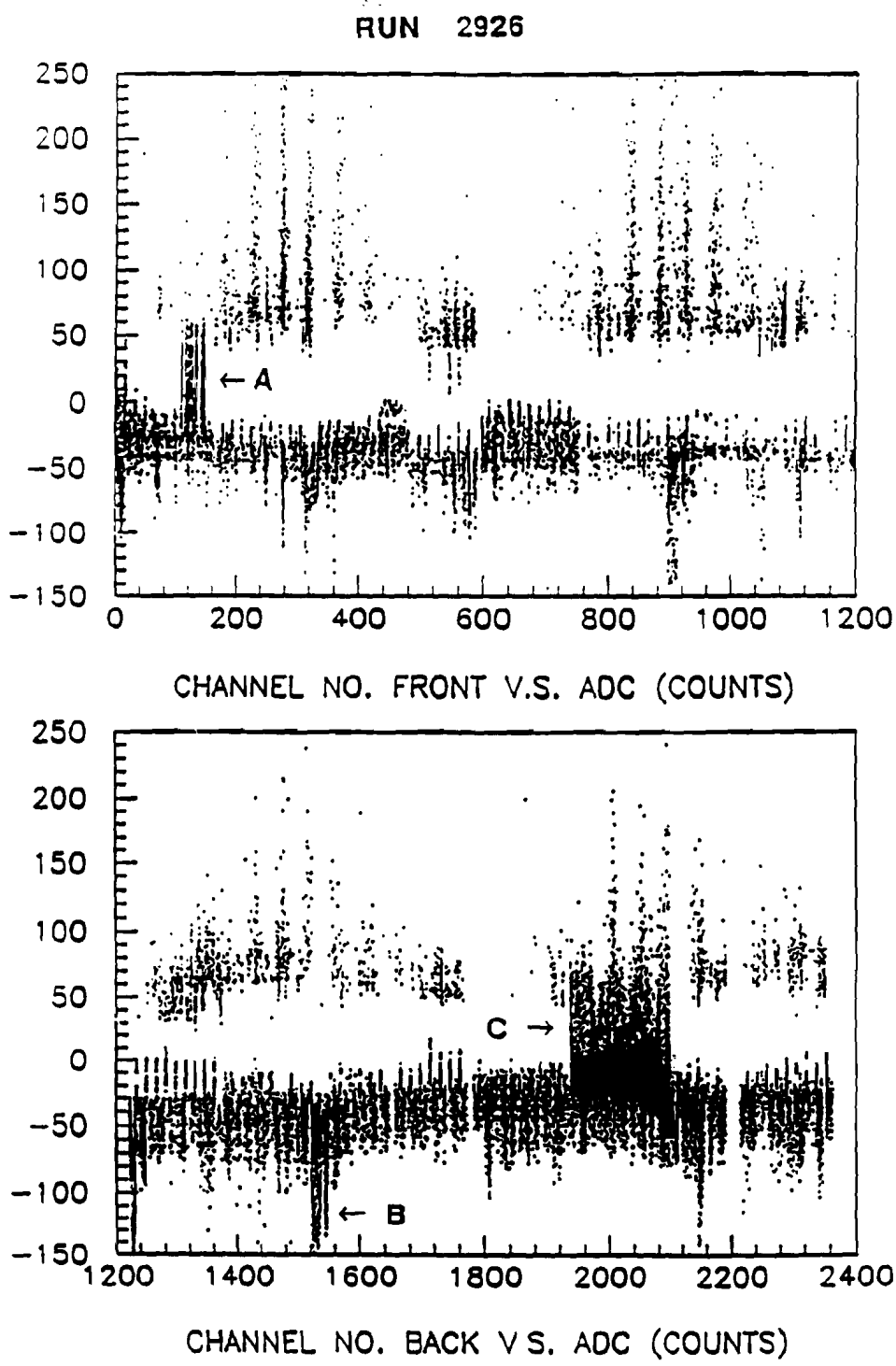

Figure 25: Pulse distribution of each channel of the front/back HALAC sections.

During the experimental run, the pedestals of all channels were determined roughly every eight hours. This was done with a calibration procedure that used the on-board calibrators in the LACAMP cards, and the recorded values were stored in a data base to be used later by the offline data analysis program. Studying the calibration data (along with the online data), it was found that in some cases the pedestal positions deviated by as much as 20 counts (this value corresponds to 65 Mev for the EMLAC and 1 GeV for the HALAC).

3.8. Forward Calorimeter

The forward calorimeter (FCAL)[61] was designed to cover the forward jet region which was not covered by the LAC. This calorimeter was placed approximately 15 m downstream of the target. The showers that were produced by the hadrons in the forward jet could be contained within the forward calorimeter acceptance. No attempt was made to identify individual hadrons. The total energy and the total p_T vector of all hadrons in the FCAL was measured.

The device consisted of three units of alternating layers of steel and acrylic scintillator (Figure 26). Each of the three modules contained 32 steel plates, 1.9 cm thick, by 114.3 cm diameter. The steel plates were separated by gaps of 0.635 cm into which were placed 0.46 cm thick sheets of acrylic scintillator. The scintillator sheets contained 76 holes of 1.12 cm diameter on a 11.43 cm grid, through which the 86.4 cm long wavelength-shifter bars (BBQ) were inserted. The BBQ doped rods also contained an ultraviolet absorbing agent which absorbed UV light up to wavelength of 375 nm, to minimize any effects of Cherenkov light produced by particles passing through the rods. The apparatus contained a central 3.18 cm

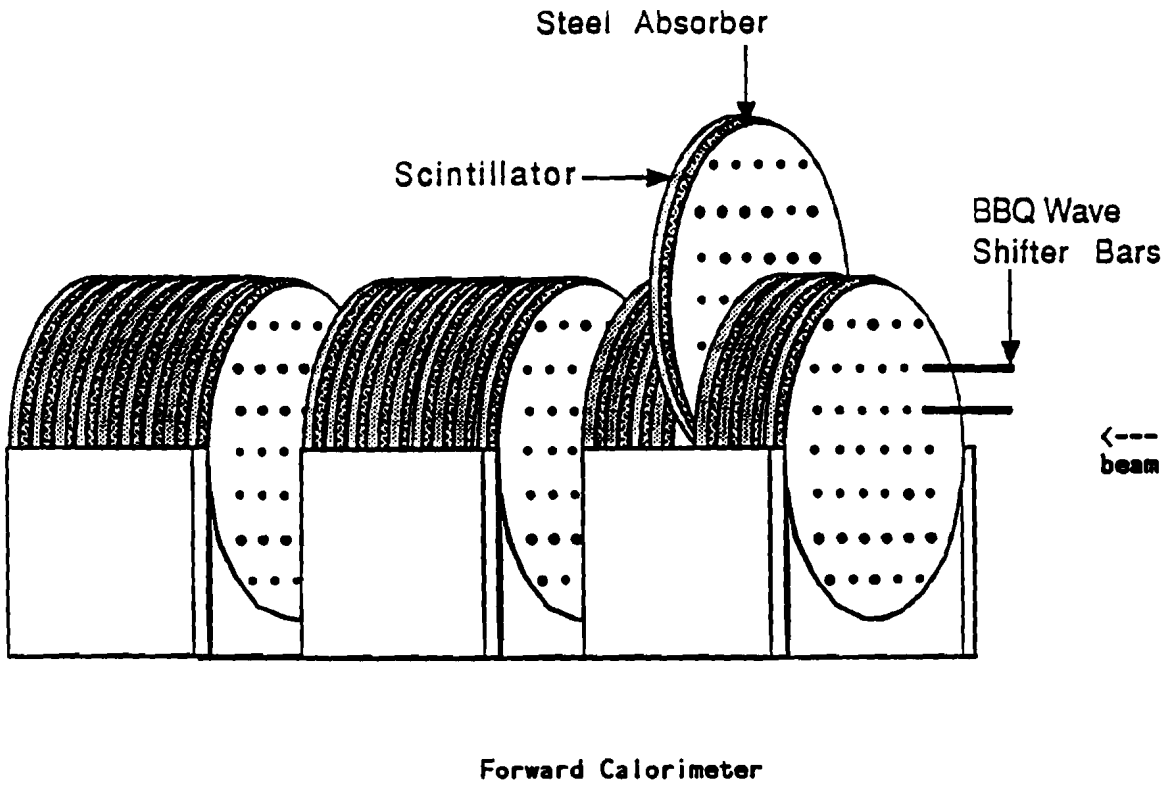

Figure 26: The forward calorimeter.

diameter hole to allow passage of the non-interacting beam. The readout system was connected to the BBQ rods. The signals from photomultiplier tubes (PM) coupled to each rod were digitized by a flash ADC system operating at 100 MHz. This device is capable of operation at rates up to 10 MHz of interactions in the E-706 target.

3.9. Trigger

The E-706 trigger was designed to select events containing electromagnetic showers with high transverse momenta. During the 23 second beam spill, (an average of 5×10^7 protons/pions), there were about 5×10^6 interactions in the target. At 530 GeV the level of γ production above p_T of 4.0 GeV/c was below 10^{-7} per interaction. The trigger was designed to select events which were of interest. This was accomplished by using only the electromagnetic section of the liquid argon calorimeter.

3.9.1 Logic and Electronics

The trigger for this experiment required large transverse energy deposition in the r-view cells of the EMLAC, provided that an inelastic interaction had taken place in the target region and no particles were detected by both of the upstream veto walls. During the 1988 physics data run, we recorded data using six (and occasionally seven) triggers. The trigger type of the event was written in the event header word. The following table lists the triggers used along with their rate from a typical run.

Trigger Name	Short Description	Rate
HI	local LO * global HI	33%
LO (pre-scaled)	local LO * global LO	21%
SINGLE LOCAL	local HI	10%
TWO GAMMA	Nearly Opposite Octants	5%
	each satisfying local LO	
DIMUON	E-672 Trigger	30%
PRE-SCALED BEAM		9%
PRE-SCALED INTERACTION		10%

Table 5: Trigger Characteristics for E-706 1988 Data Run.

Figure 27 shows the triggering scheme for one quadrant. Its features as outlined in Table 5, above, are described in some detail below.

First we describe the most fundamental part of the trigger system which was implemented on the LAC. The basic idea was to trigger on events that showed a high p_T signal in any octant of the EMLAC. Since the detector measured the energy of an electromagnetic particle, the p_T was formed by multiplying the sine of the angle of an EMLAC channel relative to the beam direction with the signal from this channel. Two methods were used to calculate the p_T in a given octant; the LOCAL PT and the GLOBAL PT. The LOCAL PT required a large amount of energy to be confined in a small area of the octant. The local Pt consisted of 16 contiguous r view strips. The GLOBAL PT was the total p_T of the octant, calculated by simply summing all the LOCAL PTs.

The main components of the trigger system were the p_T attenuator board and

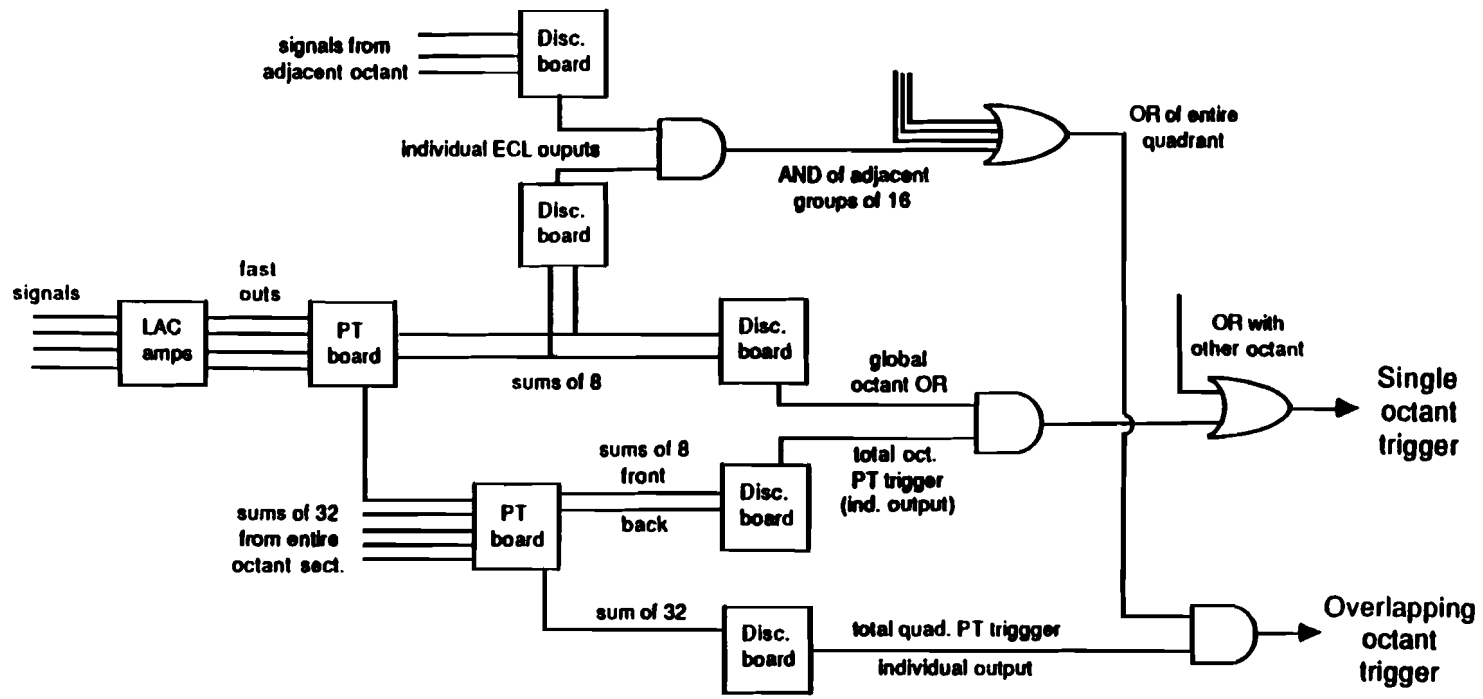

Figure 27: Triggering scheme of one quadrant.

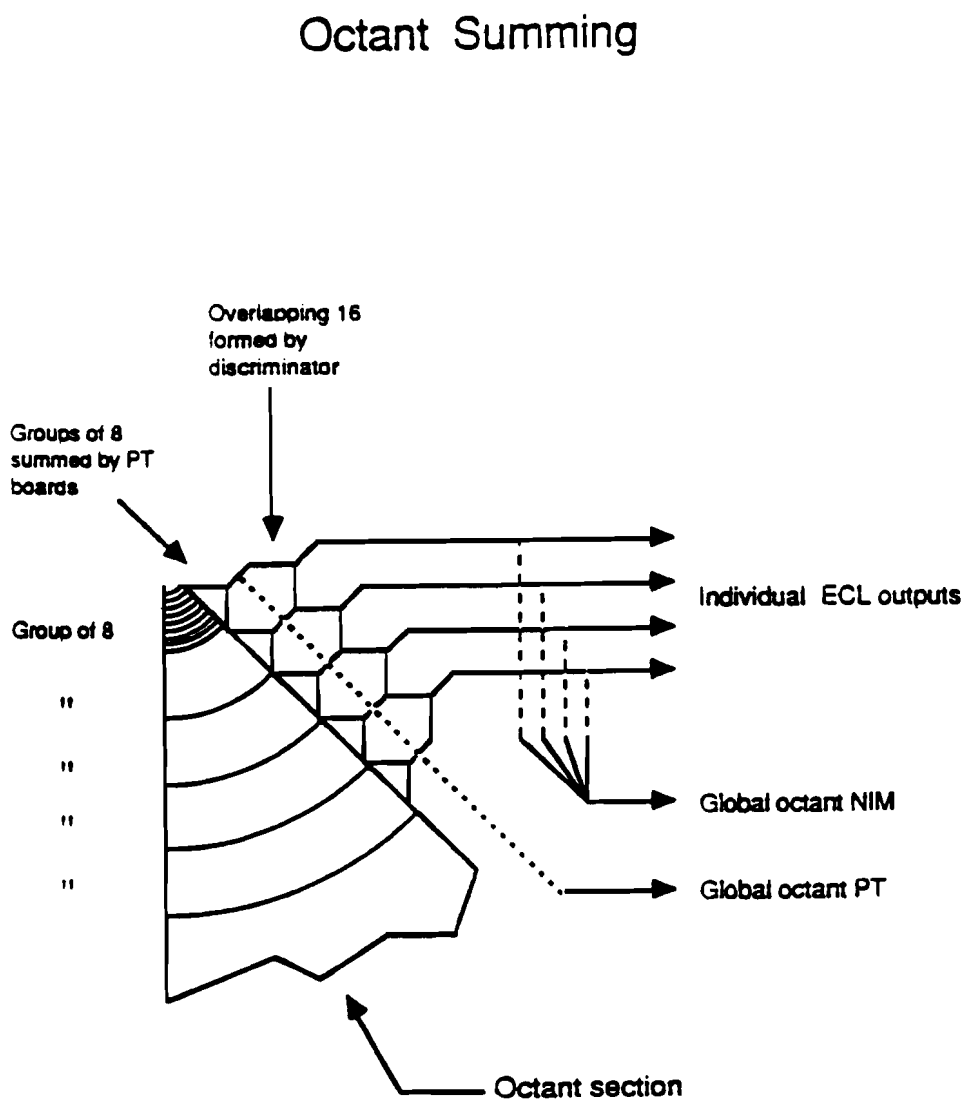

Figure 28: Octant summing scheme of the LAC trigger.

the Discriminator boards[62] The "fast-out" signals from the 254 strips of each octant (front or back section) were fed into 8 PT boards to provide 32 sum-of-8 signals and 8 sum-of-32 signals. The sum-of-32 signals for the entire octant were then sent to a PT board of which the sum-of-8 outputs now represent octant section p_T and the sum-of-32 now represents the total octant p_T. These were sent to a discriminator board to generate the octant GLOBAL PT signals, respectively. The original sum-of-8 outputs from each octant were "daisy chained" to two discriminator boards in such a way that corresponding front and back signals were added and overlapping sums of 16 were formed at the discriminators. The first of these boards was used for the single GLOBAL PT octant trigger and the second for the adjacent octant trigger, used in the two gamma trigger. During the experimental run one sum-of-32 outputs was disconnected from the trigger in order to reduce the effect of the image charge on the trigger (see the LAC readout section). The output disconnected was the one close to the outer perimeter. Figure 28 illustrates the octant summing scheme.

The roles of the LOCAL PT trigger are summarized as follows:

i) Identifies localized high p_T showers.

ii) Helps to discriminate against "noisy" GLOBAL PT triggers. In the GLOBAL PT trigger the p_T of all channels in the octant is summed. Consequently, the GLOBAL PT trigger is sensitive to coherent noise.

Two thresholds were used for both GLOBAL and LOCAL PTs, the LOw threshold and the HIgh threshold. The following table lists the settings used in the 1988 physics data run. Since these settings were both octant dependent and run dependent, here only the average values are listed. The columns represents the

reconstructed p_T of the shower that triggered the event, calculated from the off - line analysis electromagnetic reconstruction program.

Trigger Name	LO(Rec)	HI(Rec)
LOCAL (in GeV)	1.5	2.8
GLOBAL (in GeV)	2.7	3.1

Table 6: Average trigger thresholds for 1988 E-706 Data Run.

Various counters were used to form the interaction logic for the triggers. Figure 29 (top) shows the locations of the beam (BA,BB, and BH) and interaction counters (SW1, SE1, SW2, and SE2) used to form the INTeraction trigger and the veto walls (VW1 and VW2).

The beam (BM) signal is set according to:

BM = BA .and. BB .and. BM GATE

where BM GATE is the beam spill gate set to 23 nsec.

The interaction signal is defined as:

INT = BM .and. (SW1 .or.SE1 .or.SW2 .or.SE2)

To avoid pile up in the LAC we required that there is no other interaction within ±60 nsec (i.e., ±3 rf buckets).

The triggering requirements that lead to the formation of the LAC PRETRIGGER and the OCTANT PRETRIGGER were the following. The LAC/octant pretrigger was defined by a coincidence of the octant's GLOBAL LO PT signal

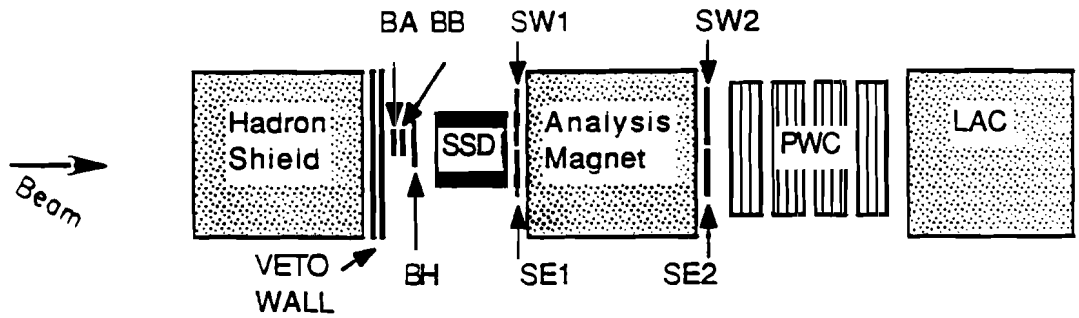

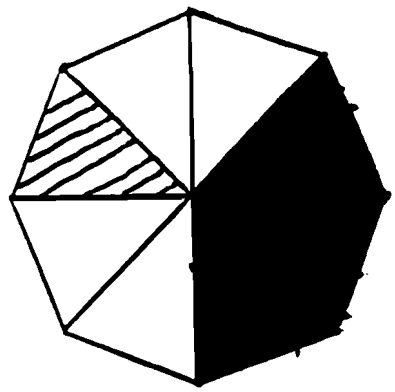

TWO GAMMA TRIGGER

(A local LO is required in any of the octants opposite the shaded one)

Figure 29: (top):Schematic of the counters used to form the logic of the triggers. (bottom): The "two gamma trigger" octant combination .

from the PT boards and the GATED INT1* with the anticoincidence of the VETO WALL, EARLY PT** and SCRKILL.***

The final triggers, as listed in Table 5, were formed as the final result of a combination of satisfied requirements involving many different pieces of the E-706 apparatus. Here we will focus our attention only on the triggers used in the analysis of the data presented in this thesis, i.e., the HI, SINGLE LOCAL and TWO GAMMA triggers. The requirements of the previously listed Pt triggers are the following:

i) The SINGLE LOCAL trigger was defined as a coincidence of the LAC PRETRIGGER, the octant LOCAL Pt HI and the OCTANT PRETRIGGER.

ii) The LOCAL HI trigger was defined as a coincidence of the LAC PRETRIGGER, the octant LOCAL Pt LO, the octant GLOBAL Pt HI and the OCTANT PRETRIGGER.

iii) The TWO GAMMA trigger was defined as a coincidence of opposite (or next to opposite, see Figure 29(bottom graph)) octant LOCAL Pt LOs and the octant pretriggers.

3.9.2 Trigger Efficiency

The triggers that were used in the analysis did not include the MUON trigger

---

* The GATED INT1 strobed the trigger and was defined as a coincidence between the interaction signal and the CLEAR2 GATE. The latter was set to 5 μsec to give time to the BAT to be reset when there was a computer reset signal.

** The EARLY PT was satisfied when there was a signal in any Pt board within 300 nsec with respect to the interaction signal. This was implemented to suppress out of time triggers.

*** The SCRKILL was set when a noise spike was generated (usually from the power supplies) within $\pm$ 15 μsec.

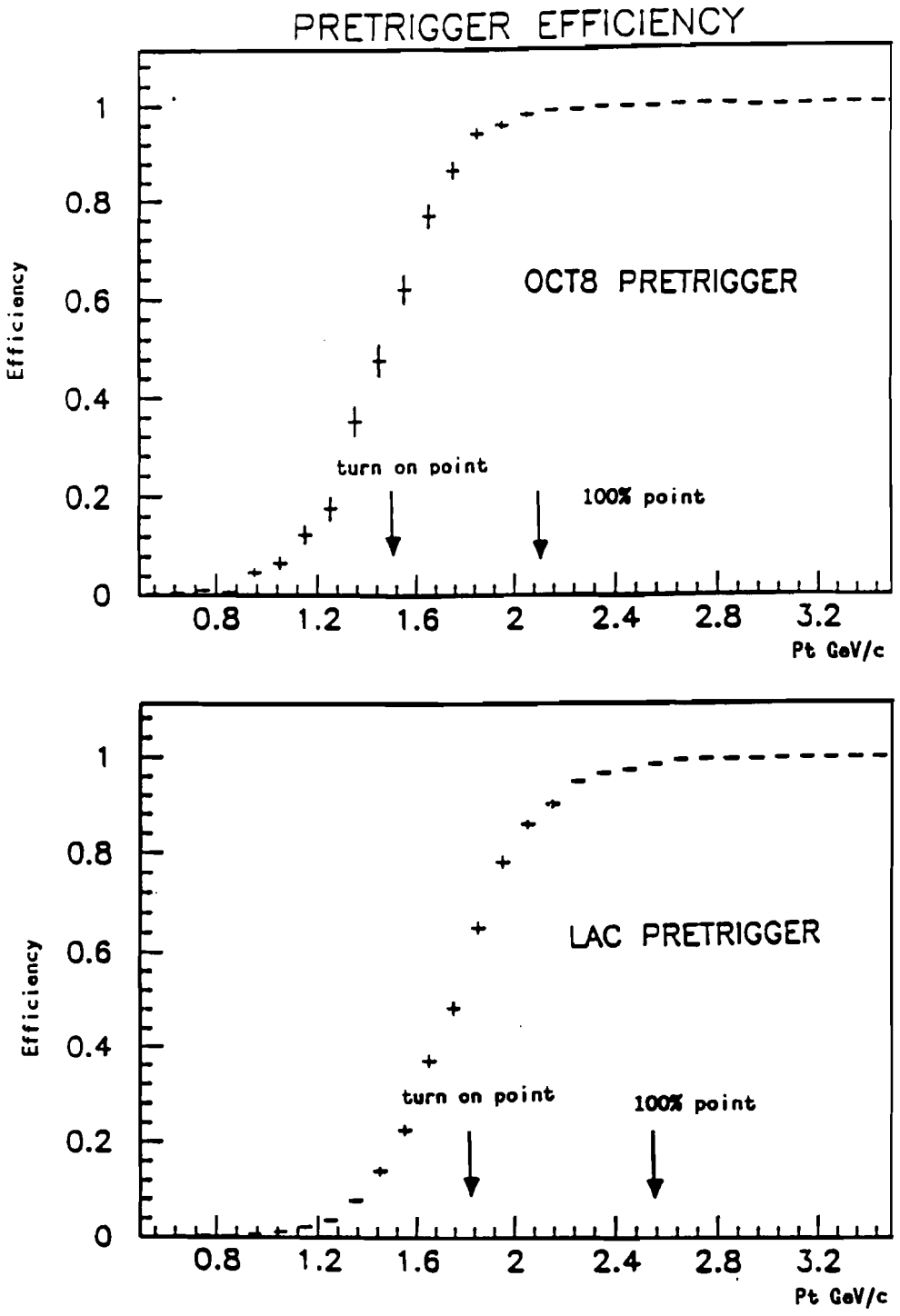

Figure 30: LAC pretrigger efficiency curves.

(see Table 5).* The trigger efficiency of the interaction part of the trigger is believed to be close to 99%. Figure 30 shows the pretrigger efficiency for Octant 8 and all octants. The turn-on and the 100% efficiency points (p_T's) are shown on the graphs.

It was more complicated to establish the trigger efficiency for the high p_T trigger. The efficiencies of the HI, SINGLE LOCAL and TWO GAMMA trigger were measured relative to the LO triggers as a function of p_T as well as relative to each other. Figure 31 shows the efficiencies of the SINGLE LOCAL trigger mentioned above for Octant 5 and for all octants. The SINGLE LOCAL trigger turned out to be the more efficient and in general the most reliable trigger among the triggers. The turn-on and the 100% efficiency points are shown on the graphs.

3.10. On-Line Data Acquisition and Monitoring

The detectors used by E-706 during the 1987-88 data run were interfaced to three PDP-11/34's and a PDP-11/45. Event data were accumulated in the front end buffers on the PDPs. One PDP handled the LAC electronics, one the forward calorimeter, one the data of the experiment E-672, and another the tracking system (SSDs and PWCs) and the trigger logic. The PDPs were connected to a μVax II computer which was used as the event process controller to concatenate the data

* During the experimental run there were many changes made to the original trigger configuration and to the octant p_T thresholds. The most serious problem identified was the image charge effect. The ballast capacitors attached to the lead plates in the EMLAC could not respond fully to the current demand on the trigger time scale (i.e., 200 nsec) so that a large percentage (~ 50%) of the current was provided by positive (i.e., wrong sign) charge "imaged" on the calorimeter anode board. Large changes to the trigger were required to minimise image charge effects to provide a workable trigger. The net effect was that the trigger worked but it turned on slower, and the threshold was somewhat position and event topology dependent. Because of the long signal integration time scale of the LAC (~600 nsec) the offline analysis appears to be unaffected.

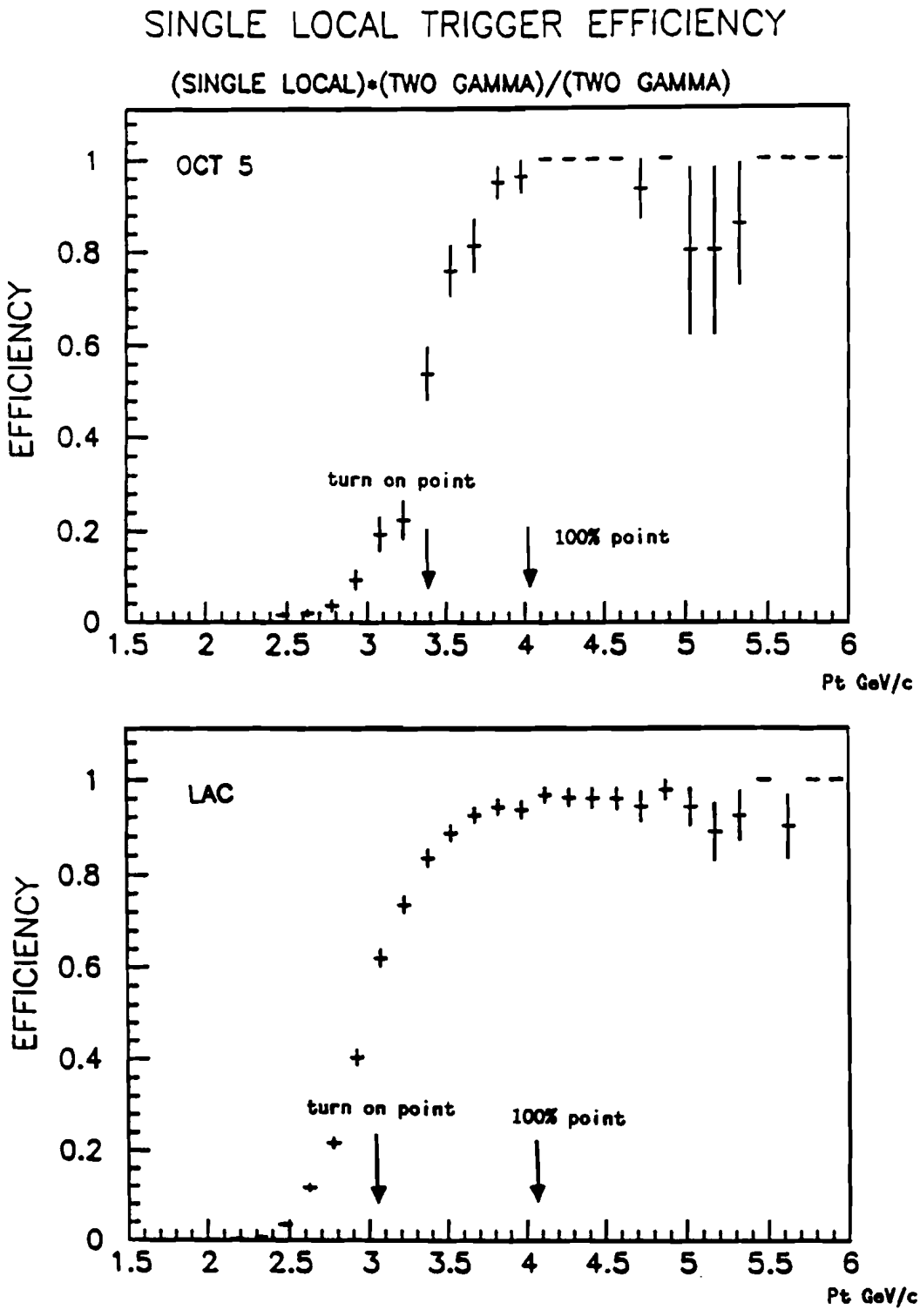

Figure 31: SINGLE LOCAL trigger efficiency curves.

E706 SUMMARY
1987 - 88 DATA RUN

KEY DATES

Suspend LAC	Jan 1987
Begin LAC Cooldown	Jul 1987
First LAC Signals	Aug 1987
LAC Studies	Sep - Oct 1987
Data Collection	Nov 1987 - Feb 1988
LAC Calibration	Feb 1988

Beam	Target	# Triggers	Comments/Dates
π^-	C	330 K	Shakedown Data Nov - Dec 1987
π^-	C	690 K	
p/π^+	C	160 K	Physics Data Jan - Feb 1988
p/π^+	Be	1500 K	
p/π^+	Cu/Be	1300 K	
π^-	Be	1240 K	
π^-	Cu/Be	790 K	

Table 7: Summary of E-706 1987 - 1988 data run.

from the different parts of the apparatus and to run part of the online analysis and monitoring program. After the concatenation, the events were stored in an event pool in the computer memory and from there were logged to tape. The μVax II was also connected to a Vax 11/780 computer which was used to create and execute the processes that monitored the data flow from the PDPs to the event pool and sample the events in the pool. All the diagnostic and monitoring tasks (i.e., event dumps, histograms, graphics displays and the online data base) ran on the Vax 11/780. The software package used to run the data acquisition tasks was the VAXONLINE system[63] which was developed by the Fermilab computing department. The average event size was 10 kBytes (or 5,135 words) and the average event rate was 20 Hz during each 23 sec spill. The amount of data collected in this run was roughly 1 event equals 1 pbarn^{-1} (live time interactions), counting the positive and the negative beam data. The data were taken from November 1987 to February 1988. Table 7 shows a summary of the data run along with several key dates.

4. LAC CALIBRATION

4.1. Introduction

Since the Liquid Argon Calorimeter (LAC) was newly built, it was necessary to study, in detail, its response to hadronic and electromagnetic showers. During the experimental run, two calibration runs were carried out; one in December 1987 (prior to the physics data taking run), and the other in mid February 1988, near the completion of the data taking run. The response of the LAC was measured for pions with energies from 50 GeV to 400 GeV and for electrons with energies from 25 GeV to 200 GeV.

The liquid argon calorimeter was assembled in the MW experimental area of Fermilab. It was not possible to move the calorimeter to other existing test beam lines because of its size and structure. Instead the MW beam line was designed to provide test beams for the detector, in addition to the beam needed for the physics run. To do this, the beam had to be able to operate at low energies and included a dipole magnet to sweep the beam vertically across the apparatus. The calibration beam consisted of both electrons and hadrons (mostly π^-) which were used to calibrate the electromagnetic and the hadronic sections of the LAC. The particles with zero production angle from the interaction of the 800 GeV/c primary proton beam and the production target MW6TGT (see MW secondary beam line Figure 13 in the previous chapter) were transported through the MW beam line. By adjusting the magnetic field of the dipole magnet MW6W, particles having the desired momentum were selected. The particle compositions for the beam energies used are listed in the following table.

Beam Energy →	50 GeV	100 GeV	200 GeV	400 GeV
e^- →	38%	22%	6%	~1%
hadrons →	62%	78%	94%	~98%

Table 8: Particle compositions for the LAC calibration beam.

The length of the beam spill was 23 seconds and a spill occurred every 61 seconds. The beam intensity was adjusted using the collimators to about 10^4 particles per second to reduce pileup of signals in the detector.

The first calibration run studied the detector response, and the second calibration run studied its position dependence. During the first calibration run, the study of the detector response was done using a small area of the detector near a quadrant boundary in the EMLAC and the corresponding area of the HALAC.* The two scintillation counters BH and SW2 (see Figure 29) were employed in coincidence as the trigger.

The last two days of the experimental run was the final calibration run. The analysis magnet was rolled out of the beam line and the hadron shield blade was pulled out. Data was taken at various geometrical points on the LAC by moving the LAC horizontally and steering the beam vertically. As in the first calibration run, the SSD/target system was rolled out of the beam. The two scintillation

* The center piece of the hadron shield was not removed. This shield limited the capability of sweeping the LAC with the calibration beam. The beam could be swept vertically from Y= -4.8 cm to Y= 4.8 cm at the EMLAC front face. For the calibration, the beam was steered in the negative Y direction by the magnet MW8D and hit the front face of the EMLAC at y = -4.1 cm. The LAC was moved off the beam line horizontally from the beam and hit at x = 52.85 cm. Because the dead region between two quadrants of the EMLAC extended from Y=±2.9cm to Y=±4cm, we had a window for testing the LAC which varied from a minimum of 1.0 cm to a maximum of 2.0 cm in width.

counters SCS2 and SCS3 were placed upstream and downstream of the beam Cherenkov counter. They were set in coincidence to trigger* the LAC:

CALIBRATION TRIGGER = SCS3 .and. SCS2 .and. COMPUTER READY

Figure 32 shows the positions where the test beam hit the front face of the EMLAC for the calibration runs. The underlined numbers indicate the runs with the 100 GeV/c beam. The rest of the numbers are the 50 GeV/c calibration runs. We took twice as many data to calibrate the HALAC (about 6K) as we did for the EMLAC in order to have enough statistics for particles that deposited all of their energy in the HALAC.

The beam energy was calculated using the beam line magnets. Throughout the text the nominal values 25, 50, 100, 200, and 400 GeV/c should be understood as the values 22.4 $\pm$0.1 GeV/c, 56.4 $\pm$0.1 GeV/c, 103.6 $\pm$ 0.1 GeV/c, 193 $\pm$1 GeV/c, and 378 $\pm$3 GeV/c, respectively. The momentum spread of beam was typically $\Delta P/P = 1.5\%$.

The main differences between the two runs were the following:

i) Test runs with beam momenta of 200 and 400 GeV/c were taken only during the first calibration run.

ii) The energy thresholds for all channels in the entire LAC were 4.02 GeV for the HALAC and 250 Mev for the EMLAC for the first calibration run and 2.7 GeV for the HALAC and 168 Mev for the EMLAC for the second run. In the following sections we will not distinguish between these two runs. The reconstructed energies

* There were more fake triggers (mostly muons) in the second run due to a different trigger configuration.

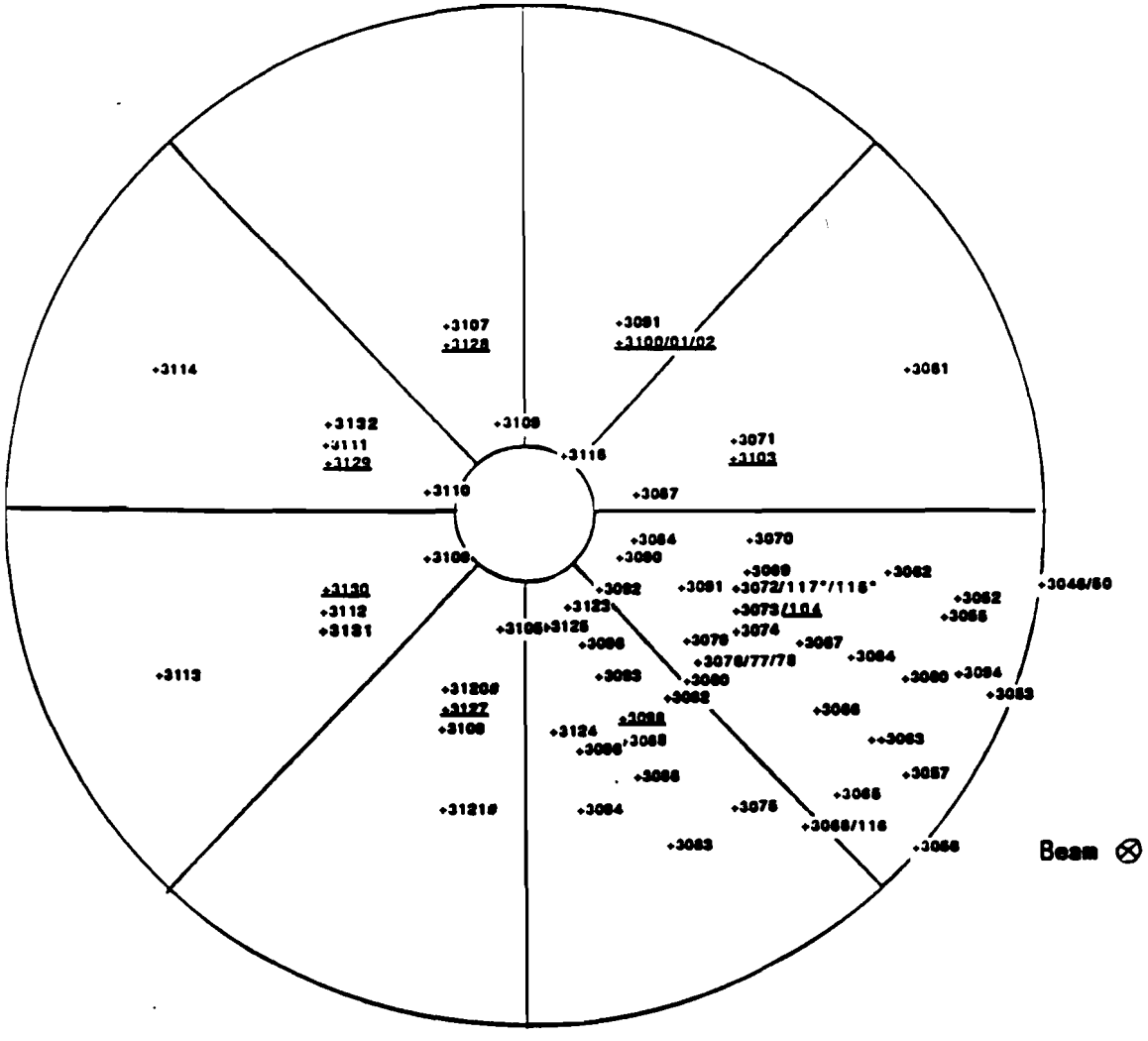

RUN numbers of Feb. 88 LAC Calibration.

Underlined numbers indicate 100 GeV test beam.
Run number 3132 is taken with 25 GeV test beam.
All other runs were taken with 50 GeV test beam.

Figure 32: Data points of the Feb. 1988 LAC calibration indicated by the run numbers on the front face of the EMLAC.

from the first calibration run were corrected for the different threshold used for the second run.

iii) During the second calibration run the Cherenkov counter was used to tag electrons and pions.

The goals of the calibration runs were to study the following topics:

1) To perform high voltage tests in order to see how much voltage could be applied to the LAC to maximize the charge collection in Liquid Argon without creating discharge between electrodes, and to study the high voltage dependence of charge collection.

2) To perform timing tests in order to set the Before -After -gate width in the timing circuit.

3) To study the effect of the digitization threshold of the ADC (or Zero Suppression window) on the measured energy deposited in the LAC.

4) To measure the energy calibration constants used to convert ADC counts to energy for both sections of LAC.

5) To measure the energy dependence of the energy resolution.

6) To measure the position dependence of the energy resolution and energy deposition.

A more detailed discussion of each of the above follows in this chapter.

4.2. Charge Collection & High Voltage Response

Electrons produced by ionization in the liquid argon gaps were collected by the readout strips of the EMLAC or triangular pads of the HALAC, on the copper-clad G-10 boards. The amount of collectible charge produced in liquid argon calorimeters can be written

$$Q_o = \frac{fEe}{2 \times I} \tag{4.1}$$

where f is the fraction of energy deposited in the liquid argon , E is the energy of the incident electron/photon or hadron, I is the ionization potential of argon and is equal to 26.4eV and e is the electron charge. For the EMLAC the expected charge Q_o^E is

$$Q_o^E = (1.6 \times 10^{-19}C) \times (10^9 eV/GeV) \times (0.2) \times (2 \times 26.4eV)^{-1} = 0.6 \text{ pC/GeV}$$

and for the HALAC,

$$Q_o^H = (1.6 \times 10^{-19}C) \times (10^9 eV/GeV) \times (0.014) \times (2 \times 26.4eV)^{-1} = 0.0424 \text{ pC/GeV}$$

where the factors 0.2 and 0.014 are the sampling fractions of ionizations for the EMLAC and the HALAC, respectively.

There is a factor 1/2 in Eq. (4.1) because it is assumed that the charge is distributed uniformly in the liquid argon gap. Only half of the induced charge in the liquid argon can be collected because half of the electron charge is frozen in order to image the positive ion charge (the positive ions do not contribute to the signal). The induced charge on the electrodes when an ionizing track is present across the liquid argon is given by the equation:

$$\frac{Q_c}{Q_o} = \frac{2\lambda}{D}(1 - \frac{\lambda}{D}(1 - e^{\frac{-D}{\lambda}})) \tag{4.2a}$$

and,

$$\lambda = \frac{\alpha|E|}{P} \tag{4.2b}$$

where[64], D = gap width, $\alpha = (.13 \pm .03)\text{cm}^2\ \text{kV}^{-1}$ ppm, and λ = mean free path length for electron absorption by oxygen admixtures of concentration P in the liquid argon, and Q_o and Q_c are the expected charge and the collected charge respectively.

The total drift time t_{drift} can be parametrized as[65]

$$t_{drift} = \frac{D}{v_{drift}} \tag{4.3}$$

where[64], $v_{drift} = 2.1 \times 10^4 [E(V/cm)]^{1/3}$ and D = gap width.

For the EMLAC having D = 2.5 mm and an operating electric field of 10kV/cm we get a drift time of 552 nsec from Eq. 4.3. After the cryostat was completely filled with liquid argon and high voltage was applied on the detector the output of an amplifier was measured to have a rise time of 300 nsec. In order to explain the difference between the expected velocity and the measured one we have to assume that either the drift velocity was less than 221 nsec/mm or that we were not collecting all the charge, i.e., $Q_o/Q_c = 54\%$ where Q_o is the expected charge and Q_c is the collected charge.

Table 9 below lists the measured charge response of LAC at various times during the experimental run.

	DATE	DETECTOR	BEAM ENERGY (GeV)	Qc(pC)	Qo(fC)	Qo/Qc(%)
1	8-26-87(1)	EMLAC	50	15.1	30.0	50
2	12-9-87(2)	EMLAC	100/200	27.0	60.0	45
3	2-15-88	EMLAC	50	13.5	30.0	45
4	10-26-87(3)(4)	HALAC	200	3.69	8.48	43
5	12-9-87(3)	HALAC	200	3.72	8.48	44
6	2-15-88	HALAC	100	1.68	4.24	40

(1) only the r-view front section of the EMLAC was calibrated (2) corrected for about 5% energy leakage at Quadrant Boundary. (3) corrected for a zero suppression = 82 counts (or about 4 GeV). (4) corrected for a 5% leakage to the beam hole.

Table 9: Charge response of LAC at various times during the experimental run.

Figure 33 shows the data in Table 9 (the measurements of 2-15-88 are plotted) along with calculated high voltage curves based on Eq. 4.2a. We see that at the operating point (i.e., the selected value of the high voltage applied in each layer) of both detectors only 44-48% of the expected charge was actually seen. Note that the experimental curves in Figure 33 fit better to the 4ppm (O_2 concentration) curves even though the measurements of the gas, taken from the top of the cryostat in early 1988 showed an oxygen level of less than 1 ppm. Other researches have found that Eq. 4.2a gives a value approximately 30% higher for incident electrons[66],[67], compared to other beam particles. However this does not explain the observed discrepancy and no explanation has been found.

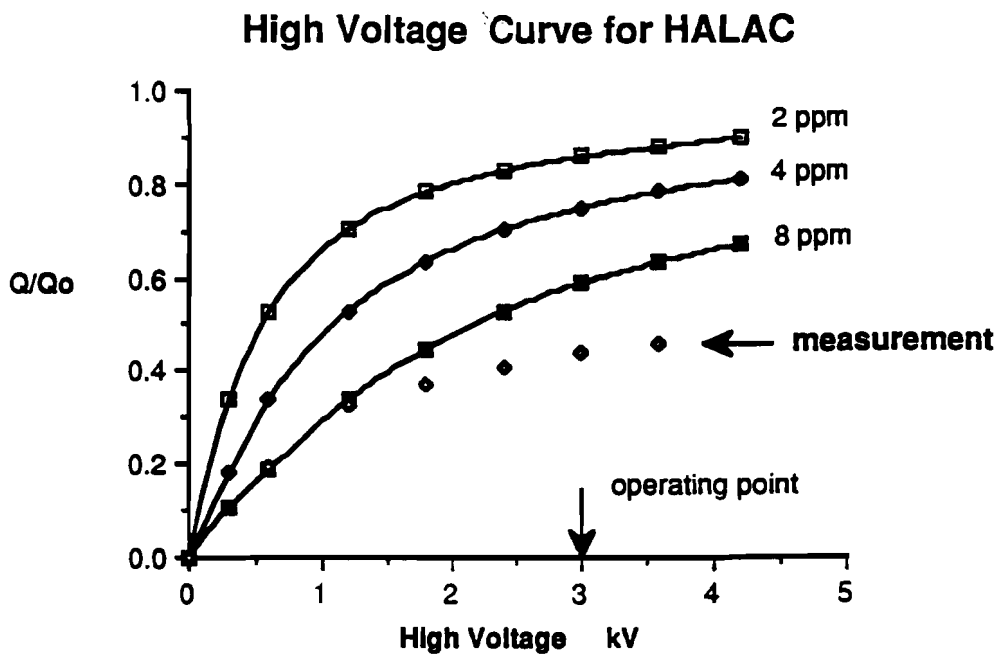

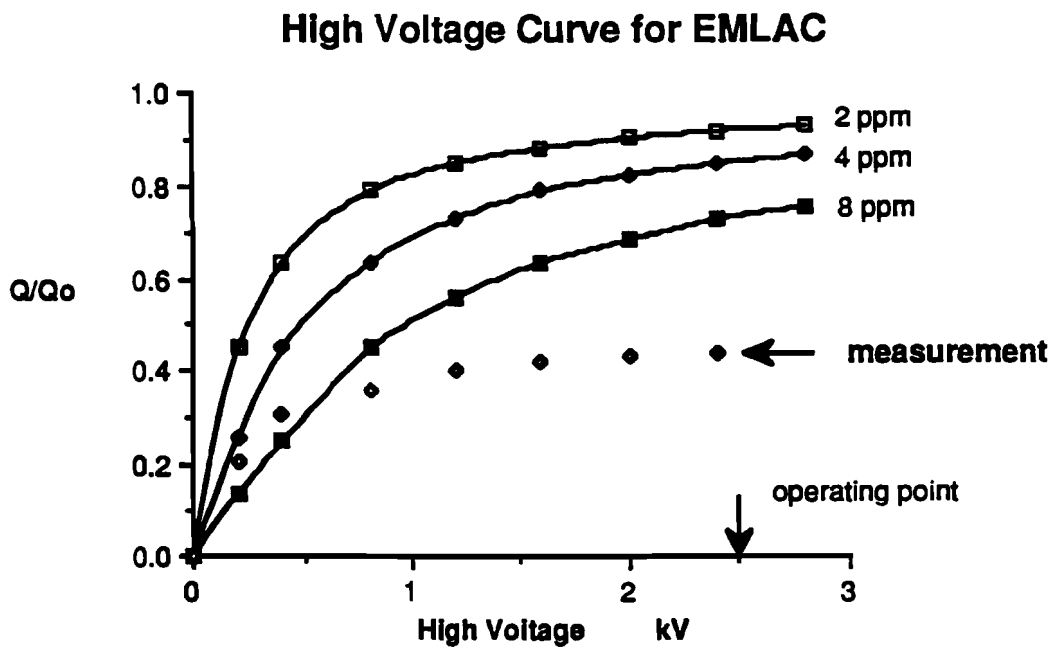

Figure 33: High Voltage curves for the HALAC (top graph) and the EMLAC (bottom graph).

4.3. Timing Tests

The output of each channel of the calorimeter was connected to an amplifier module, LACAMP. There were about 8,600 of the channels in all. The output signal was sampled twice for each event to cancel the base line shift of the amplifier caused by possible preceding events. When the trigger condition was satisfied the BAT circuit (the before-after timing device) generated a gate pulse. The leading edge of the gate pulse caused the first sampling and the trailing edge caused the second. The width of gate pulse was adjustable via an eight bit DAC on the BAT. The output of each amplifier was sent to the "sample and hold" section of the LACAMP module where the output levels were held on two separate capacitors. The difference between these two levels was digitized by the EWE and read out. The total energy deposition was obtained by summing the outputs of all channels around the spot the test beam hit the detector. The optimum gate width was determined by maximizing the summed channel outputs and minimizing the detector resolution, and it was 500 nsec. It was not set at the exact point where the resolution is minimum because we wanted to keep the gate width as small as possible. The energy's measured dependence on the before-after gate width for the hadron calorimeter, is shown in Figure 34 (top graph). The bottom part of Figure 34 shows the dependence of the energy resolution on the before-after gate width.

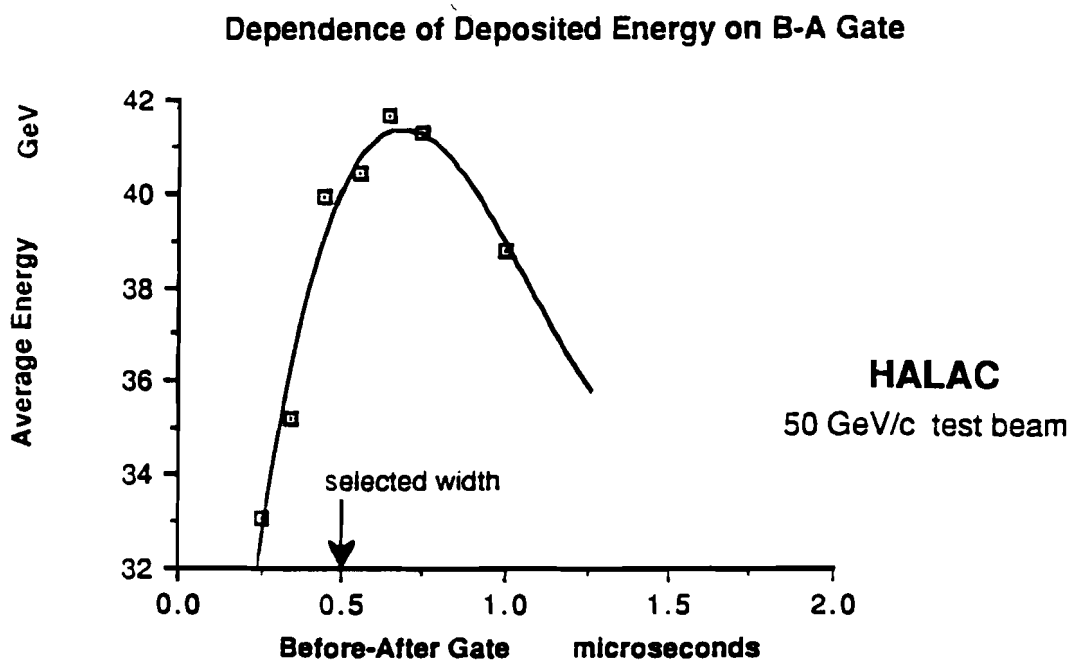

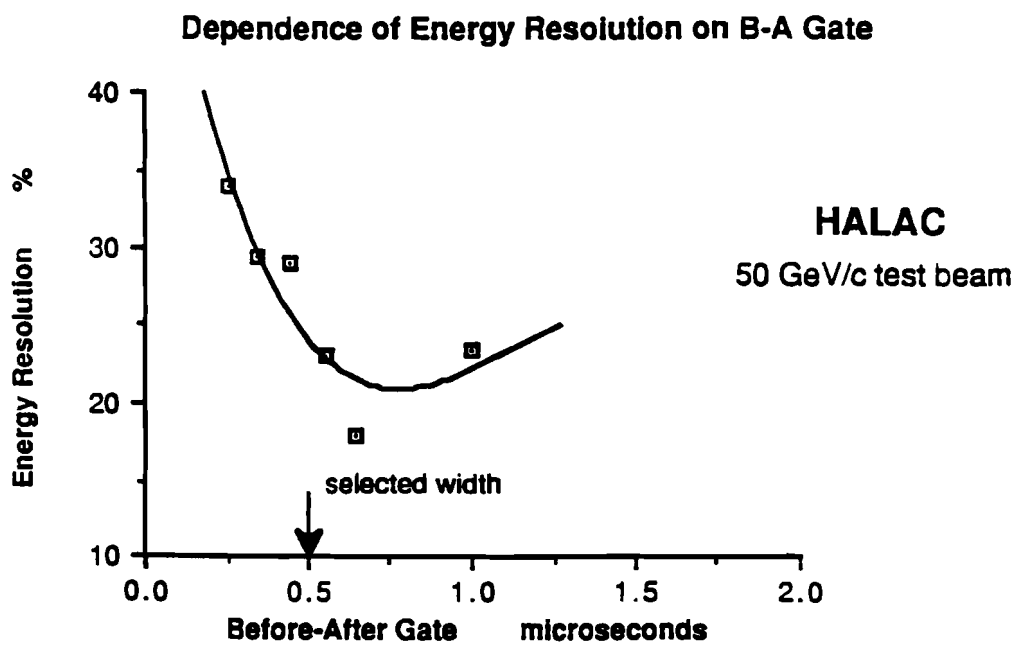

Figure 34: Dependence of the energy measured on the before-after gate width for the hadron calorimeter.

4.4. The Zero Suppression Window

Only the channels with substantial pulse heights were read out by the data acquisition system. The decision to read out a channel was made by comparing the signal with a reference voltage. This scheme was called "zero suppression". The channels with pulse heights in a certain range around zero-signal were not readout. This range was called the "zero suppression window". The half width of the range was called "zero suppression threshold".

There were two effects of the Zero Suppression window on the data. First, the low energy tails due to the lateral shower spread were lost. A correction to the data had to be applied in order to recover this lost energy. Second, the Zero Suppression window was not centered at the effective zero of each channel, i.e., the pedestal. In Figure 35 (top graph) the pulse height distribution of the zero suppressed channel is overlapped with the distribution of a non-zero suppressed channel from the same EWE but for a different run.

A method was developed to calculate the effective channel zero from the measured pulse height distributions. Figure 36 (top) shows the center of the zero suppression window for all channels of a typical EWE. The pedestal was relatively stable throughout this run. Figure 36 (bottom) shows the zero suppression window difference between two runs for all channels of the EMLAC. Because of the relatively large noise of the HALAC channels the effective channel zero could not be calculated reliably for each channel. Instead all channels in a EWE (i.e., about 160 channels) were assigned the same correction. The pulse heights of all channels in the EWE except the first and last ones (because, the first and last channel of each LACAMP were noisier than the rest) in each amplifier card (i.e. 14 channels

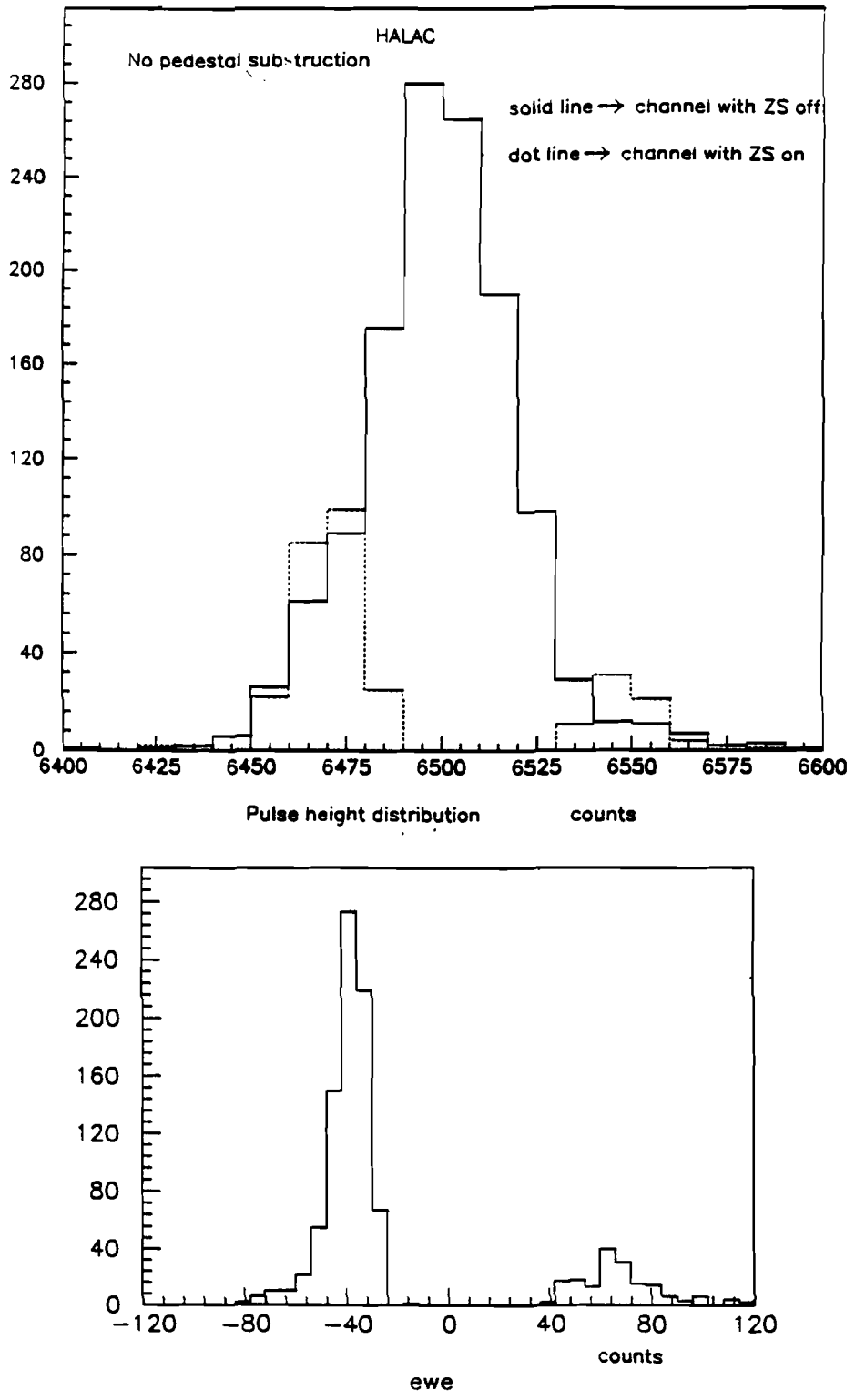

Figure 35: (top): Channel with non - centered zero suppression window (bottom): Pulse height distributions of the channels in a EWE with zero suppression window turned on.

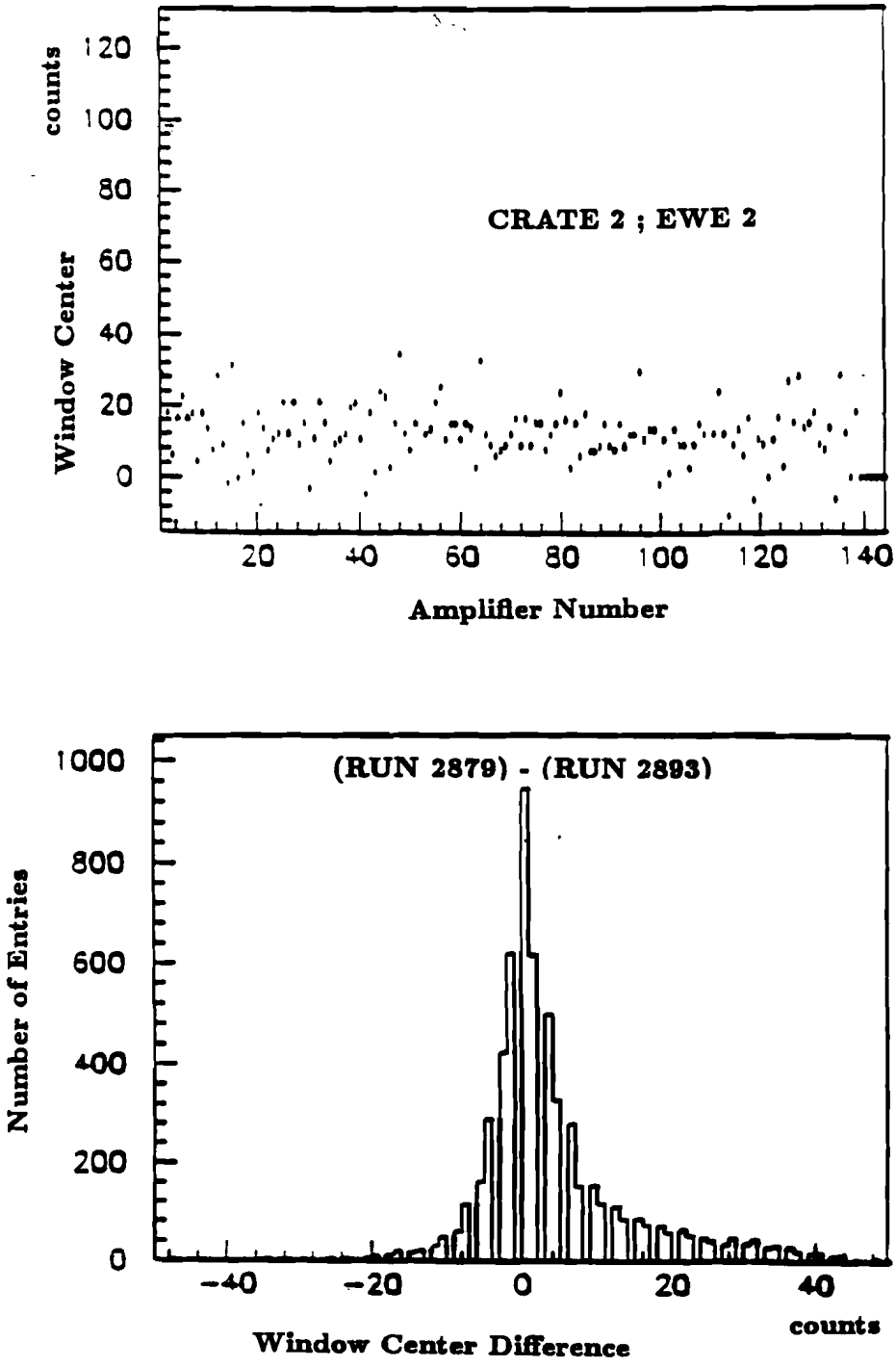

Figure 36: (top): The zero suppression window for all channels of a typical EWE. (bottom): Zero suppression window difference between two runs of the EMLAC.

total were summed. The effective zero of the EWE was set to the mid distance between the two peaks of the summed tail distributions.*

Figure 35 (bottom graph) shows the summed distributions of the channels in a EWE, the tail distributions and the zero suppression window effect.

4.5. Energy Calibration

One of the main tasks in the calibration of any apparatus is to determine the constants for converting the readout to the physical quantity, in this case ADC counts to energy. Before describing the procedure to measure the conversion constants, we will first show and comment on the energy distributions as measured from both sections of the LAC with the calibration beam. In Figure 37 we show the total energy distributions for the 100 GeV/c calibration beam as seen in the EMLAC(graph a) and the HALAC(graph b). In graph (c) we plot the energy distribution in the HALAC from the same calibration run for cases where the beam particles did not deposit any measurable energy in the EMLAC. We can distinguish four peaks in these plots. Peak A is the energy distribution due to the incident electrons; it has a low energy tail (the left side of A) because some

---

* In the EWE circuitry the energy threshold was calculated using the following series of conversions :

$$E_{zs} = (50mV) \times (T/255) \times (1/65) \times (1/2) \times (65535 counts/2.5V) = 2600 counts/T$$

where, 50 mV is the hardware window at the output of the TOT (Test Over Threshold) circuitry in the EWE. (T/255) is the scaling factor applied by the threshold DAC where T is the DAC setting in decimal(during the run it varied from 82 counts (beginning of run) to 55 counts(close to the end of it),

65 is the hardwired gain of the input to the TOT section of the EWE,

2 is the hardwired gain of the pedestal correction section of the EWE,

2.5V/65535 counts is the nominal gain of the ADC used.

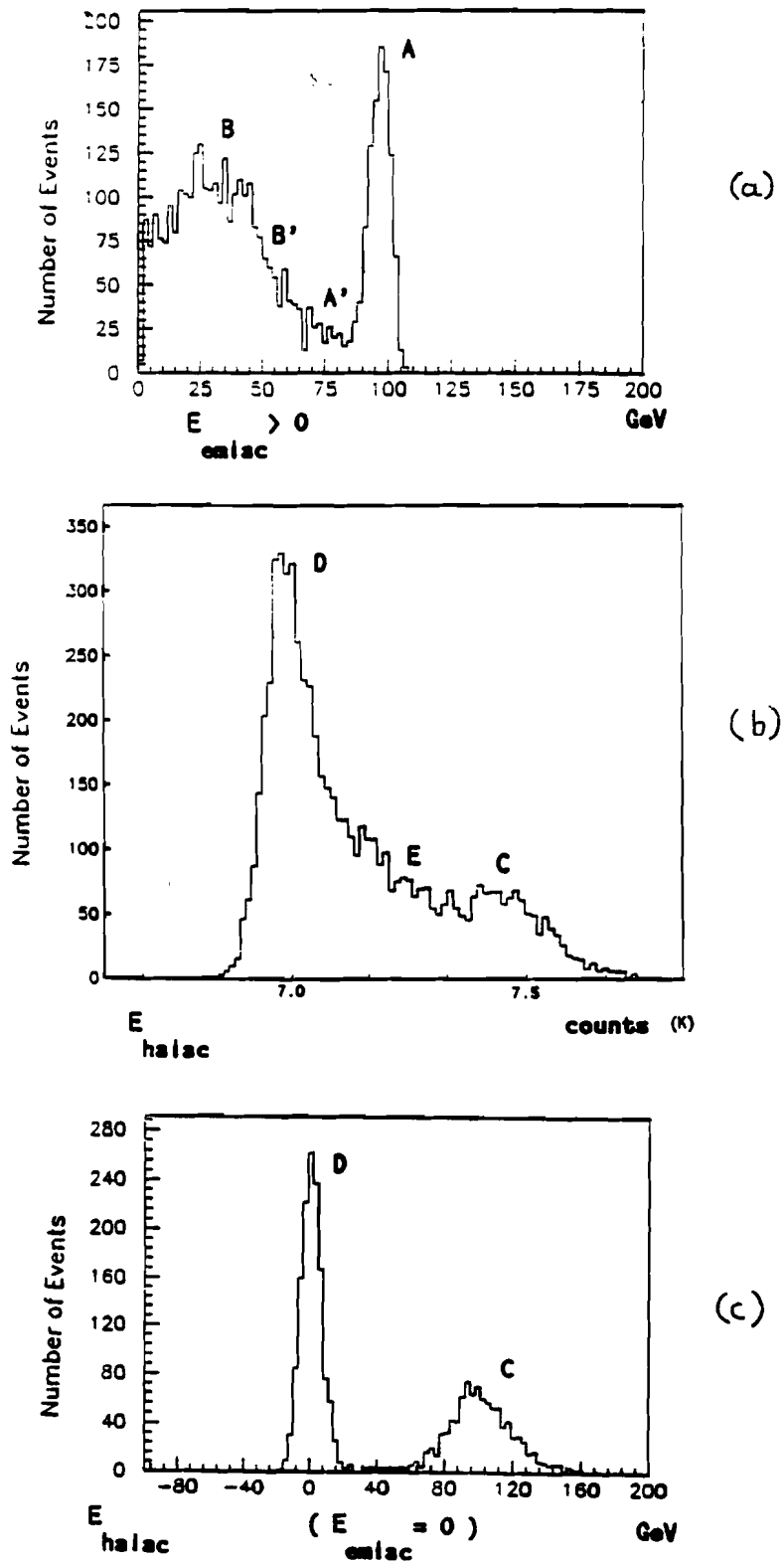

Figure 37: Total energy distributions for the 100 GeV/c calibration.

of the electron showers deposit some of their energy before reaching the active layers of the detector (such as in the cryostat wall or the filler vessel in front of the EMLAC). The distribution in region B comes from hadrons that start showering in the EMLAC, and continue in the HALAC(region E). The tail to the right of B (i.e., B') is due to hadrons that deposit most of their energy in the EMLAC. Peak C is the energy distribution of hadrons that deposit all of their energy in the HALAC. Finally peak D is the noise distribution in the HALAC (the sum of the ADC counts for 25 channels) for those events for which neither a hadron nor an electron was present even though the trigger requirements were met.

The constant that converts ADC counts to units of energy can be expressed as follows. The total energy deposited in the LAC by an incident electron, ${E_{Dep}}^{e^-}$, is calculated according to

$$ {E_{Dep}}^{e^-} = C_E \times \sum_{i=1}^{n} {g_i}^E \times (ADC_i - PED_i) \qquad \text{Eq. (4.4)} $$

For an incident hadron, now both calorimeters are involved, ${E_{Dep}}^{hadron}$, is calculated according to

$$ {E_{Dep}}^{hadron} = C\prime_E \times \sum_{i=1}^{n} {g_i}^E \times (ADC_i - PED_i) + C_H \times \sum_{i=1}^{m} {g_i}^H \times (ADC_i - PED_i) \qquad \text{Eq. (4.5)} $$

where, $C_E, C\prime_E$ and C_H are the calibration constants, ${g_i}^E, {g_i}^H$ are the channel gains, ADC_i is the raw ADC counts for channel i, and PED_i is the pedestal for channel i, i.e., the effective zero level for this channel. The summation runs over all channels above pedestal corresponding to the shower caused by one incident particle.

There are two calibration constants for the EMLAC because it responds differently to electromagnetic and hadronic showers. The same is also true for the

HALAC but since it will not be used to study the electromagnetic showers, only one calibration constant is important (the EMLAC is about thirty radiation lengths thick, and thus there is practically no electromagnetic energy leakage into the HALAC). Using only the electrons from the test beam and only the hadrons that did not interact in the EMLAC, we can obtain the calibration constants C_E and C_H. This is done by measuring the average of the energy distributions as shown in Figure 37 for the 100 GeV/c calibration run (peaks A and C).

4.6. Energy Resolution

4.6.1 General

Figure 38 shows the reconstructed energy in the HALAC from a calibration run with beam energy of 100 GeV (the solid line). The shaded area is the reconstructed energy in the HALAC from the same run but for particles that did not interact in the EMLAC, i.e., when no signal, over threshold, was read out from this detector. The gaussian fit was done in the interval $-2\sigma \rightarrow +2\sigma$ around the peak value. Without applying any of the corrections discussed later, the HALAC energy resolution for 100 GeV/c incident π^- beam was 22% .

The energy resolution of the HALAC depends on the following factors:

a) The intrinsic energy resolution of the detector.

b) The different responses of the detector to the electromagnetic and hadronic showers (denoted by $\frac{e}{h} > 1$.)

c) The energy sampling fraction.

d) The detector imperfections.

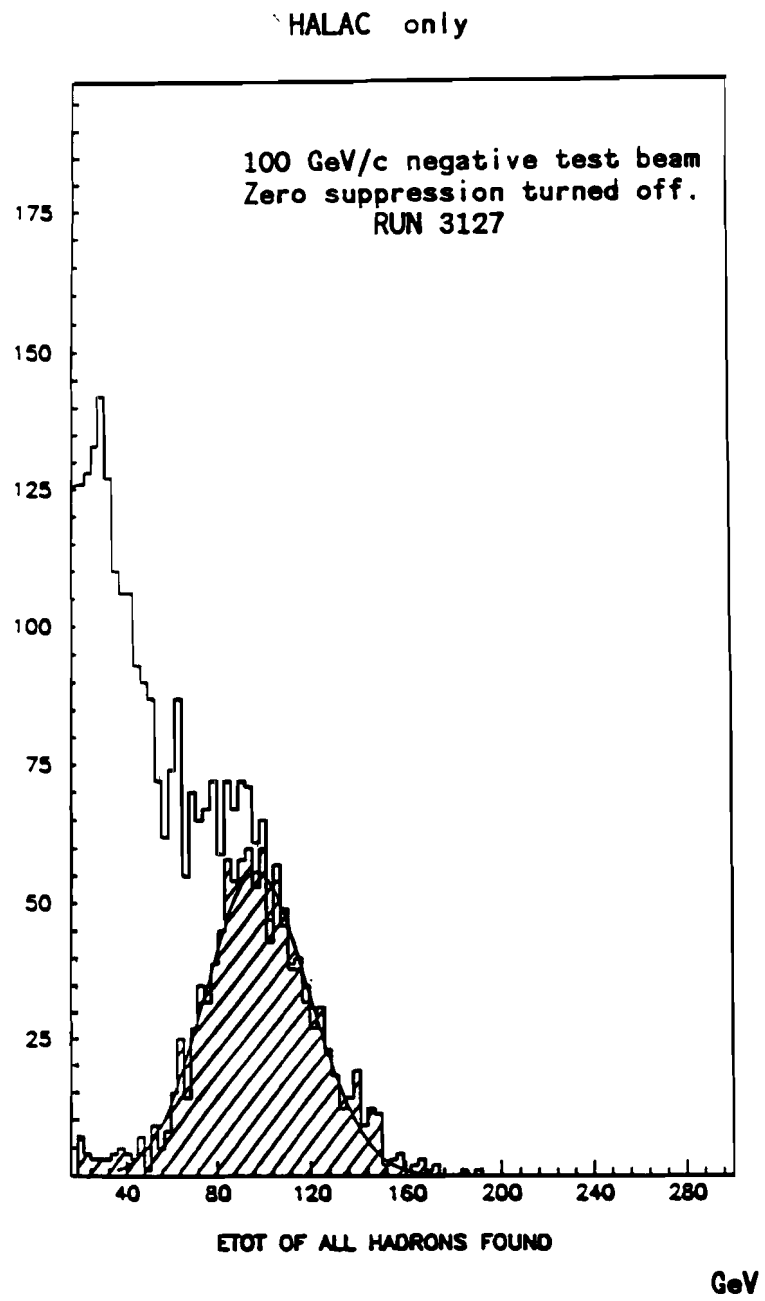

The background line is the energy distribution in HALAC.
The shaded line is the energy distribution in HALAC when $E_{em} = 0$

Figure 38: Reconstructed energy in the HALAC from a calibration run with beam energy of 100 GeV. Note the zero shift.

e) The electronic noise.

f) The readout threshold.

g) The inefficiencies of readout system.

The overall energy resolution can be expressed in the form:

$$[\frac{\sigma_{HALAC}(E)}{E}]^2 = (\frac{\sigma_o}{\sqrt{E}})^2 + (\sigma_n^2 + \sigma_b^2) \tag{4.6}$$

where σ_n^2 is the uncertainty introduced by the relative amplifier gains and the fluctuations of the amplifier pedestals, σ_b^2 is the energy spread of the beam and σ_o is the energy resolution of the detector which can be broken down into the following terms[58]:

$$\sigma_o{}^2 = \sigma_{intr}{}^2 + \sigma_s{}^2 \times t_{abs} + \sigma_{e/h}{}^2$$

where σ_{intr}^2 is the intrinsic energy resolution of the detector, σ_s^2 the sampling fluctuations , t_{abs} the thickness of the absorbing material ($t_{abs} = 8X_o$) and $\sigma_{e/h}^2$ the non-Gaussian contribution of $\frac{e}{h} \neq 1$.

Each of the factors above is discussed in the following subsections. Throughout the calibration studies the beam energy fluctuations were $\Delta P/P = 1.5\%$.

a) Intrinsic Energy Resolution

The intrinsic energy resolution is determined by the choice of passive material (the stainless steel in our case), active material (the argon in our case) and the thickness of the detector. For the estimation of the intrinsic energy resolution of the detector a perfect readout system is assumed. Using our Monte Carlo (described in Section 4.7) we calculated the HALAC energy resolution for incident

pions in the momentum range of 50 to 200 GeV/c. The energy dependence of the energy resolution can be parametrized in the following form:

$$\frac{\sigma}{E} = (0.017 \pm 0.019) + \frac{(0.95 \pm 0.41)}{\sqrt{E}}$$

This is the expected energy resolution of the detector for hadrons.

b) Ratio of Electron/Hadron response

The significance of using calorimeters whose response to incident electrons and hadrons is the same (i.e., $\frac{e}{h}^{intrinsic} = 1$) has been reported recently by many authors. During the development of a shower generated by a high energy hadron, a certain number of π^o's and some η's are produced. These particles decay into photons which deposit their energy in the form of electromagnetic showers. This has two effects:

i) The calorimeter response to the purely hadronic part of a hadron shower has a broader energy distribution than the response of the electromagnetic part, at the same energy.

ii) The average response to the electromagnetic and purely hadronic components will in general be different when $\frac{e}{h}^{intrinsic} \neq 1$. For a hadronic shower the undetected energy (i.e., the energy carried by neutrinos, and muons, which does not interact in the detector) is fractionally higher than in the case of electromagnetic showers. Thus one expects to first order $\frac{e}{h}^{intrinsic} > 1$.

The energy sharing between the two components of hadron shower is different from event to event. If the first interaction in the shower development is of

the charge exchange type, the fraction of the energy going into electromagnetic component (f_{π°) will be large; in other cases it can be very small.

The $\frac{e}{h}$ is related to $\frac{e}{h}^{intrinsic}$ as follows:[68]

$$\frac{e}{h}^{intrinsic} = \frac{e}{h}(E) \times \frac{(1- < f_{\pi^\circ}(E) >)}{[1- < f_{\pi^\circ}(E) > \times \frac{e}{h}(E)]}$$

where $< f_{\pi^\circ}(E) >= 0.1 \times ln(E)(GeV)$ is the average energy fraction of the hadronic shower spent on the production of π° and η's (the e.m. component). This is a reasonable approximation in the energy range from 10 to 100 GeV.*

In general, if a calorimeter is sufficiently segmented, especially in the longitudinal direction (LAC has four sections, two in the EMLAC and two in the HALAC), one may correct f_{π° on an event-by-event basis and hence eliminate, at least partially, the effect of the f_{π° fluctuations on the energy resolution. The contribution of fluctuations in f_{π° to the resolution will become more important as $\frac{e}{h}^{intrinsic}$ goes further away from 1. The CDHS collaboration[69] developed an algorithm to correct the f_{π° effect:

$$E_i l = E_i \times \frac{(1 - c \times E_i)}{\sqrt{E}} \tag{4.7}$$

$$E = \sum_{i=1}^{n} E_i$$

$$El = \sum_{i=1}^{n} E_i l$$

where,

* In this energy range the above formula gives for the Monte Carlo calculations the values, $\frac{e}{h}^{intr} = 1.44$ for the HALAC and $\frac{e}{h}^{intr} = 1.33$ for the EMLAC.

n is the total number of longitudinal segments (4 in our case),

E_i is the energy deposited in the longitudinal segment i,

E_i' is the corrected energy deposited in segment i,

E is the total uncorrected energy deposited,

E' is the corrected energy deposited, and

c is the correction factor which will be optimized according to the calibration data and Monte Carlo studies.

Using our Monte Carlo, we obtained the energy resolution of the LAC for the hadronic showers after we corrected for the above effect using the Equation 4.7. The energy dependence of the improved resolution from Monte Carlo studies is shown in Figure 39. The improvement is about 10% and the parametrization of the energy dependence has the following form:

$$\frac{\sigma}{E} = (0.017 \pm 0.019) + \frac{(0.78 \pm 0.21)}{\sqrt{E}}$$

The measured energy resolution of the detector for the hadronic showers will be presented in Section 4.6.2.

The HALAC would be capable of a considerably better performance if $\frac{e}{h}^{intrinsic}$ was closer to one. Moreover, the average response is not linear with energy. This situation could be improved if the calorimeter was longitudinally subdivided to such an extent that fluctuations in the fraction of energy spent on π^o production could be corrected on an event by event basis.

c) Sampling Fraction

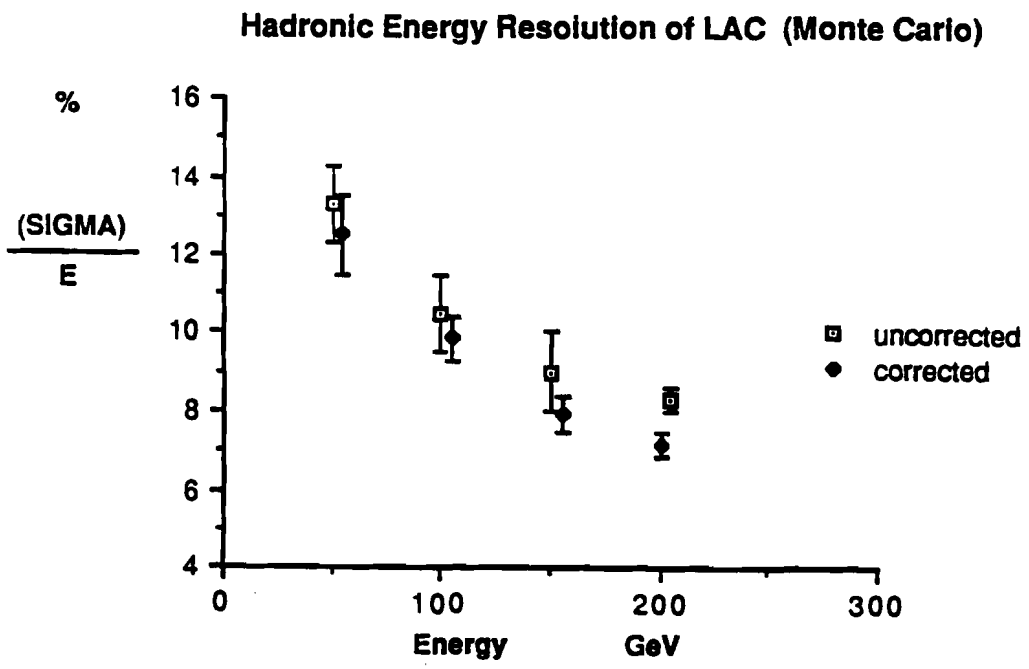

Figure 39: Energy resolution of the HALAC from Monte Carlo calculations.The "uncorrected" data points have been shifted artificially to make the plot clear.

The contribution of sampling fraction to the energy resolution is:[68]

$$\frac{\sigma_{SAMP}}{E} = .009 \times \sqrt{\frac{\Delta E(MeV)}{E(GeV)}}$$

where ΔE is the energy deposited by a minimum ionizing particle in one sampling layer. In our detector

$$\Delta E = \frac{E \times f_{sampling}}{\#oflayers} = \frac{1000(MeV) \times 0.014}{49} = 0.291\ MeV,$$

and

$$\frac{\sigma_{SAMP}}{E} = \frac{4.8\%}{\sqrt{E}.}$$

d) Detector Imperfections

The detector imperfections are mainly liquid argon impurities that limit the charge collection locally, and thickness variations of both the active and passive layers. These limitations cause deviations of the energy resolution of the detector from the $\frac{1}{\sqrt{E}}$ behavior and limit the high energy performance of the detector. In the HALAC, their contribution is estimated to $\frac{\sigma}{E} \sim 4\%$.

e) Electronic Noise

There are three effects that contribute to the fluctuations of the output of the channels. First is the amplifier noise, second the pedestal fluctuations and third the variations of the relative gain of the channels. The r.m.s. noise width of a channel was expected to be about 1 GeV in the front section and 1.4 GeV in the back, based on calculations using measured capacitances of the detector. Studies

showed that noise for channels belonging to the same EWE were not correlated with each other. Thus, the uncertainty introduced by the noise of a channel to the measurement of the energy of a reconstructed hadron is incoherent. Figure 37 (bottom graph) shows the energy distribution in the HALAC for the 100 GeV/c calibration run when we require no energy deposited in the EMLAC. The energy was obtained by adding the energy deposited in an area of 25 pads (13 front + 12 back) around the pad that the beam hit. The peak labeled with the letter D (at the left) is due to fake triggers (most of them due to the muons).

Since the noise is incoherent, the noise level for a reconstructed hadron is:

$$\sigma_{noise} = \sqrt{\sum_{i=1}^{N} {\sigma_{o_i}}^2} = \sqrt{\sum_{i=1}^{Nfront} {\sigma_{F_i}}^2 + \sum_{i=1}^{Nback} {\sigma_{B_i}}^2} = 6.2 \ \ GeV$$

(for N = 13 + 12 = 25 pads). This agrees with the width of the noise peak (D) in plot 37.

f) Zero Suppression Window

The readout threshold for signals was adjustable. The values were stored in the MX and could be varied by program control. During the experimental run the readout thresholds varied either intentionally or because of the baseline drift of the circuits. The minimum detectable energy is directly related to the amount of detectable energy, since it cuts the low energy tails of the shower. It was important to study the relation between the reconstructed hadronic energy and the readout threshold. We also studied how the reconstructed energy of each hadron was related to the number of pads. Figure 40 shows the relation between the reconstructed energy and the number of pads used. The number of pads was

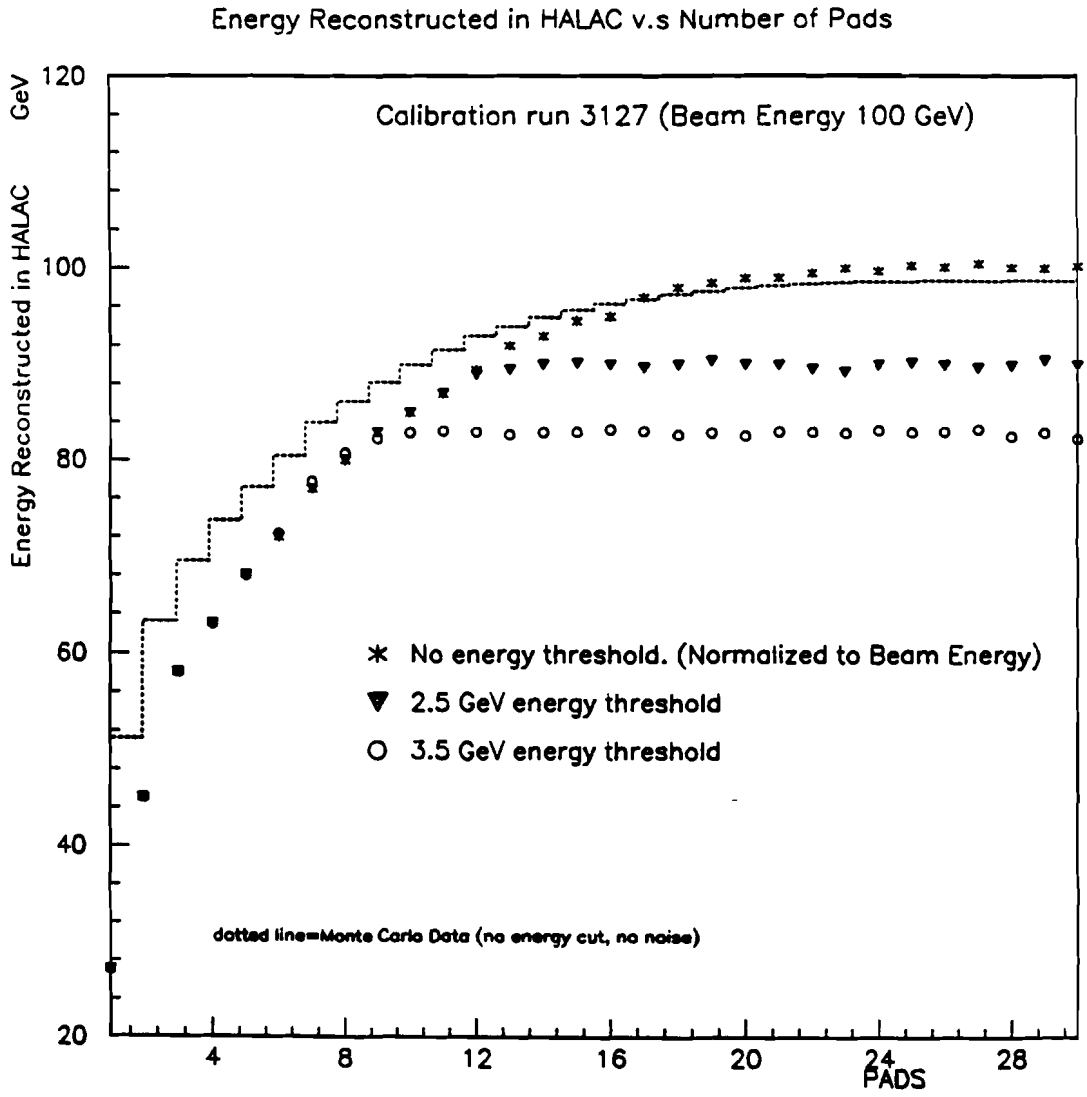

Figure 40: The relation between the reconstructed energy and the number of pads used in the reconstruction.

counted, starting from the pad with the highest energy toward the pads with lower energies. The plotted data come from a calibration run of 100 GeV particle energy in which the zero suppression was turned off. The window was simulated by applying a threshold to the data in the reconstruction program.

As it was mentioned earlier, the energy resolution of the HALAC and the reconstructed energy was strongly affected by the readout threshold (or zero suppression window). The reconstructed energy was corrected for this effect. In figure 41 we plot the energy reconstructed in the HALAC, from three different runs, as a function of the energy threshold assigned by the analysis program. Curve A is the 100 GeV/c run in which the zero suppression was turned off, curve B presents another 100 GeV/c run in which the window was set at ±2.5 GeV and curve C presents a 50 GeV/c run with the same window as in curve B. During the physics run, the readout threshold varied between 2.5 GeV and 4.5 GeV per channel.* This threshold range was of particular interest to us during the calibration analysis. Curve A (i.e., the calibration run with the zero suppression turned off) was fit in the region between 2 and 10 GeV. The best fit at 100 GeV is the function:

$$E_{REC} = 115.74 \times Z^{-0.283} \tag{4.8}$$

where, Z is the zero suppression window and E_{REC} the reconstructed hadronic energy. This fit is used during the first level analysis of the Hadron Reconstructor in order to correct the reconstructed energy.

* The width of the zero suppression window was set to 4.5 GeV (for the HALAC) during the last 2 months of the experimental run and it was relatively stable. Since the window was not centered at the effective zero for each channel, the actual threshold of each channel varied between 2.5 and 4.5 GeV.

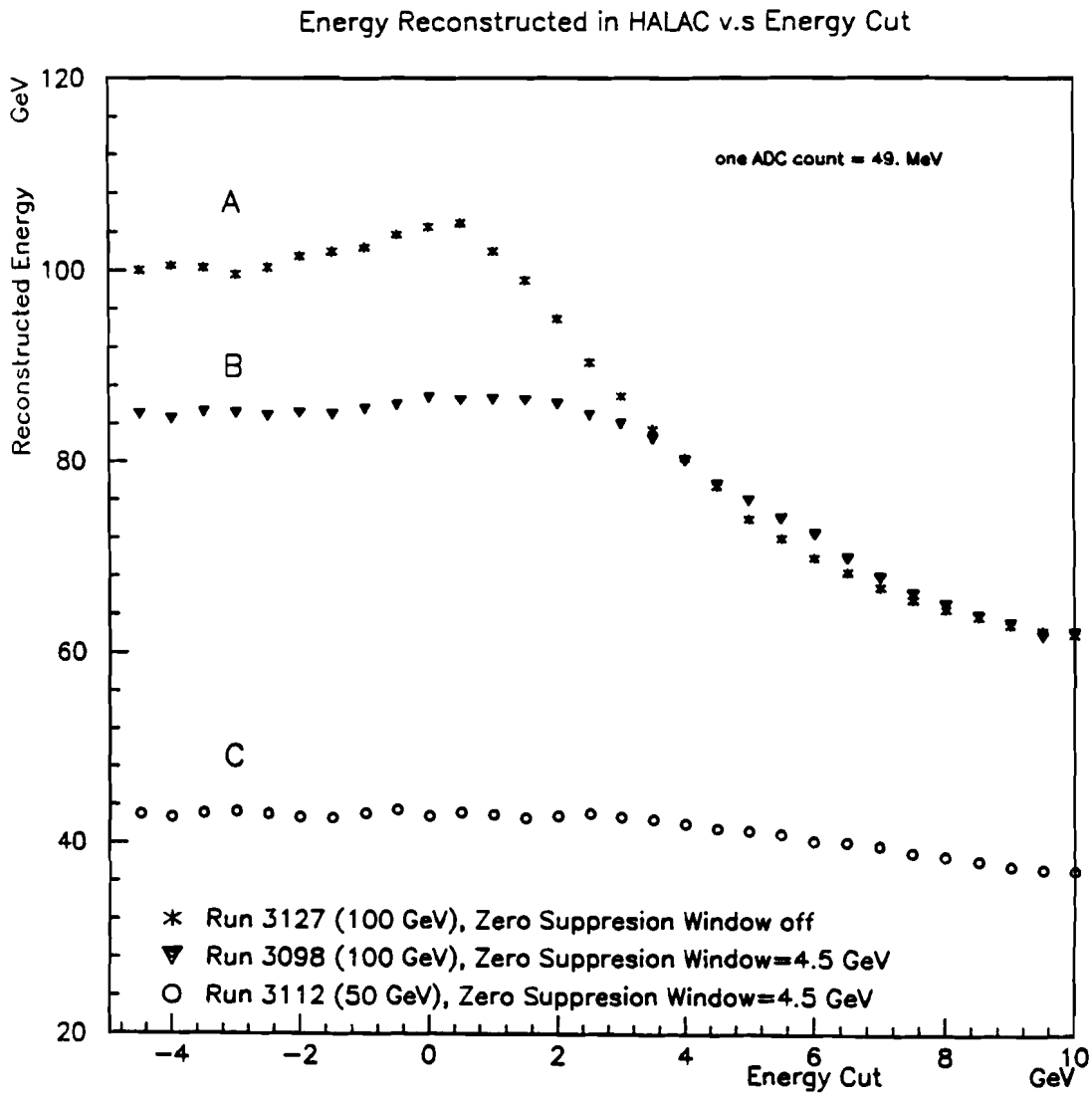

Figure 41: Energy deposited in the HALAC versus the software energy threshold assigned by the calibration program (for three different runs).

g) Readout system inefficiencies

In our calibration studies we did not consider the calibration runs that included channels which could not have their pulse height distribution corrected by a simple method even though they shared a significant amount of the particle energy deposited in the HALAC. The most common problem of such channels was that some of their least significant bits of the digitized analog signal were dropped (as many as four bits). This was observed in less than 1% of the total number of the HALAC channels.

4.6.2. Energy Resolution of the HALAC

We discuss the energy resolution of the HALAC for hadronic showers. In this section we consider data which does not have measurable energy deposited in the EMLAC unless it is otherwise stated. In order to avoid any reconstruction inefficiencies we chose not to reconstruct the hadronic shower but to simply add all channels around the beam in an area of $\pi \times R^2$ (R $\sim$ 25cm; see previous chapter about the lateral development of hadronic showers in the HALAC).

The energy deposits in the HALAC were corrected according to Eq. 4.7. The distributions obtained before (dotted line) and after the correction (solid line) for the 100 GeV/c incident π^- at the HALAC are shown in Figure 42.

In Figure 43 we plot $\frac{\sigma}{E}$ v.s $(\sqrt{E})^{-1}$ using data from four calibration runs (50, 100, 200, and 400 GeV) , under the following three conditions:

a) The data were corrected using calibration runs in which the zero suppression

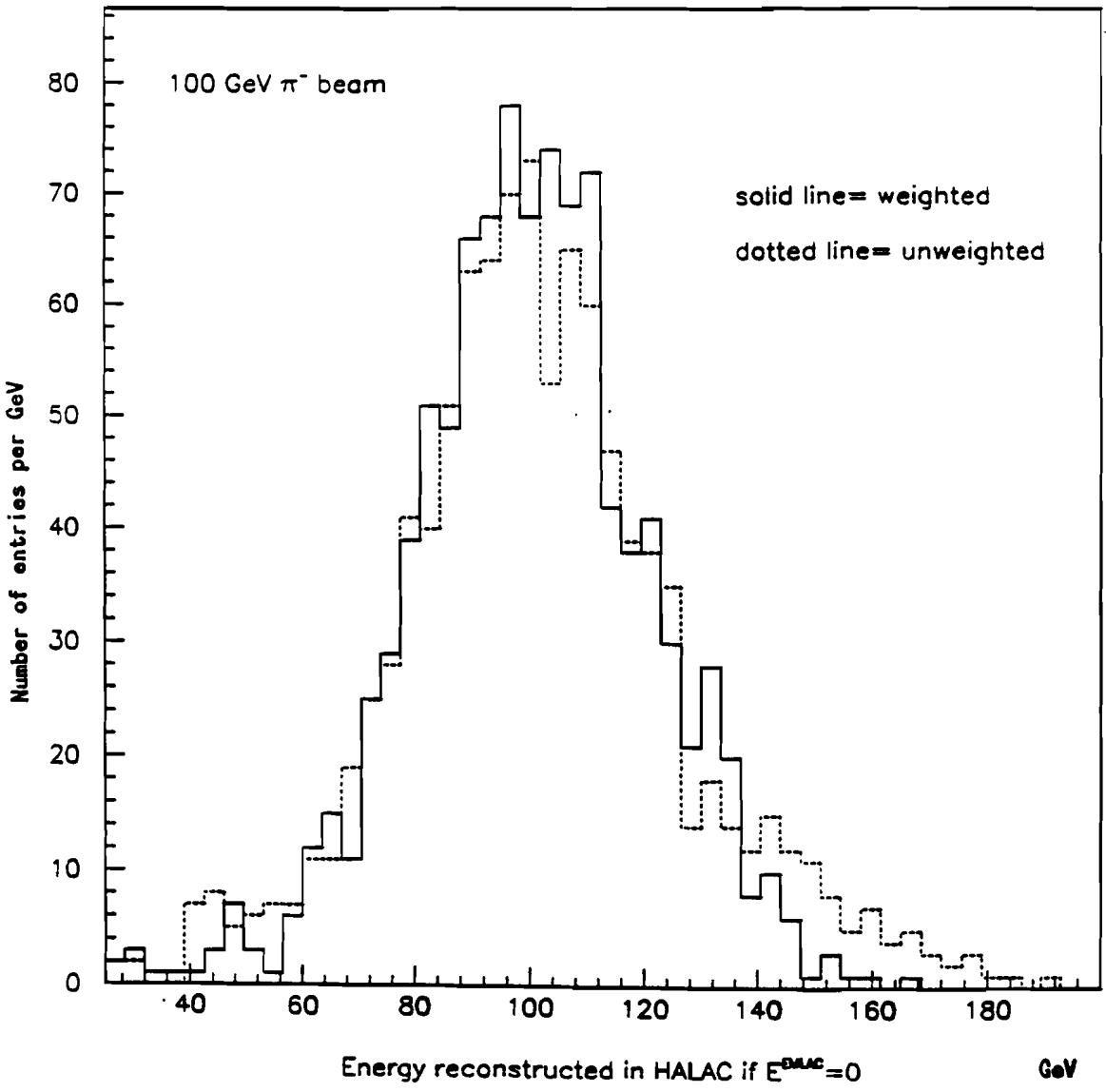

Figure 42: Comparison of the energy reconstructed in the HALAC between, before and after the application of the weighting method.

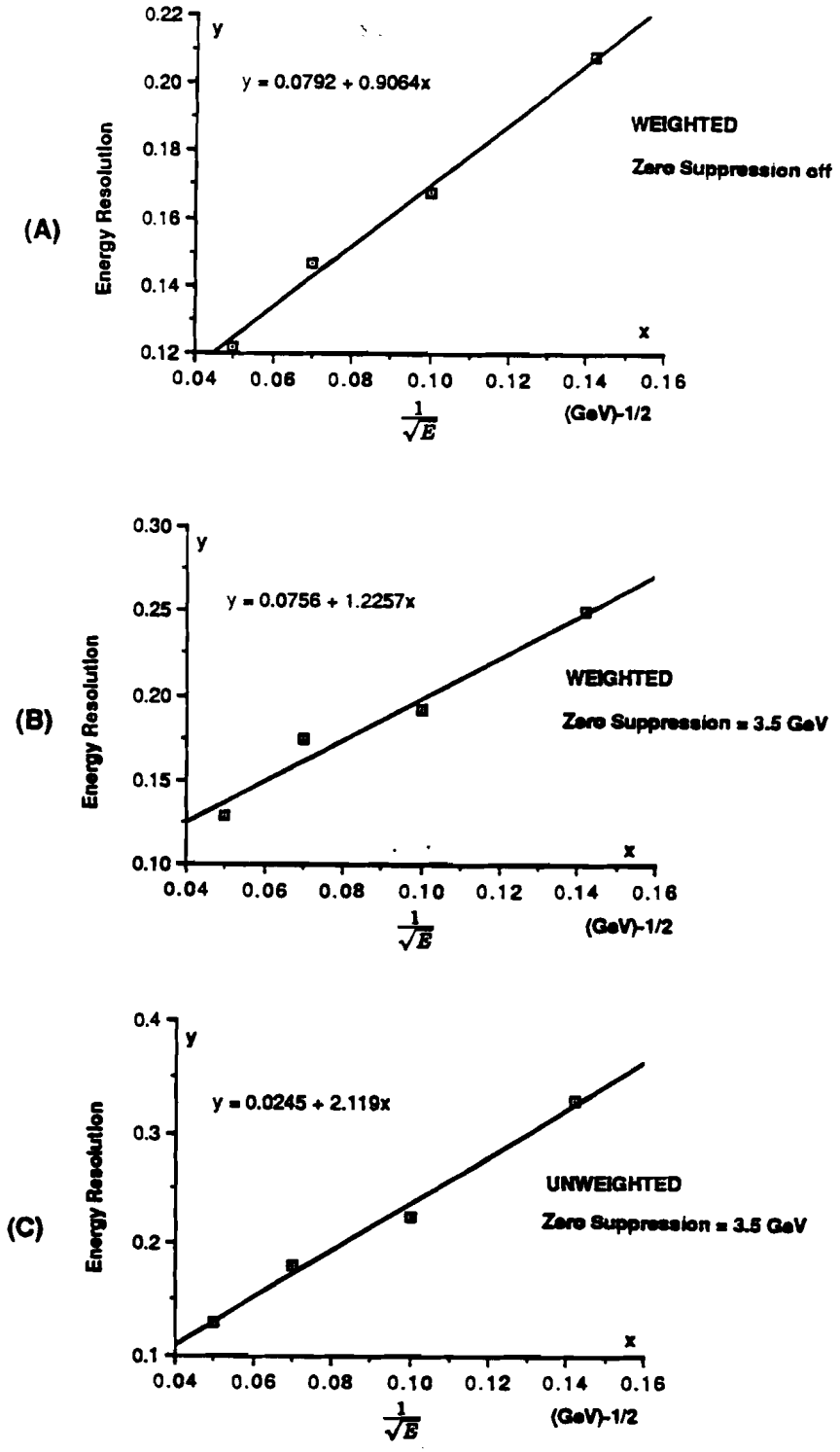

Figure 43: $\frac{\sigma}{E}$ versus $(\sqrt{E})^{-1}$ for the HALAC and for three different configurations (see text). The data points come from four calibration runs (50, 100, 200, and 400 GeV/c).

window was set to zero and the energy from all channels involved was added.* A fit to the data gives an energy resolution of $\sigma_E/E = [(91.0 \pm .5)\%/\sqrt{E}] + (.08 \pm .01)$

b) The average zero suppression window for all channels involved was set at 3.5 GeV by the analysis program and the data were corrected as explained in Section 4.6.

c)The data were not corrected and the window was set at 3.5 GeV.

Figure 44 (top graph) shows the relation between the corrected energy and c (the energy correction coefficient), for four beam energies.**

In the same figure (bottom graph) we plot c as a function of E_{beam}. The fitting function has the form:

$$C_{min} = c_1 \times 10^{c_2 \times E_{beam}}$$

and c_1 = .0764 and c_2 = -.0024. In order to apply this correction to the physics data c was fixed at 0.03. This value fitted better to the energy range of the measured hadrons.

In Figure 45 we present Monte Carlo results on the energy resolution as a function of the incident beam energy under various noise and zero-suppression conditions. The solid line represents calibration runs where the zero-suppression window was set at 3.5 GeV. The Monte Carlo points with the noise width at 1.5 GeV and the zero suppression window at 3.5 GeV are consistent with the data.

---

* During the calibration period the readout threshold was turned off only for two test runs with the 100 GeV/c beam. When it was necessary to compare zero-suppressed with non-zero-suppressed data, we extrapolated the 100 GeV/c measurements to other calibration energies using Monte Carlo calculations.

** In the Monte Carlo simulation of the detector, $\frac{\sigma}{E}$ of the energy distributions for four different energies (50, 100, 150 and 200 GeV) were minimised by varying c. The minimum $\frac{\sigma}{E}$ occurred at c = 0.1.

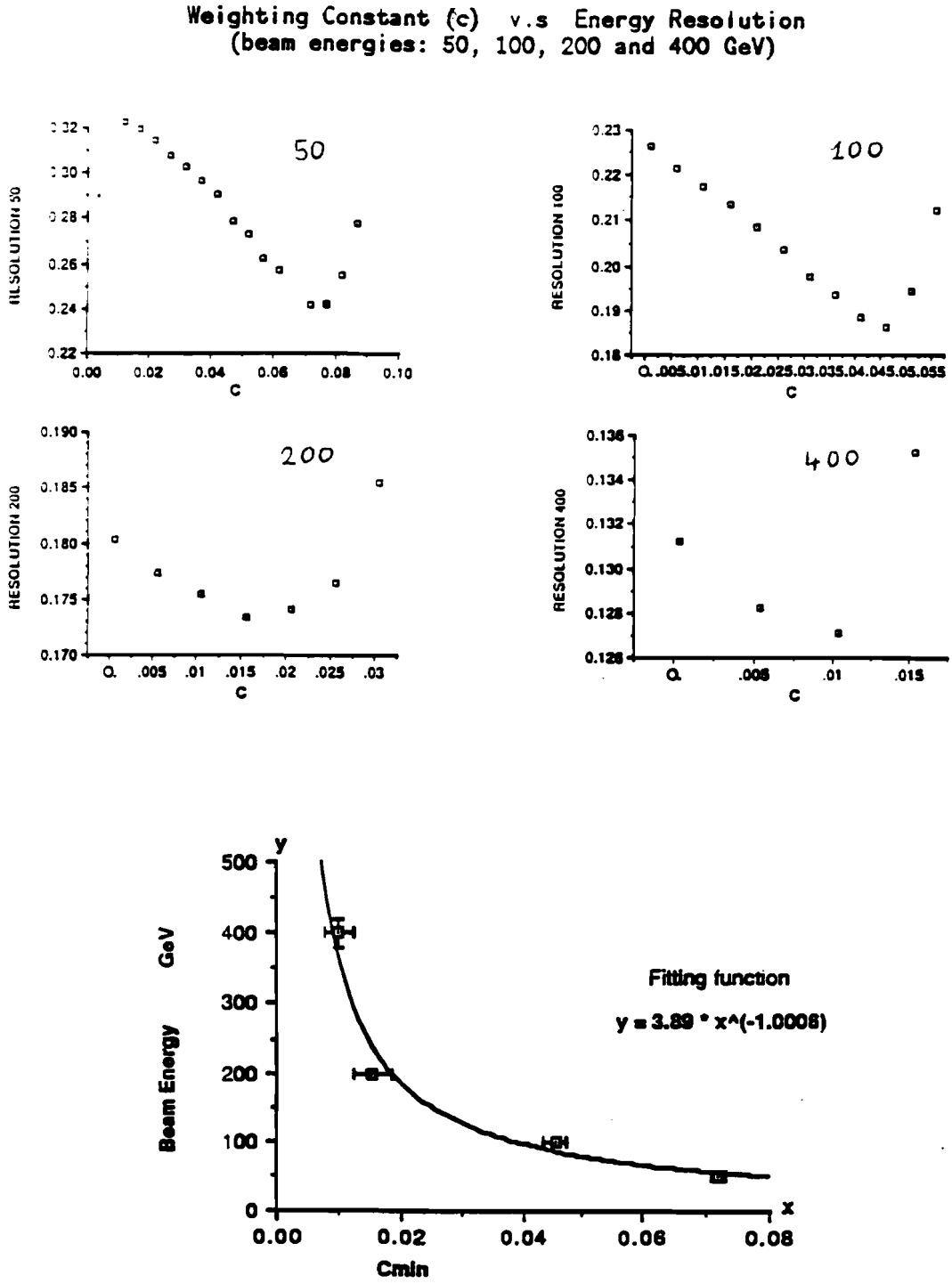

Figure 44: (top): The relation between the corrected energy and the energy correction coefficient, for four beam energies. (bottom): The beam energy correlation with the energy correction coefficient c_{min}.

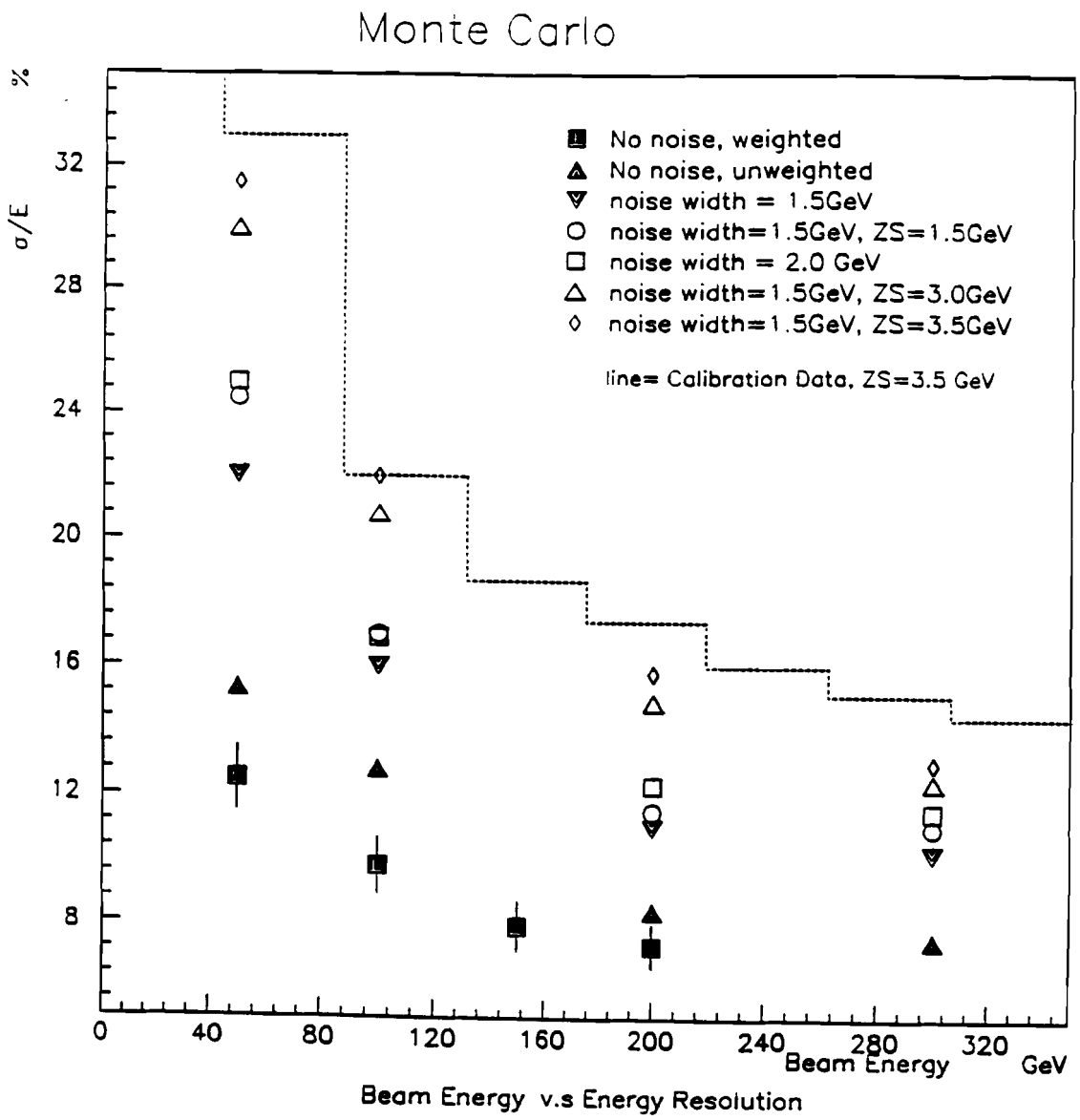

Figure 45: Monte Carlo results on the energy resolution as a function of the incident beam energy under various noise and zero-suppression conditions. The line represents simulated calibration runs where the zero-suppression window was set at 3.5 GeV.

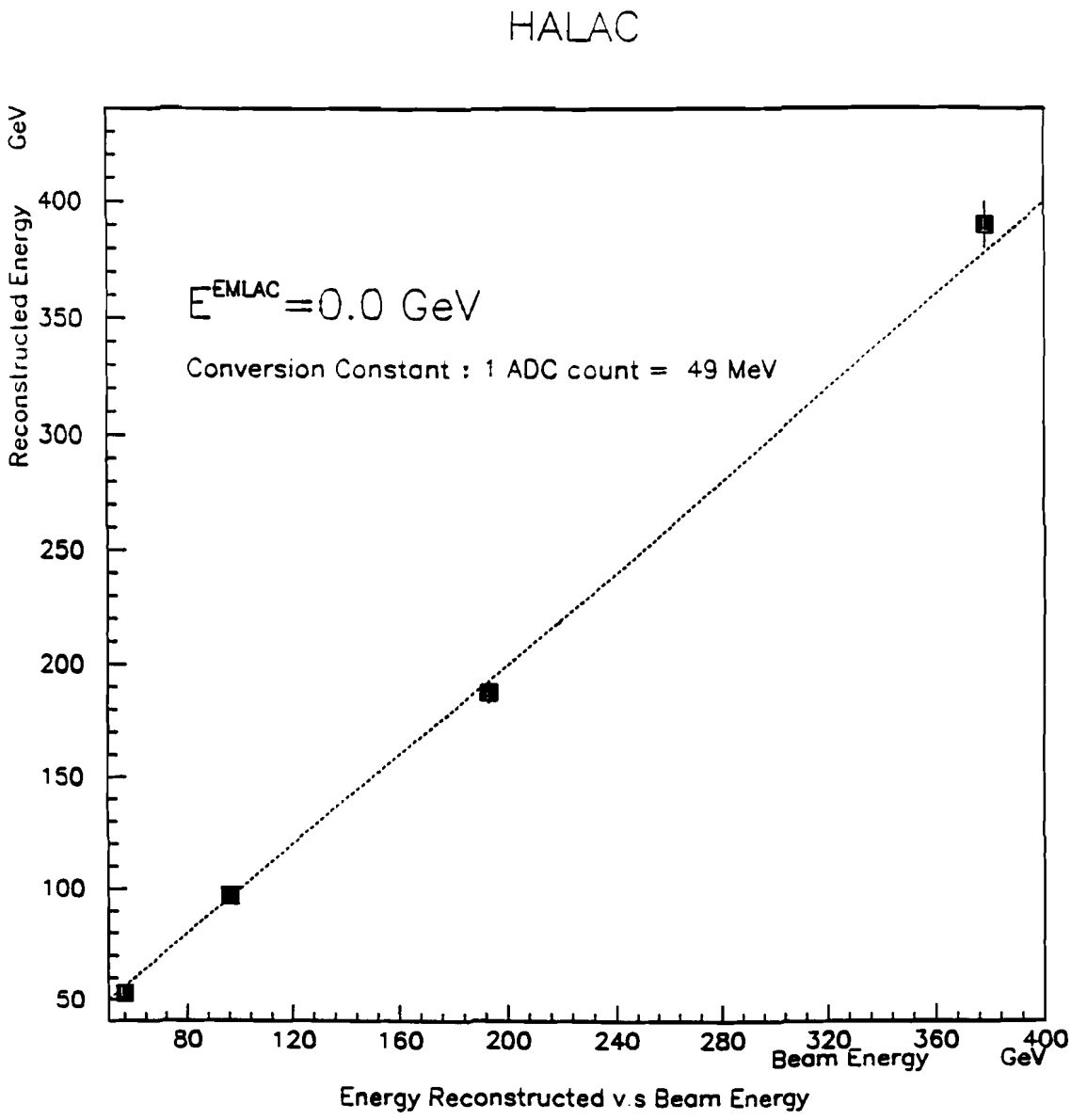

Figure 46: Reconstructed energy in the HALAC versus the beam energy.

Finally, Figure 46 shows the energy reconstructed in the HALAC for four calibration runs with four different energies. The data were corrected for the different readout thresholds . The abscissa is the beam energy determined from the pressure curves of the Cherenkov counter and the beam transport magnets. The detector has a linear response within 3% .

4.6.3. Hadron Energy Resolution of LAC

Now we will study the hadron energy resolution of the whole LAC detector.

The signals from the EMLAC and the HALAC must be weighted in a suitable way to reconstruct the energy of incident particle, because the the average response of the LAC to the e.m. and hadronic showers is different ($\frac{e}{h} \neq 1$). Figure 47 (bottom graph) shows the values of $\frac{e}{h}$ obtained as a function of beam energy from the first calibration run for the EMLAC only. The plotted $\frac{e}{h}$ is closer to the $\frac{e}{h}^{intrinsic}$ than the $\frac{e}{h}$ (i.e., the actual measured electron/hadron ratio) even though it also depends on the $\frac{e}{h}$ response of the HALAC. The same figure also shows the predicted curve based on Monte Carlo results. The $\frac{e}{h}$ ratio was not calculated from the average of the energy distributions (in ADC counts). When incident pions and electrons with the same energy hit the LAC, it was not possible to isolate the electron/pion peaks in the EMLAC. The reasons for that were the following:

i) Since the EMLAC is one absorption length long, a small percentage of pion showers (about 5%) are fully contained in this detector.

ii) The energy leakage to the HALAC from the showers that deposit significant energy in the EMLAC is not detected. This is attributed to the fact that the hadronic shower has already spread laterally when it exits the EMLAC. The aver-

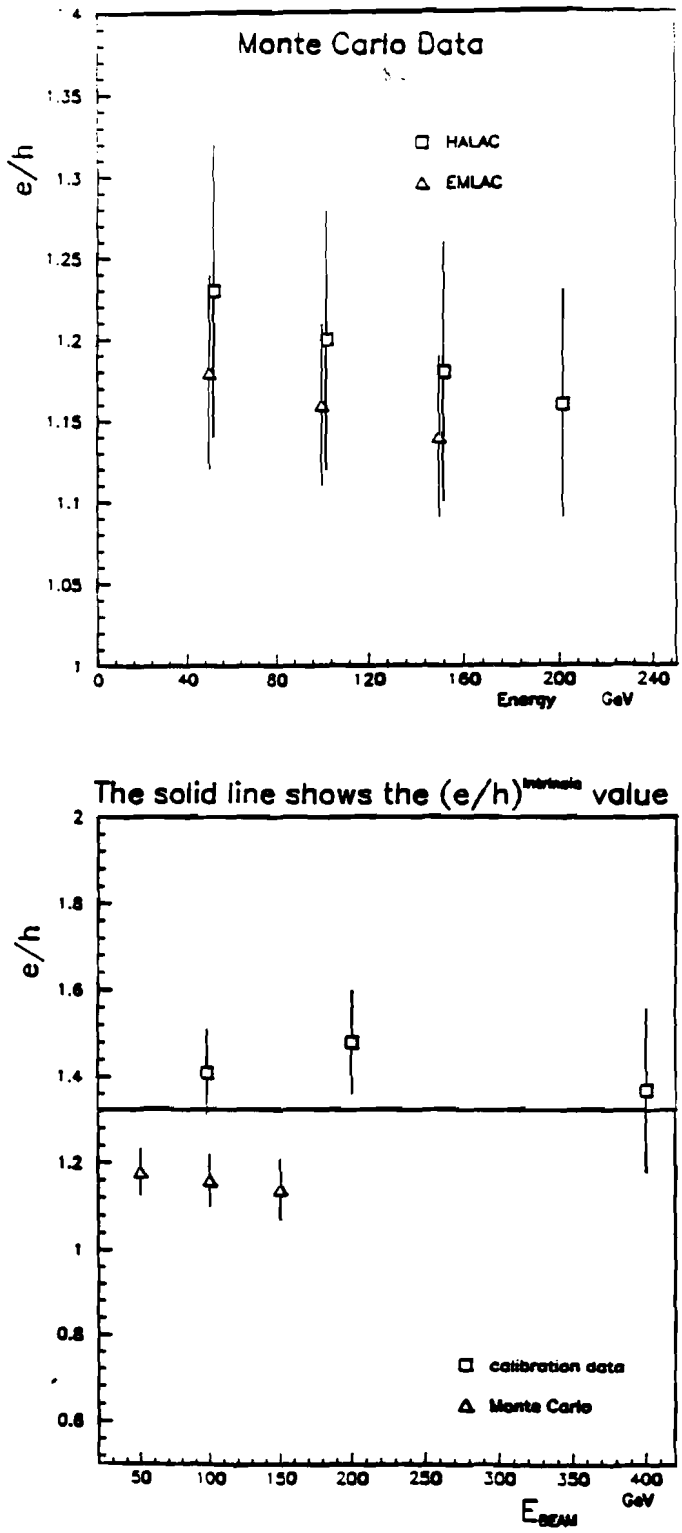

Figure 47: (top): $\frac{e}{h}$ response of the HALAC and the EMLAC, as obtained from the Monte Carlo study, (bottom): The values of $\frac{e}{h}$ obtained as a function of beam energy from the first calibration run for the EMLAC only.

age response of each hadronic channel involved is below its noise level and therefore the deposited energy in the HALAC is not detected. Part of the energy tail loss is also due to the passive material between the two detectors which is about 0.08 absorption lengths long. This material consisted of the EMLAC readout planes, the G-10 support plate, the cooling fin made of copper sheet, and about 7 cm of liquid argon. Figure 47(top graph) shows the $\frac{e}{h}$ response of the HALAC and the EMLAC separately, as obtained from the Monte Carlo study. The difference between these two is small. We see that the $\frac{e}{h}$ signal ratio is energy dependent and it also decreases as the energy is increased.

In order to measure the $\frac{e}{h}$ for the EMLAC we plot:

$$E_{em} \quad versus \quad \frac{(E_{had} \ \ in \ \ HALAC)}{(E_{lac} \ \ in \ \ LAC)}$$

where,

E_{em} is the energy measured from the EMLAC when the ADC counts are converted to energy using the conversion constant obtained from the electron beam data, and E_{had} is the energy measured from the HALAC when the ADC counts are converted to energy using the conversion constant obtained from the hadron beam data, and $E_{lac} = E_{em} + E_{had}$. Then the data was fit to a linear function and the $\frac{e}{h}$ ratio was defined as (constant term of fit)/(particle energy), as seen in Figure 48. The latter plot shows the fitted data for three different energies (400, 200, 100 GeV). Note that in an experimental measurement one does not determine $\frac{e}{h}^{intrinsic}$, but the relation between the average response of an electron and a hadron of the same energy, the latter being a mixture between the e.m. and the purely hadronic

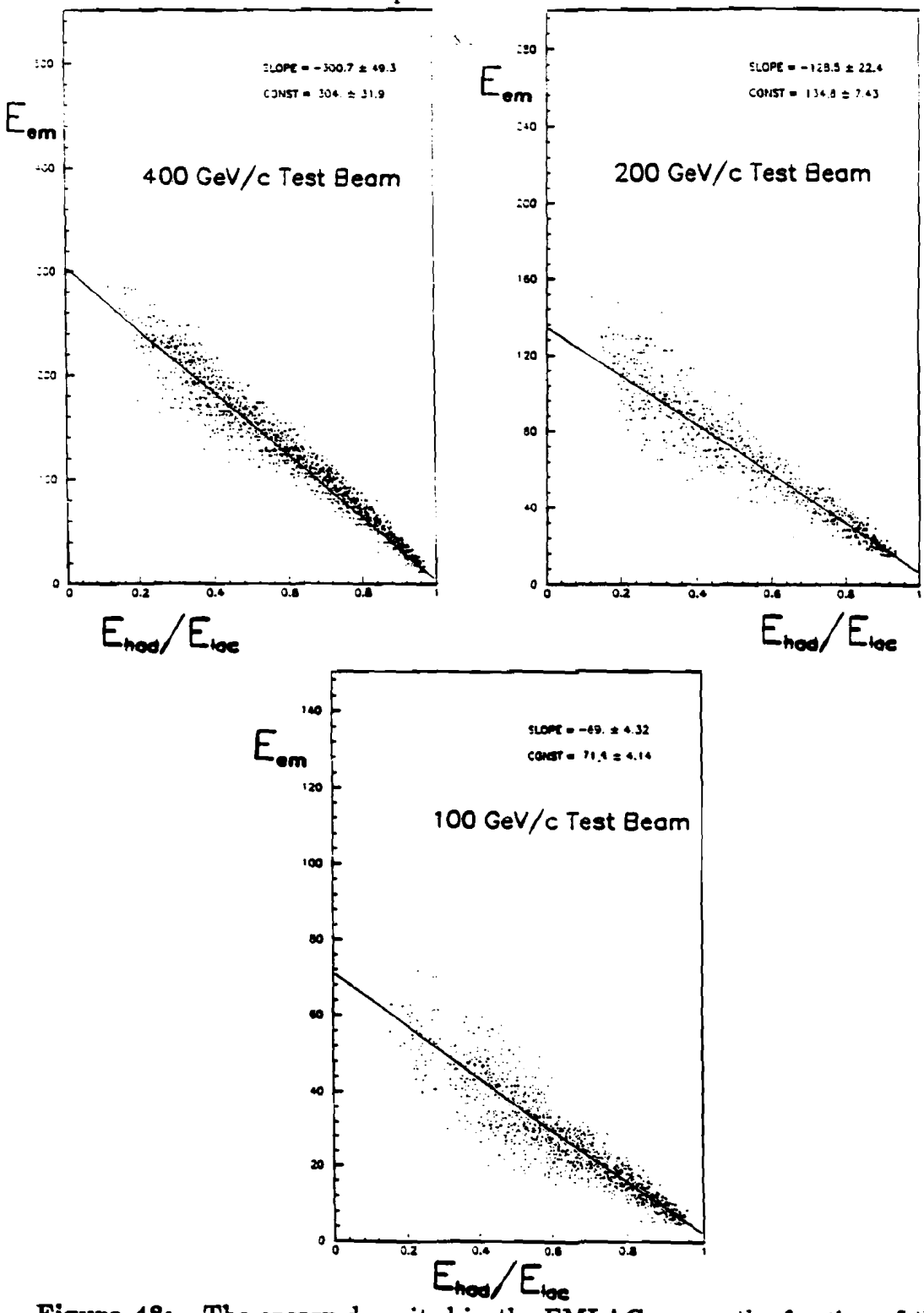

Figure 48: The energy deposited in the EMLAC versus the fraction of the energy deposited in the HALAC over the total energy deposited in the LAC, for three different energies.

components. Since the average value of f_{π^0} fluctuations depends on the particle energy, the experimentally measured $\frac{e}{h}$ value depends on the energy as well.

Fluctuations in f_π^0 are important for the energy resolution of the HALAC. When the energy of the incident hadron is increased, the number of ionizations in the liquid argon increases proportionally, and the width of the deposited energy distribution decreases according to $E^{-1/2}$. Since $\frac{e}{h} > 1$ for the HALAC, the fluctuations in f_π^0, which are of a non-Gaussian nature, will cause the energy resolution to fail to scale with $E^{-1/2}$.

The weighting method used should be roughly independent of incident energy. A simple way to calculate the combined energy of the LAC for incident hadrons is

$$E = E_{had} + a \times E_{em} \tag{4.9}$$

where,

a : the matching constant between the two calorimeters,

E : the energy of the hadronic shower,

E_{had} : the energy deposited in the HALAC, and

E_{em} : the energy measured in the EMLAC calibrated using an electron beam.

For two reasons we used a more complicated formula, motivated by the approach of Ref. [69].

i) The relation between the energy deposited in the EMLAC and the HALAC is not a linear function (as seen in Figure 49 (top graph)). The showers that deposit most of their energy in the EMLAC have a more dominant electromagnetic

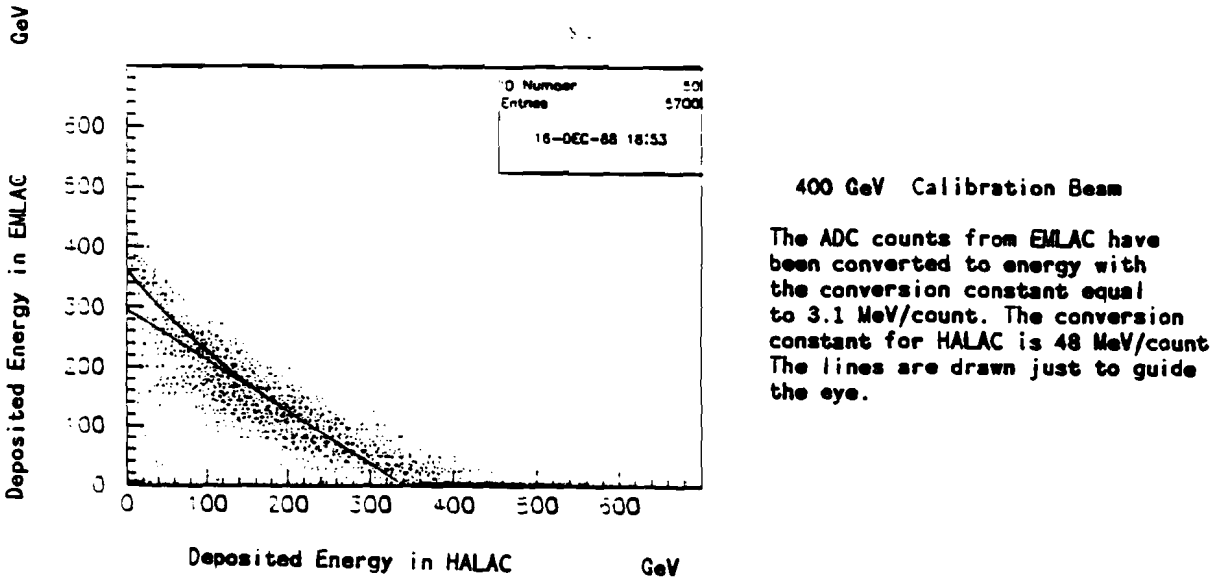

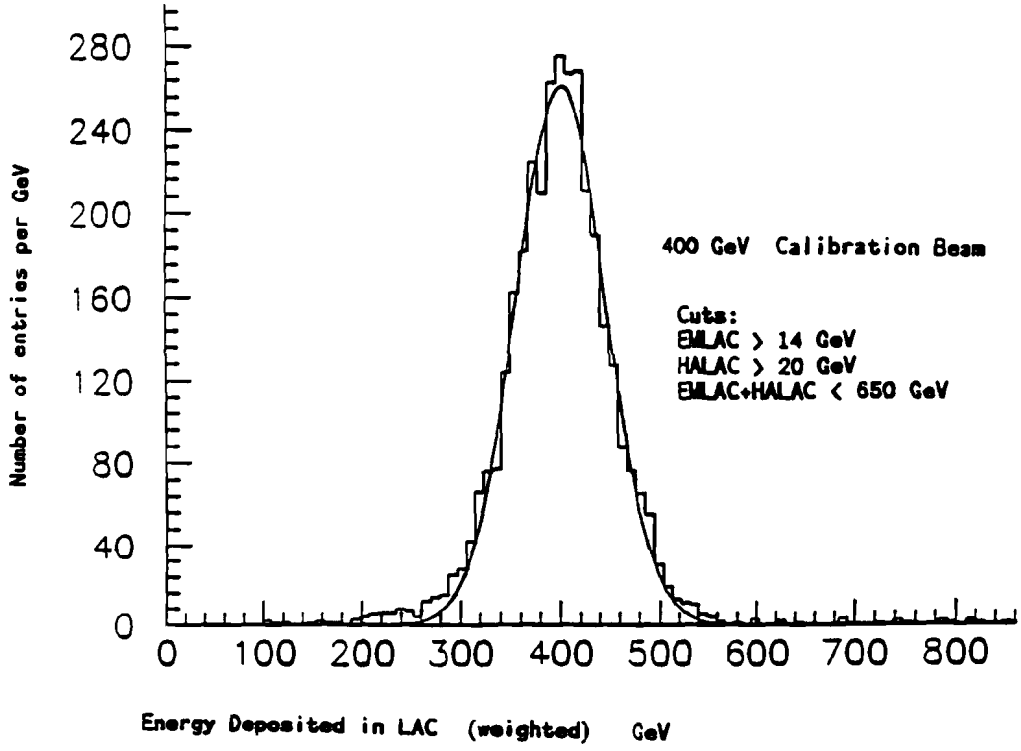

Figure 49: (top): The relation between the energy deposited in the HALAC and the energy deposited in the EMLAC. (bottom): The energy distribution for 400 GeV/c hadrons.

shower component than hadronic one. This is because when an e.m showers starts developing in the EMLAC, it deposits most of its energy in the EMLAC.

ii) We have to correct for the fluctuations introduced by the e.m. component of the hadronic shower as done before when using the HALAC alone. In this case we have informations from four longitudinal sections instead of two. The CDHS type correction can improve the energy resolution.

It turned out that the use of Eq. 4.9 and then the application of the CDHS correction (as described in a previous section) did not give as good results as the following procedure. The energies deposited in both calorimeters were combined and the response of each individual segment was weighted by the use of the following formula:

$$E = c \times [hf' + hb' + c3 \times (ef' + eb')] \tag{4.10}$$

where,

$$ef\prime = ef \times (1 - \frac{c1 \times ef)}{\sqrt{E_{lac}}} \tag{4.10a}$$

$$eb\prime = eb \times (1 - \frac{c1 \times eb)}{\sqrt{E_{lac}}} \tag{4.10b}$$

$$hf\prime = hf \times (1 - \frac{c2 \times hf)}{\sqrt{E_{lac}}} \tag{4.10c}$$

$$hb\prime = hb \times (1 - \frac{c2 \times hb)}{\sqrt{E_{lac}}} \tag{4.10d}$$

$$E_{lac} = ef + eb + hf + hb \tag{4.10e}$$

where, ef/eb is the energy deposited in the front/back section of the EMLAC weighted by the formulae 4.10a/4.10b, and the weighting parameter was c1 =

.048. hf/hb is the energy deposited in the front/back section of the HALAC weighted by the formulae 4.9c/4.10d, and the weighting parameter was c2 = .032. The other parameters take the values, c3 = 1.8, and c = 1.3.

Figure 49 (bottom graph) shows the resultant energy distribution for 400 GeV/c hadrons. The requirements for this plot were twofold. First we required at least 14 GeV of the particle energy deposited in the EMLAC and second we required at least 5% of the incident energy to be deposited in the HALAC. The net effect of Eq. (4.10) on the reconstructed energy of the incident particle was a weak function of energy.

In Figure 50 we plot the average energy deposited in LAC after the application of Eq. (4.10) as a function of the incident particle energy, using the EM-HAD matching parameters used in our data analysis. Since different calibration energy runs gave a different set of calibration constants we chose this set that showed the weakest energy dependence. The chosen set is listed on Figure 50. The energy response is linear within ~2.0% in the momentum range between 50 GeV/c and 200 GeV/c. The energy distribution of the hadronic showers in the LAC was fitted in the interval $-2\sigma \rightarrow +2\sigma$ around the peak.

The $\frac{\sigma}{E_{dep}}$ vs. $\frac{1}{\sqrt{E_{dep}}}$ is plotted in figure 51 (bottom graph).* For comparison we also plot the hadronic energy deposited in the EMLAC versus the ratio of the energy deposited in the HALAC over the total energy deposited in the LAC, before (Figure 51 top left) and after (Figure 51 top right) the corrections.

4.6.4. Electromagnetic Energy Resolution of LAC

* Note that even though we do fit the data choosing a linear fit the fitting function should not be linear in order to take into account energy dependent effects like the $\frac{e}{h} \neq 1$ [58].

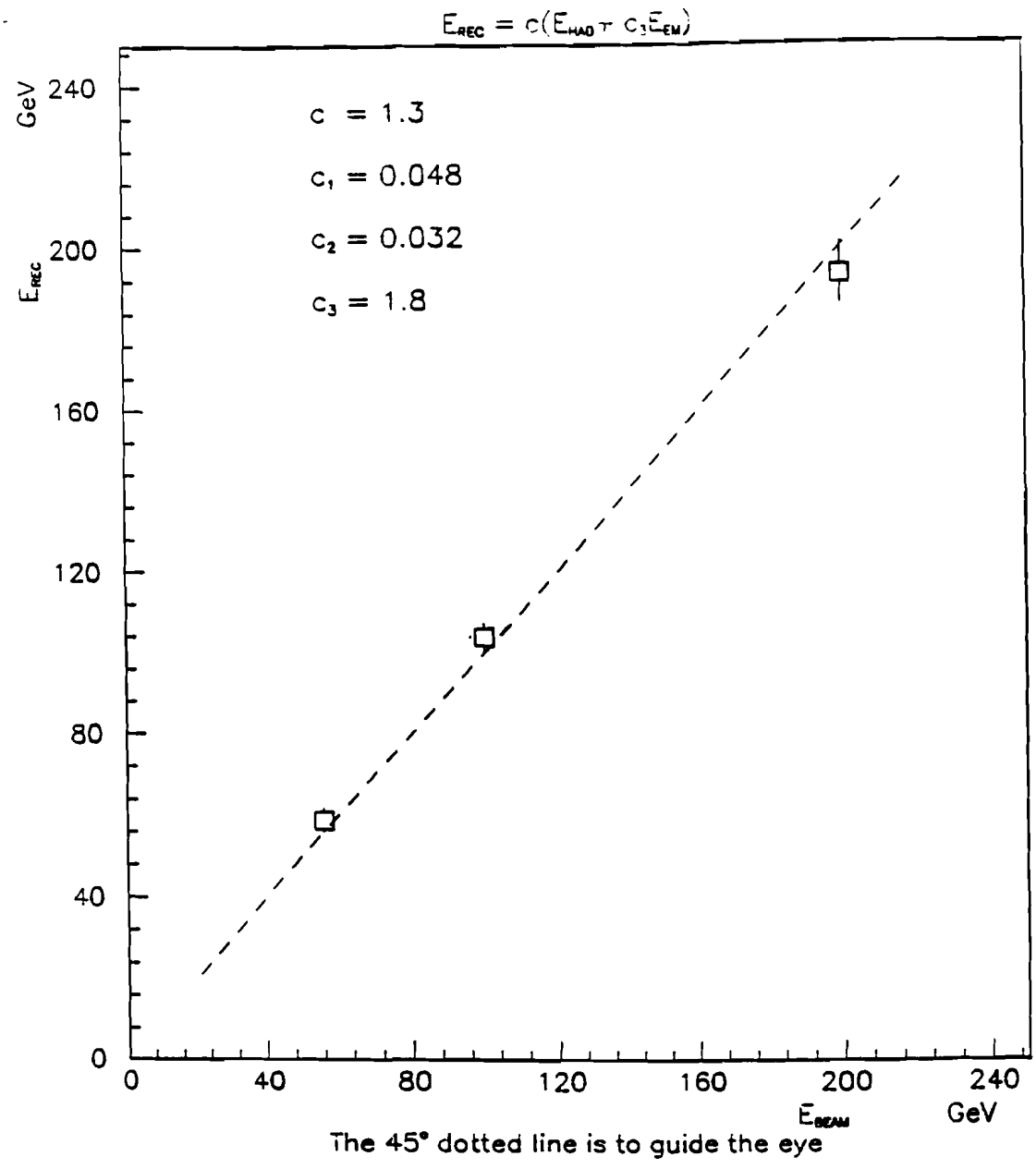

Figure 50: The average energy deposited in LAC as a function of the beam energy, after the weighting method as a function of the incident particle energy. Also shown the EM-HAD matching parameters used in the final data analysis.

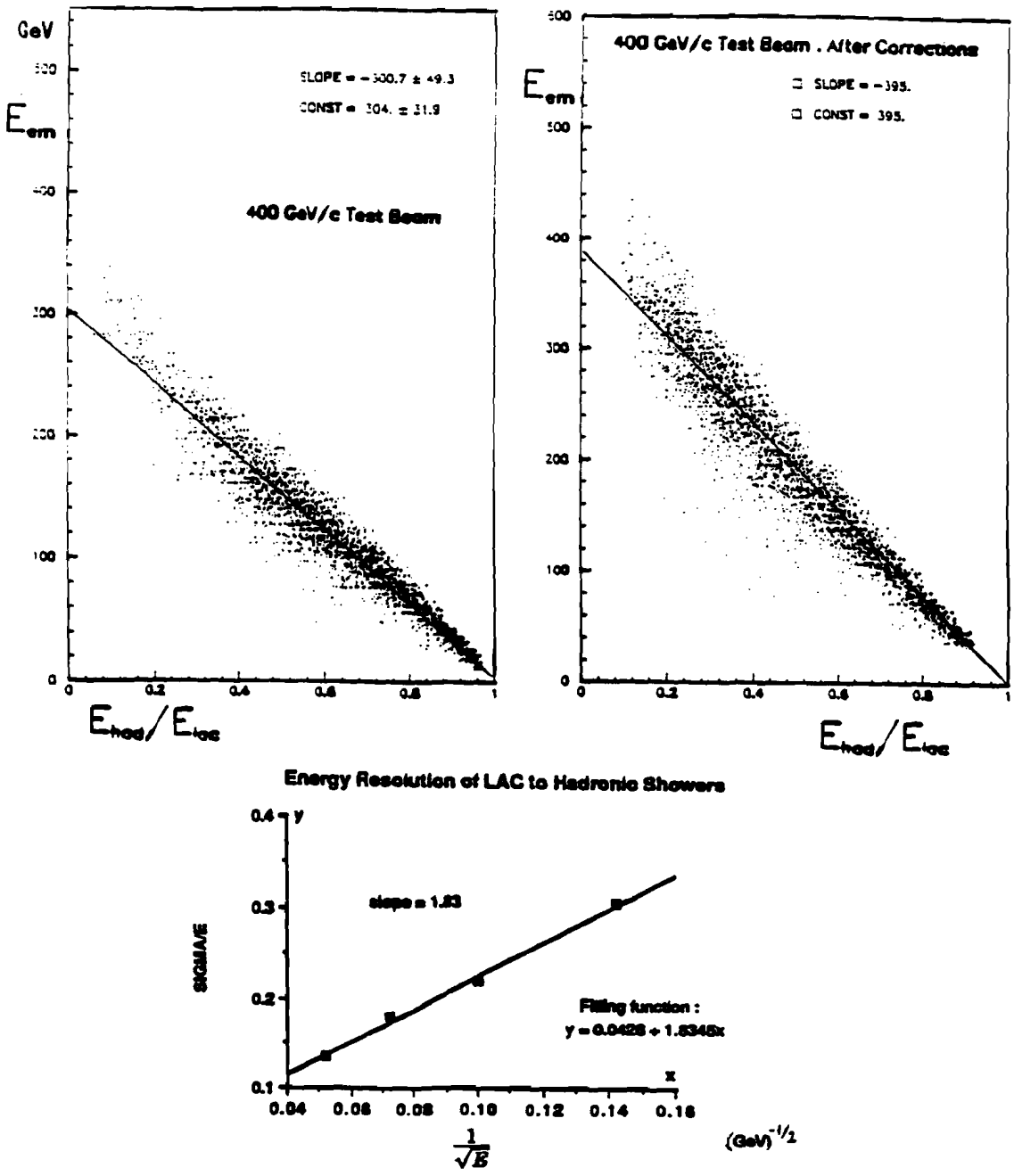

Figure 51: (top): The hadronic energy deposited in the EMLAC versus the ratio of the energy deposited in the HALAC over the total energy deposited in the LAC, before (top left) and after (top right) the corrections, (bottom): The energy resolution of hadronic showers in LAC when both sections of the LAC are combined (i.e., $\frac{\sigma}{E_{dep}}$ vs. $\frac{1}{\sqrt{E_{dep}}}$).

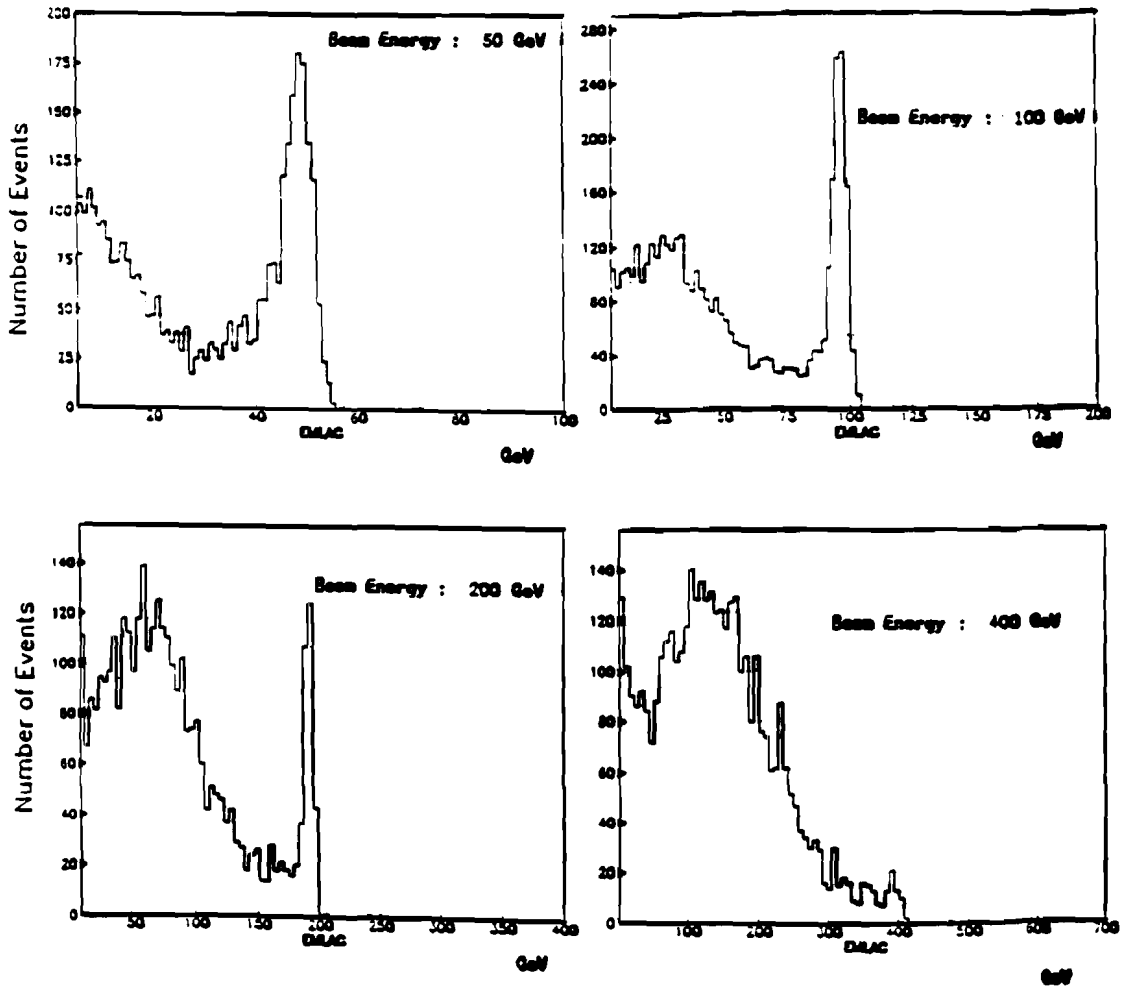

Figure 52: The energy distribution in the EMLAC for four different beam energies.

During the first calibration run the EMLAC was studied only locally at four different energies: 50, 100, 200 and 400 GeV. Figure 52 shows the energy distribution in the EMLAC for four different beam energies. The narrow peak at the right side in each plot (except the 400 GeV) is the energy distribution of the incident electrons. The wide distribution to the left of the peak were due to the hadrons that deposit only part of their energy in the EMLAC. The position response of the EMLAC to the incident calibration beam was studied extensively, during the second calibration run, at three different energies: 25, 50 and 100 GeV.

The study of the electromagnetic energy resolution was undertaken[70] by examining the measured energy difference between the two interleaved views, r and ϕ. Measuring the difference of the energy deposited in the two views instead of their sum, has the following advantages:

i) The spread in the beam energy due to the momentum spread cancels to the first order.

ii) The coherent components of noise in the readout system cancel.

Assuming that there is no coherent noise in the readout system, we can write the energy resolution as follows:

$$\sigma(_{E_r - E_\phi}) = \sigma(_{E_r + E_\phi}) = f\sqrt{E_r + E_\phi}$$

Figure 53 shows $\sigma(_{E_r - E_\phi})$ for 25, 50 and 100 GeV electrons. In Figure 53 (bottom graph), $\sigma(_{E_r - E_\phi})$ is plotted against $\sqrt{E} = \sqrt{E_r + E_\phi}$. The slope is consistent with f = 0.15. The constant intercept, due to noise contributions, is about 4.5%.

$\sigma_{(E_r - E_\phi)}$ vs the square root of the electron energy.

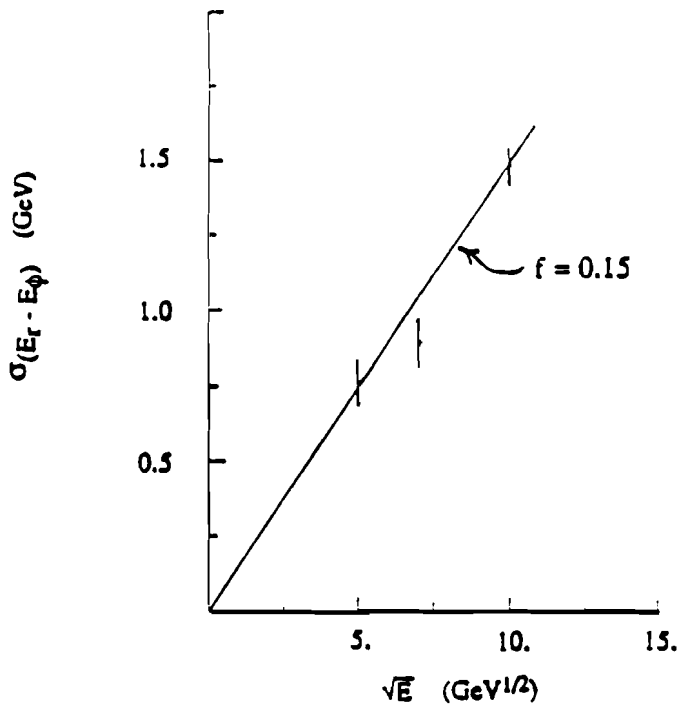

Figure 53: The energy resolution of the EMLAC.

4.7. Detector Uniformity

The study of the response of the LAC to electromagnetic/hadronic showers at different positions on the detector was carried out by moving the LAC horizontally and the beam vertically. There are four major causes for the LAC having non-uniform response; 1) variations of the thickness of the absorbing material; 2) capacitance variations (i.e., variations in the argon gap); 3) impurities in the liquid argon; and 4) image charge effect.

4.7.1. HALAC Uniformity

The response of the HALAC to the energy deposited at different places in the detector was studied during the second calibration run. Before the data from different runs were compared, they were corrected for dead or noisy channels, different readout thresholds and different pedestal values. Figure 32 indicates all the calibration runs used to study the energy uniformity of the HALAC. We used only the runs with more than 6K events in order to have enough statistics. The detected energies at all the data points were consistent within 4%.

4.7.2. EMLAC Uniformity

The variation in the energy response of the EMLAC as a function of position was studied during the second calibration run. Because of the limited experimental run time, it was not possible to calibrate the entire area of the detector. Instead, one quadrant (quadrant 3) was calibrated extensively, especially close to areas where the biggest variations were expected, i.e., the quadrant boundary, the octant boundary, the inner - outer ϕ boundary. The variations in the energy response of the EMLAC along strips in the r and ϕ views were also studied. Only limited

calibration runs were taken in the other quadrants.

The energy deposited in the ϕ view was systematically higher than the r view in the front section (the opposite takes place in the back section). This was as expected and was the length of the longitudinal shape of the showers and the placement of the r and ϕ boards longitudinally. The detected energies in quadrant 3 for 50 GeV beam data were independent of position within 1.5 %.

4.8. Pedestal Corrections

The energy resolution and the energy deposited in the HALAC was studied by using the data from the calibration runs where the zero suppression was turned off. First the energy resolution was calculated by summing the energy deposited in all channels above threshold around the position that the calibration beam hit the HALAC. Then the pedestals were corrected using the data from the previous calibration run where the beam was hitting the LAC at a different place, thus leaving the channels of interest unaffected. The energy resolution calculated by correcting for pedestals was about 5% better than with no correction. Figure 54 shows the pedestal offsets for the 45 channels around the pad the beam was hitting the HALAC. The shifts were measured using non-zero-suppressed data. This correction was not possible for the physics data because the non zero suppressed information, for each channel on a run to run basis was limited. Instead, all channels in each EWE were corrected by the same amount so that the average value of summed pulse heights in each EWE was zero. This was not done to improve the energy resolution but to assure uniform response throughout the detector. The pedestals were relatively stable during the calibration runs.

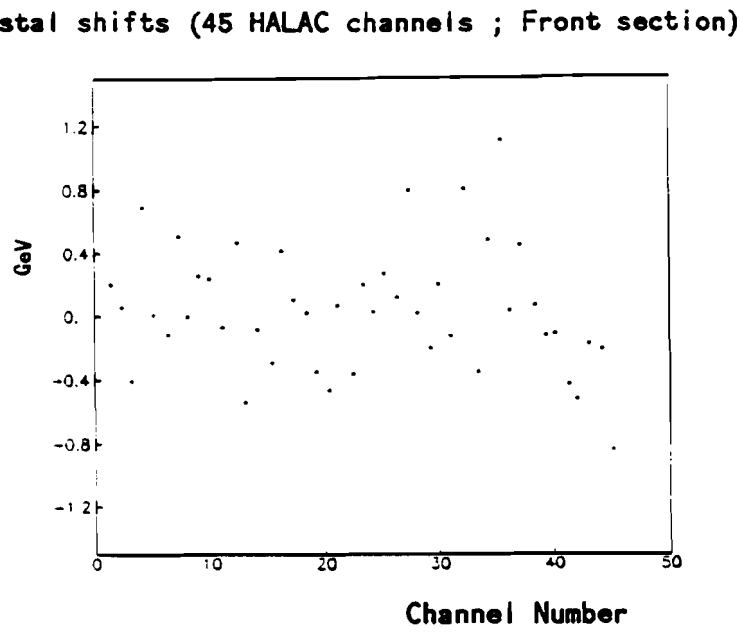

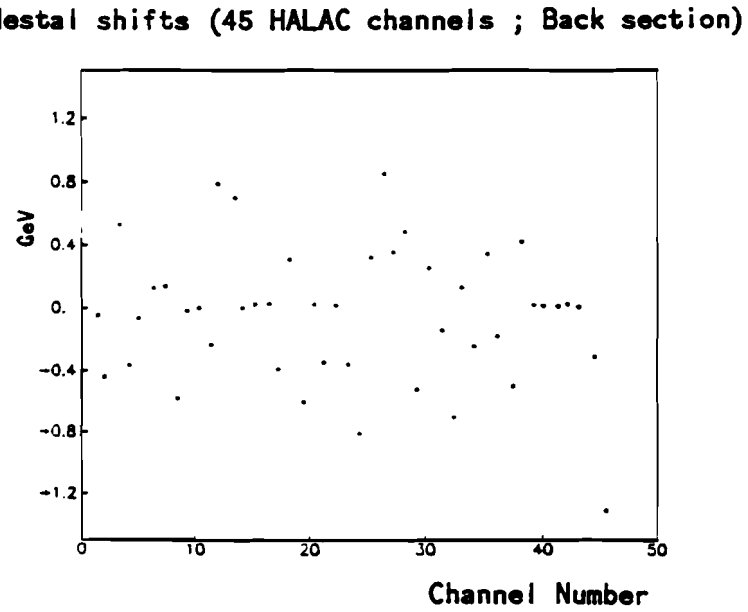

Figure 54: The pedestal offsets for the 45 channels around the pad the beam hit the HALAC. The shifts were measured using non-zero-suppressed data (the top graph is the front section and the bottom graph is the back section).

4.9. Conclusions

The EMLAC detector proved to be a good detector for $e^{\pm}$, γ,π^{o} and η due to its good[71] energy resolution ($\frac{\sigma}{E} \sim \frac{20\%}{\sqrt{E}}$) taking into account coherent noise, and its excellent position resolution ($\sigma_z \sim 0.3$ cm). This property is especially important for the identification of coalesced γ's from π^{o} or η decays, which are a major source of background to the direct γ signal.The energy leakage of the electromagnetic showers to the back of the EMLAC was negligible.

As can be seen from Table 4, a large amount of material (the EMLAC detector) is in front of the HALAC. This complicates the analysis of hadronic showers. The hadronic calorimeter did not perform as well as was anticipated for low energy hadrons. Even though the position resolution of the detector was very good for a calorimeter of this type ($\sigma_z \sim 2$ cm), the energy resolution turned out to be about twice the designed goal. Its energy resolution is $180\%/\sqrt{E}$. Almost all the hadronic cascades were contained within the two calorimeters. The HALAC was the only detector we had to measure the neutral hadronic energy and it proved to be a reliable device for measuring the energy of the energetic hadrons. Here it has to be emphasized that one of the great advantages of the hadron calorimeter is its ability to identify neutral hadrons which are missed by the magnetic spectrometer in front of the LAC.

5. OFFLINE DATA ANALYSIS

5.1. Introduction

This chapter describes the computer programs written to interpret the raw data and convert its encoded information to physical quantities. The performance of the programs is also presented. The raw data were written onto magnetic tapes from all detectors in our spectrometer. They were latched signals from the beam Cherenkov counter, the beam scintillation counters, the veto walls, the hits from Silicon strip detectors (SSDs) and Proportional Wire Chambers (PWCs), the LAC amplifier signals and the Forward Calorimeter (FCAL) signals.

The raw data were processed through the E-706 offline software program consisting of a library of routines driven by a main program called MAGIC. This included shower reconstruction in the liquid argon calorimeter, the tracking and vertex reconstruction for charged particles in the silicon strip detectors and proportional wire chambers, and energy reconstruction in the forward calorimeter. The primary analysis of the raw data was performed on the Fermilab ACP parallel processor computer system. MAGIC used FORTRAN 77 as a computer language and PATCHY as a computer code management system. The ZEBRA[72] memory management system was used to overcome the lack of dynamic memory management of FORTRAN 77. ZEBRA was also used extensively for storing the reconstructed data. The initialization of cuts and parameters was done through a list driven interface using the CERN routine FFREAD. Most of the mathematical operations in MAGIC were done by means of the CERN LIBRARY software package.

Each spectrometer component was treated independently in MAGIC. The corresponding raw data stream was first unpacked and then reconstructed. Finally each reconstructor filled the corresponding output physics banks which were the final product of MAGIC. The linking of one element's fully reconstructed information with that from another was done at the higher level analysis phase.

The data reconstruction subroutines in MAGIC were the following:

a) DLREC - Reconstructs the information about the data latches and the trigger bits.

b) PLREC - Reconstructs the data from the SSDs and PWCs and combines the reconstructed data from each system to calculate the three - momenta and the charge of the reconstructed tracks.

c) EMREC - Reconstructs the data of the EMLAC.

d) HCREC - Reconstructs the data of the HALAC.

e) FCREC - Reconstructs the data of the Forward Calorimeter.

The order in which these reconstructors were called was selected by the user. In this thesis, the following order was chosen: DLREC, EMREC, PLREC, HCREC, FCREC.

When the event reconstruction was finished, events of interest were extracted, and condensed information for each event was written to data summary tapes (DSTs). The DSTs were used for the final analysis.

5.2. Charged Particle Tracking

The charged tracks were reconstructed by the pattern recognition program using hits* in the Silicon Strip planes (SSDs) and the Proportional Wire Chambers (PWCs). For each run, the recorded data was studied to determine which PWCs and SSDs wires/strips had hits in an unusually large fraction of the events. These wires/strips were excluded from contributing entries to the reconstruction programs.

Two types of reconstructed tracks were used in the program, the view tracks and the space tracks. The view tracks were two dimensional tracks, formed by fitting hits in the same view of each chamber to straight lines. The space tracks were three dimensional tracks formed from view tracks. The terms space/view will be used throughout the text.

The PLREC proceeds in the following sequential steps:

a) Beam tracking.

b) Down stream tracking.

c) Upstream tracking.

d) Vertex reconstruction.

e) Link upstream - downstream tracks.

f) Momentum and Charge reconstruction.

Figure 55 shows the Y-views of the SSDs and the PWCs. The picture is drawn

* A hit is the coordinate of a wire or strip in a plane which registered a charged particle.

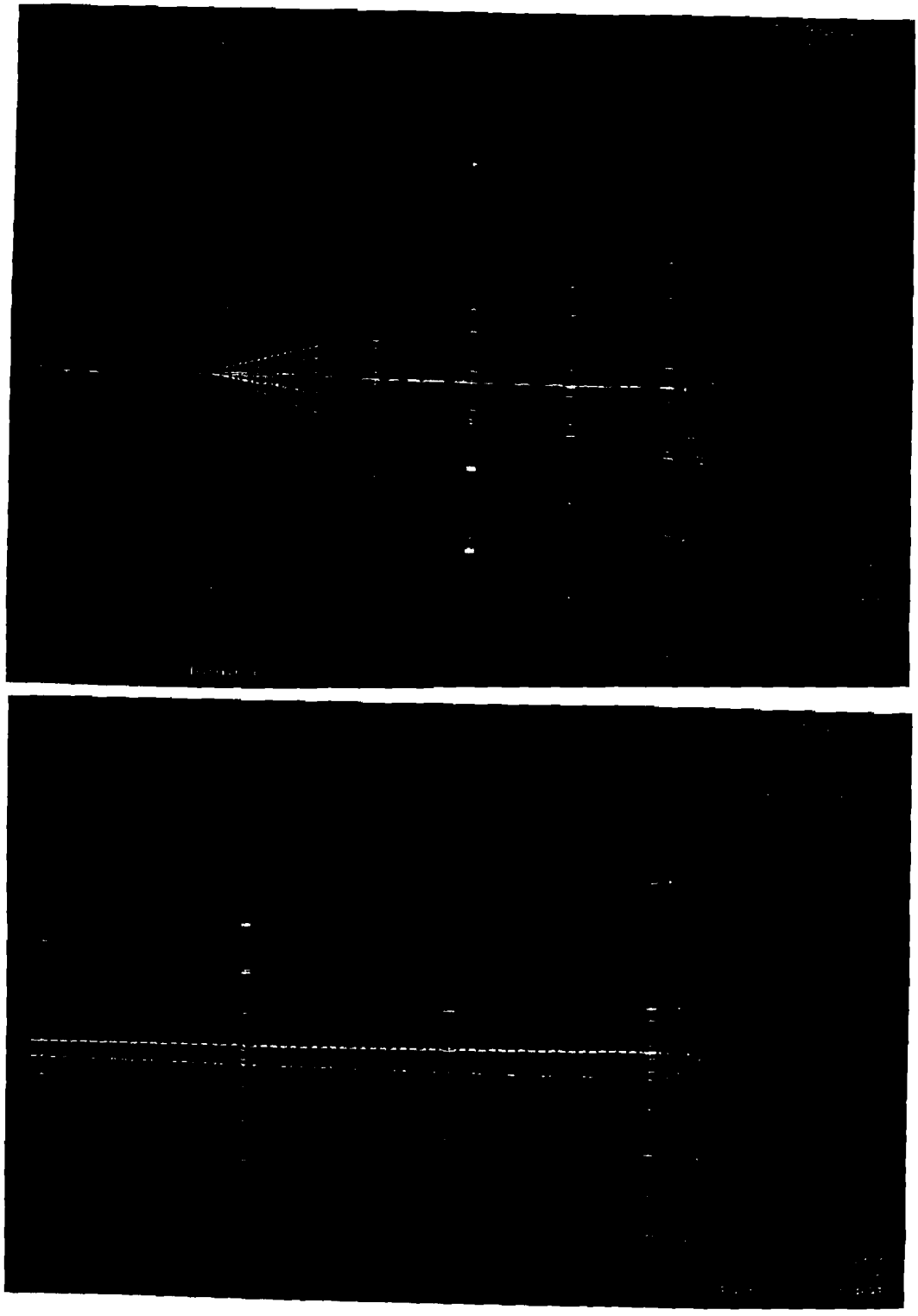

Figure 55: A picture of the y-view of the SSDs and the same view of the PWCs.

using the E-706 graphics package. The hits are shown as crosses and the reconstructed 3-dimensional tracks are shown as lines.

Now we will describe in more detail the steps a) through f) listed above.

5.2.1 Beam tracking

Three silicon strip detectors were used upstream of the target, each of them consisting of an x-view and a y-view. The beam track was defined in two steps:

i) Initial space tracks were formed by looping over all hits of any two detectors. Next, the tracks were projected to the third detector. The hits in the third detector were assigned to the tracks if they were close enough to them. Then, the tracks were refitted using hits from all three chambers.

ii) When the three-hits tracks were exhausted, tracks were formed using the remaining two hit combinations.

Due to noise extra beam tracks and readout inefficiencies, it was possible for more than one beam track to be reconstructed per event. In the higher level analysis, only the best three-hit track was used. If two three-hit tracks with comparable chi-squares were reconstructed, then both of them were rejected.

5.2.2 Downstream Track Reconstruction

The tracking downstream of the magnet involved four PWC modules, that is, a total of 16 planes (four independent views each with a maximum of four coordinates). The downstream tracking proceeded in the following two steps:

First Step

View tracks were reconstructed by fitting 4 or 3 points in a view to a straight line. This was done in two passes. In the first pass the first and fourth planes in

the view were taken as the "seed" planes, and the second and third planes were taken as the "search" planes. In the second pass the "seed" and "search" planes were interchanged.

In the first pass a seed pair* was used to form a 3 or 4 hit track. The track composed of a seed pair was projected onto the search planes where all hits found within a tolerance ($\pm$ 1.5 wire spacings) were taken. If there were hits only in one plane of the two search planes, the view track formed was a 3-hit track. If there were hits in both search planes, the view track was a 4-hit track. The tracks so formed were fit with a least squares fit and if the chi-square of a 4-hit track was greater than a preset limit (cut), the hit contributing the largest value to the chi square was removed and the track was refit.

In the second pass the "seed" and "search" planes were interchanged and the tracks from the new seed pairs were projected on the search planes. Only the combinations which were not part of the 4-hit tracks of the previous pass were considered.

After the 3 and 4-hit view tracks were formed they were compared among themselves for common hits. The 4/3-hit tracks were converted to a single track if they shared three or more hits. If there were only two tracks in the cluster the one with the higher chi-square was dropped. The remaining 4-hit tracks were compared with the 3-hit ones and if they shared two hits or more then the 3-hit tracks were dropped.

The same procedure was repeated for all four views.

---

* A "seed pair" is a pair of hits in which one hit is from one seed plane and the other from the other seed plane.

Second Step

The space tracks were constructed by combining the 3 and 4-hit view tracks, in two passes as done before with the view tracks. In the first pass the "seed views" were the X and Y views and the 'search views' were the U and V views, and vice versa for the second pass. We started by taking any pair of view tracks from the seed views and each track was projected onto each of the planes of the search views. The hits of the search view plane, that were closer than ± 1.5 wire spacings to the projected positions of the seed view tracks, were stored along with the hits of the seed view tracks. This set of hits was used to form a space track if the following requirements were met:

a) At least two hits from each view.

b) At least four hits in all search views.

c) At least six hits in all projected seed view tracks.

d) At least thirteen hits in all views.

e) All hits that passed criteria a) to d) were fit with a least-squares fit to define a candidate track.

A list of candidate space tracks was created after the second pass and tracks kept if the space track candidate did not share more than five hits with another track. If this was the case, the track with the smaller number of hits was dropped. In case they had the same number of hits, then the one with the higher chi-square value was dropped.

5.2.3 Upstream Track Reconstruction

Upstream tracking involves only the four SSD detectors, that is, 8 planes and

two views (X and Y view). The upstream tracking proceeds in the same fashion as the previously described downstream tracking. The main difference is that there is one "seed plane" and one "search plane". Other than that the reconstruction algorithm is the same.

5.2.4 Vertex Reconstruction

The vertices were reconstructed using tracks in the SSD system (the upstream tracks). Only the upstream tracks that were linked to the downstream tracks (tracks in the PWC system) in the magnet were used. In case there were less than three upstream tracks linked to the downstream tracks, only the 4-hit upstream view tracks were used in the vertex reconstruction. The vertices were reconstructed separately in XZ plane and YZ plane. The vertex point (X, Z_x) was calculated in XZ plane minimizing the following χ^2 equation:

$\chi^2 = \sum_{i=1}^{N}(X - X_i)^2 = \sum_{i=1}^{N}(X - a_i Z_x - b_i)^2$ where a_i and b_i are the slope and the intercept of the ith track and N is the total number of tracks. X, Z_x were calculated by solving the following equation:

$$\frac{\partial \chi^2}{\partial X} = 0, \frac{\partial \chi^2}{\partial Z_x} = 0$$

Similar calculations were done for the y-view.

Figure 56 shows the z distribution of the reconstructed vertices in the segmented target region. z is defined as the weighted mean of Z_x and Z_y. The structure of the target is evident in Figure 56 . In the same figure the vertex z- resolution ΔZ is also shown. ΔZ is defined along the beam direction as follows:

$\Delta Z = Z_x - Z_y$ where

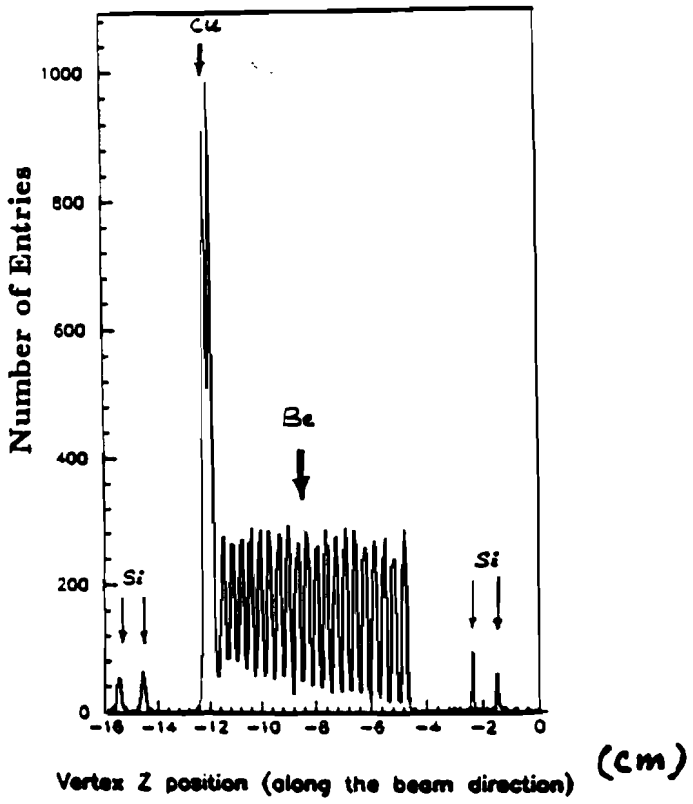

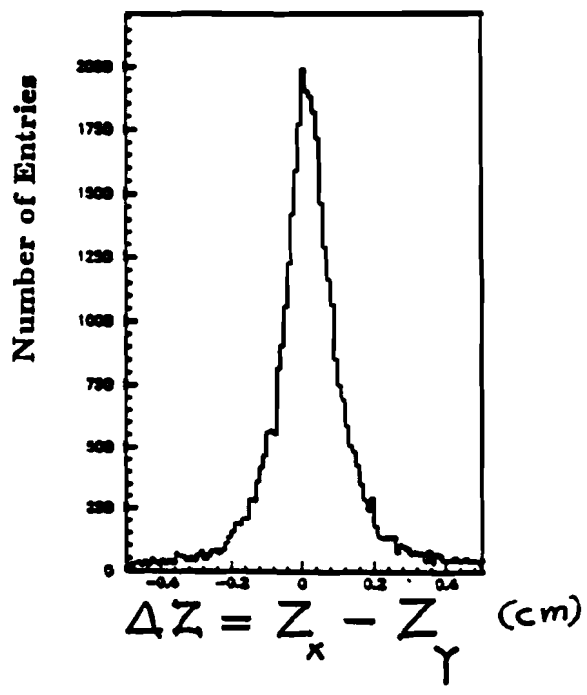

Figure 56: (top): The z distribution of the reconstructed vertices in the segmented target region. (bottom): The reconstructed vertex resolution in the z direction.

Z_x is the z-position of the vertex in the x-view and Z_y is the z-position of the vertex in the y-view

5.2.5 Linking Upstream and Downstream Tracks

To a good approximation, the magnetic field of the dipole magnet bent the tracks in the X view only. The XZ plane was called the "bending plane" and the YZ plane was called the "non-bending plane". The bending of the tracks in the field was considered as a sudden bend at the mid-plane of the magnet. There were two problems with linking the PWC - SSD tracks in the magnet[73]:

a) The finite curvature of tracks inside the magnet, as well as the leakage of the magnetic field, make the "kick approximation"* inaccurate.

b) The magnetic field was measured with a search coil probe and the measurements were calibrated with the nuclear magnetic resonance technique. The measurements were done only for z>72.7 cm (although the front face of the magnet is at z = 55 cm). The extrapolation to smaller z values makes the effective center of the magnet uncertain at the level of 1% of the magnetic length.

The magnetic field was refit taking Maxwell's equations into account. The deviations of the magnetic field from the effective field approximation were parametrized in a form suitable for PLREC. Details on this method can be found in Ref. [73].

Every upstream and downstream track was extrapolated to the magnet mid-plane. For each PWC track, the SSD tracks were scanned to find the proper upstream - downstream pair in both X and Y views.

* Kick approximation is the replacement of the magnet by a single kick at some nominal center.

If the projected difference, in the XZ plane, was less than a cut ($\sim \pm 0.7$ cm) then the pair of tracks was put in the list of matched tracks. The list was arranged in ascending order of the projected difference.

In the YZ plane, non-bend plane, the weighted sum of the squares of the projection difference and the slope difference of a pair was calculated and the pair was selected if it satisfied a cut. The pairs of tracks were arranged in ascending order of the weighted sums.

Every space track was checked, in the non-bend view, to see if it came from the vertex region (see vertex reconstruction below). Two cases can be distinguished here:

a) The linked track in the top of the list came from the reconstructed vertex. Then this pair was selected as the final linked pair.

b) The track in the top of the list did not come from the vertex. Here we calculated the weighted sum of the squares of the impact parameter (i.e., the minimum distance of the track to the reconstructed vertex) and the projection difference to the magnet midplane for the first five linked pairs in the list. The pair that gave the minimum weighted sum was the selected linked pair.

Figure 57 (top graphs) shows the distribution of the impact parameter of a reconstructed track in the XZ and YZ plane at the event vertex. Figure 57 (bottom graphs) shows the projected difference at the magnet midplane of two linked upstream - downstream tracks in the XZ and YZ planes.

Finally we list few special cases concerning the linking of upstream - downstream tracks.

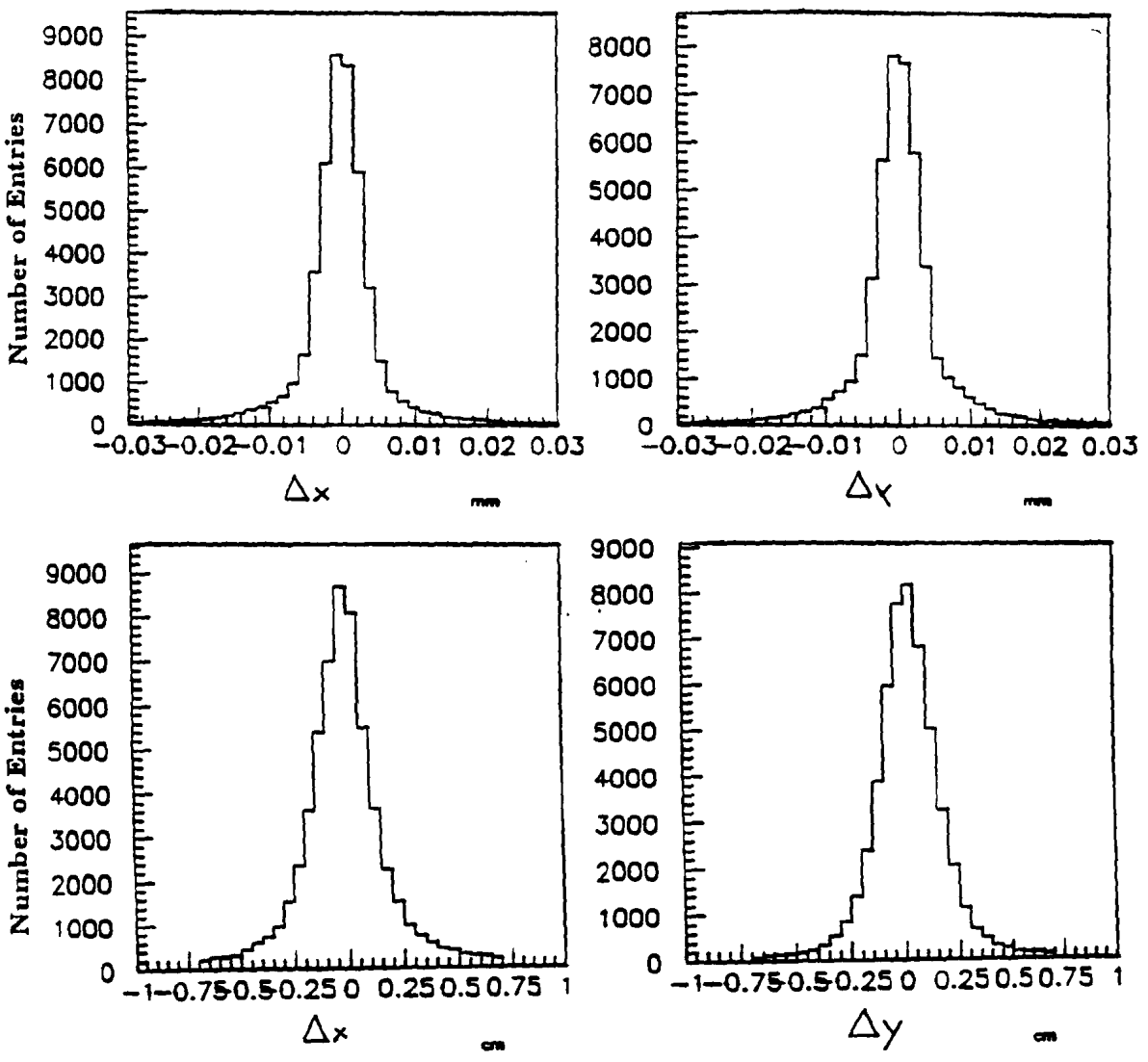

Figure 57: (top): The distribution of the impact parameter of a reconstructed track in the XZ and YZ plane at the event vertex. (bottom): The projected difference to the magnet midplane of two linked upstream - downstream tracks in the XZ and YZ planes.

a) If there was no upstream link for a space track in the XZ plane, then a line that connected the track intersection at the center of the magnet and the primary vertex was assigned to the x-view upstream track.

b) If there was no upstream link in the YZ plane for a space track, then the projection of the downstream track to the primary vertex replaced the y-view upstream track.

c) If there was no vertex found in the event then the center of the target was assigned to the vertex.

5.2.6 Momentum and Charge Reconstruction

Momenta of particles were calculated by the following formula:

$$\vec{p} = \frac{\Delta\vec{p}}{\sin(\theta_i) - \sin(\theta_o)}$$

using their trajectories before and after the analyzing magnet, where θ_i is the incoming angle of the upstream track and θ_o is the outgoing angle of the downstream track. The magnetic field was set to a value corresponding to 450 MeV/c transverse momentum kick (Δp). The value of Δp set by the mass peak of J/Ψ.

The charge of a particle was determined from the direction of bend in the XZ plane.

5.3. Alignment of PWCs and SSDs

Prior to the data run, the SSDs, PWCs and LAC were carefully measured and positioned using the optical survey method. Special data was taken turning off the field of the analyzing magnet. Data from these runs were used to obtain the positions of SSD planes and PWC planes with a better accuracy than the optical survey. The tracks used in the alignment were required to have hits from all planes. The residual distribution between a hit location and the intercept of the particle trajectory at the plane (as fitted to the hits of the other chambers) was centered at zero by making small adjustments to the transverse location of the plane entered into the tracking program. After the residual distributions of all planes were centered, the z-location of the plane was optimized by looking at the width of the residual distribution. For rotated planes, the tilt angle was also optimized in the same manner. The shape and the width of these residual distributions were consistent with that of the position resolutions.

5.4. Performance of PWCs and SSDs

The performance of the magnetic spectrometer is presented in this section. Figure 58 (top) shows the average reconstructed track multiplicity for high p_T events. In the same figure, the momentum and p_T distributions of the reconstructed tracks are shown.

The following table presents the fraction of the 4 or 3-hit tracks in the total sample. 94% of the events in a typical run were reconstructed in PLREC. The rest (6%) were not reconstructed because of high hit multiplicity in the planes.

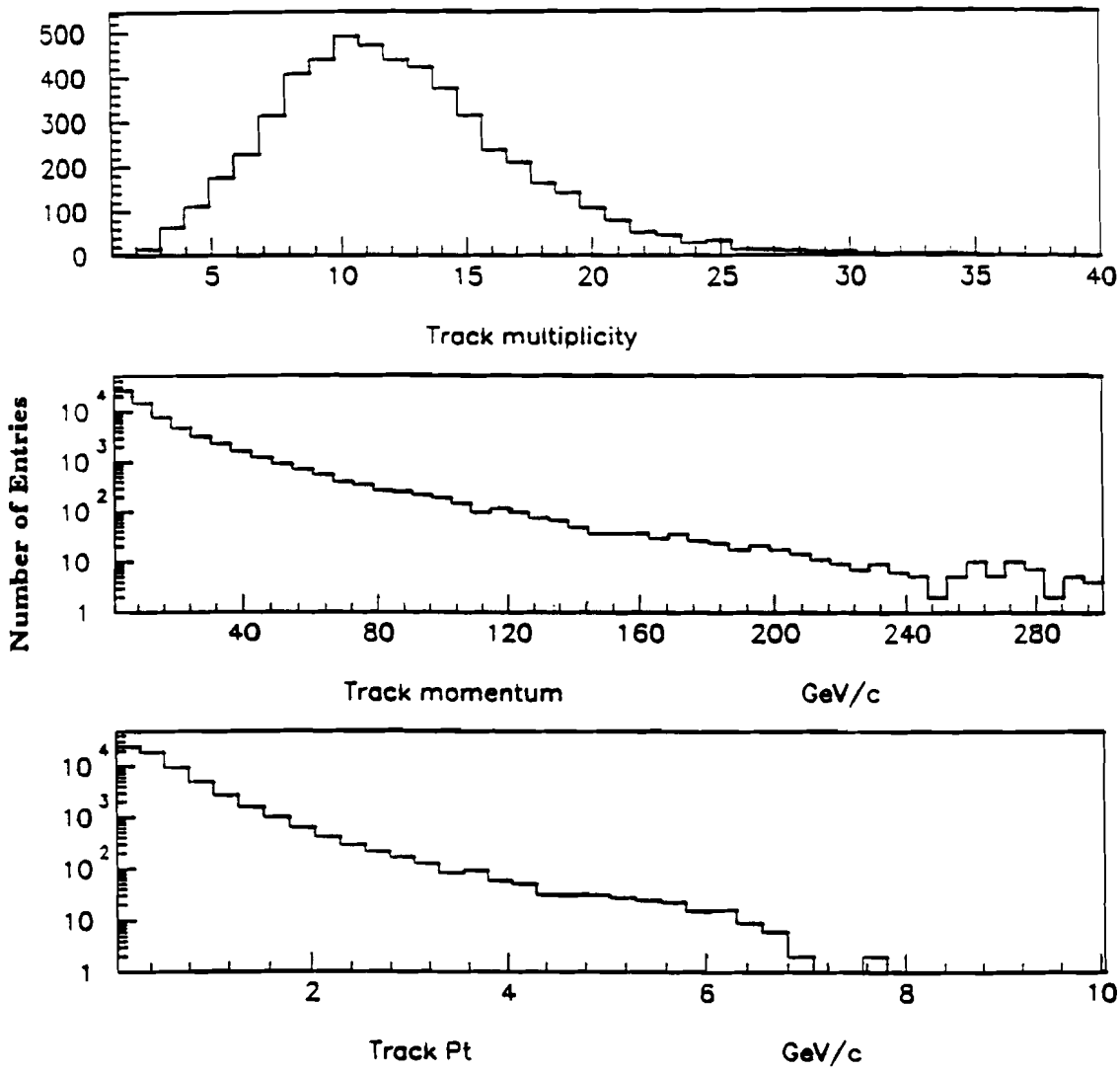

Figure 58: The multiplicity, momentum and p_T (< 8 GeV/c) distribution of reconstructed tracks (no quality criteria in the selection of tracks have been applied).

No. of hits per view track/event	X-view	Y-view
4 hits (PWC tracks)	50%	60%
3 hits (PWC tracks)	50%	40%
4 hits (SSD tracks)	55%	59%
3 hits (SSD tracks)	37%	23%
SSD tracks not linked	8%	18%

Table 10: Characteristics of SSD and PWC tracks. Here all the view tracks are involved, not just the ones that formed space tracks.

A Monte Carlo study was performed for the tracking system. Figure 59 shows the momentum resolution of the magnetic spectrometer according from this study. The reconstructed momentum agreed with the momentum generated by the Monte Carlo. The momentum resolution has a Gaussian distribution with rather large tails. The root mean square (RMS) of the distribution depended on the generated momentum: $\frac{\delta P}{P} = 0.09\% P$ with P in GeV/c. For comparison, the momentum resolution of the magnetic spectrometer without the upstream tracking system (SSD) is also shown.

The average efficiency of the PWC plane was calculated using only tracks which pointed to a shower in the LAC. The average efficiency of SSD was calculated using data which was taken without the magnetic field in the analyzing magnet. In this analysis, the upstream tracks which were linked to the downstream tracks were used. The efficiency of each PWC module was measured by taking tracks which were matched to LAC showers and then looping over the hits to find whether or not there was a hit in a given plane. The measured efficiency of each module

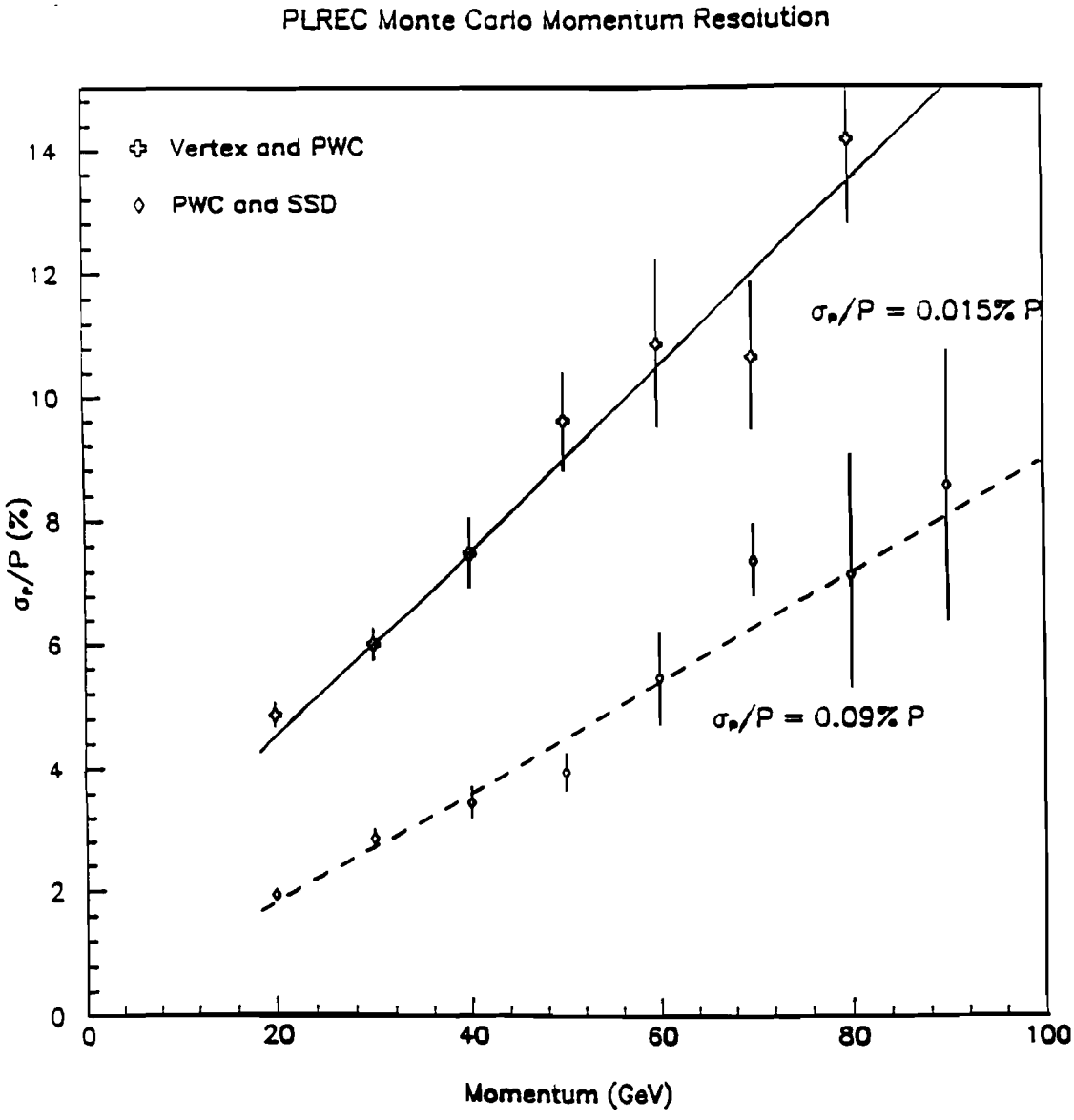

Figure 59: The momentum resolution of the magnetic spectrometer according to the Monte Carlo study.

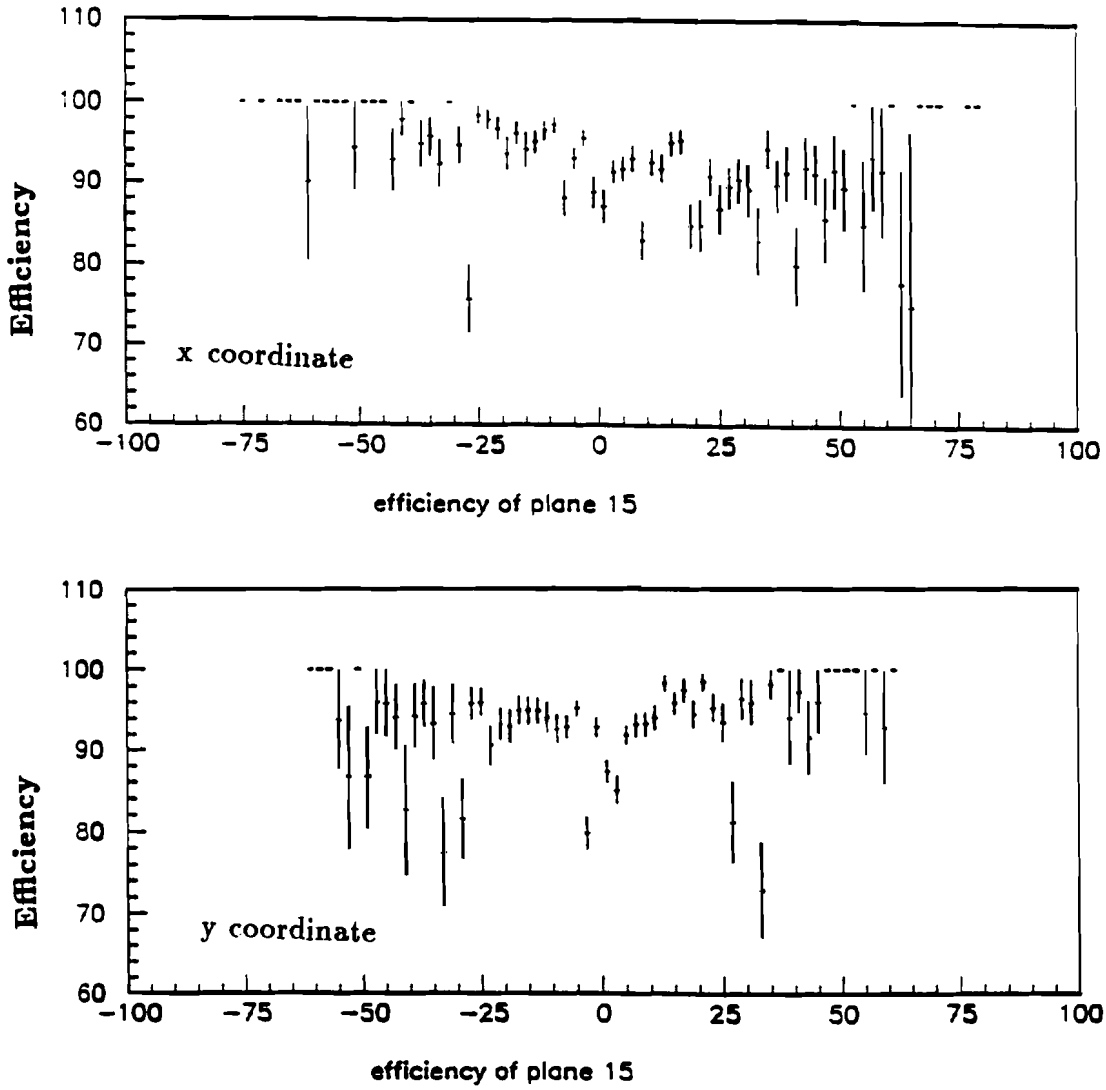

Figure 60: The efficiency of a module measured with two methods. In the figure at the top the tracks were projected on the plane along the x coordinate and in the figure at the bottom, the tracks were projected on the plane along the y coordinate.

varied from 91% to 96%. The average efficiency for all modules was close to 95%. Figure 60 shows the efficiency of a module measured with two methods. In the plot at the top, the tracks were projected on the XZ plane of the module and in the bottom plot the tracks were projected on the YZ plane. The efficiency of this module is 92%. The reconstruction efficiencies, if a module efficiency is 95%, as a function of the number of hits are listed in Table 11. For 14 hits or more, the overall track finding efficiency was 96%.

No. of hits per track (total 16 hits)	Fraction of tracks
16 hits	44%
15 hits	37%
14 hits	14.7%
13 hits	3.6%

Table 11: Efficiency of PWC tracks.

The performance of the tracking system was also checked by using the tracks which were the decay products of known particles. Figure 61 shows the reconstructed mass of K_s^os which decayed into $\pi^+\pi^-$ before the magnet. Photons converted to e^+e^- pairs in the target. A "zero mass pair" combination of these tracks was formed as follows. First, the closest track to a shower with $E^{front}/E^{total} > 0.6$ was found. If its radial distance from the shower was within 1 cm, the shower - track pair was tagged. Next the tracks linked to a shower were combined with all other charged tracks of opposite sign with a similar y-view slope ($|Y_{slope\ trk1} - Y_{slope\ trk2}| < 1.5\ mr$). The invariant mass of the pair of tracks

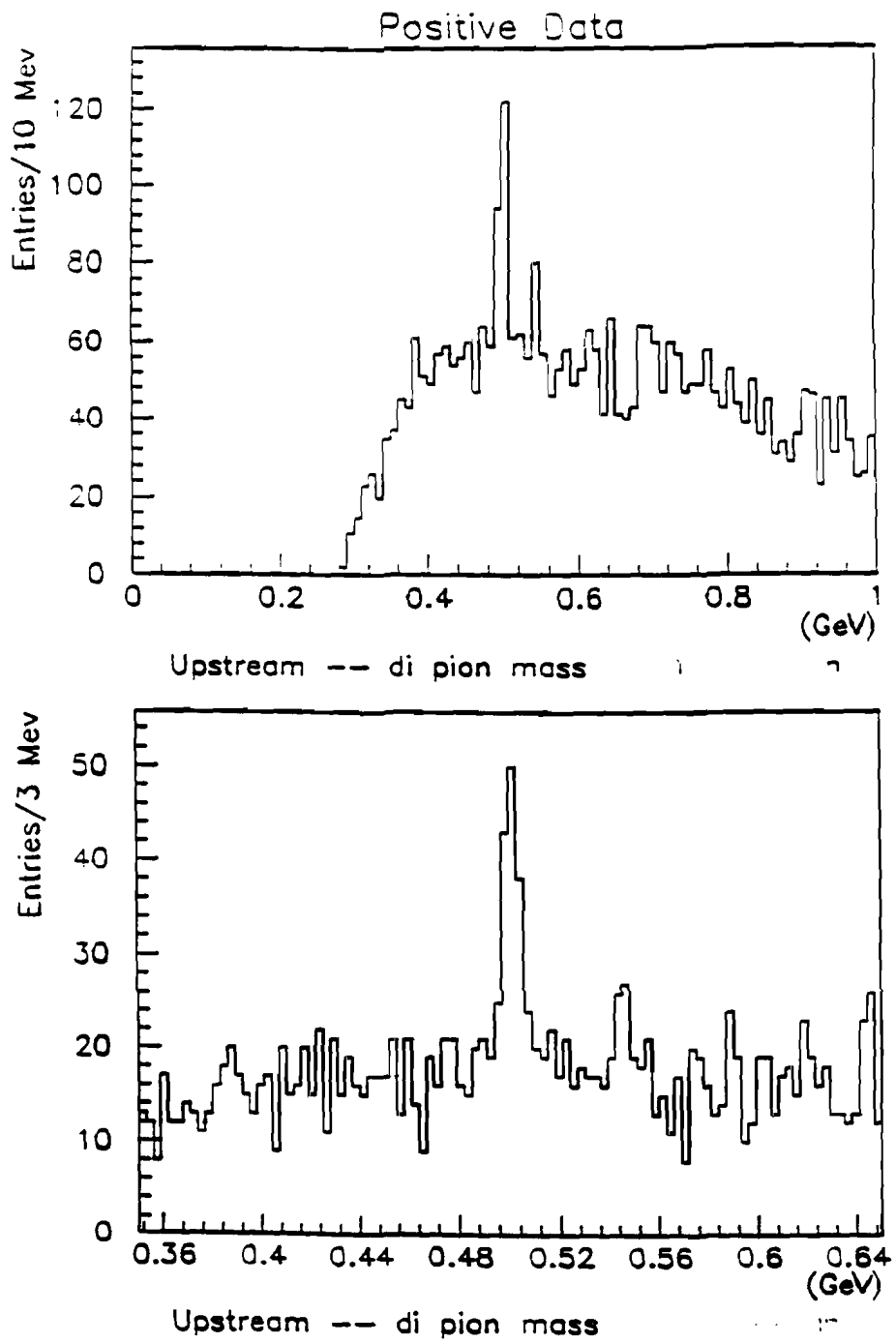

Figure 61: The reconstructed mass of K_s^os which decayed into $\pi^+\pi^-$.

which intersected at the center plane ZX of the magnet (± 6.0 cm) was formed. The pair with the smallest mass was chosen, and the original track and a zero mass pair formed. If the second track linked with a shower, the zero mass pair was considered fully reconstructed.

The reconstructed mass spectrum of π^0 which decayed into $\gamma\gamma$ and one or both γs converted to an electron - positron pair (γe^+e^- and $e^+e^-e^+e^-$) is shown in the Figure 62.

5.5. Data Bank Structures for the EMLAC and the HALAC

The raw data consisted of 32 bit words which gave the packed address of the readout strip in the EMLAC or the readout pad in the HALAC and the pulse height of the channel. There was another data word per four amplifier outputs carrying timing information. Raw data was decoded into strip number or pad number and the pulse height of the channel by the subroutines, EMUNP and HCUNP.

For each run, the data was studied to determine which of the LAC amplifiers had recorded abnormally high values. These LAC channels were excluded from contributing entries in the raw data input list to the reconstruction programs. The pulse height data were processed in the following steps. First, a pedestal was subtracted from the ADC count for the channel. Then the subtracted ADC count was multiplied by the relative gain of the amplifier. Corrections due to the effects of detector RC risetimes on the pulse were also applied. This had practically no effect for detector capacitances less than 3 nf (EMLAC) but was about 10% at 10 nf (HALAC channels). The ADC count was converted to energy by an overall

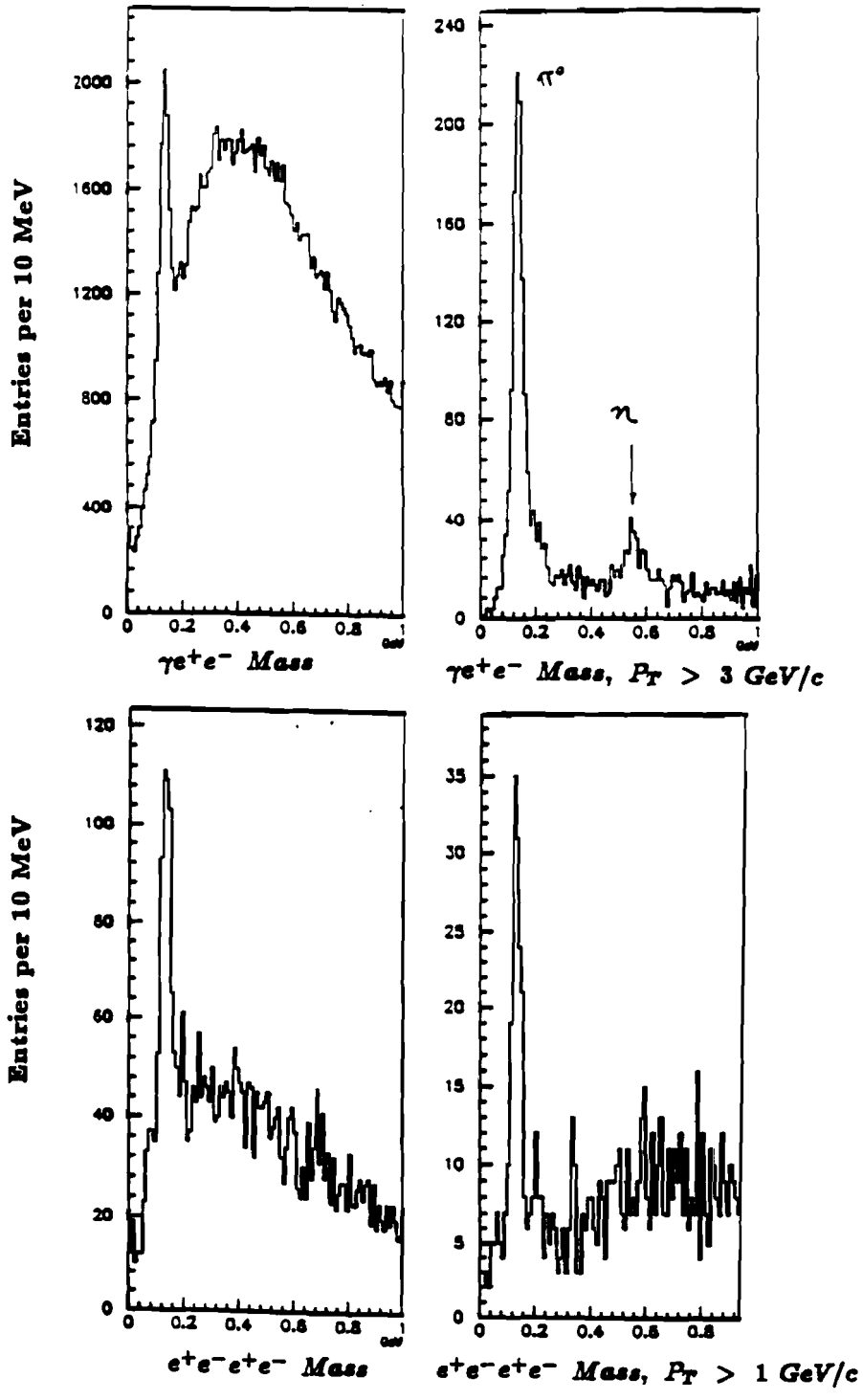

Figure 62: The reconstructed mass of π^0s which decayed into $\gamma\gamma$ and one or both γs converted to an electron - positron pair (γe^+e^- and $e^+e^-e^+e^-$).

constant. This constant was 3.1 MeV/count for the EMLAC and 49 MeV/count for the HALAC.

A) EMREC Data Bank Structure

The EMLAC consisted of four quadrants which were numbered in order of increasing azimuthal angle. The readout was subdivided in four views. The r strips were divided in two views, the left r and right r view. For each quadrant the left r view comprised the r strips in the first octant, the right r comprised the strips in the second octant (the octants were numbered in order of increasing ϕ). The inner ϕ view was view 3 and the outer ϕ was view 4. The front and back longitudinal sections were referred to as Section 1 and Section 2, respectively. In the reconstruction program for the electromagnetic shower for this thesis the energies of the front and the back section were summed. The combined sections were referred to as Section 3.

The input and output data to the EMREC had the following form:

i) Input Banks

The input banks were created by the unpacking routine, EMUNP. The address of an amplifier channel given by the readout system of the EMLAC was a 16-bit packed word. The EMUNP decoded each word and extracted the address, ADC and TDC information and put them in ZEBRA banks (called input banks) to be read by the EMREC. There were 24 banks (4 views$\times$ 6 types) for each quadrant of the EMLAC. Each view consisted of six banks; the first one contained the strip address, the second and third ones contained the strip energies in the front and back sections, respectively; the fourth one contained the energy sum of the front

and back strips, and the fifth and sixth ones contained the TDC values of the front and back sections, respectively.

ii) Output Physics Banks

Temporary storage banks and output banks were created in EMREC. Only the output banks were written on the data summary tapes. Here I discuss only the output bank which contains the physics informations referred to as the "photon" bank. An energy cluster reconstructed by EMREC was called a "photon".

There was a main "photon" bank for each quadrant consisting of three daughter banks. The first daughter bank contained information about the "photons" reconstructed in the front section; the second bank contained information about the "photons" reconstructed in the back section; and the third one has all "photons" found in the sum of the front and back sections. In the analysis presented in this thesis, only the third "photon" banks were used.

Some of the values transferred to the output physics banks (or photon banks) for each reconstructed photon were the photon energy, r position and width, ϕ position and width, photon χ^2/DOF (Degree of Freedom), (Front Energy)/(Total energy).

B) HCREC Data Bank Structure

The hadron calorimeter consisted of two sections. There were 1206 pads in the front section (14 detector layers) and 1134 pads in the back section (39 detector layers). Figure 63 shows the pad numbering scheme. IROW and ISLA numbers ran from 0 to 29 in the front section and for the back section IROW ran again from 0 to 29 but ISLA ran from 1 to 28. In the discussion below consider the

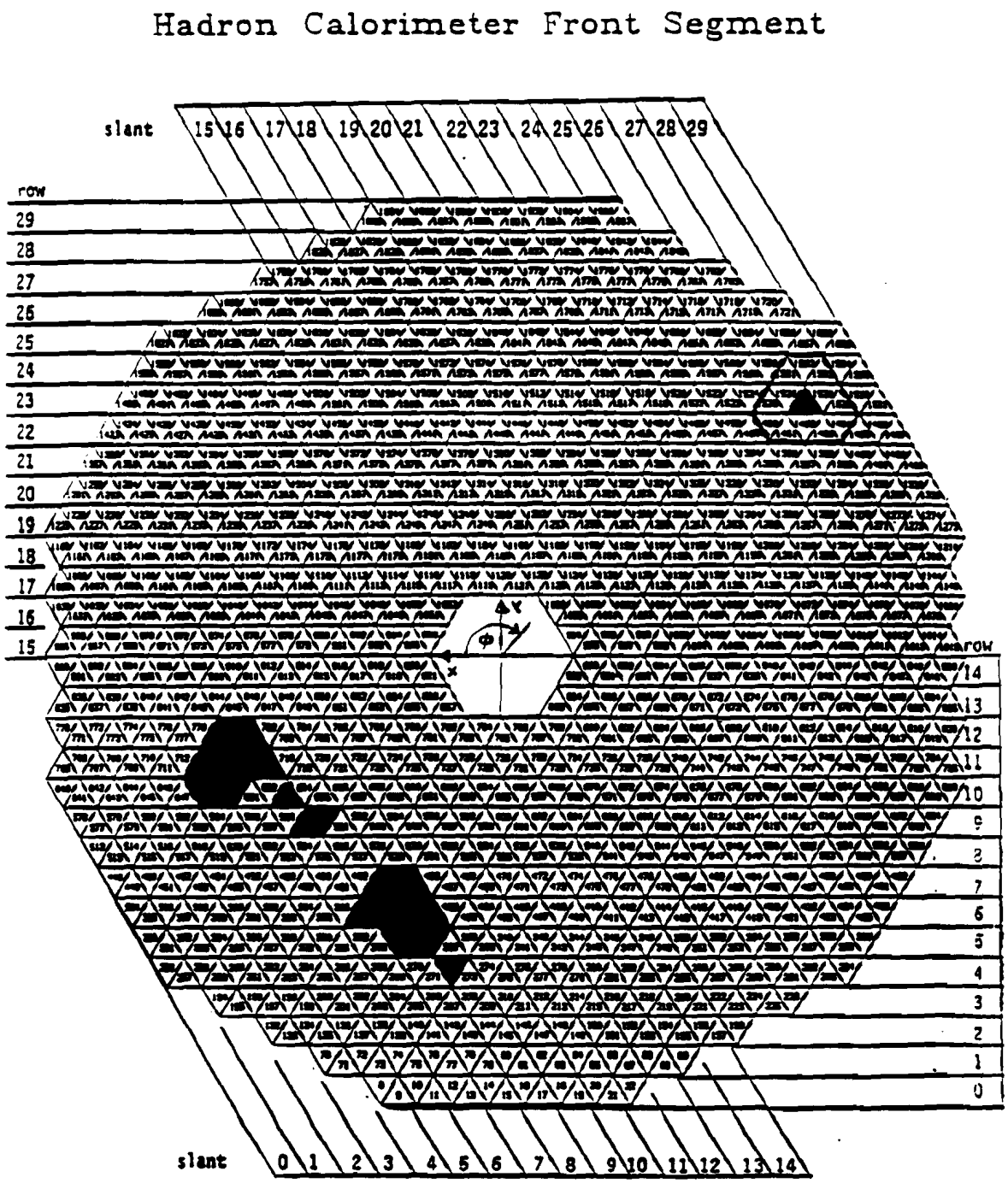

Figure 63: The HALAC channel numbering scheme.

front/back sections to have the same pad sizes.

In this scheme two neighboring pads shared the same IROW, ISLA number. We distinguished them by assigning the UP or DOWN flag IUD(=0 for the up pads,=1 for the down pads). Pads with identical IROW, ISLA and IUD belonged to the same tower. For example the pads 470 and 471 shared the same IROW(=7) and ISLA(=11) number but IUD was 0 and 1, respectively.

The raw data from the HALAC was decoded by the subroutine HCUNP. The address of a pad given by the readout system of the HALAC was not the amplifier number. It was a packed 16 bit word which included 5 bits to specify a horizontal row of pads(0-29), 5 bits to specify a slanted row(0-29) and a bit to distinguish UP(=0) from DOwn(=1). For example the pad tower with the amplifier address(i.e., physical address) IROW=07, ISLA=08, IUD=0 is written as:

00111010000 = 464
irow |isla | iud

The full packed address (assuming that the most significant bit is on the left) has the form[74]:

MSB:|type(15:13)|unused(12:11)|irow(10:6)|isla(5:1)|iud(0)|:LSB

where type is

BIT 13 : HADRON (=1) or EM (=0)

BIT 14 : Back (=1) or Front (=0)

BIT 15 : TDC (=1) or ADC (=0)

The input data to the Hadron Reconstruction Program were first sorted in order to be managed more efficiently by the program. The raw data contained

the energy deposited and the TDC data in random order. The raw data were copied into ZEBRA raw data bank when first read during the unpacking phase. The data consisted of six banks; front pad addresses and associated energies and TDCs, back pad addresses and associated energies and TDCs.

To rearrange the data we created, for each bank of pad addresses, another bank with only the IROW entries and reshuffled the index numbers according to them. We then shuffled each set of identical IROWs in terms of the ISLAs, and finally, if both IROW and ISLA were identical, according to IUD. The shuffling along an IROW line stopped when there was a discontinuity in ISLA and one moved in contiguous IROW data if they had the same ISLA values, i.e., ran along IROW at constant ISLA.

We used the data banks with the same pads for the front and back sections for convenience in the data analysis. Pads which had signals either in the front or in the back section were entered in the bank.

The values transferred to the output physics banks were the following (the names used in the computer code are in capitals):

IETOT - total energy of the reconstructed hadron
IEFTOT - ratio between the energy in the front section and the total energy of the reconstructed hadron
IX - x Cartesian coord of reconstructed hadron
IY - y Cartesian coord of reconstructed hadron
IXFR - x Cartesian coord of rec. hadron using only the front section
IYFR - y Cartesian coord of rec. hadron using only the front section
IXBCK - x Cartesian coord of rec. hadron using only the back section
IYBCK - y Cartesian coord of rec. hadron using only the back section
IHCHSQ - Flags indicating the quality of the reconstructed hadron

The last word was a packed word carrying the quality factor of the reconstructed hadron. It returned the number of channels used to reconstruct the hadron. It

also flagged a hadron if the channel with the maximum energy in the hadron was next to either detector boundary or next to a dead channel.

For each reconstructed hadron we kept the list of the channel addresses that were used to reconstruct the hadron in the output bank. This information was used to flag reconstructed hadrons when the noisy channels were included in the pads. A list of malfunctioning channels was created for each run and the channel addresses were compared to the address of the most energetic pad for the reconstructed hadrons. If a match was found, the reconstructed hadron was rejected.

5.6. Electromagnetic Shower Reconstruction (EMREC)

The electromagnetic shower reconstructor processed the data from the EMLAC. The reconstruction proceeded independently for each quadrant. EMREC searched the r and ϕ views of the detector for clusters of energy (called gammas) and then correlated gammas in the two views on the basis of energy matching. The correlated gammas were called photons and they were the final output of EMREC.

The energies of the strips in the front section and the energies of the corresponding strips in the back section were added prior to the pattern recognition in EMREC.

The overall photon reconstruction, in each quadrant, consisted of the following steps:

a) Group and peak finding in a given view.

b) Shoulder finding in a peak.

c) Splitting of peaks inside group.

d) Correlation of gammas in r and ϕ view.

The above listed steps are explained in detail below.*

A) Group and Peak finding

Each quadrant was divided into four views: left r (254 channels), right r (254 channels), inner ϕ (92 channels) and outer ϕ (188 channels). The left and right r views corresponded to the left and right octants, respectively. The energy pulse array in a given view was searched for groups of consecutive channels that were above a threshold (150 MeV). Each group of channels was termed a "group". A group could be either an isolated peak or it could consist of two or more peaks, the valley in between peaks being above threshold (see Figure 64). A group was rejected if; i) it was less than 3 channels wide; or ii) peak channel energy was less than 300 MeV; or iii) the group energy sum was less than 750 MeV.

Each group was scanned for local peaks and valleys. A peak was rejected if the peak to valley energy difference was less than 3σ on either side of the peak.

B) Shoulder Finding in a Peak.

At high p_T ($p_T > 7$ GeV/c, $E_{\pi^0} > 150$ GeV) a good fraction of the π^0 decay photons coalesced in r and/or ϕ views. At this energy the minimum distance between the two photons from the symmetric π^0 decay is less than 1.6 cm and for highly asymmetric π^0 decays the low energy photons appear as shoulders in the distribution of deposited energy. The peak finding algorithm did not reconstruct them as two separate peaks. The shoulder finding algorithm was implemented

* This subsection is an updated version of the E-706 memo 130/85 (Reference [75])

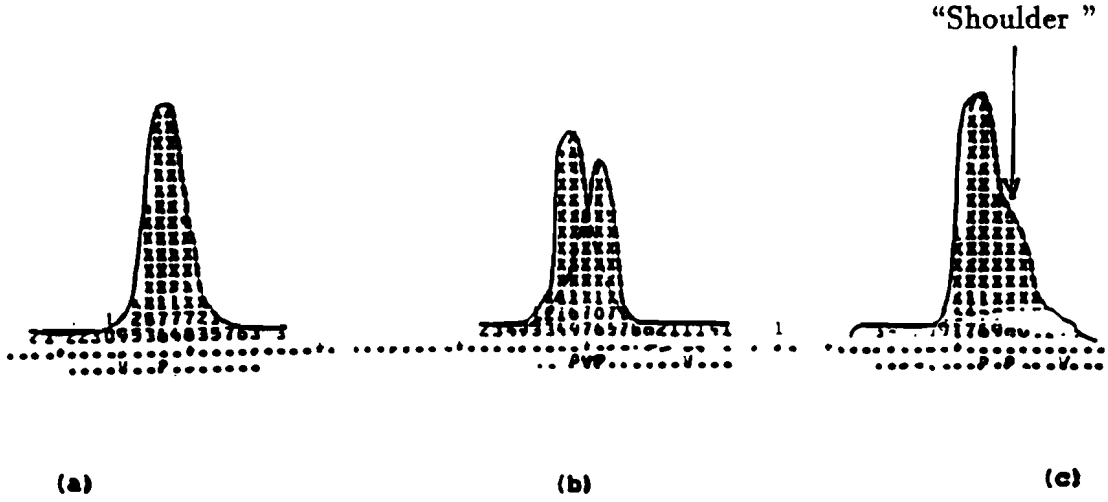

Some representative "groups" of showers in the front section of the LAC. a) Single peak group, b) double peak group and c) single peak group with a shoulder.

Figure 64: Examples of 'Groups', 'Valleys' and 'Shoulders'.

to recover some of them as two separate peaks. The algorithm looked for peak (shoulders) in the logarithmic energy derivatives of the adjacent strips (Figure 64). Shoulders were searched for only in single peak groups and only one shoulder per peak was allowed. The code was optimized to make sure that no artificial shoulders were generated. This was done by running the code, without the shoulder finding algorithm, on single photon Monte Carlo events at various energies. The result was compared to the reconstructed data when the algorithm was turned on. This algorithm was also able to separate two accidentally merged single photons that showed up as a shoulder.

C) Splitting of Peaks Inside a Group.

For multiple peaks (overlapping showers) in a group the peaks were split by the following chisquare minimization method:

$\chi^2 = \sum_i [P_i - \sum_j (E_j F_{ij})]^2$

Minimizing χ^2 we get,

$$\frac{\partial \chi^2}{\partial E_k} = 0 = (\sum_i P_i - \sum_j E_j F_{ij}) \cdot F_{ik} \rightarrow \quad \sum_j E_j \sum_i F_{ij} F_{ik} = \sum P_i F_{ik}$$

Setting $A_{jk} = \sum_i F_{ij} \cdot F_{ik} = A_{kj}$ and $B_k = \sum_i P_i F_{ik}$ the last equation is written:

$\sum_j E_j A_{jk} = B_k \rightarrow E_j = A_{jk}^{-1} B_k$

where, P_i is the energy in the ith strip, F_{ij} the fraction of energy in the ith strip due to the jth shower and E_j the true energy of the jth shower.

The energy of an individual shower was calculated by solving the previous equation. The corrected energy in the strip was calculated by subtracting the contributions of the neighboring showers from the actual energy in the strip, i.e.,

$$P_i^{correct} = P_i - \sum_k^{(j \neq k)} E_k F_{ik}$$

The position of the shower was calculated by using the $P_i^{correct}$ as input to a chi-squared minimization process.

D) Correlation of Gammas in r and ϕ view.

Showers reconstructed in r and ϕ views were correlated using their energy match ($E_r \simeq E_\phi$). The criterion used was:

$$\Delta X = \frac{|E_r - E_\phi|}{(0.1 + 0.14\sqrt{E_r + E_\phi})}$$

All r and ϕ combinations were searched and for multiple correlations the best match was taken. Showers that coalesced in one view but were separated in the other were split into two with the energy taken from the split view. The energy matching in two views was tried repeatedly, loosening the cut, starting with 1 unit of the expected fluctuation and increamenting it by 1 unit in successive iterations, up to six units. The iteration was stopped when the total uncorrelated energy in both views became less than 1.5 GeV.

5.7. Alignment of the LAC

Prior to the data run the LAC were carefully measured and positioned using the optical survey method. The results of this survey were used as initial values for the location of the detector. The position of the LAC was determined using

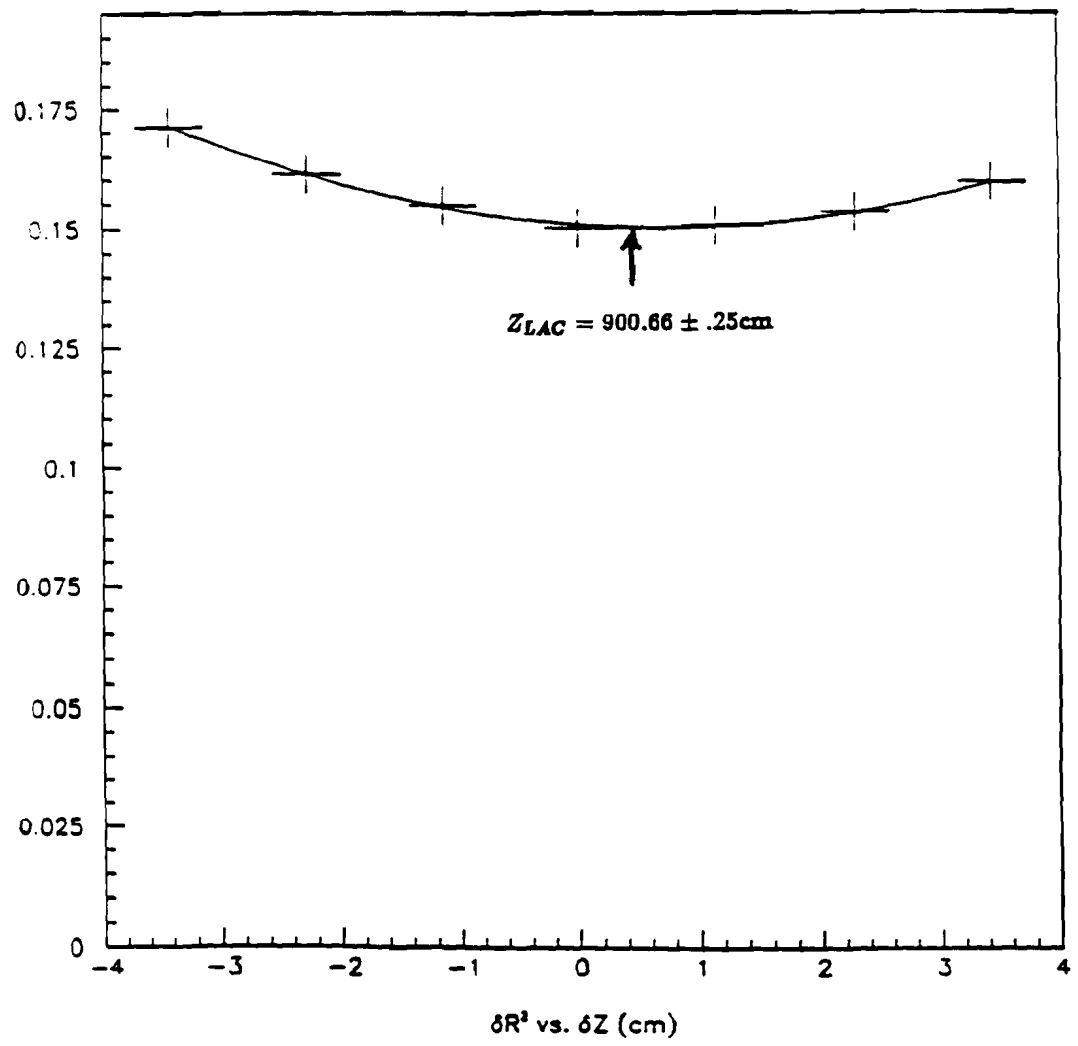

Figure 65: The width of the distribution of the distance between the EMLAC showers and PWC tracks for different z values of the LAC.

the reconstructed tracks projected on the LAC and the reconstructed showers in the LAC. The relative position of the EMLAC and the rest of the spectrometer was determined using the charged particle tracks. This was an iterative procedure based on minimizing the width of the distribution in the position differences tracks projected onto the calorimeter. The relative shifts of the LAC and PWCs were found to be independent of time. The z-position of the LAC (i.e., the front face of the EMLAC) was determined by assigning different z-positions for the LAC and by studying the width of the above distributions. Figure 65 shows the behavior of the width of the distribution of the distance between the EMLAC showers and PWC tracks for different z values of the LAC. The value of z that minimized the distribution was $Z_{LAC} = 900.66 \pm 0.25$cm.

5.8. Performance of the EMLAC

Figure 66 shows the ΔX and ΔY distributions between the EMLAC showers and PWC tracks. The obtained position resolution was $\sigma_x = 0.1$ cm and $\sigma_y = 0.1$ cm.

An electron or positron was found by searching for a track which struck the calorimeter near a reconstructed EMLAC shower. A distribution of the shower energy divided by the momentum of the track that hit closest to the shower was formed. The track was required to be within 1 cm of the shower and the E^{front}/E^{total} of the shower to be greater than 0.6 (hadron rejection). Figure 67 (top graph) shows the ratio of shower energy to track momentum. The peak near unity is a clear indication of an e^+/e^-, which deposited all of its energy in the EMLAC. The structure to the left of the peak is due to hadrons that did not

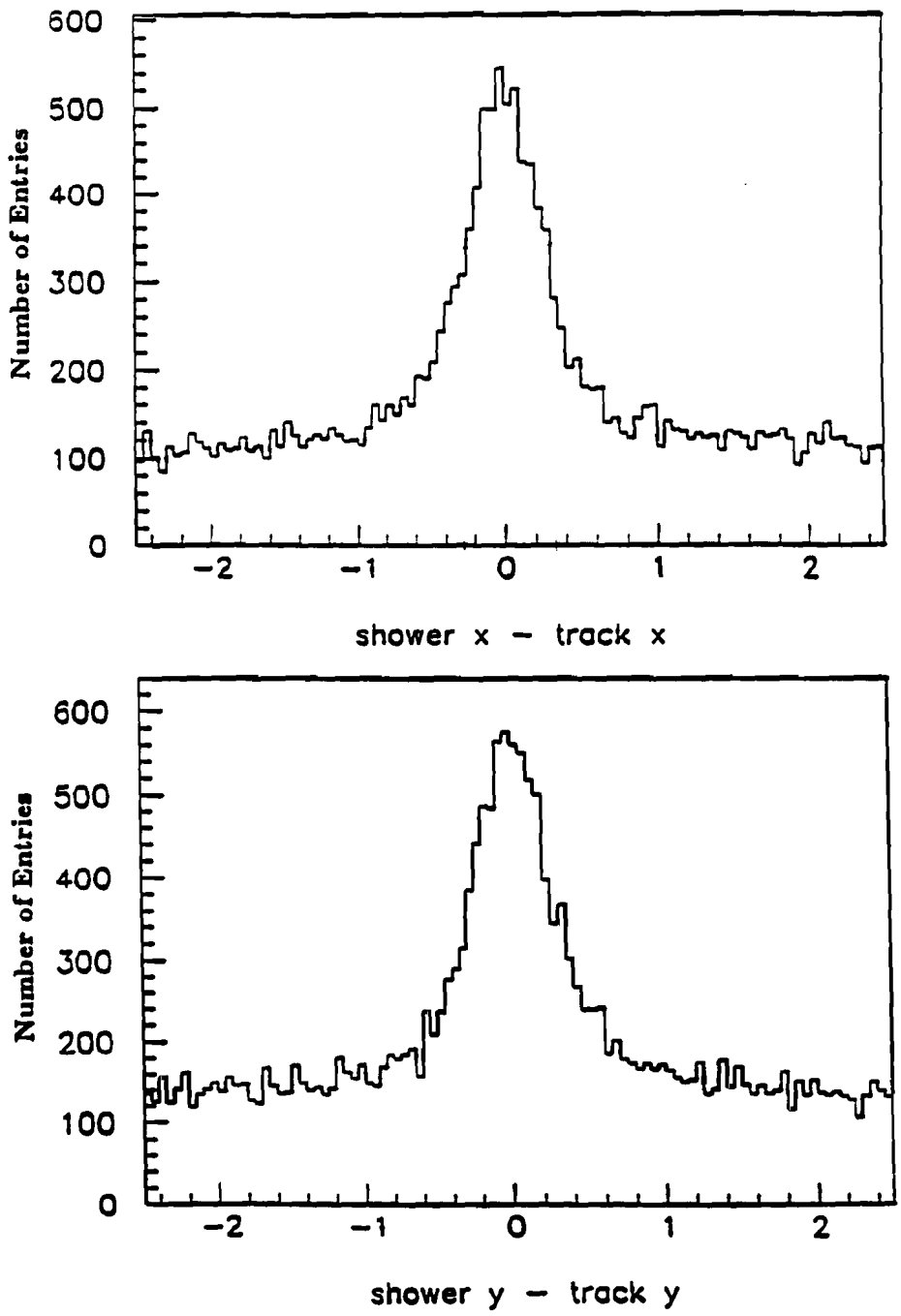

Figure 66: Position resolution of the EMLAC.

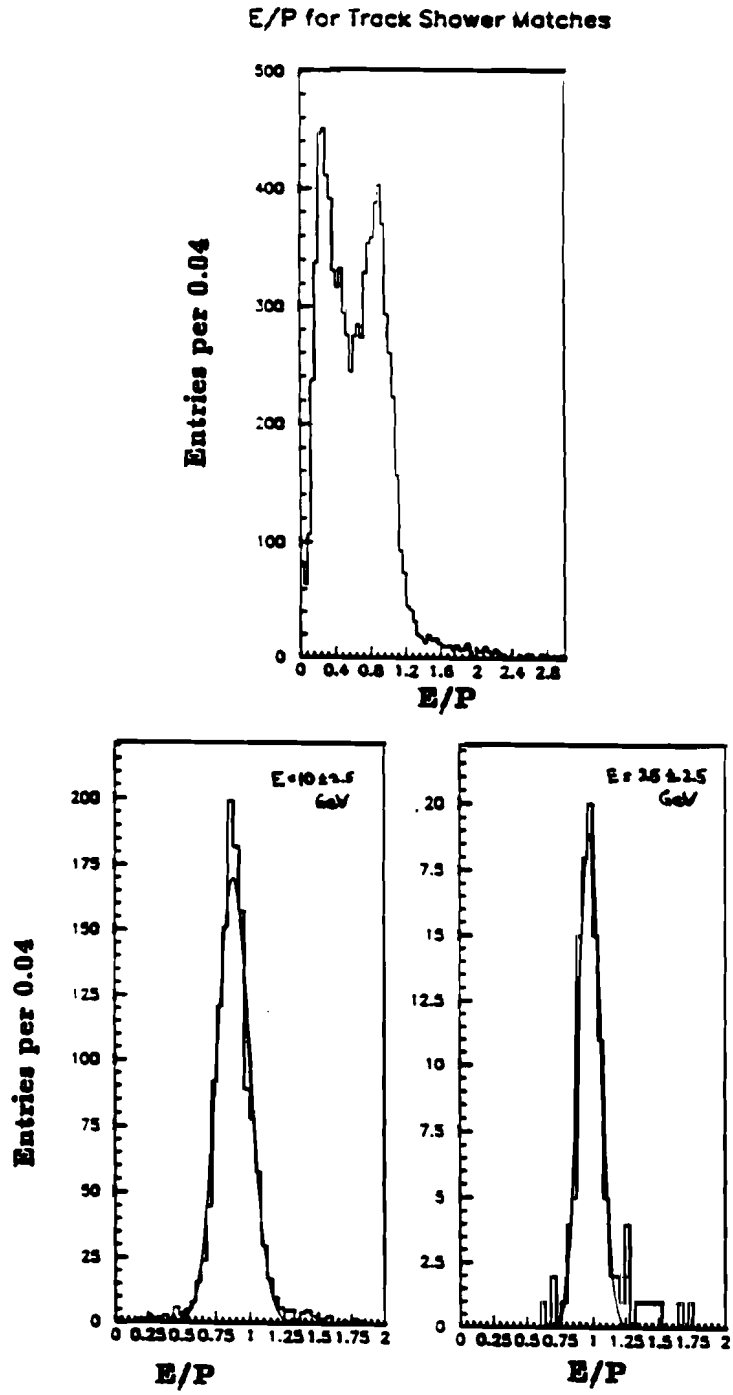

Figure 67: The ratio of shower energy to track momentum (i.e., E/P).

deposit all of their energy in the EMLAC.

Events with photon conversions were used to study the performance of the EMLAC. The "zero mass pairs" (see previous section) were used to study the behavior of the EMLAC to low energy electrons as well as to study its efficiency. Figure 67 (bottom graphs) shows the E/P distribution for tracks that belong to zero mass pairs and their associated showers, for two energy ranges. First we notice that most of the hadronic background has been eliminated. Second we notice that the energy scale for low energy electromagnetic showers is not consistent with the measured momentum.

Figure 68 shows the mean value of the E/P distribution versus the momentum of the incident e^+/e^-. The plots are shown for four different energy depositions in the back section (0, 1., 1.5, and 2. GeV). The E/P deviation from unity, at lower energies, is at least partially due to the loss of the low energy shower tail in the back section of the detector. This loss is due to the zero suppression window and the amplifier fluctuations.

5.9. Hadron Shower Reconstruction (HCREC)

This section describes the program which was used by the E-706 Group to reconstruct and analyze hadron showers in the LAC.*

First we will explain how the Hadron Reconstruction program works. Then we describe the code used to match the showers reconstructed in the EMLAC with

* The data obtained from the Hadron Calorimeter were used in the final data analysis to reconstruct neutral showers. HCREC reconstructs both neutral and charged particles and the distinction between them is done only when the LAC reconstructed data are compared with the reconstructed tracks from the magnetic spectrometer.

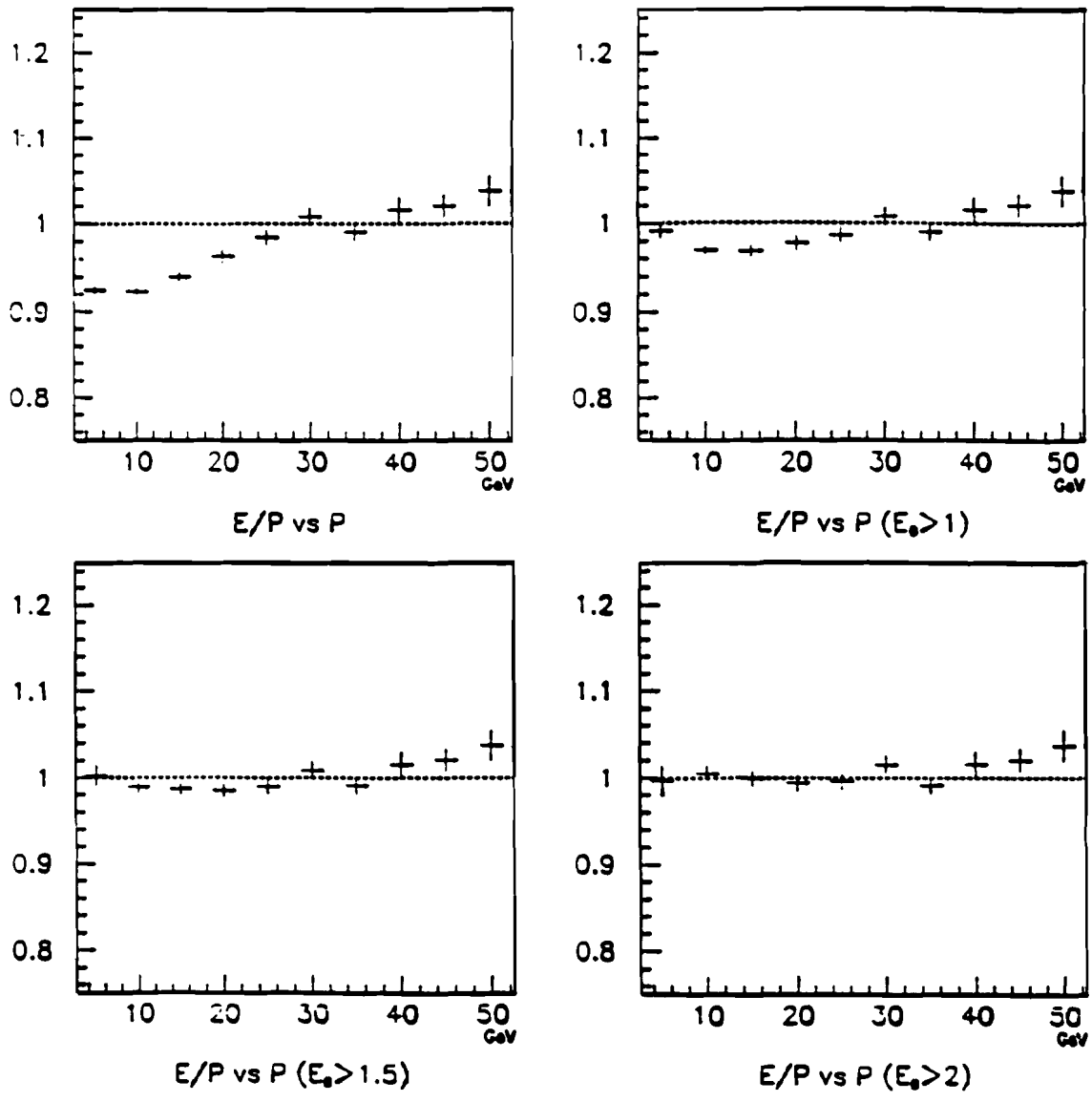

Figure 68: The mean value of the E/P distribution versus the momentum of the incident e^+/e^-. The plots are shown for four different energy depositions in the back section (0, 1., 1.5, and 2. GeV).

the showers reconstructed in the HALAC to form the final reconstructed hadronic showers. Finally, we present results from the reconstructor testing done with the E-706 Monte Carlo package, the calibration data and the physics data.

5.9.1 Description of Hadron Reconstruction

The purpose of the hadron reconstruction program is to find hadrons and to calculate their energies, their positions, and from front/back correlation their directions. This is done from information contained in the "raw sorted data input banks" and the Electromagnetic Calorimeter "photon banks". The program can be divided into six logical steps:

A) Group input data in energy clusters

B) Loop through the clusters to subdivide them into hadrons

- B1) Reconstruct one hadron per cluster
- B2) Extract more hadrons per cluster
- B3) Reconstruct the Isolated Pads

C) Calculate energy and position of hadrons

- C1) Resolve neighboring hadrons

D) Correct reconstructed energy for shower tail loss

E) Correct reconstructed energy for the e/h effect

F) Fill the output hadron banks

The Hadron reconstruction package tried to identify hadron showers mainly according to their distribution in a group of pads. A typical shower was expected

to deposit its energy in the so called area of the 'three overlapping hexagons'. This area spanned 13 pads. There were two "overlapping hexagons" schemes depending on the up/down orientation of the center pad. The two schemes are shown in Figure 69. In this scheme we defined three types of pads neighboring the center pad. The neighbor classes and their respective pad numbers were as follows:

1st neighbors : 1 , 2 , 3

2nd neighbors : 4 , 5 , 6

3rd neighbors : 7 , 8 , 9 , 10 , 11 , 12

During the description of the reconstruction program which follows all the numeric values of the reconstruction parameters are printed next to the parameter when the parameter is introduced. All parameters have been "fixed" from calibration data and extensive Monte Carlo studies.

A) Group input data in energy clusters

A cluster (or patch) was defined as an area spanned by pads with non-zero energy (energy above threshold) and sharing common sides. The program searched the sorted input data banks for neighboring pads. Two pads were considered to be neighbors if they shared a side, i.e., if their IROW or ISLA numbers differed by ± 1 (+ for UP starting pad, − for DOWN). The pad grouping process started from the pad at the very top of the input data list and found its neighbors, working its way down. Then it looked for the neighbors of the first neighbors and so on. At the end the pads were grouped in patches. Figure 63 shows two examples of patches. Notice that pads 272 and 653 do not belong to these patches. By sorting

the raw data, the time to group pads was significantly reduced. The minimum number of pads required to form a patch was MINPAD (=2). All the pads that did not satisfy this requirement were stored in the ISOLATED PAD BANK.

B) Loop Through the Clusters and Subdivide them into Hadrons

The patches were examined if the energy distribution in it was consistent with the expected energy distribution from one of hadron. If this was true then the energy of the hadron was calculated from the energies in the pads of the patch.

In the following description of the reconstruction program, a global energy threshold and a local energy threshold cut were applied:

i) Each pad energy should exceed EGLOB (=2 GeV).

ii) The pad with the maximum energy in this patch should be over ETHRES (=5 GeV).

The energy was summed over the front and back sections of the hadron calorimeter and the FRONT/BACK information appeared in the final output physics bank.

B1) Reconstruct One Hadron Per Cluster

We do not go directly into a more detailed and complicated reconstruction process because the topology of the majority of the hadron events is relatively simple, in the sense that a patch corresponds to one hadron only. By trying to identify these "simple" events at the very beginning, we reduced the average reconstruction time without losing any information about the reconstructed hadrons.

One hadron was reconstructed per patch if the patch satisfied the following three requirements:

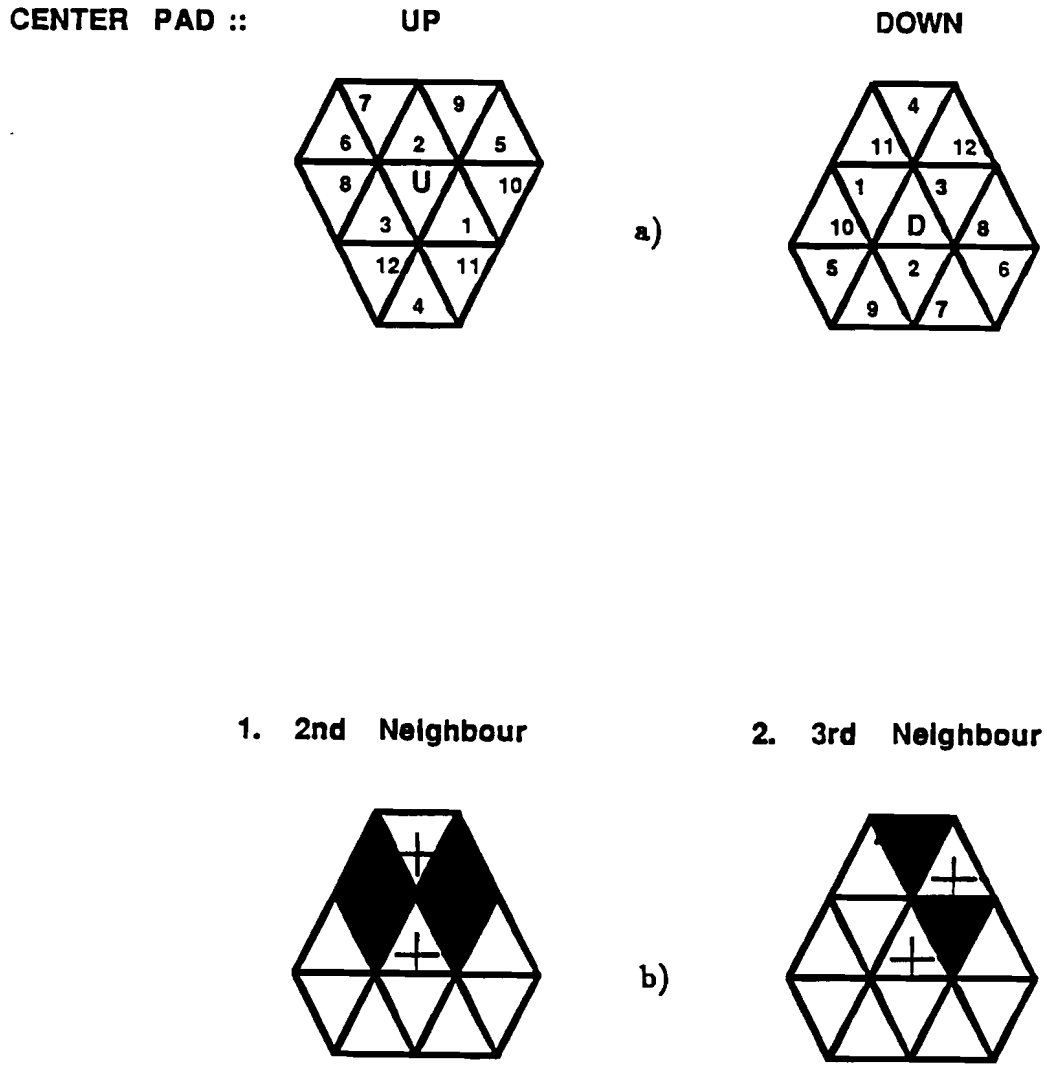

Figure 69: a) The two 'overlapping hexagons' schemes. b) The common pads of two neighboring maximum energy pads (see text). The blackened pads denote the common pads of the two hadrons. The crossed pads are the two maximum energy pads.

i) The pad population in this patch (despite any cut) was below MAXPAD (=12).

ii) There were no more than MINEFR (=3) pads with a fraction EFRAC (=0.4) of the maximum energy pad. If the energy of the maximum pad in the patch was close to the threshold (i.e., < 7 GeV) then MINEFR was set to a higher number.

iii) The energy distribution in the patch should have a non-negative "gradient". The energy "gradient" had the following meaning. When there was only one hadron in the patch, the energy deposited in the pads surrounding the maximum pad should decrease in value. The energy distribution over the pads was checked as follows; a) There were, at most, 12 pads surrounding the pad with the maximum energy. The energy of each of the remaining pads in the patch (i.e., the pads not included in the 12 neighbors) should be less than the average energy in the 12 pads. b) The energy of the 2nd and 3rd neighbors in the patch should be less than the average energy of the 1st neighbors.

If one hadron was reconstructed from the patch and if the number of pads in the patch was less than NSMPCH (=8), we examined the ISOLATED PAD BANK and tried to extract low energy pads that were close to the patch (but not close enough to be part of the patch during the clustering phase). It was found (from GEANT and calibration studies) that most of the low energy isolated pads that were close to a reconstructed hadron were part of it. They appeared as isolated because the energy deposited in the pad between the isolated pad and the pads of reconstructed hadron was below the readout threshold. The percentage of the reconstructed hadrons that included isolated pads neighboring a patch was $\sim$7%.

If the above three requirements were satisfied, the program proceeded to the

calculation of the physical properties of the hadron. If one of the requirements was not satisfied, then the patch was examined more carefully as explained in the following section.

B2) Extract more Hadrons per cluster.

When a patch has only one energy peak the reconstruction is relatively easy. This is not always the case.

Even though the lateral fluctuations of the hadronic shower were very large there were two shower characteristics that were applicable to the great majority of the showers. About 90% of the shower energy was contained in the three overlapping hexagons area with the peak pad at the center. In Figure 63a 'three overlapping hexagons' areas are displayed. The U and D pads are the center pads, which are the only common pad to three hexagons. About 50% of the shower energy is typically contained in one pad or shared by two pads.

Taking these general characteristics into account we established the following procedure: The 'three overlapping hexagons' area was searched around the peak pad. If any 2nd or 3rd neighbor pad had energy greater than the average energy of the 1st neighbors then this pad was not counted (since this energy variation was probably due to a neighboring hadron).

Due to the high readout threshold ($\sim$ 3.0 GeV) the reconstructed hadrons from the physics data were more isolated than the ones reconstructed from the Monte Carlo data. In 4% of the total cases more than one hadron was extracted from a patch.

B3) Reconstruct the Isolated Pads

All pads in the isolated pad bank were reconstructed if their pulse height was above ETHRES (=5 GeV). The energy of the reconstructed hadron was the same as the pad energy and the reconstructed position was the same as the center of the pad.

C) Calculate Energy and Position of Hadrons

The energy and the position of each hadron was weighted according to the following formulas:

$$E_{hadron} = \sum_i (E_i^{front} + E_i^{back})$$

$$X_{hadron} = \frac{\sum_i X_i (E_i^{front} + E_i^{back})}{\sum_i (E_i^{front} + E_i^{back})}$$

$$Y_{hadron} = \frac{\sum_i Y_i (E_i^{front} + E_i^{back})}{\sum_i (E_i^{front} + E_i^{back})}$$

where X_i, Y_i, E_i^{front}, E_i^{back}, are the x(center), y(center), front energy and back energy of the ith pad, respectively. The position information extracted from the back section of the calorimeter was used in the calculation only if the energy deposited in the back section was significant (> 5 GeV).

C1) Resolve Neighboring Hadrons

Neighboring hadrons were searched for within a patch. A typical single hadron energy distribution consisted of a well defined energy maximum close to the shower centroid and then an exponentially decreasing energy distribution around the energy peak. Taking into account the pad size, the shower size and the expected

fluctuations, it was found that deviations from the above described energy pattern were not significant. The program called the hadron resolving subroutine in the case that there was a 2nd or 3rd neighbor pad that had energy greater than the 1st neighbor pad.

The energy sharing algorithm was used only between hadrons with their maximum energy pads contained in the same "three overlapping hexagons area". The reason was that the lateral energy shower distribution formula [71] indicated that the energy correction to these hadrons would be very small for distances between them greater than the pad side (= 12.48 cm). A set of common pads was defined according to the positions of the two maximum energy pads (i.e., the two neighboring hadron candidates) in the 'three overlapping hexagons' area. Only two maximum energy pads were considered. An example of the common pads of two neighboring maximum energy pads (i.e., hadron candidates) is shown in Figure 69b. The common pad energy sharing between the hadrons was calculated using the lateral shower shape [71]. The goal was to find what fraction of the energy of each common pad i (i=1,...,4 or i=1,2) belonged to the hadron with the maximum energy pad (possibly the most energetic hadron of the two). This fraction a was defined as :

$$a(i) = \frac{Q1(r1_i)}{Q1(r1_i) + Q2(r2_i)}$$

where Q(r1) and Q(r2) are the lateral shower distribution for the two neighboring hadrons. The subscript 1 refers to the hadron with the maximum energy pad, $Q1(r1_i) = e^{-5} \cdot e^{-r1_i/a1} + e^{-r1_i/a2}$ where,

a1 = c1 + z·c2

a2 = 7·a1

c1 = .4

c2 = $.25/\sqrt{e}$

$r1_i$ = Distance from the center of gravity of the common pad i to the hadron number 1

$r2_i$ = The same for the second hadron

e = incident energy of hadron with the maximum pad, in GeV

z = z-axis coordinate for the effective location of all showers in the HALAC as measured from the front of the first HALAC absorber plate.

Here the only parameter we had to fix was z. We wanted the z that gives the best position resolution. Figure 70 shows the z value that minimizes the ratio $\Delta R^{after}/\Delta R^{before}$ (z_{min}= 10.25), where ΔR^{before} and ΔR^{after} are the position resolutions before and after the application of this algorithm, respectively.

The position and energy of each hadron were corrected according to the common pads energies assignments, by the use of the weighting method.

D) Correction of Reconstructed Energies for Shower Tail Losses

As it was mentioned in the LAC Calibration Chapter, the reconstructed energy of a hadron was affected by the readout threshold (or zero suppression window). During the physics run, the readout threshold was varied between 2.5 GeV and 4.5 GeV. In the reconstruction procedure, an average value for the window was used. It was 3.1 GeV. The effect of the window on the reconstructed energy of the

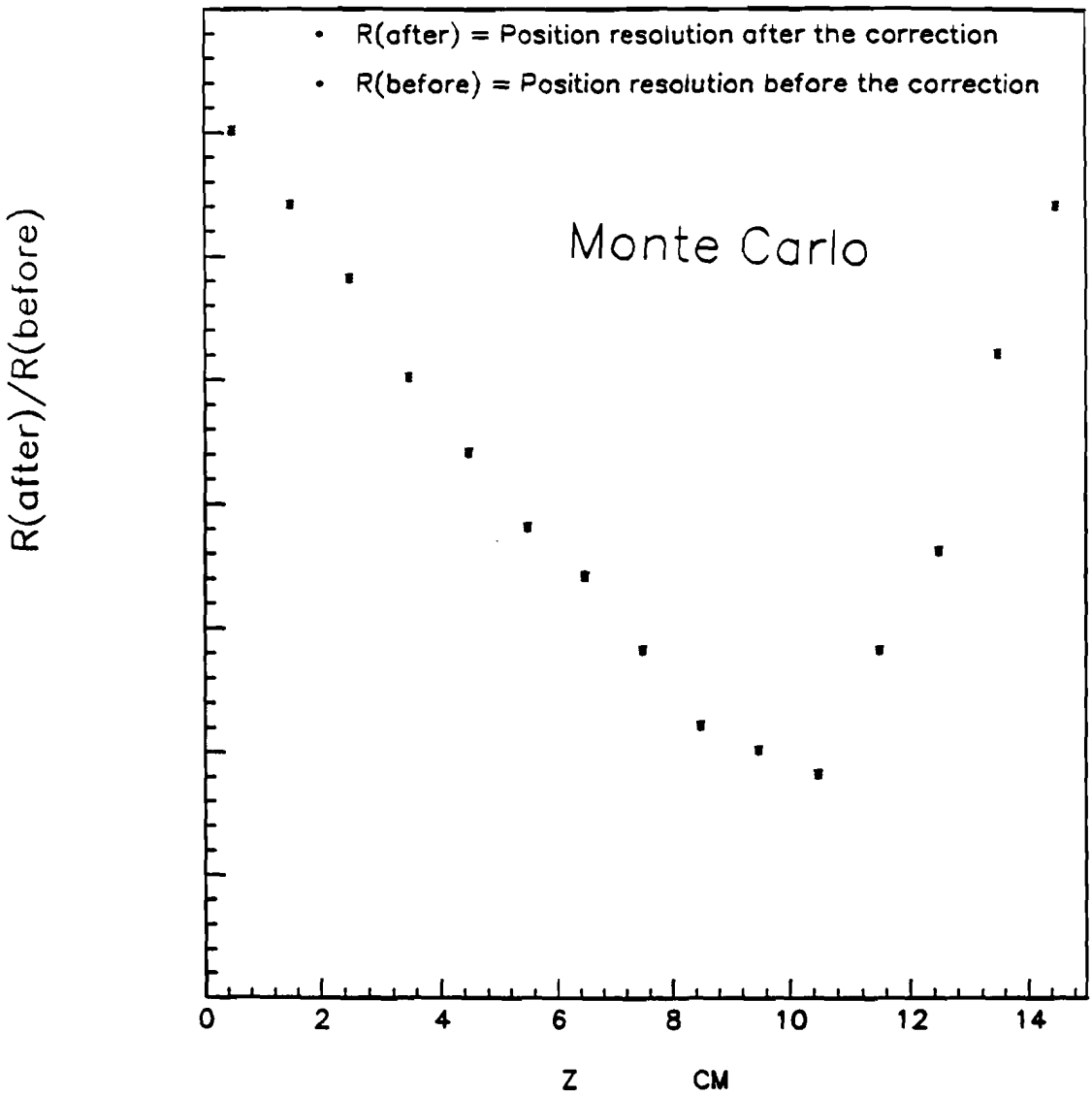

Figure 70: The z value, in cm of Fe, that minimizes the ratio ΔR^{after} / ΔR^{before} (z_{min} = 10.25 cm) (see text).

hadrons was studied using calibration data when the zero suppression was turned off. The effect of the window was simulated by applying different thresholds and then calculating the reconstructed energy (see the Chapter 4). Finally, the energy of each reconstructed hadron was corrected according to the function obtained by fitting the zero suppression curve:

$$E^{Corrected} = E^{had} \cdot (\frac{100}{z_1 \cdot Z^{z_2}})$$

where, $z_1 = 115.74$, $z_2 = -0.2833$ and Z = 3.1 GeV

E) Correction of Reconstructed Energies for the e/h Effect

The Hadron Calorimeter has a different response to the electromagnetic and hadronic showers. The consequence is that the measurement of the energy of a hadronic shower depends on the fraction of the e.m and purely hadronic components in the shower. The method used to correct the reconstructed energy for this effect is explained in the LAC Calibration Chapter, Section 4.6.1b.

5.9.2 HALAC - EMLAC Correlation

In the LAC a fraction of the hadronic showers starts in the electromagnetic calorimeter section and then develops in the following section. The incident energy is thus shared between the two different types of calorimeter. Therefore, to reconstruct the hadronic shower, we must know not only the response of the hadronic section alone, but also that of the combined calorimeter. Since the electromagnetic calorimeter was calibrated with mainly electromagnetic showers, the way to add hadronic signals from both the detectors was not clear *a priori*.

The response of the HALAC to pions, with and without taking into account the EMLAC in front of it, was presented in the previous chapter (Section 4.6.3). The response of the EMLAC to electrons has already been presented (see Section 4.6.4). Next I discuss the method used to combine the outputs of the two reconstructors (EMREC and HCREC) to form hadrons.

First the hadronic energy deposited in the EMLAC was extracted and added to the hadronic energy found in the HALAC. All the information concerning hadronic showers extracted from the EMLAC was regarded only as improvement to the information from the HALAC. We did not to define new hadrons or even drastically change the hadronic shower data already found in the HALAC, as a result of the EMLAC information. The HALAC - EMLAC correlation program served mainly two purposes:

a) Identified the hadronic energy deposited in the EMLAC (used as a complementary criterion to the E^{front}/E^{total} cut in the EMLAC).

b) Improved the energy and position resolution of hadrons and also provided additional information about the directionality of the hadron tracks (especially the neutral hadrons).

The procedure to combine the output data of the two reconstructors was the following:

i) The position(in the X-Y plane) of energy clusters found in the HALAC was projected on the front face of the EMLAC, taking into account the focusing. We simply assumed that the hadron was fully contained in a circle centered at the shower centroid and spanned an area πr^2 where the radius r was defined by the parameter RMIN (= 7.5 cm).

ii) The next step was to add all the energy found in the above described area of the EMLAC to the hadron energy found in the HALAC. This was done only if the fraction of the energy deposited in the front section of the EMLAC to the total energy deposited in the EMLAC was less than 0.6.

The energy of the matched showers from the two calorimeters was combined as described by Eq.(4.10).

5.10. Performance of Hadron Shower Reconstructor

Figure 71 shows a multi-hadron event (from the positive beam data) in the front section of the hadron calorimeter. Only the pads with energy more than ~5 GeV are shown. The circles and crosses indicate the positions and energies of the reconstructed showers (the radius of the circle corresponds to 10 GeV). The small crosses indicate projected PWC tracks on the front face of the HALAC.

The hadron reconstructor was tested with multi-hadron events generated with ISAJET and the GEANT code. This Monte Carlo simulation was important for three main reasons:

i) Code debugging.

ii) Studying and understanding the detector behavior and acceptance for hadrons.

iii) Fixing the program parameters and cuts.

The ISAJET package was used as an event generator. Only the hadrons produced from the proton - proton interaction were submited as an input to GEANT (the particles that shower electromagnetically, i.e., γs, e^-s, and π^0s, were ignored).

Figure 72a shows the ratio of the total energy reconstructed by the HALAC over

Figure 71: Picture of a multi-hadron event (from the positive beam data) in the front section of the hadron calorimeter.

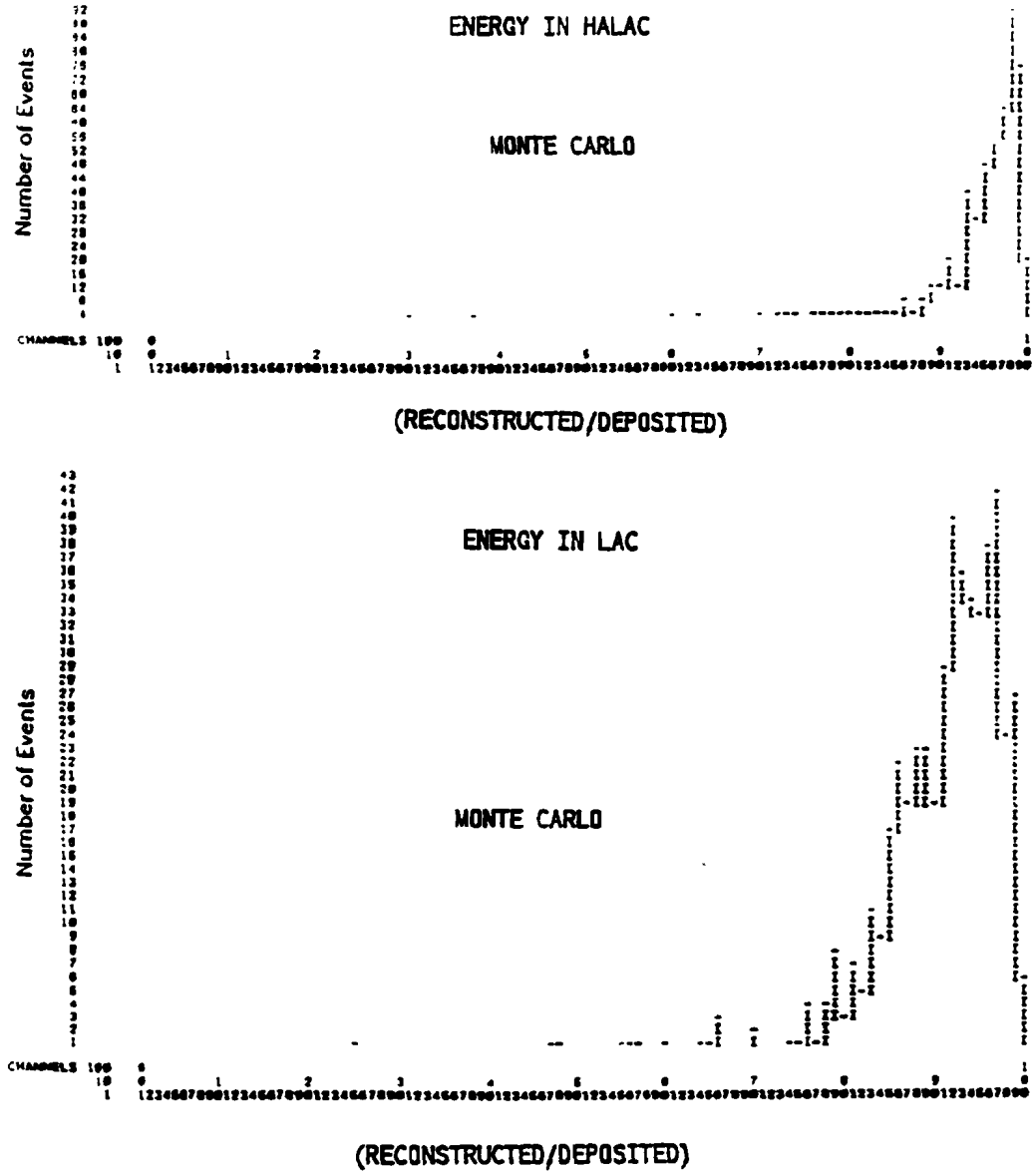

Figure 72: (top): The ratio of the total energy reconstructed by the HALAC over the total energy deposited in it. (bottom): The ratio of the total energy reconstructed by the HALAC plus the EMLAC over the total energy deposited.

the total energy deposited in it. On the average 95% of the deposited energy was reconstructed. Figure 72b shows the same ratio for the hadronic energy deposited in the whole LAC. The average reconstructed energy was 91%. The value of the ratio is lower than before because the deposited energy in the EMLAC is reconstructed (as being part of the hadronic shower) only if the particle deposits part of its energy in the HALAC. The low energy hadrons that stopped in the EMLAC were not taken into account in these tests.

The performance of the reconstructor with the online data is presented below.

A) Position and Energy Resolution of the HALAC

Figure 73 shows the radial distance between showers reconstructed in the HALAC and the EMLAC. The reconstructed position in the HALAC was projected on to the front face of the EMLAC. Only the radial distances, ΔR, between the closest HALAC and EMLAC showers with $E^{front}/E^{total} < 0.5$ in the EMLAC, were plotted. Only the showers in the three opposite octants from the trigger octant were used. Figure 73 also shows the difference between the x and y coordinates of the showers reconstructed in the HALAC and the EMLAC.

Figure 74 shows the ΔX, and the radial distance between all showers reconstructed in the HALAC and the closest PWC track. The data were taken from a sample of high p_T events. The position resolution of the HALAC was determined to be 2.5 cm in X and 3.0 cm in the Y for all hadronic showers. This difference in X and Y was due to the fact that the HALAC's lateral segmentation was not symmetric in x-coord and y-coord.

Figure 75 shows the distribution of the shower energy divided by the momen-

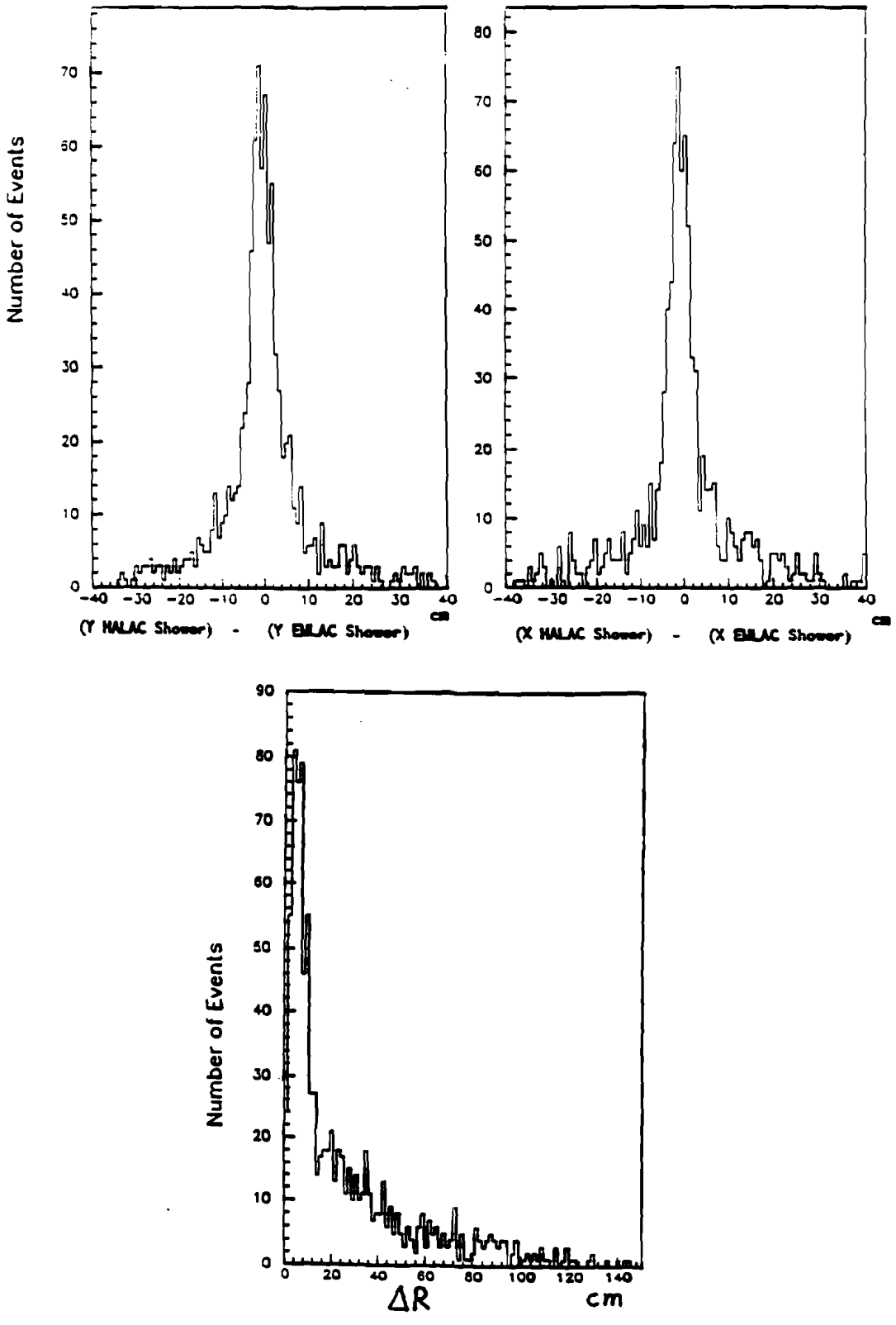

Figure 73: Distances between the showers reconstructed in the HALAC and the EMLAC.

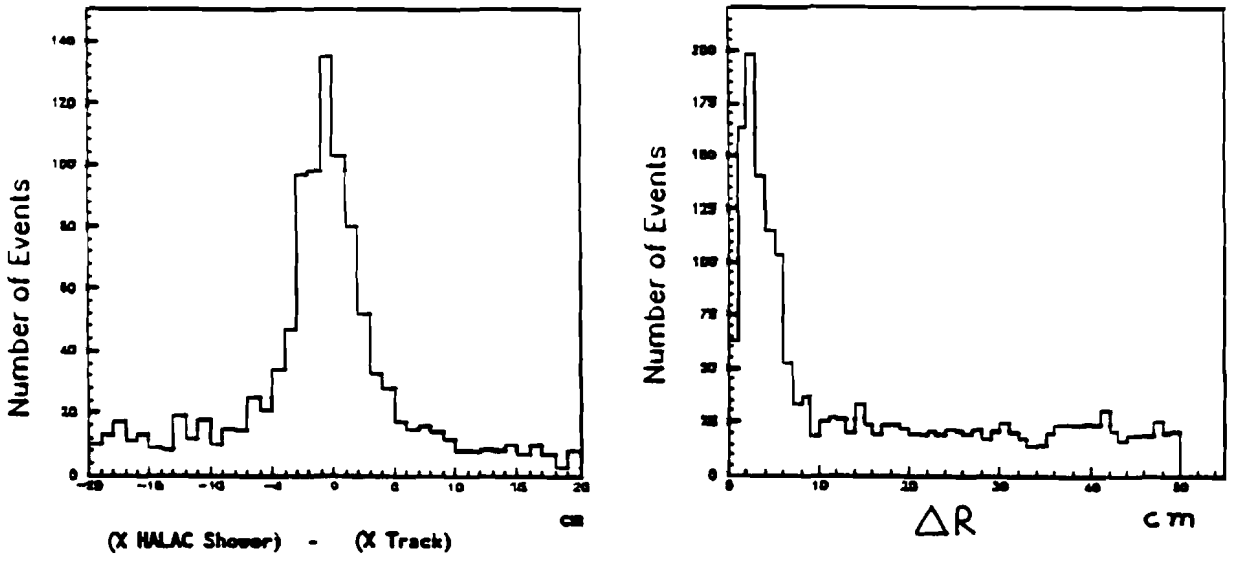

Figure 74: Distances between the showers reconstructed in the HALAC and the tracks.

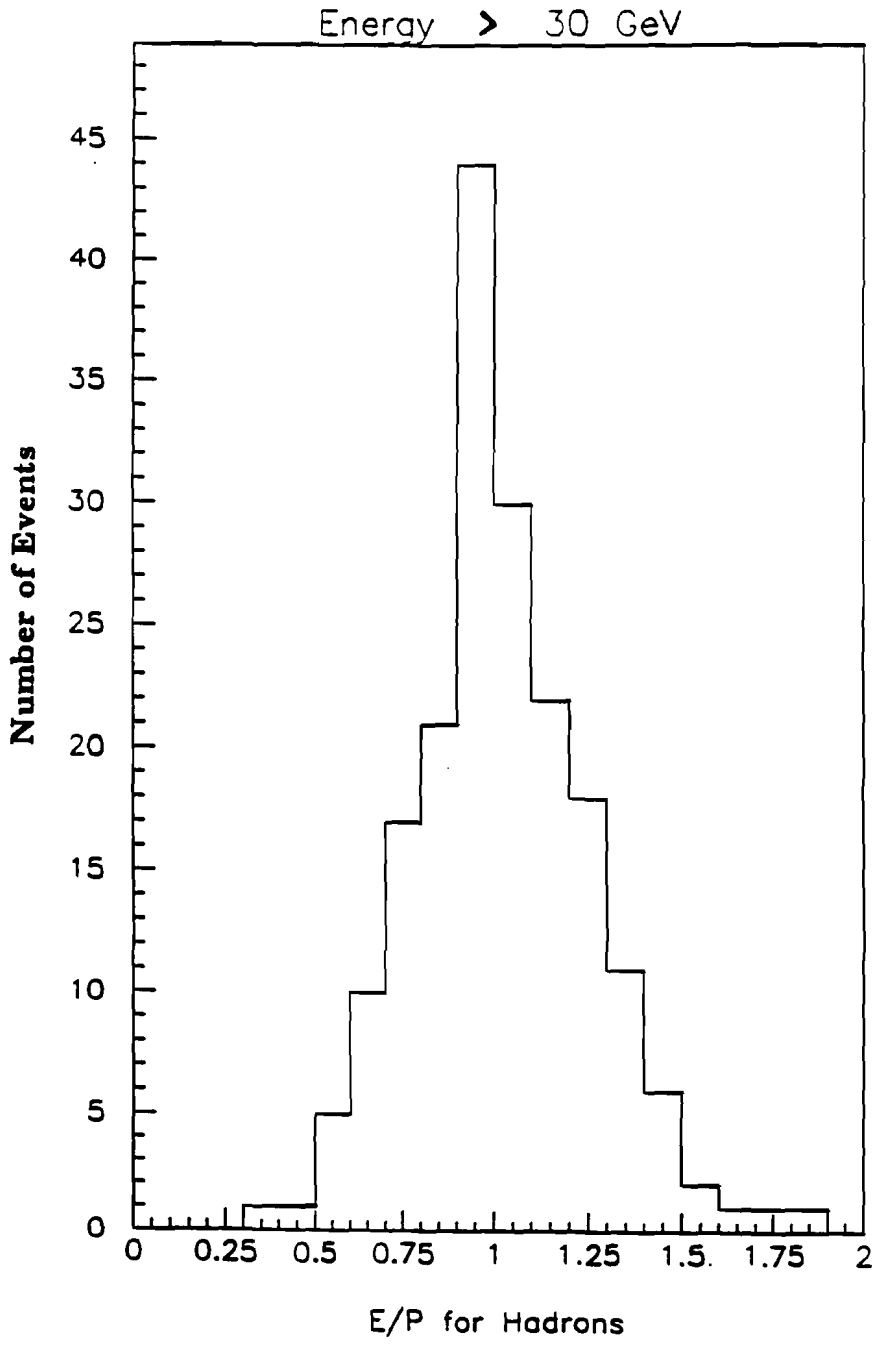

Figure 75: The distribution of HALAC energy divided by the PWC momentum of particles. The maximum allowed radial distance between the showers reconstructed in the HALAC and the tracks is, $\Delta R < 10.$ cm.

tum of the track for the reconstructed energy of particles and their reconstructed momenta for matched showers and tracks ($\Delta R < 10$ cm). In these events it was required that there was no energy deposited in the EMLAC in front of the hadronic shower ($\Delta R > 10$ cm). Assuming a momentum resolution of $\frac{\delta p}{p} \sim 0.1$P (P in GeV/c) for the tracking system, and measuring the sigma of the E/P distribution to be 0.35 the energy resolution of hadronic showers is estimated to be consistent with the LAC calibration measurements (i.e., $\sim 180\%/\sqrt{E}$).

B) Efficiency of Hadron Identification

The charged hadron detection efficiency of the LAC was measured using high quality reconstructed tracks from the physics data. The tracks were reconstructed using data from the magnetic spectrometer. In this study we did not distinguish between hadrons and electrons. The fraction of electrons in the sample was estimated from the E/P plot of the matched tracks and electromagnetic showers. This fraction was 15.0% $\pm$5.0% , 10.0% $\pm$3.0% and 4.7% $\pm$1.0% for particles with energies around 10 GeV, 15 GeV and over 20 GeV, respectively.

All tracks were selected from events that satisfied the following requirements:

a) One reconstructed vertex.

b) No veto wall hit from either set of veto wall counters.

c) At least one reconstructed electromagnetic shower had $p_T > 3.5$ GeV/c with no charged track pointing to it. Its directionality (directionality is defined in Section 6.1) should be less than 0.4 cm and the E^{FRONT}/E^{TOTAL} ratio greater than 0.3.

d) The charged track multiplicity was ≤ 35.

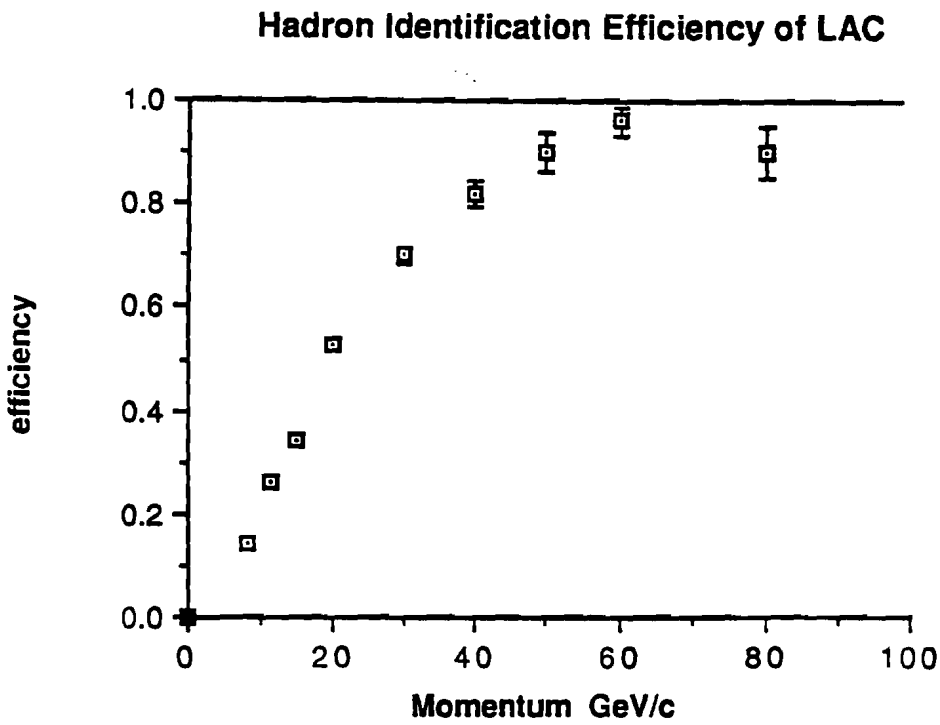

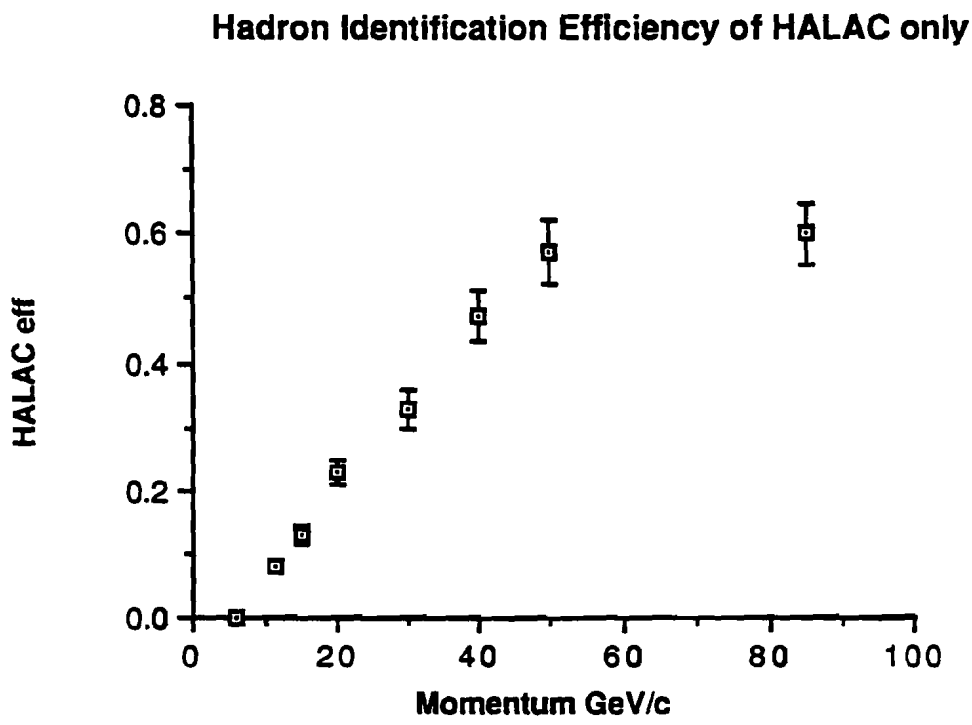

Figure 76: (top): Calculated hadron identification efficiency of LAC. (bottom): Hadron identification efficiency of the HALAC.

The high quality tracks were selected, from the above event sample, according to the following criteria:

a) All tracks should point well within the LAC acceptance so that LAC boundary reconstruction inefficiencies are negligible: 145 cm $> R_{track}{}^{LAC} >$ 29 cm, where $R_{track}{}^{LAC}$ is the radial distance of the point the track intercepts the front face of the EMLAC. Tracks pointing to the quadrant boundaries are rejected.

b) The χ^2/DOF of the track should be less than 1.5.

c) The downstream reconstructed track links with an upstream track in the magnet within a window of 0.1 cm. The linking should be successful in both views. The tracks that had an 'extra link' as a 'best link' in any view were rejected from the sample.

d) The impact parameter of the upstream track in both X and Y views was less than 100 microns.

e) The selected tracks were isolated from other tracks. The isolation distance of the selected tracks from the closest track, when both tracks are projected on the front face of the EMLAC, was set to be greater than 7.0 cm.

The energy threshold in the EMLAC for each reconstructed photon was 2 GeV. In the HALAC a threshold was imposed on the channel with the maximum pulse height in a given cluster of channels. This cut was set at 5 GeV. There was also a cut of 2 GeV for all channels. No attempt was made to reject tracks pointing to known dead regions of the detector.

The efficiency curve was measured as follows: the tracks that satisfied the above criteria were grouped in six momentum bins. For each momentum range we looped over all reconstructed showers in the LAC (both detectors separately) and we

counted the tracks that struck the calorimeter near the centroid of a shower. The matching distance for tracks and HALAC showers was 12 cm and for tracks and EMLAC showers was 1.5 cm. The measured efficiency is defined as the fraction:

$$Efficiency = \frac{Number\ of\ tracks\ matched\ to\ showers}{total\ number\ of\ tracks\ in\ the\ momenta\ bin}$$

The accidental matching of tracks to showers is estimated from the radial distributions between the showers and tracks by fitting the background to the right of the peaks and subtracting it from the peaks (see Figure 74, right plot). The data (background subtracted) are plotted in Figure 76. Two quantities are shown. The efficiency of the LAC and the efficiency of the HALAC alone (i.e., ignoring any energy deposited in the EMLAC). The errors are statistical only and they are calculated according to the binomial distribution.

6. HIGHER LEVEL DATA ANALYSIS

This chapter describes the methods and cuts used to reduce the reconstructed data to the event sample used in the final analysis. The event sample presented in this thesis consists of all the data taken with the negative and positive beams in the period between January 10 and February 13, 1988.* After the primary analysis, the summary of the results was written to Data Summary Tapes (DST). The DSTs were used for the secondary analysis. The major background to high p_T single photon and π^0 events was caused by the muons in the beam halo. Hadrons produced from the interaction of the beam particles in the target was a secondary source of background. These events were rejected by several steps in the secondary analysis. The detail of this data reduction will be described in the following subsections.

6.1. Pre-selection of Events

The events from the primary analysis were classified and written onto separate tapes according to the requirements of the secondary analysis. Events meeting the following conditions were used:

i) The event trigger satisfied at least one of the following triggers; HI, LO, SINGLE LOCAL, TWO GAMMA (see Table 5 in Chapter 3). About 60% of the events recorded during the physics run satisfied these triggers.

ii) There was either one reconstructed photon (in the EMLAC) with p_T greater than or equal to 5 GeV/c or the sum of the p_T of any two photons was greater

* The E-706 collaboration decided to process only the data tapes it believed contained highest quality data. This data was taken within one and a half months of the end of the experimental run. Five million triggers were recorded during this period.

than or equal to 5 GeV/c.

iii) Neither of the two veto walls, overlapping with the trigger quadrant, fired. 10% of the high p_T events satisfied this condition.

About 1% of all the events after the trigger type selection, survived these two cuts. For some part of the analysis we used data from other classes of events when it was necessary, e.g., minimum bias events or muon triggered events or events containing triggers with p_T less than 5 GeV/c, etc.

6.2. Event Selection

The events which survived the pre - selection were written to the DSTs.

A series of cuts were applied to the events contained on the DSTs. The purpose of these cuts was to select the high quality triggers, above 5 GeV/c p_T. The events which survived the cuts were classified into the following two categories: a) events which included high p_T π^os. This class of events will be referred to as "π^o events"; and b) events which included high p_T single photons. This class of events will be referred as "single photon (γ) events". Sets a) and b) were further subdivided in two subsets each. One subset contained the events taken with positive beam and the other one contained events taken with the negative beam. The cuts and the event classification criteria, which are going to be described in detail in the following sections, were applied to the reconstructed data in two phases and their effect on the data is summarized in Table 12. The cuts listed in the table were applied to the shower in the EMLAC with the highest p_T only. If this photon failed any cut, the entire event was rejected.

A) Event Quality: Event selection requirements were imposed primarily to

A) Event Pre-selection Phase

	Type of cut	Events survived (: 1000)
A1)	LAC trigger	3000
A2)	Veto wall	~ 300
A3)	"Trigger"[1] $P_T \geq 5GeV/c$	~ 30

B) Background Suppression Phase[3]

	Type of Cut	Events Rejected (%)
	Requirements on Electromagnetic Shower Reconstruction output	
B1)	At least one shower recon. in the trigger octant	2
B2)	TVC's	13
B3)	Directionality	8
B4)	E^{FRONT}/E^{TOTAL}	6
B5)	Fiducial and Rapidity cut	15
B6)	Hadron or e^- cut	5
B7)	Uncorrelated Energy	4
	Requirements on Charged Tracking Reconstruction output	
B8)	One reconstructed vertex per event	8
B9)	Track multiplicity[4] $(0 < N \leq 35)$	14

C) Event Classification Phase

	Event Sample	Number of Events Survived[2]					
		$5. < P_T < 5.5$	$5.5 < P_T < 6.$	$6. < P_T < 7.$	$7. < P_T < 8.5$	$8.5 < P_T$	Max P_T GeV/c
C1)	Single γ (π^- beam)	497(516)	206(212)	141(141)	34(34)	6(6)	10.5
C2)	Single γ (p beam)	481(495)	160(171)	97(99)	17(17)	1(1)	8.5
C3)	π^0 (π^- beam)	1377(1416)	505(523)	231(237)	42(42)	3(3)	9.5
C4)	π^0 (p beam)	1412(1470)	499(520)	215(220)	36(36)	3(3)	10.2

[1]There is EITHER one reconstructed photon (in EMLAC) with P_T greater than or equal to 5 GeV/c, OR the sum of the P_Ts of any two photons is greater or equal to 5 GeV/c.

[2]In parenthesis is the number of events surviving all cuts except the ones applied to the particles recoiling from the high P_T single photon or π^0. These requirements are: a) At least one charged particle in the away hemisphere; b) the P_T of this particle is greater than 500 MeV/c.

[3] The fraction of events rejected by a particular cut is independent of the other cuts.

[4] The effect of this cut is not uniform over all runs. The biggest contribution (~10%) comes from a small number of runs.

Table 12: Number of events surviving various cuts.

suppress backgrounds in the single photon and π^0 samples. The same cuts were applied to both event samples (i.e., single photon and π^0).

B) Event Classification: These cuts were applied in order to classify the events into either the "π^0 events" or the "direct γ candidate events".

Only the events that satisfied the following four LAC triggers (see Table 5 of Chapter 3) were selected in this phase: HI, LO, SINGLE LOCAL, TWO GAMMA. About 60% of the total number of events satisfied one of these triggers. Some studies required using events selected with other trigger types, for example, the minimum bias studies required the INTERACTION triggers only. Only events which were triggered by either a single γ with $p_T \geq 5$ GeV/c or a π^0 or η with $p_T \geq 5$ GeV/c were used. Figure 77 (middle graph) shows the p_T distribution of the single photons having the highest p_T in each surviving event, called the maximum p_T photon in the following discussion.

The cuts grouped under the letter B were divided into three categories depending on their purpose. The first category included all cuts intended to improve the quality of the photon signal (event quality cuts); the second category included the cuts meant to reduce the muon background (muon background cuts); and the third to reduce the hadronic background (hadronic background cuts).

I) Event Quality Cuts.

The cuts listed in Table 12 which were used to improve the quality of the single photon events, are explained in detail below (the numbering scheme corresponds to that of Table 12).

◇ Fiducial cut (B5)

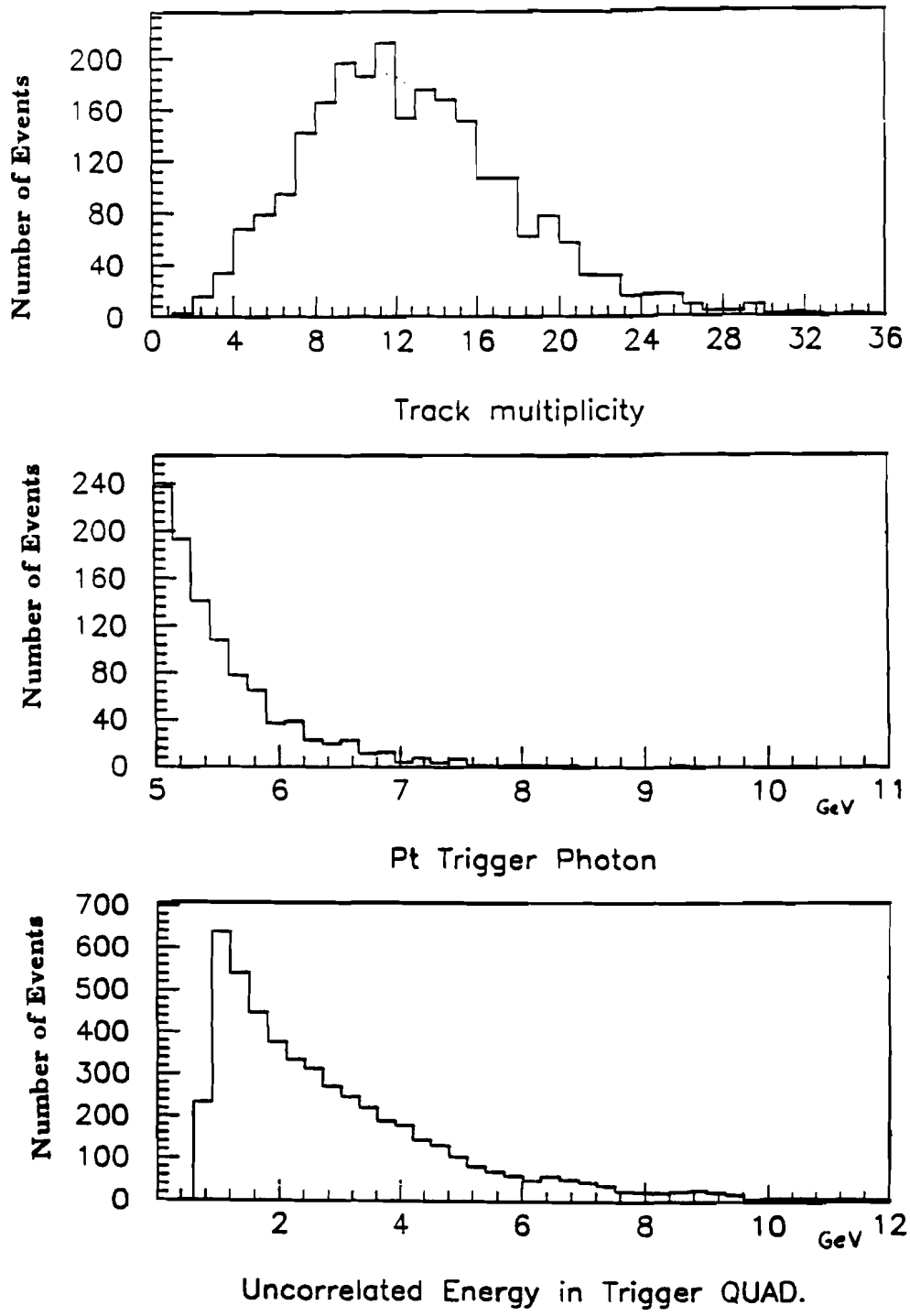

Figure 77: (top): The average track multiplicity per event. (middle): The p_T distribution of the single photons with the maximum p_T in the event. (bottom): The distribution of the uncorrelated energy per event per trigger quadrant. Only a fraction of the total data is shown. The distributions have not been corrected for trigger efficiency or detector acceptance.

The photon with the maximum p_T in the event was required to be incident within a fiducial boundary. The detection efficiency of π^0s was significantly lower around the edges of the colorimeter. The energy measurement of the single photons was also compromised. The centroids of the reconstructed photons were required to be at least 2.0 cm away from the inner edge (beam hole) and 22.0 cm from the outer edge.* In addition, the reconstructed photon was required to be away from the quadrant boundaries. Thus, the photon was required to reside within the following azimuthal angles:

$$\begin{array}{lll} 0.0492 \leq & \phi^{Max\ p_T\ photon} \leq & 1.5216 \quad (rad) \\ 1.6200 \leq & \phi^{Max\ p_T\ photon} \leq & 3.0924 \quad (rad) \\ 3.1908 \leq & \phi^{Max\ p_T\ photon} \leq & 4.6632 \quad (rad) \\ 4.7616 \leq & \phi^{Max\ p_T\ photon} \leq & 6.2340 \quad (rad) \end{array}$$

◇ Uncorrelated Energy (B7)

Uncorrelated energy in an EMLAC quadrant was defined as follows,

$$E^{UNCORR} = \sum(Cluster\ Energy) - \sum(Photon\ Energy)$$

It was required that the uncorrelated energy, in the quadrant where the trigger photon resided, be less than 10 GeV. Figure 77 (bottom graph) shows the distribution of the uncorrelated energy per event per trigger quadrant. This cut rejected two kinds of events: a) events where particles deposited energy in the LAC and the program could not reconstruct their energy, and b) events where the uncorrelated energy was due to channels which fired accidentally.

◇ One Reconstructed Vertex (B8)

* In the final data sample the highest p_T photon was restricted in the rapidity interval $|y| \leq 0.75$. This cut restricted the radial distance of the photons from the beam axis to be less than $\sim$ 123.0 cm (or 42.0 cm from the outer edge).

It was required that there should be one reconstructed vertex in the event. The vertex reconstruction efficiency was 90%. The vertex reconstruction code used in this analysis does not reconstruct secondary vertices.

◇ Track multiplicity cut (B9)

An upper and lower cut in the multiplicity of the tracks per event was set at $0 < N^{TRACKS} \leq 35$. The upper cut was set in the first pass of the raw data (the ACP pass), and it was implemented to serve two purposes:

a) Eliminate events where either the PWC planes or the SSD planes were noisy making the tracking system to be confused.

b) Force the tracking reconstructor (PLREC) to quit at track multiplicities higher than 35 tracks, thus saving computing time. Note that the average reconstruction time per event for PLREC is 6 sec on a Vax/3200 (compared to 800 msec for EMREC and 100 msec for HCREC).

Figure 77 (top graph) shows the average track multiplicity per event after these cuts.

II) Muon Background

A description of each cut in this category is as follows:

◇ Veto Wall Cut (A2)

This cut reduces the background from particles produced far upstream of the target which were moving parallel (or within a small angle) to the beam axis, but offset by 1/2 to 2 meters. In the calculation of the p_T of a particle it is assumed that it comes from the target region. Thus, the production angle is systematically

overestimated for particles moving parallel to, but displaced from, the beam. This class of events appears to have large p_T and contaminates the single photon trigger.

This cut was a software implementation of the veto wall in the trigger. The veto wall consisted of two planes of scintillation counters upstream of the target. If the part of the veto wall that overlapped the quadrant(s) in which the trigger particle resided had a hit in either plane between time ticks 1 and 15 inclusively, then the event was rejected.* In the data acquisition, a veto wall signal was generated to veto the event when there was at least one hit in both veto walls within ± 80 nsec from the interaction. This implementation of the veto in the trigger was not strong enough to entirely eliminate the muon contamination in the single photon trigger. The software veto used required only one hit in two veto walls while the trigger required a hit in each plane.

◇ TVCs Cut (B2)

The TVCs (Time to Voltage Converters) received the sum of the outputs of four adjacent amplifiers of the EMLAC. Their function was to produce a voltage proportional to the time between the beginning of the LAC pulse and the trigger "event"** signal. This made it possible to measure the arrival time of energy in the detector relative to the trigger pulse. The timing resolution was $\sim$ 9 nsec.

◇ Directionality Cut (B3)

The directionality cut is based on the angle of arrival of a particle at the LAC. The incident angle at the LAC for photons produced in the target differed sig-

* The time ticks run from 1 to 15 and they are synchronised with the accelerator clock. The beam bucket reaches the target region at time tick 8.

** If the trigger has been satisfied sends an "event" signal to the BAT instructing it to generate a sample and hold signal for each LAC amplifier

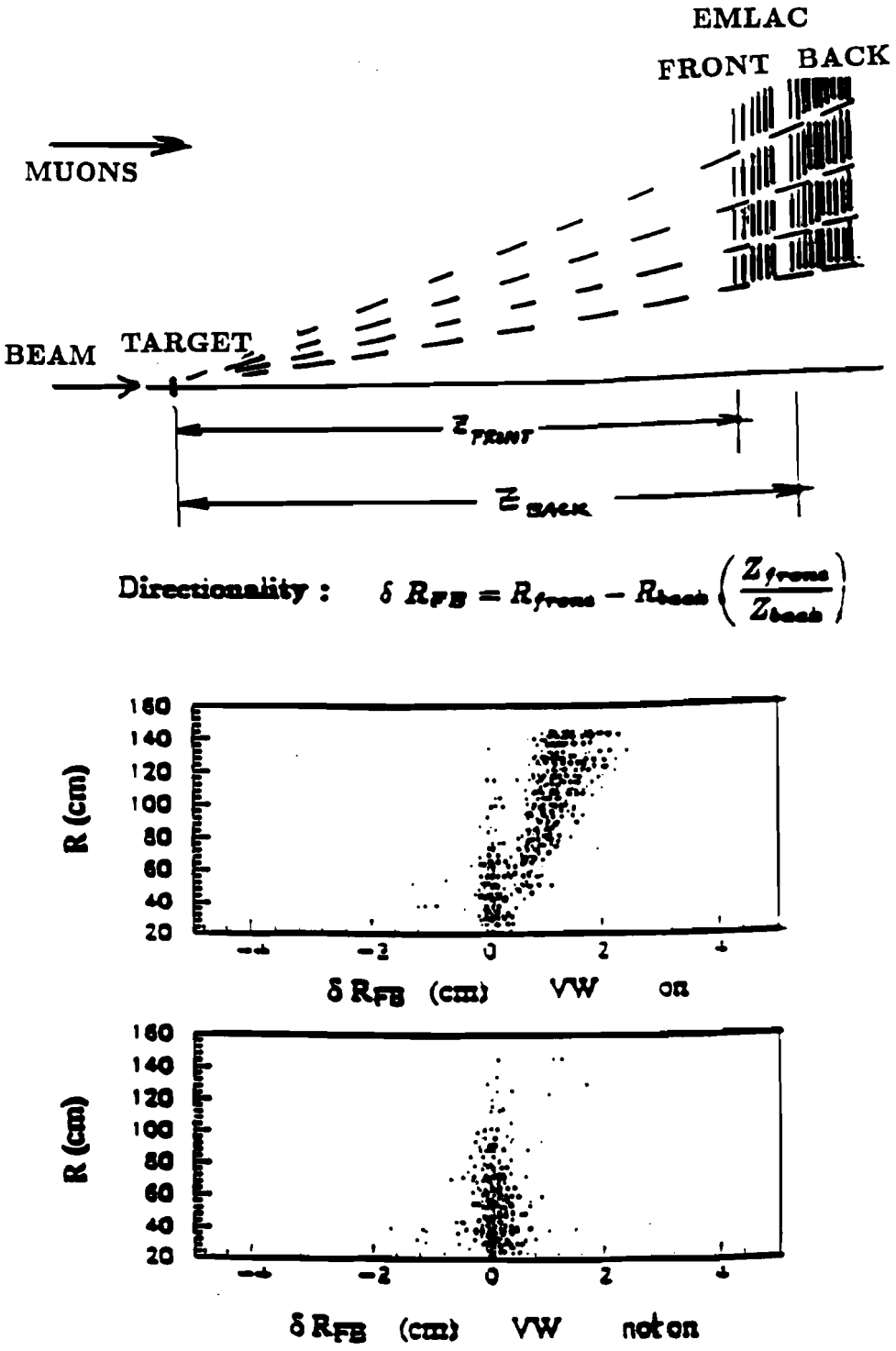

Figure 78: (top): The geometry used to measure the directionality of particles in the LAC. (bottom): Two plots of the r position of the single photon that triggered the event in the detector versus the directionality. In the upper of these plots the veto wall fired, and in the lower plot the veto wall did not fire.

nificantly from the cases of particles moving parallel to the beamline. The good position resolution of the EMLAC made the determination of a shower's entrance angle possible by comparing its position in the front and back sections of the detector. The directionality (δR_{FB}) is defined as follows:

$$\delta R_{FB} = R_{front} - R_{back}\left(\frac{Z_{front}}{Z_{back}}\right)$$

Figure 78 (top graph) shows the geometry used to measure the directionality of particles in the LAC. Figure 78 shows two plots of the r position of the shower that triggered the event in the detector versus the directionality. The top plot shows the distribution when one or more of the veto walls fired and the bottom one when no veto wall fired. Showers with $\delta R_{FB} \sim 0$ come from the direction of the target.

The timing, directionality, and veto wall cuts were highly correlated. All these cuts tended to reject the same high p_T events and were used to check one another. Figure 79 shows the p_T of the trigger photon versus the directionality for the cases when the veto wall fired (VW=1) and did not fire (VW=0). In the analysis it was required that $\mid \delta R_{FB} \mid < 0.4$ cm which rejected most of the high p_T triggers, as seen in Figure 79. The same figure also shows the p_T of the trigger photon versus the photon time for the two veto wall configurations. It was required that the photon signal should be in the time interval

$$-15 \text{ nsec} < T^{trigger} < 40 \text{ nsec}$$

Figure 80 shows the directionality versus time. The events in the regions marked by X were rejected by the combination of these two cuts.

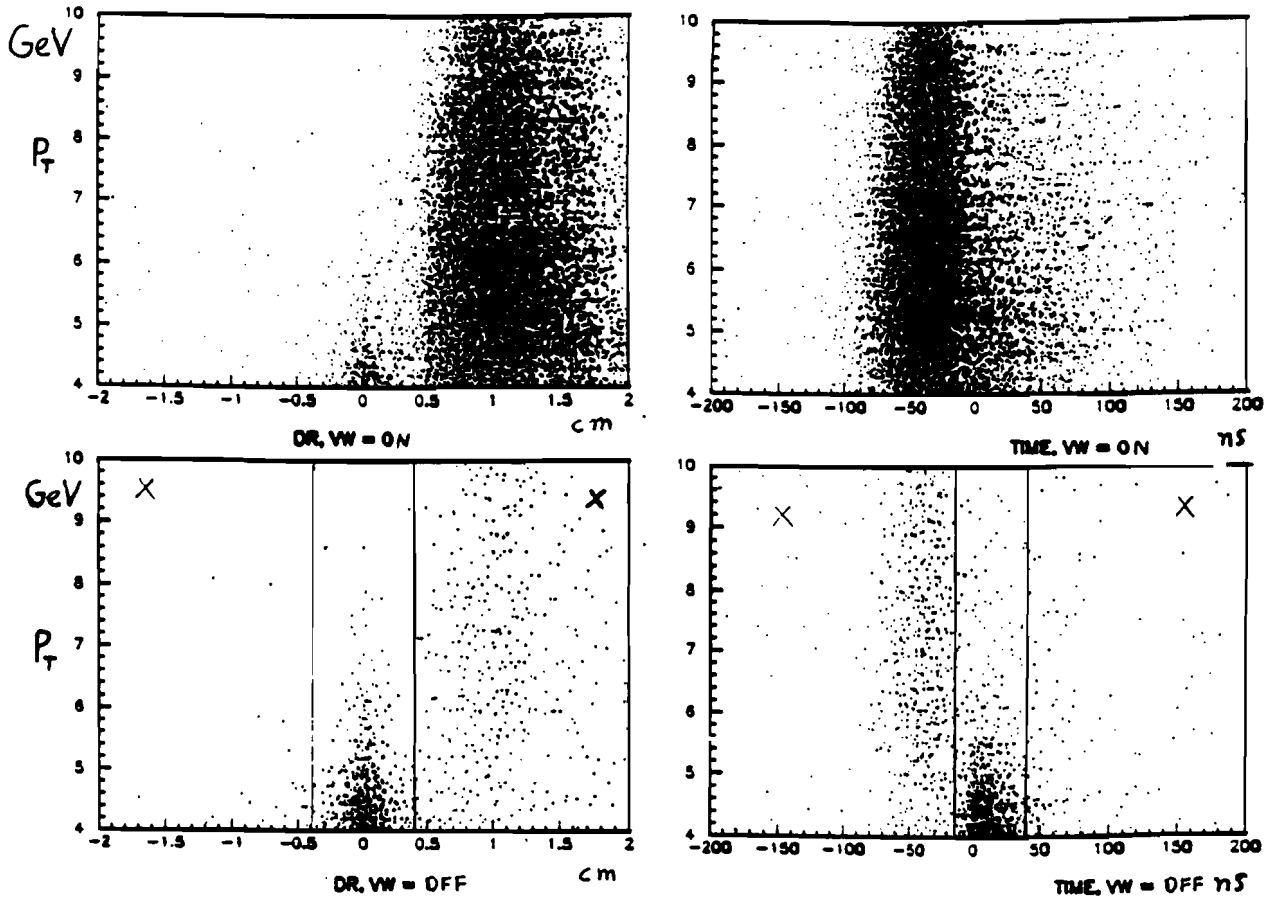

Figure 79: (top): The p_T of the trigger photon versus the directionality for the cases that the veto wall fired (VW=1) and did not fire (VW=0) (bottom): the p_T of the trigger photon versus the photon time for the two veto wall configurations.

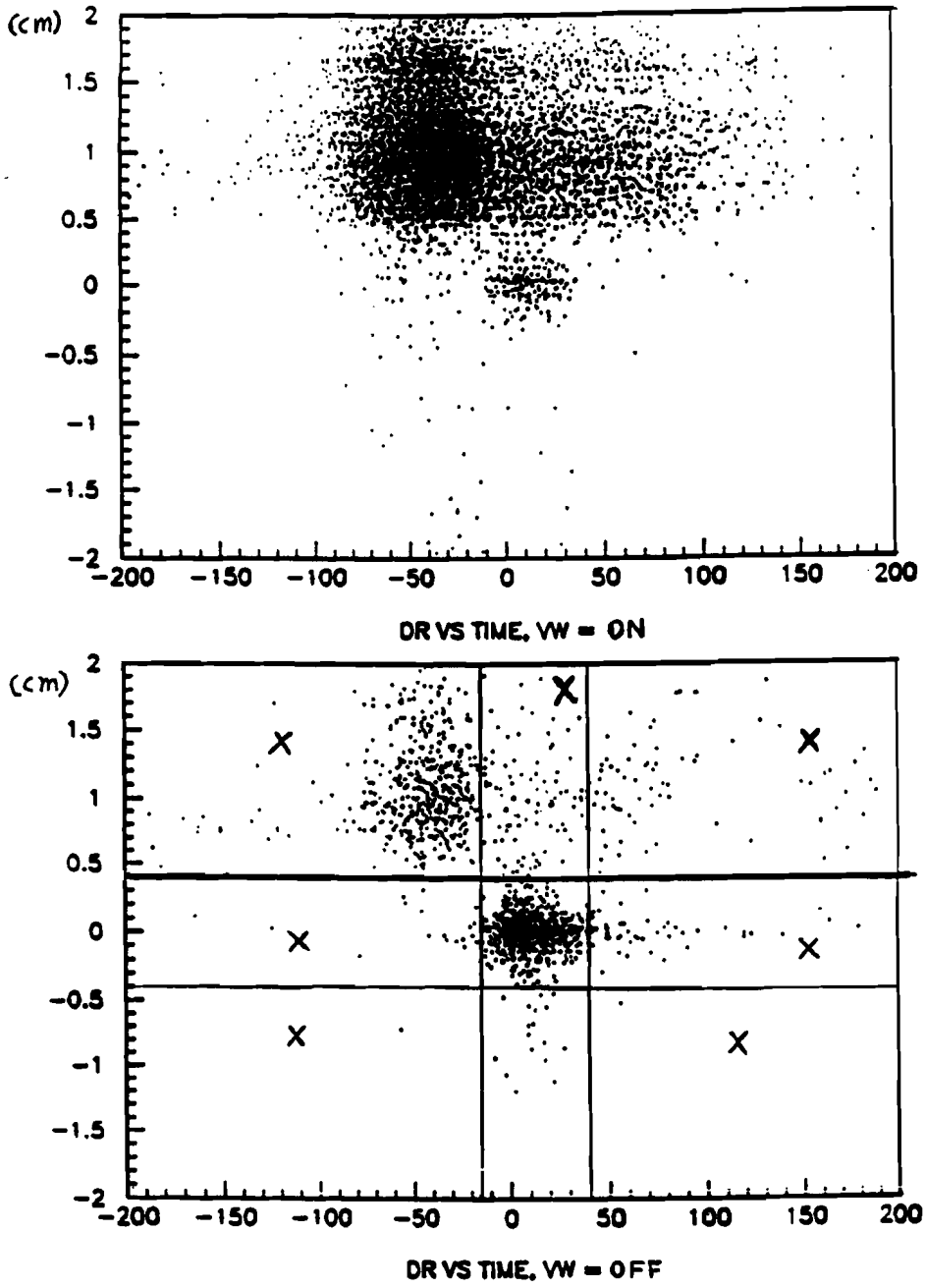

Figure 80: The directionality versus time (TDC). The events in the regions marked by Xs were rejected (see text).

III) Hadron Background

Stable hadrons produced in the target were one source of background in the single photon and π° events. A description of cuts used to reduce this source of background follows (the numbering scheme corresponds to that of Table 12).

◇ E^{FRONT}/E^{TOTAL} Cut (B4)

The design of the LAC and the distinctive properties of cascades produced by photons and hadrons helped to suppress this background. The hadron rejection capability of the apparatus was enhanced by the longitudinal segmentation of the LAC readout. This made it possible to independently measure the energy deposited in the front and back sections of the detector, and to impose a cut based on the longitudinal shower profile. Figure 81 (top graph) shows the E^{FRONT}/E^{TOTAL} ratio for electrons and pions from the data obtained with the 50 GeV calibration beam. Both electrons and pions were identified by the Cherenkov counter. As seen from the plot most of the hadronic background is rejected when it is required that $E^{FRONT}/E^{TOTAL} > 0.2$. Finally, Figure 81 (bottom graph) shows the distribution of E^{FRONT}/E^{TOTAL} for the photons with the maximum p_T in the event ($p_T \geq 4$ GeV/c) after the implementation of all cuts.

◇ Hadron Cut (B6)

The data from the magnetic spectrometer was used to identify charged particles (hadrons or e^+, e^-) and the hadron calorimeter data was used to identify neutral hadrons. The track cut required that there was neither a track pointing to the highest p_T shower nor a reconstructed hadronic shower behind it. The matching radial distance between the tracks and electromagnetic showers is 1.5 cm and be-

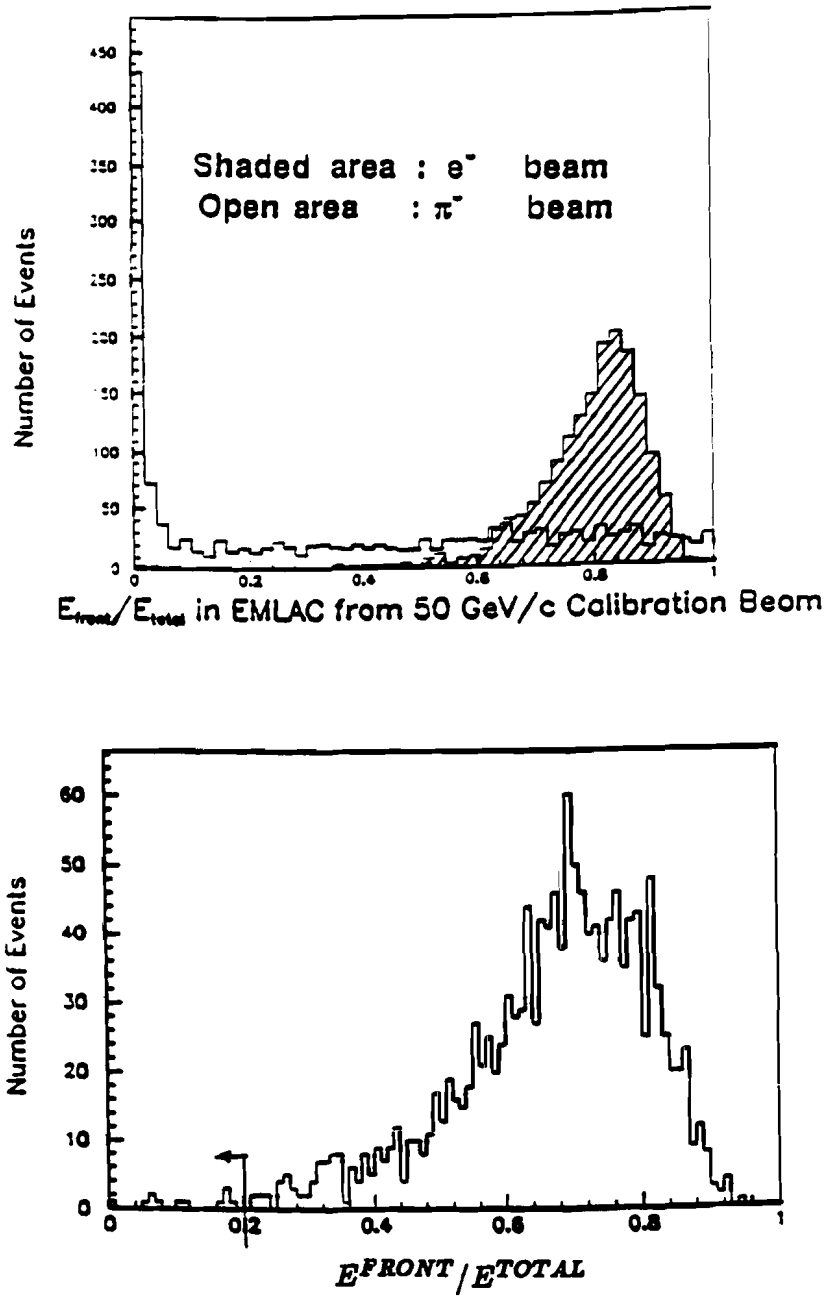

Figure 81: The E^{FRONT}/E^{TOTAL} ratio for electrons and pions from the data obtained with, (top): 50 GeV calibration beam, (bottom): final data sample.

tween the e.m. showers and hadronic showers is 7.0 cm. This second matching distance is chosen to be less than the one derived from the HALAC position resolution studies (i.e., 9.0 cm). This was done to keep the accidental overlapping (and consequent rejection of the event) of the e.m showers and hadrons at a minimum.

Figure 82 shows the distributions of the radial distances between the high p_T single photon and the hadronic shower closest to it (top), and between the high p_T single photon and the track closest to it (bottom). The number of events rejected by this cut after the application of the E^{FRONT}/E^{TOTAL} cut was of the order of 5%. The percentage of rejected events due to overlapped high p_T single photons and neutral hadrons was less than 1%.

The application of veto wall, directionality, isolation, E^{FRONT}/E^{TOTAL} and timing cuts on the showers left a clean sample of high p_T photons originating from the target. The other cuts were used to further improve the quality of the events.

6.3. Event Classification

The events that survived the cuts were classified as "π^o events" or "single photon candidate events". We considered events with a single photon candidate or a π^o in the fiducial region of the calorimeter within the rapidity interval $|y| \leq 0.75$. There was an additional cut used for only a part of the data analysis. It was required that there be at least one charged particle in the hemisphere opposite the high p_T photon (away side). The effect of this cut is shown in Table 12. It had a very minor effect at low p_T and virtually no effect at higher p_T. For high p_T photons above $\sim$ 6 GeV/c, it had no effect at all. The data obtained with the positive charged beam were divided into two groups according to the type of the

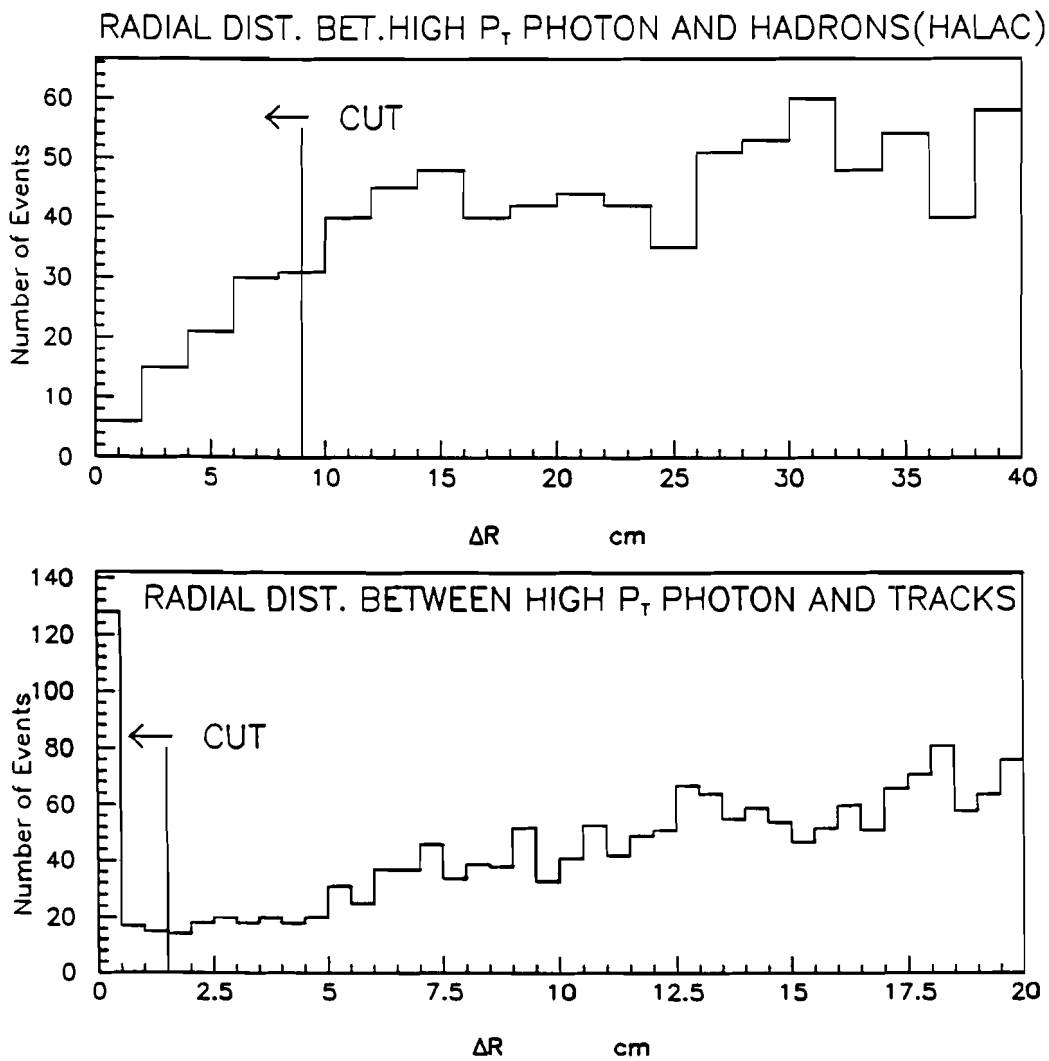

Figure 82: The distributions of the radial distances between the high p_T single photon and the hadronic shower closest to it (top), and between the high p_T single photon and the track closest to it (bottom).

incident hadron (p or π^-). In this analysis only the proton data ($\sim$ 92%) were used.

π° sample

The data sample was searched for π°s, ηs and η's in the $\gamma\gamma$ mode, and statistically significant signals were obtained for π°s and ηs. The branching ratios for π°s, ηs and η's going to $\gamma\gamma$ are $96.802 \pm 0.03\%$, $39.0 \pm 0.8\%$, and $1.9 \pm 0.2\%$, respectively[18].

The π° decays electromagnetically with mean life of the order of 10^{-16} sec. The photons from its decay are essentially produced at the point of the production of the π°. By measuring the interaction vertex, the energy, and the positions of the photons in the EMLAC, and knowing the photons originated from the vertex, one can determine their four momenta. The invariant mass was formed for any combination of two photons in the same octant by:

$$m = \sqrt{[(p_4{}^a + p_4{}^b)^2 - \sum_{i=1}^{3}(p_i{}^a + p_i{}^b)^2]}$$

where, $P^j = (p_4{}^j; p_1{}^j, p_2{}^j, p_3{}^j)$ is the four-momentum of the j-th photon. Figure 83 shows the invariant mass of di-photons with $p_T > 3.0$ GeV/c and for two different asymmetry cuts.

The π° candidate was defined as follows:

1. Invariant mass range: $110 \leq M_{\gamma\gamma} \leq 160$ (MeV/c^2)
2. Rapidity interval $| y | \leq 0.75$.
3. Energy asymmetry A* ≤ 0.75.

* The energy asymmetry (A) is defined as: $A = |E_1 - E_2|/(E_1 + E_2)$

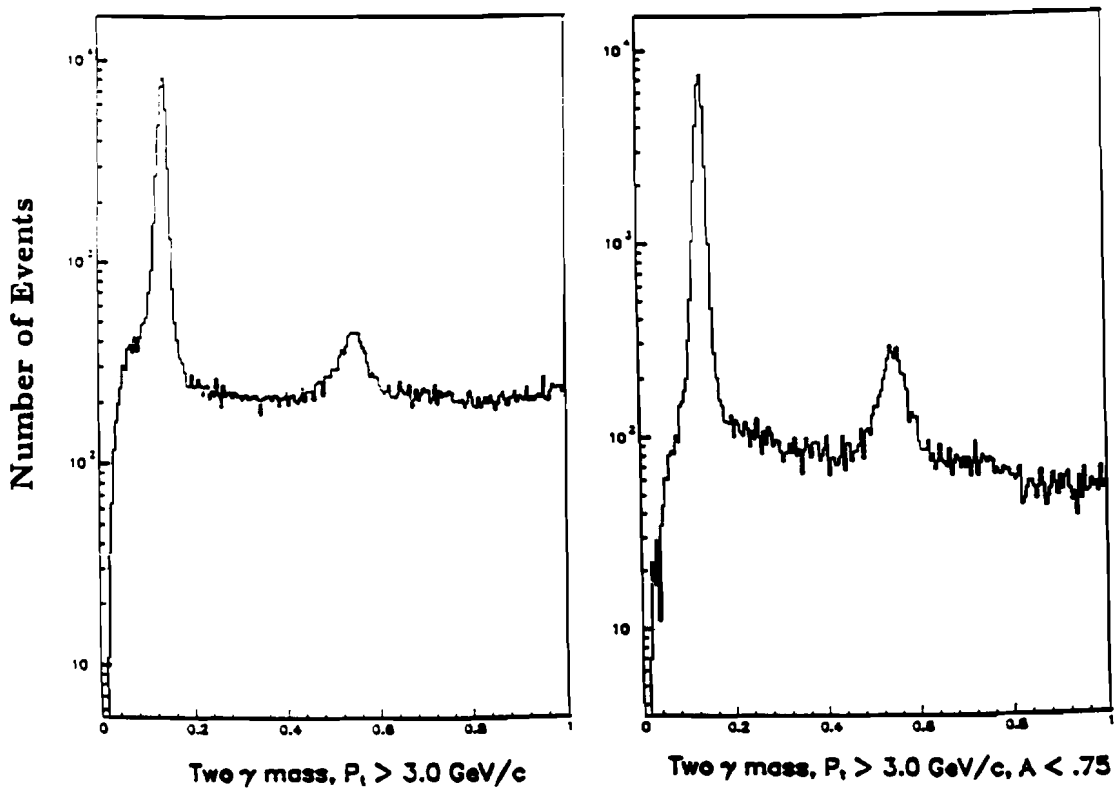

Figure 83: The invariant mass of di-photons with $p_T > 3.0$ GeV/c and with (right plot) or without asymmetry cut (left plot). Only a fraction of the total data is shown. The distributions have not been corrected for trigger efficiency or detector acceptance.

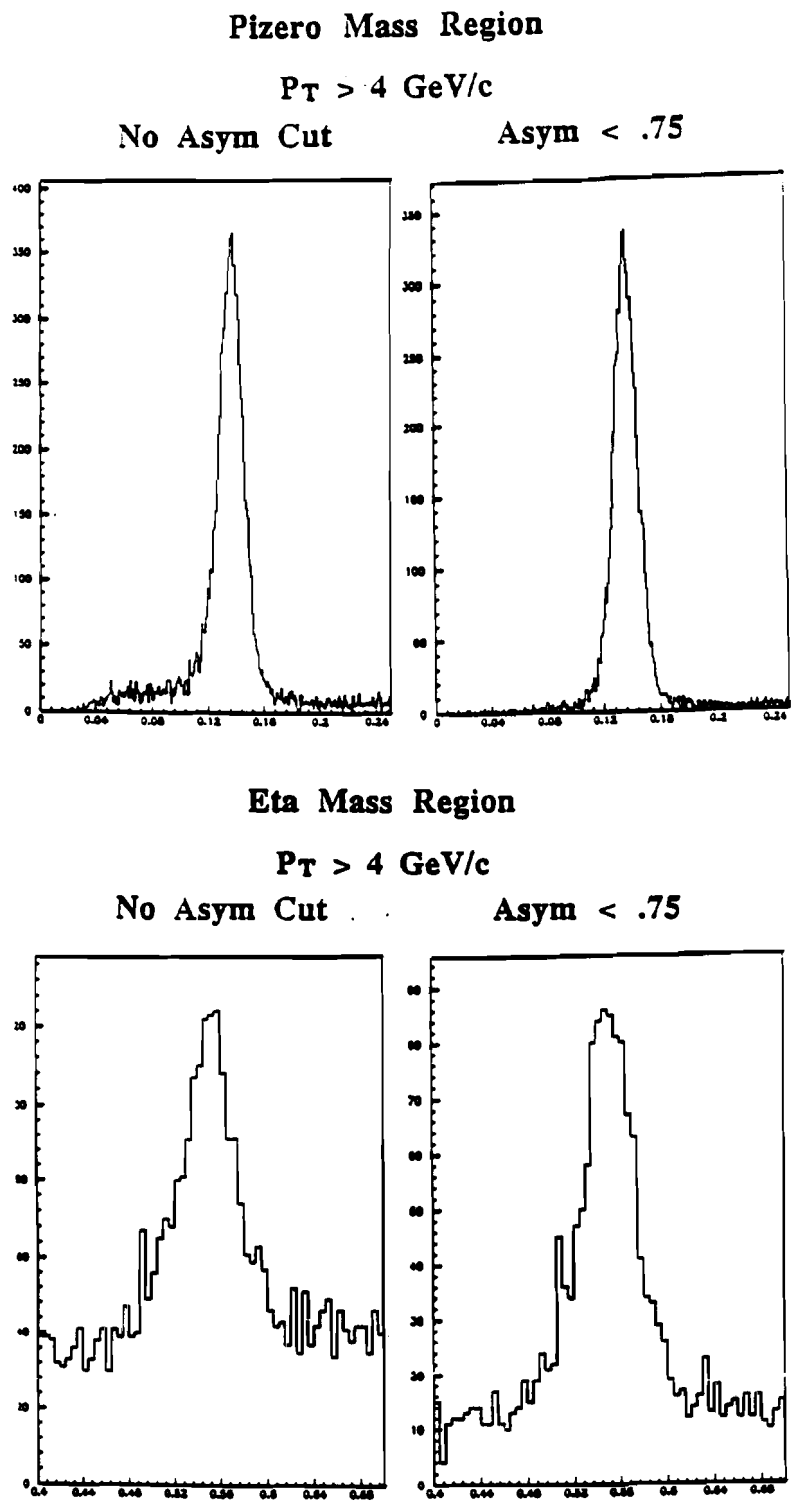

Figure 84: π^0 and η mass distributions for $p_T > 4$ GeV/c. Only a fraction of the total data is shown. The distributions have not been corrected for trigger efficiency or detector acceptance.

The background to π^os arises from the combinations of high p_T photon and low p_T photon which are abundant in the data. To improve the signal to background ratio, the energy asymmetry cut was set to 0.75 (see Figure 84). Figure 84 also shows the invariant mass of di-photons around the η mass range.

Figure 85 shows the rapidity distributions of the π^o sample used for this analysis ($p_T \geq 5.0$ GeV/c) for both positive and negative data. Figure 86 shows the asymmetry distributions for the same sample.* Figure 87 shows the p_T and energy distributions. The p_T distributions fall sharply as expected.

The trigger efficiency as a function of the π^o p_T is shown in Figure 88. For $p_T >$ 4.5 GeV/c the efficiency is 100%.

The event sample of π^o candidates yielded a signal of 4470 π^os, in the p_T range between 5.0 and 10.2 GeV/c.

Single γ sample

Pairs of photons which formed π^os or ηs were rejected from the photon sample. π^o and η were defined with the following conditions on the invariant mass (no requirement on the energy asymmetry was used here),

a. π^o mass range: $0 < M_{\gamma\gamma} \leq 170$ (MeV/c^2)

b. η mass range: $480 \leq M_{\gamma\gamma} \leq 620$ (MeV/c^2)

A "gamma" could be shared by more than one shower especially when two showers were close to each other (as in the π^o events). About 10% of the very

* The decrease in the region close to A = 0 in the asymmetry plots of the π^o, $p_T < 6.0$ GeV/c, is an artifact of the pre-selection requirement A3) (see footnote of Table 12). It certainly does not affect the results of this analysis.

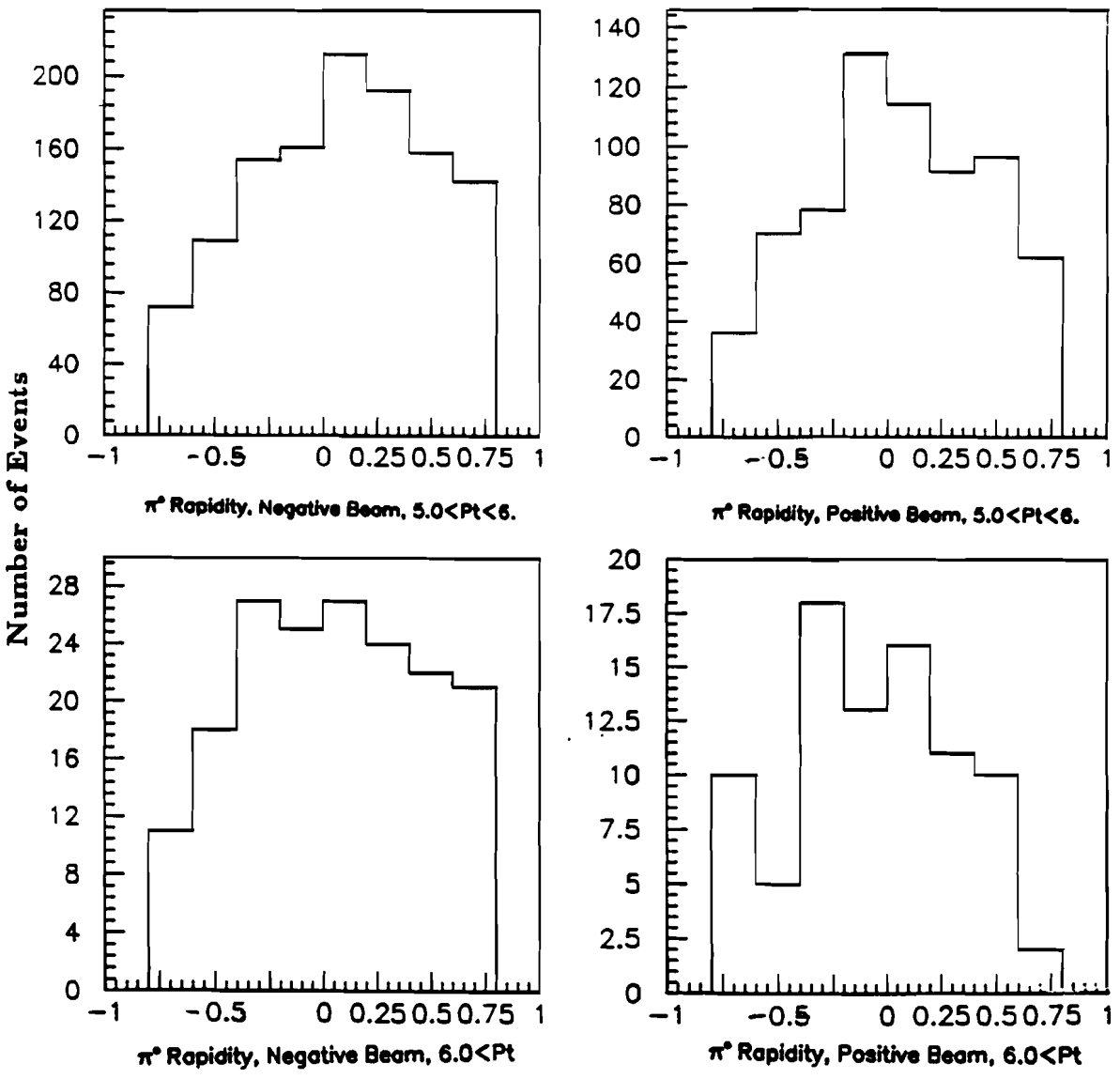

Figure 85: The rapidity distributions of the π° sample used for this analysis ($p_T \geq 5.0$ GeV/c) for both positive and negative data. Only a fraction of the total data is shown. The distributions have not been corrected for trigger efficiency or detector acceptance.

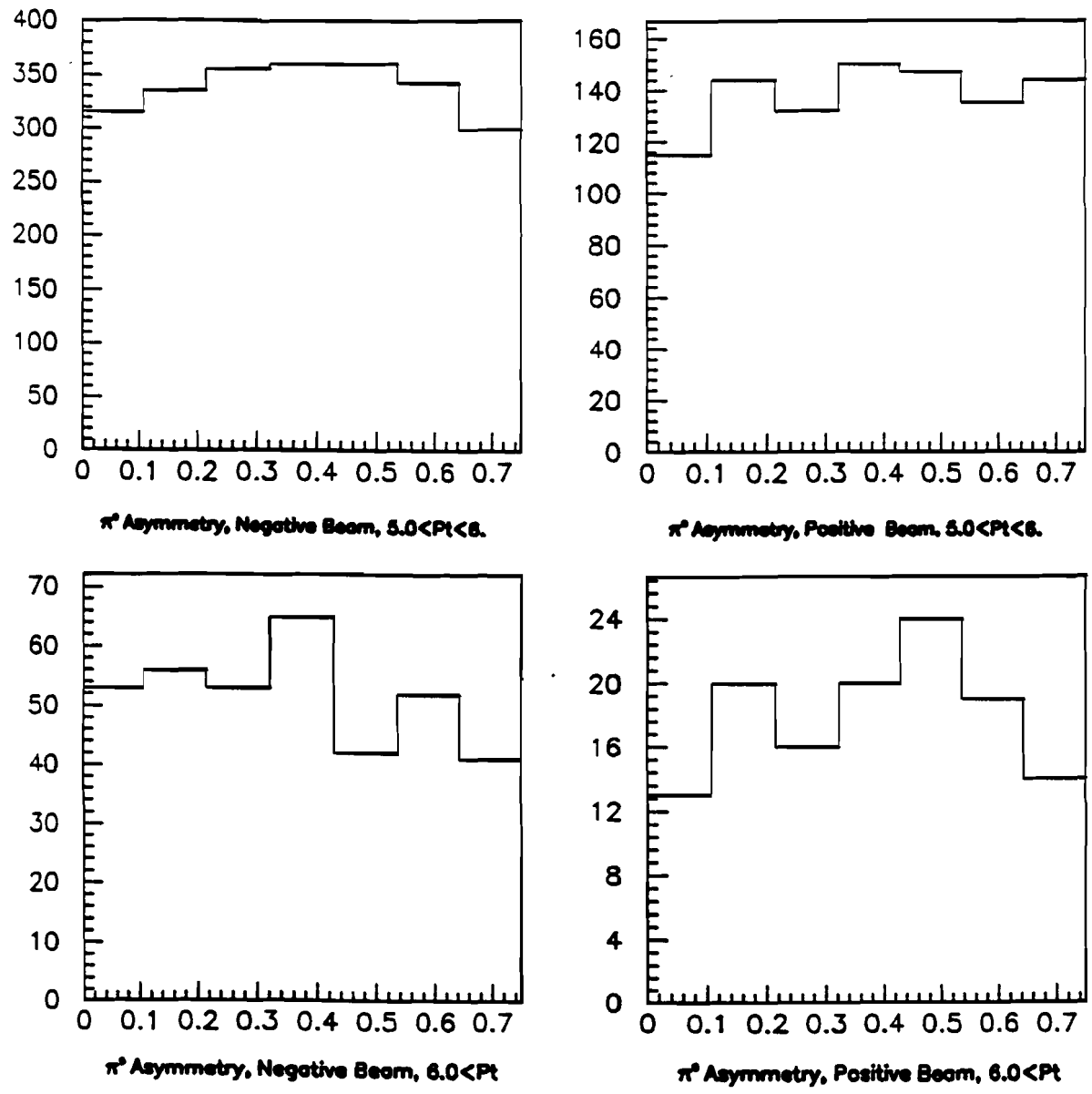

Figure 86: The asymmetry distributions of the π^0 sample used for this analysis ($p_T \geq 5.0$ GeV/c) for both positive and negative data. Only a fraction of the total data is shown. The distributions have not been corrected for trigger efficiency or detector acceptance.

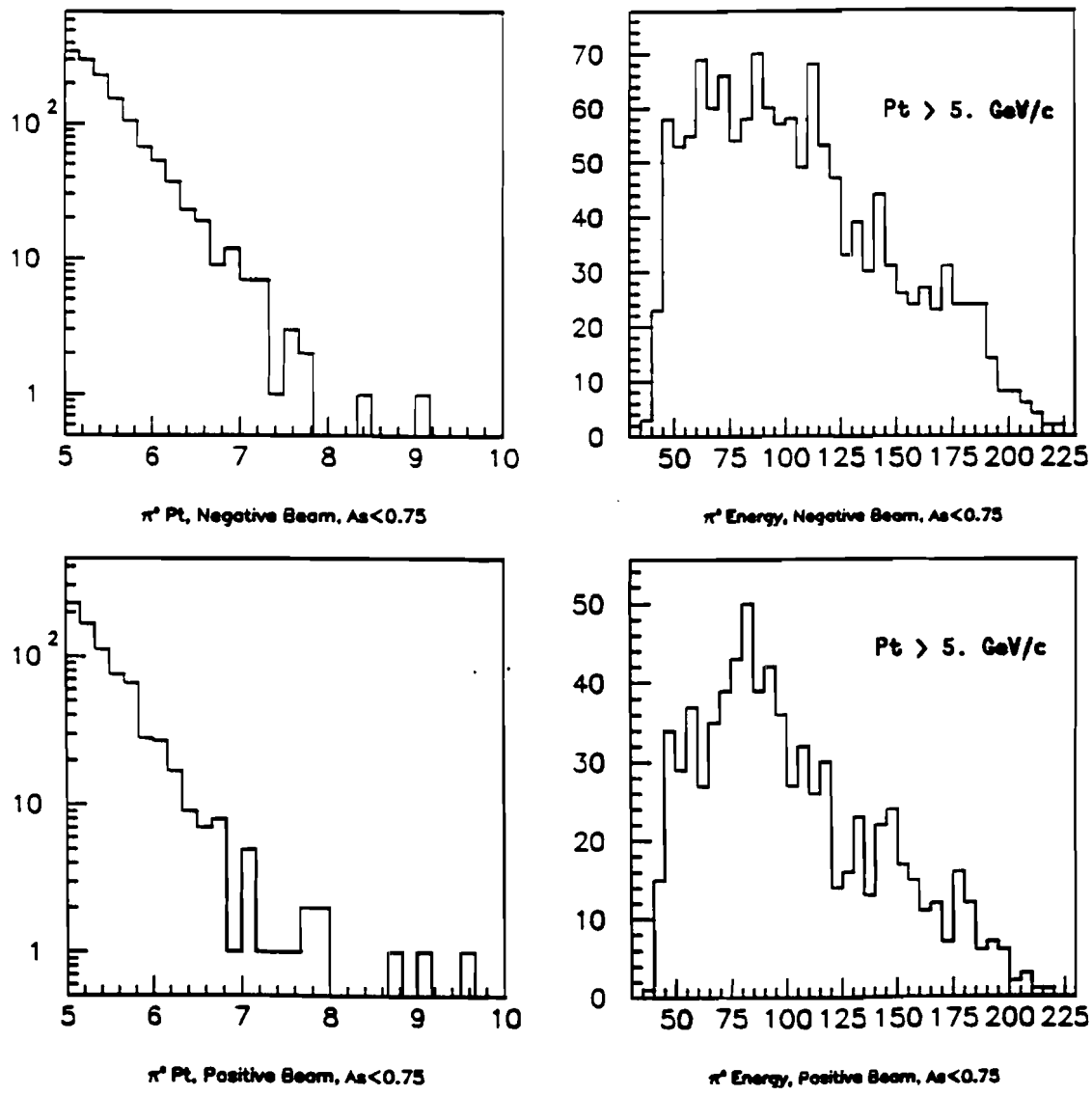

Figure 87: The p_T and energy distributions of the π° sample used for this analysis ($p_T \geq 5.0$ GeV/c) for both positive and negative data. Only a fraction of the total data is shown. The distributions have not been corrected for trigger efficiency or detector acceptance.

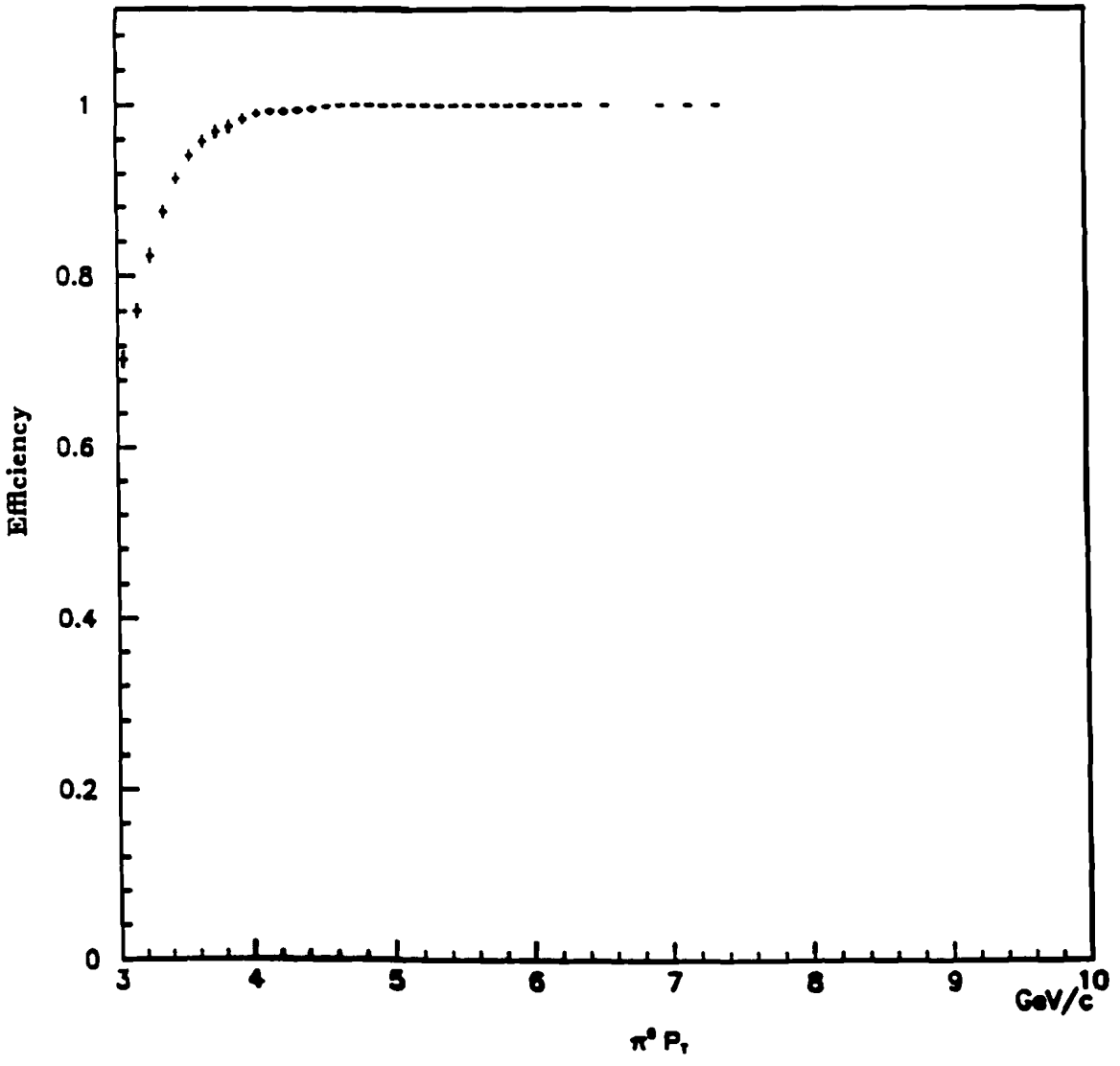

Figure 88: The trigger efficiency as a function of the π° p_T.

energetic showers ($E_\gamma > 50.0$ GeV) were accompanied by a less energetic shower ($E_\gamma < 10.0$ GeV) within a radial distance of 5.0 cm. It was found that in most cases the accompanying shower was a result of a shower tail fluctuations in the energetic shower. In the single γ sample this situation introduced significant reconstruction errors. If the maximum p_T photon was sharing a energy with any other photon in the event, then the event was removed from the sample. This cut should not remove many direct γ candidates because direct γs should be relatively isolated from accompanying particles. This cut was applied after the implementation of the low mass pair rejection cut (i.e., $0 < M_{\gamma\gamma} \leq 170$ (MeV/c^2)) and it removed less than 1% of the events from the direct photon sample because the low mass pair cut removed most of the events where the trigger photon shared energy with another photon.

The rapidity, p_T, and energy distributions of single photon candidates are depicted in Figures 89 and 90. The p_T distributions fall sharply with increasing p_T, as expected.*

The event sample of single photon candidates yielded a signal of 1692 photons in the p_T range between 5.0 and 10.5 GeV/c.

* All distributions have been corrected for "fake" single photons. The background to the single photons arose mostly from the decays $\pi^0 \rightarrow \gamma\gamma$ and $\eta \rightarrow \gamma\gamma$. The background was calculated using Monte Carlo method, as discussed in the last section of the current chapter. The single γ background is referred to as "fake" single photons.

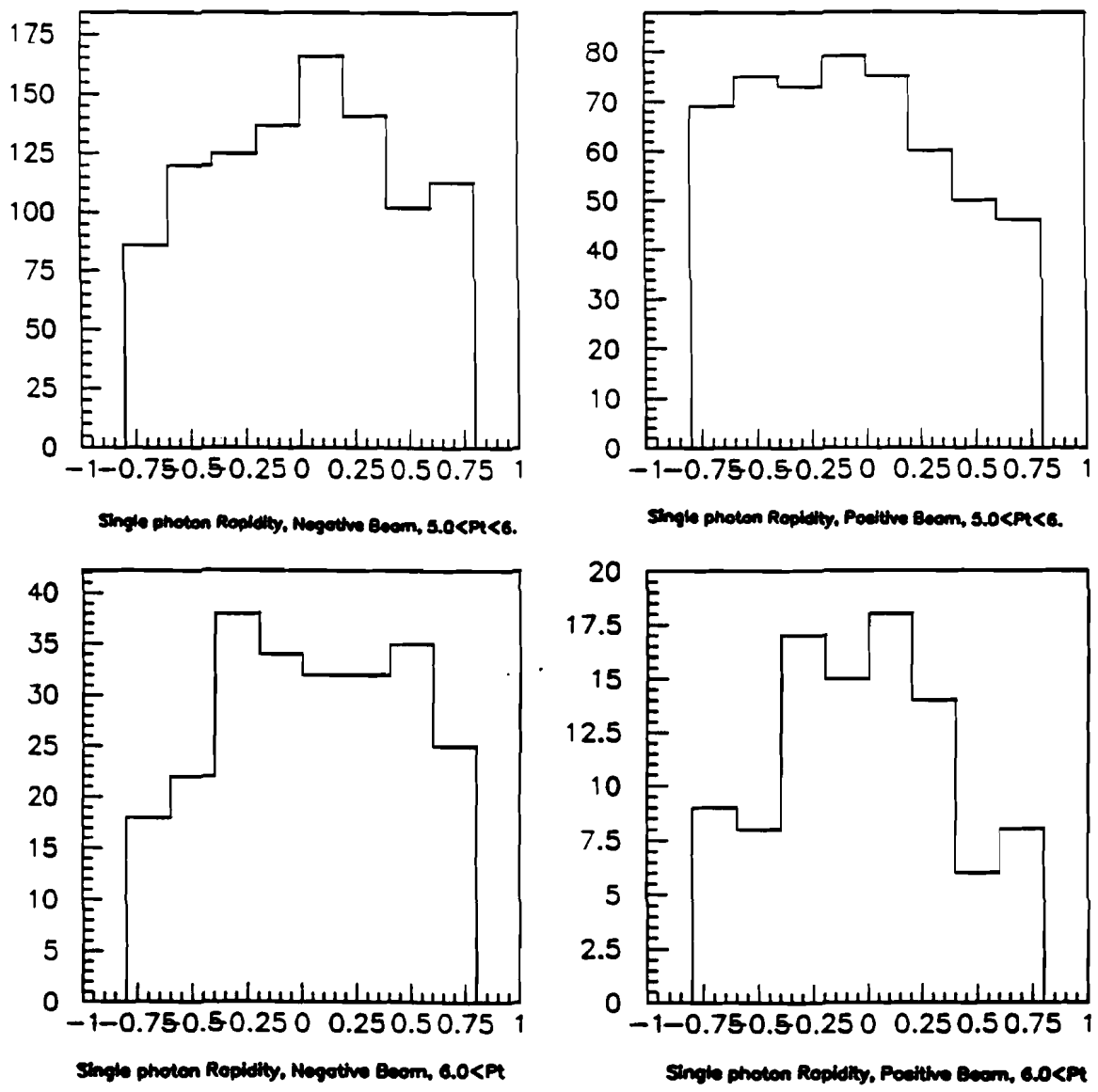

Figure 89: The rapidity distributions of high p_T single photon candidates. Only a fraction of the total data is shown. The distributions have not been corrected for trigger efficiency or detector acceptance.

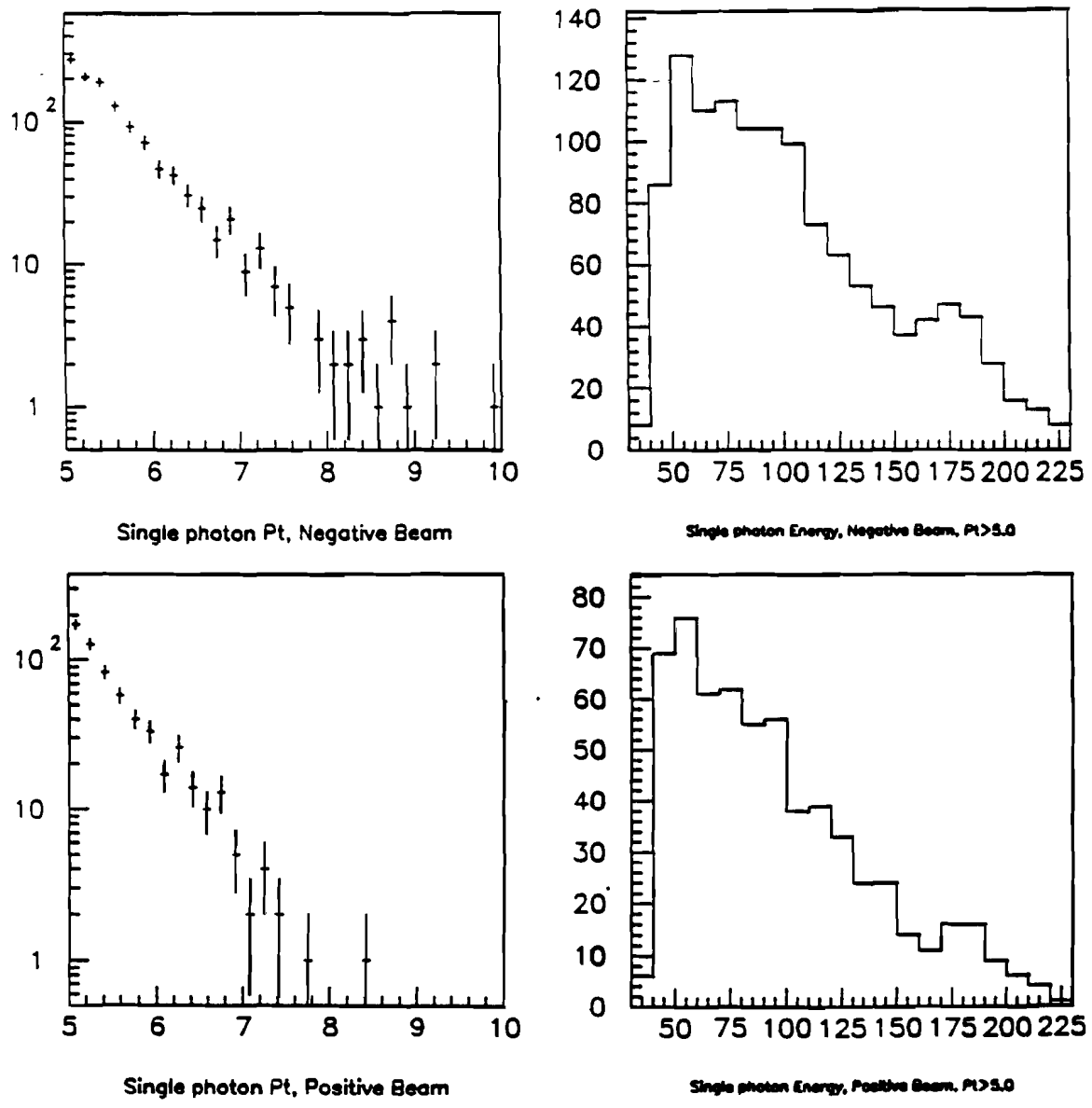

Figure 90: The p_T and energy distributions of high p_T single photon candidates. Only a fraction of the total data is shown. The distributions have not been corrected for trigger efficiency or detector acceptance.

6.4. Particle Selection and Classification

Not all of the reconstructed particles were used in the final analysis. Each reconstructed track or shower had to satisfy certain requirements in order to be considered in the final analysis. The requirements for each particle classification scheme were the following:

i) Charged Tracks. Each track should point to the vertex region. We defined the quantity D_Y as the calculated distance in the YZ plane of the track to the vertex when the downstream track was extended to the vertex region. That is,

$$D_Y = |\frac{c_y}{c_z} \times V_z \ + \ i_y \ - \ V_y| \leq 1.0 \ cm$$

where, c_y is the directional cosine in the YZ-plane of the downstream track, c_z is the directional cosine in the YZ-plane of the downstream track, i_y is the distance of the upstream track from the reconstructed vertex on the YZ- plane, V_z, V_y are the z and y coordinates of the reconstructed vertex, respectively. Only tracks with $\chi^2/DOF < 2.5$ were used. An upper limit in the reconstructed momentum of each track was set at 150 GeV/c.

ii) Showers reconstructed in the EMLAC. An upper energy limit was set at 250 GeV for all showers in the EMLAC.

iii) Showers reconstructed in the HALAC. An upper energy limit was set at 250 GeV and a low energy threshold at 10 GeV for all showers. The 10 GeV cut was set in order to avoid noisy channels.

An upper limit in the p_T was set at 12 GeV/c for all particles. This cut reduces the unphysicaly high momentum charged tracks. It has very small effect on the reconstructed showers.

All the reconstructed particles in the event (except the particle that triggered the event) were classified into the following four groups:

a) Charged particles. The magnetic spectrometer data was used to reconstruct the charged particles.

b) Low energy neutral hadrons ($\leq$ 10 GeV), neutral mesons and photons. The EMLAC data was used to reconstruct these particles. All showers that overlap with a reconstructed track from the PWCs were considered to be charged particles ($\Delta R^{Trk-Shower} \leq 1.5$ cm). Particles which neither were matched to a track nor deposited any detectable energy in the HALAC, were classified as low energy neutral hadrons or photons. The photons and low energy hadrons were separated using their different longitudinal energy distribution. The photons deposit most of their energy in the front section of the detector and the hadrons in the back section.

c) High energy neutral hadrons ($\geq$ 10 GeV mostly $K_L{}^{\circ}$ and neutrons). The HALAC and the EMLAC data were used to reconstruct these particles. Each reconstructed shower in the HALAC was matched to the overlapping the EMLAC showers as explained in the Section 6.3.2. All showers that overlapped with a reconstructed track from the PWCs were classified as charged particles ($\Delta R^{Trk-Shower} \leq 9.0$ cm). To avoid classifying a particle twice (i.e., in both groups a) and c)) the hadronic showers which were matched to a track were removed from the event particle list. Only one matched shower was removed per charged track. Figure 91 shows the minimum radial distance between the tracks and all showers in the EMLAC and the HALAC.

d) Leading p_T π°s reconstructed in the away hemisphere relative to the

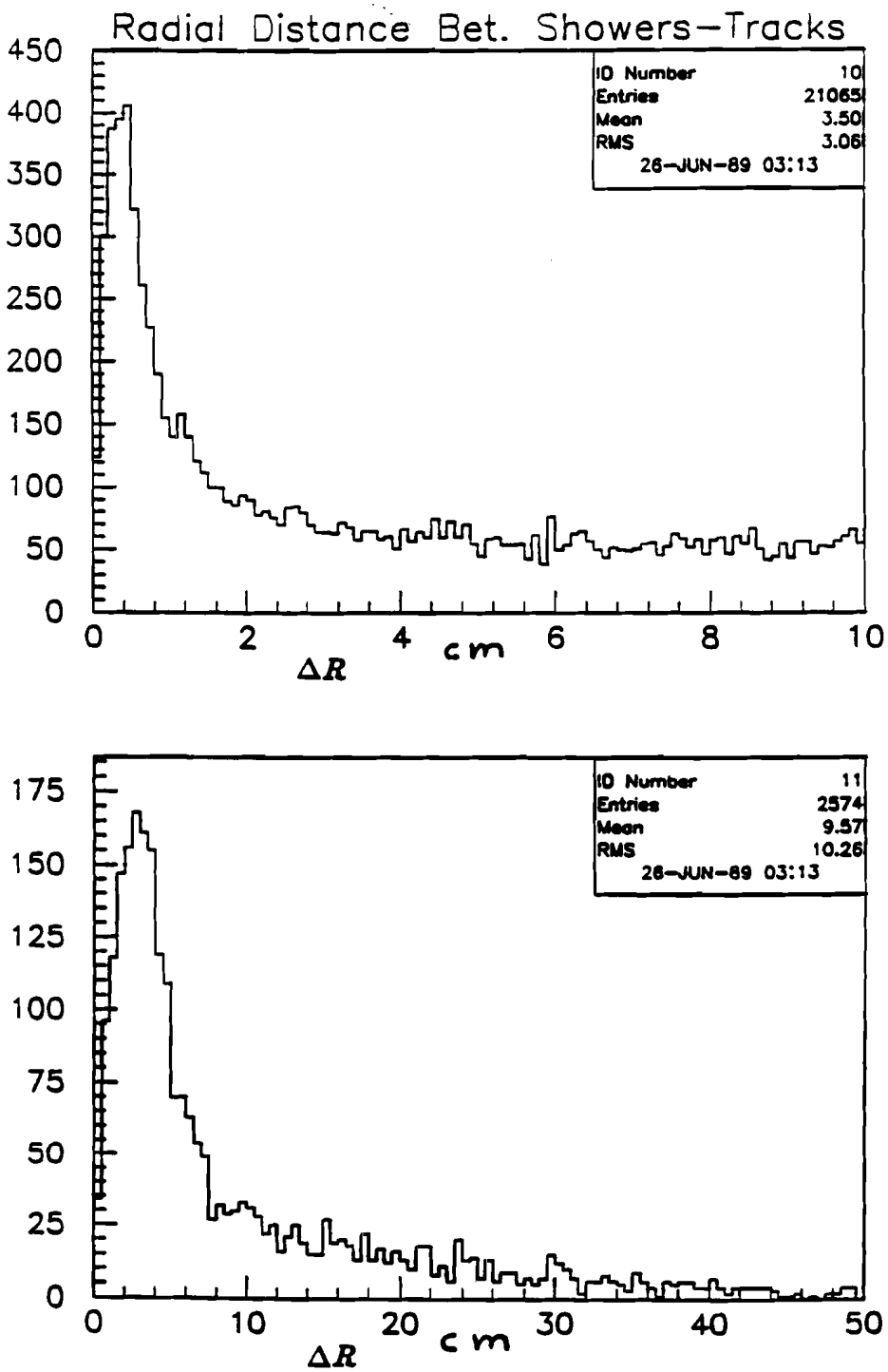

Figure 91: The minimum radial distance between the tracks and all showers in the EMLAC (top graph) and the HALAC (bottom graph).

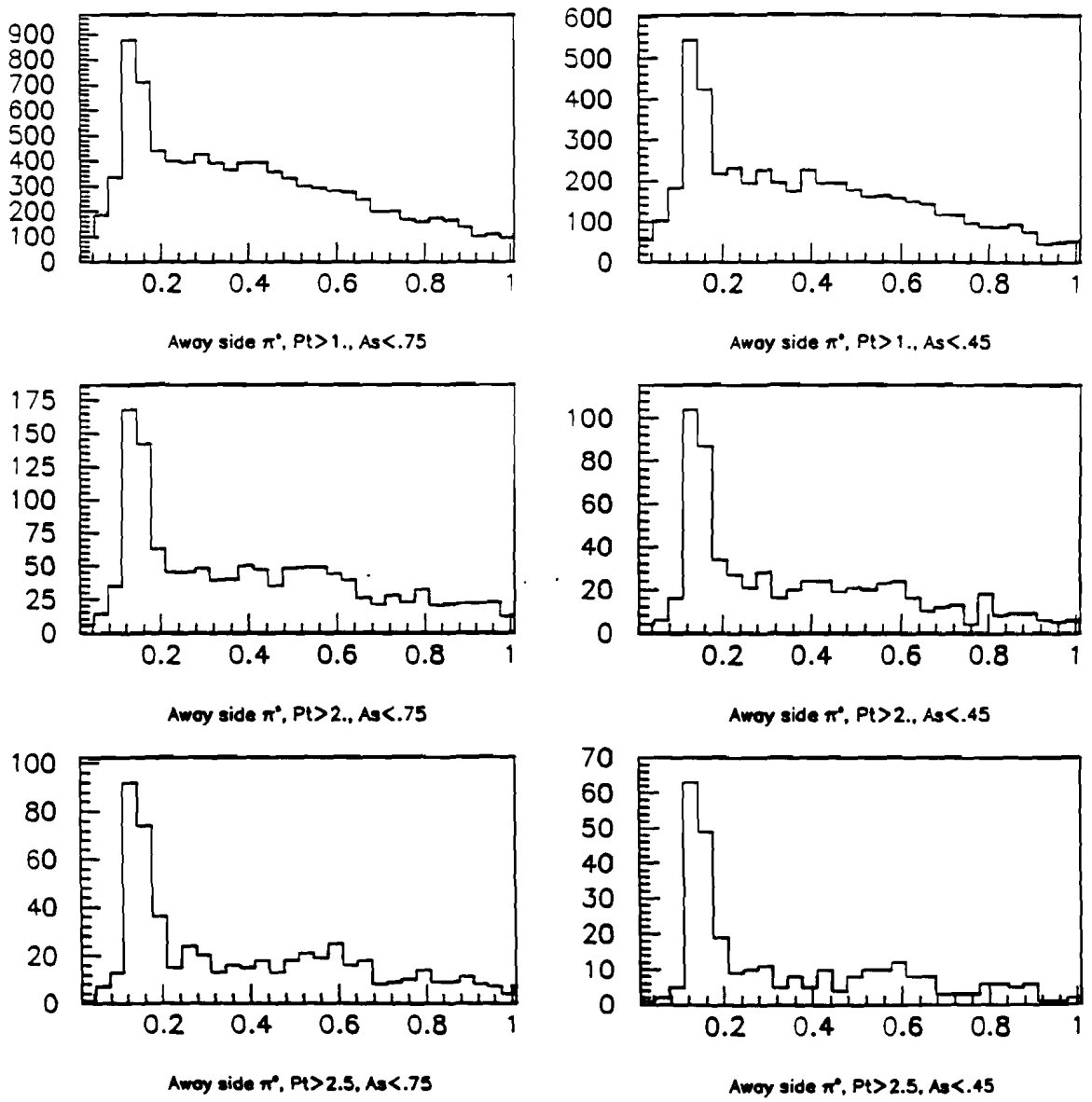

Figure 92: The mass spectrum of the awayside 2γs for various p_T and asymmetry cuts. Only a fraction of the total data is shown. The distributions have not been corrected for trigger efficiency or detector acceptance.

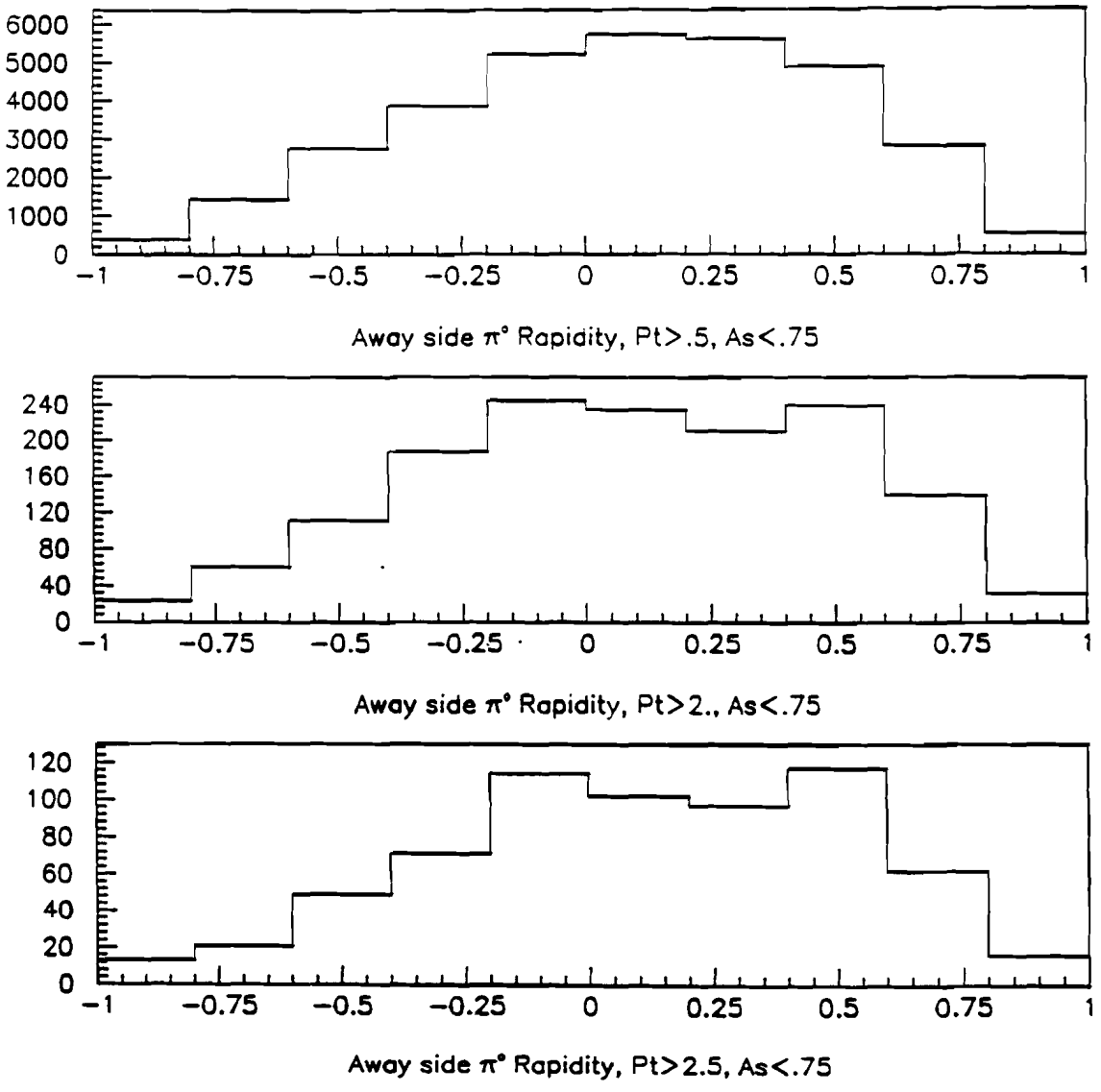

Figure 93: The rapidity distributions of the awayside π^0s for three p_T cuts. Only a fraction of the total data is shown. The distributions have not been corrected for trigger efficiency or detector acceptance.

high p_T photon or π^0 ($p_T{}^{\pi^0} > 500$ MeV/c). The invariant mass was formed for any combination of two photons, residing in the away hemisphere relative to the high p_T single γ or π^0. Figure 92 shows the mass spectrum of the two γs for various p_Ts and asymmetry cuts. The π^0s formed from that way are called "awayside π^0s". Most of the awayside π^0s with p_T above 2.0 GeV/c came from events where the "two gamma" trigger was satisfied. The rapidity distributions of the away side π^0s for three p_T cuts are shown in Figure 93. Most of the reconstructed π^0s reside in the forward region.

6.5. Event Structure

This section presents the structure and topology of the events which passed the cuts described in the previous sections.

The particle multiplicity distributions in the LAC and magnetic spectrometer for all events which passed the cuts described in the previous sections are shown in Figure 94. The average multiplicity for the charged tracks is 10.3 tracks per event (Figure 94, top graph). The average multiplicity for the showers in the EMLAC (not counting the high p_T photon or π^0) is 5.8 per event (Figure 94, middle graph). The average multiplicity for the showers in the HALAC is 1.21 showers per event (Figure 94, bottom graph).

Figures 95 and 96 show the p_T and energy distributions for each of these classes of particles. In Figure 97, the transverse momentum distributions of the charged particles with rapidity, $|y| < 0.9$, and energy greater than 10.0 GeV are normalized to be equal in the region 2 to 4 GeV/c with the neutral hadron p_T distribution.

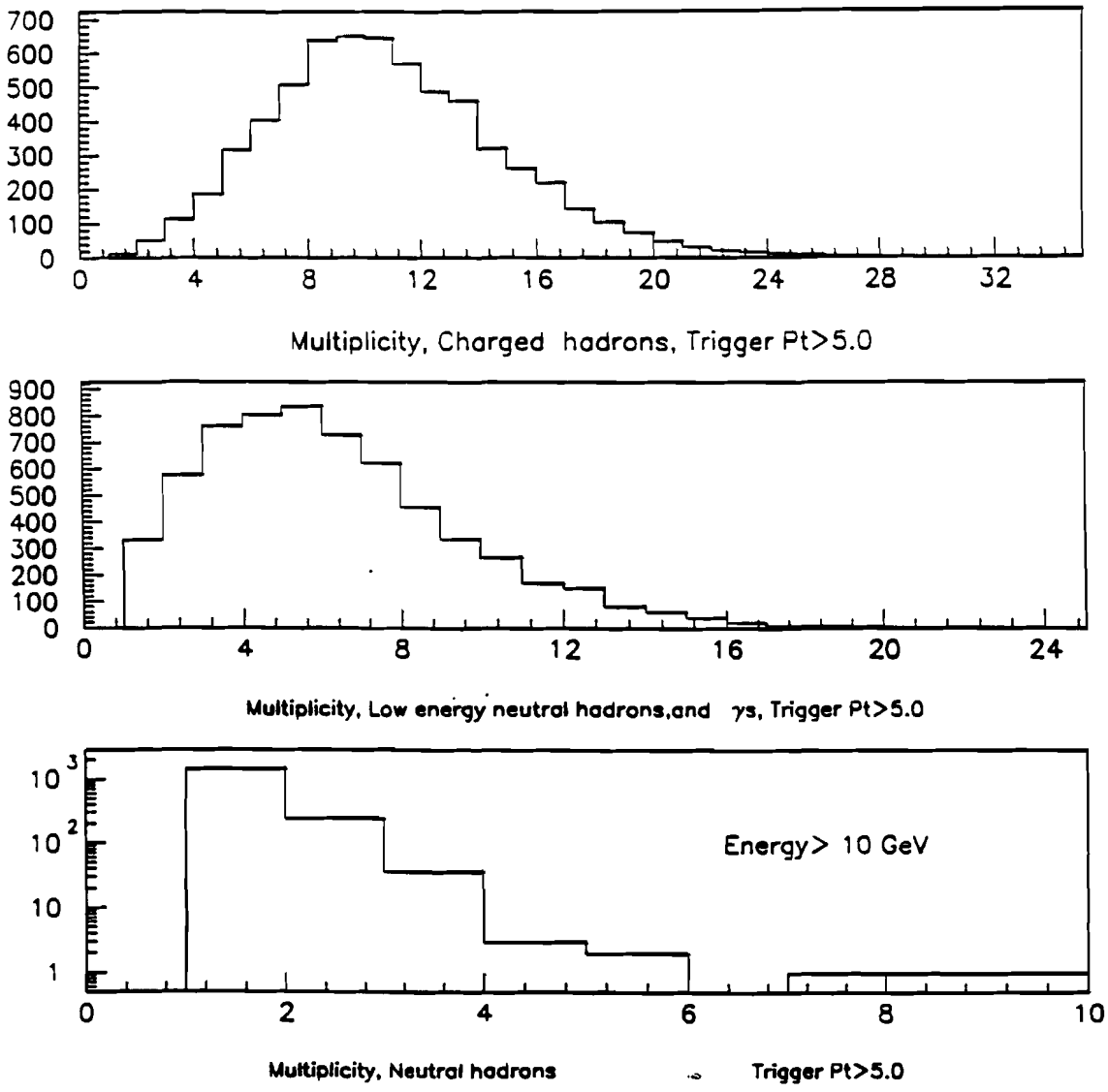

Figure 94: The particle multiplicity distributions in the LAC and magnetic spectrometer. The events with no particles reconstructed are not shown. Only a fraction of the total data is shown. The distributions have not been corrected for trigger efficiency or detector acceptance.

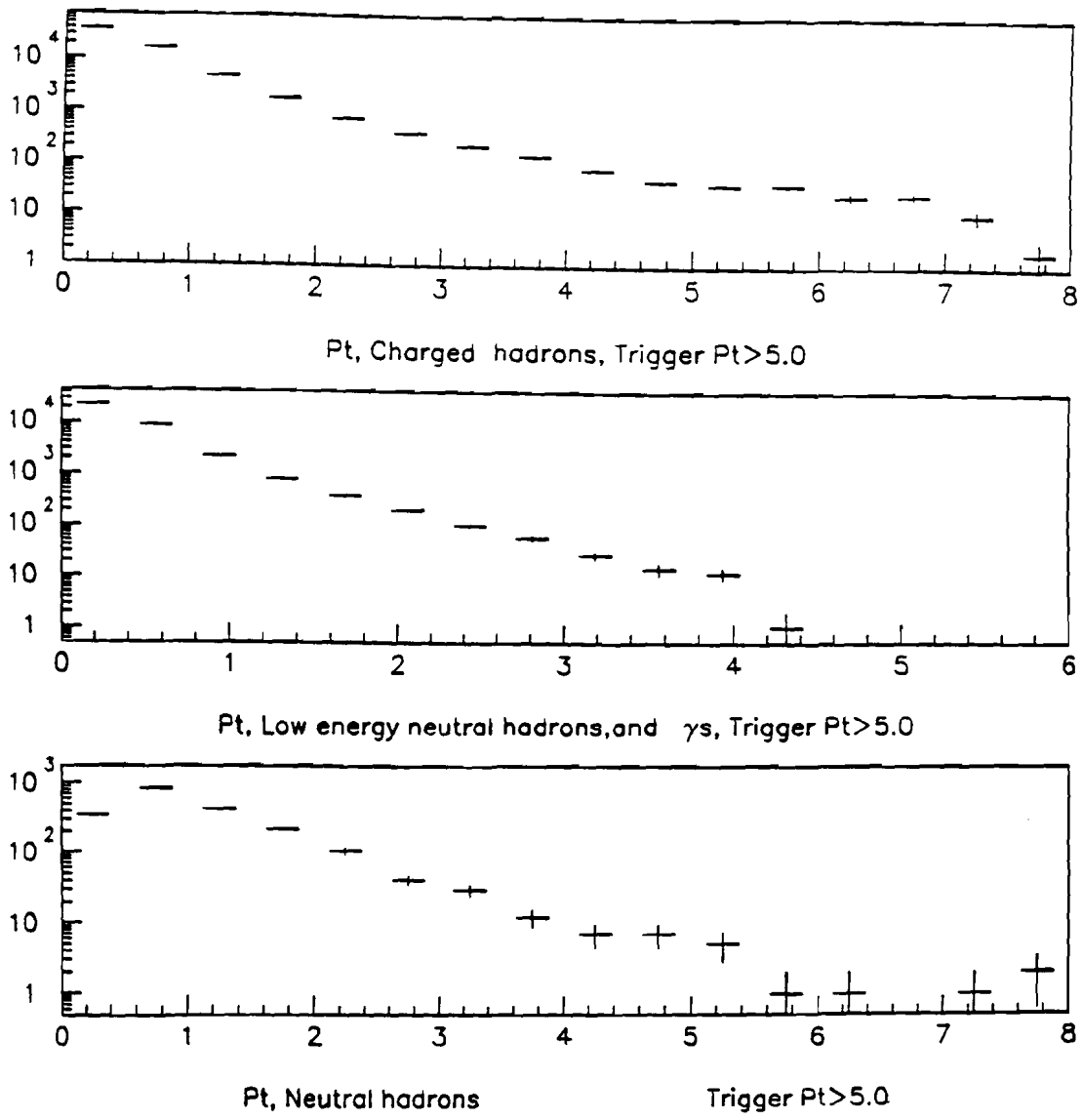

Figure 95: p_T distributions of all particles (see text). Only a fraction of the total data is shown. The distributions have not been corrected for trigger efficiency or detector acceptance.

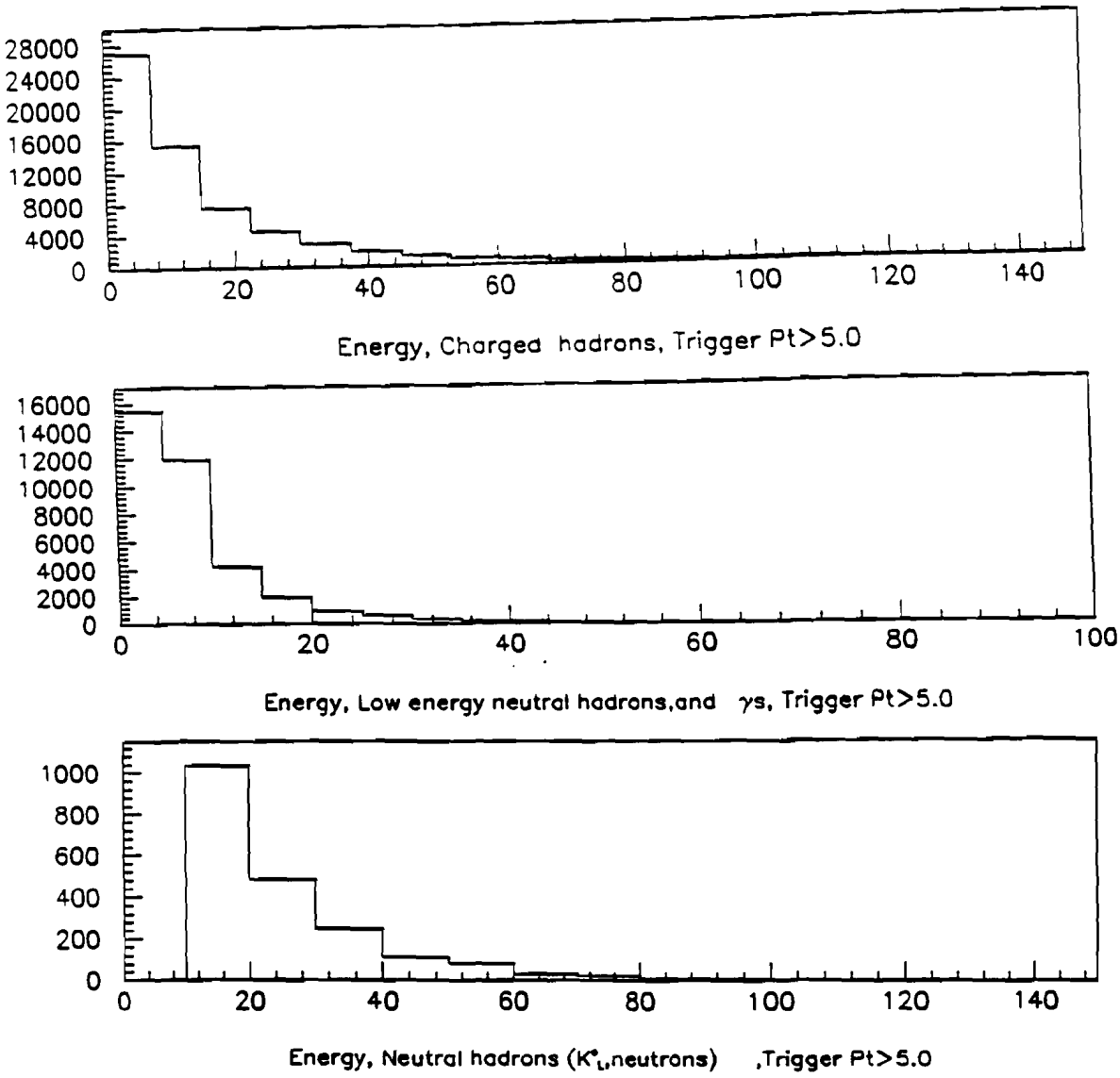

Figure 96: Energy distributions of all particles (see text). Only a fraction of the total data is shown. The distributions have not been corrected for trigger efficiency or detector acceptance.

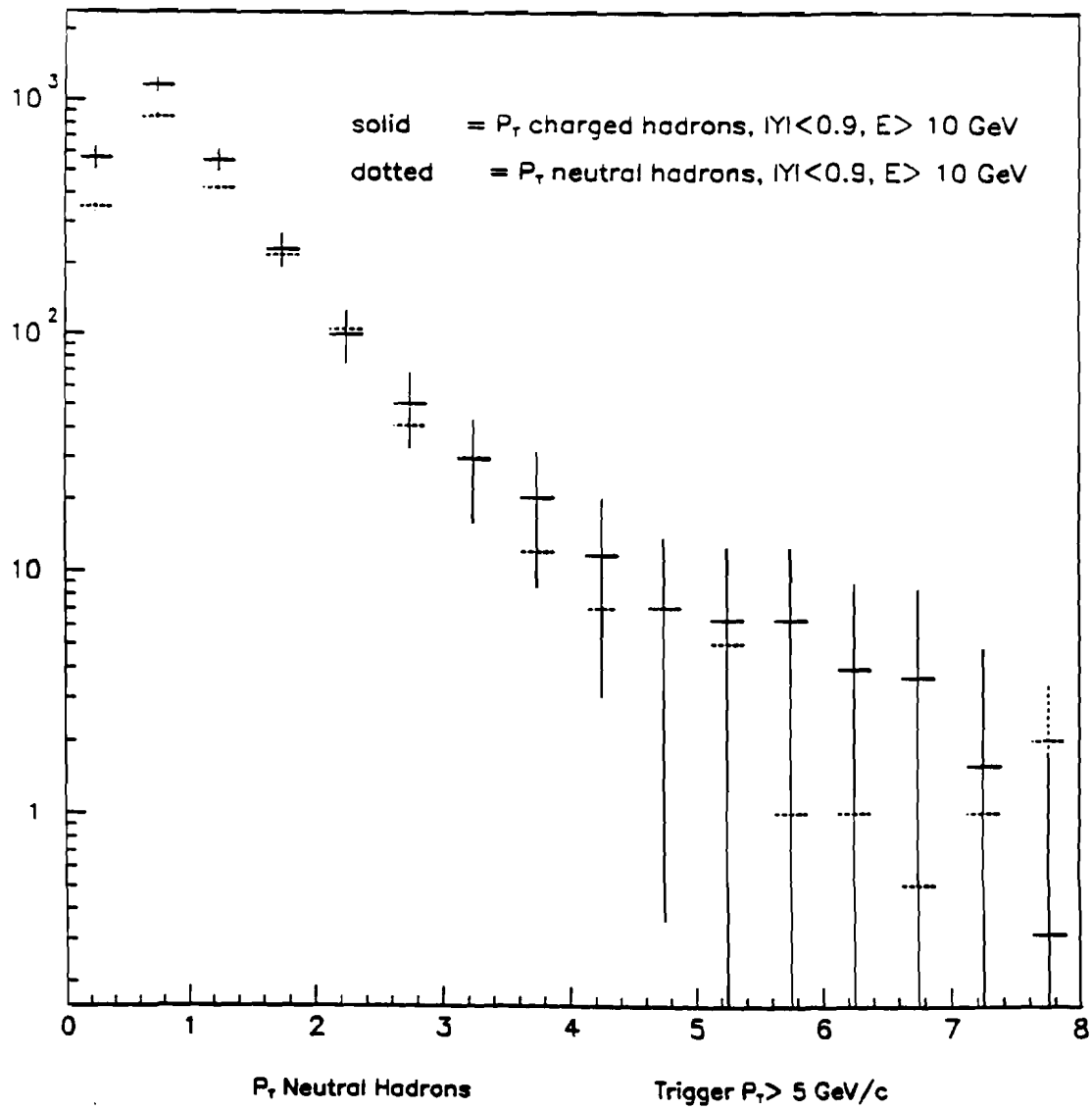

Figure 97: The transverse momentum distributions of the tracks with $|y| < 0.9$ and energy greater than 10.0 GeV are are normilized to be equal in the region 2 tp 4 GeV/c with the neutral hadron p_T distribution. Note the scale change of the neutral distribution. Only a fraction of the total data is shown. The distributions have not been corrected for trigger efficiency or detector acceptance.

The distributions differ from each other at low p_Ts because the HALAC efficiency is lower than the tracking efficiency in this region.

The percentage of events where the leading particle (i.e., the the highest p_T particle residing in the hemisphere away from the high p_T shower) was a neutral hadron (mostly $K^o{}_L$ or neutron) or a π^o or charged hadron, are shown in the following table for the high p_T single photon or π^o events, for the proton and π^- beam data. The measurements have not been corrected for reconstruction inefficiencies and detector acceptance. All leading particles were restricted to the rapidity interval $|\Delta y| \leq 0.9$ and their $p_T \geq 1.5$ GeV/c.

LEADING PARTICLE	Proton Beam		π^- Beam	
	Direct Photon	π^o	Direct Photon	π^o
Charged hadron (%)	73	76	73	71
Neutral hadron (%)	9	7	8	9
π^o (%)	18	17	19	20

Table 13: The percentage of events where the highest p_T particle residing in the hemisphere away from the high p_T photon, was a neutral hadron a π^o or charged hadron. The measurements have not been corrected for reconstruction inefficiencies and detector acceptance.

The 3-momentum of each particle is projected on the plane transverse to the beam. This plane is called the p_T plane. Figures 98 and 99 each show an event where all particles that survived the cuts described in the previous sections are projected on the p_T plane. Evident are the two dimensional vectors on the

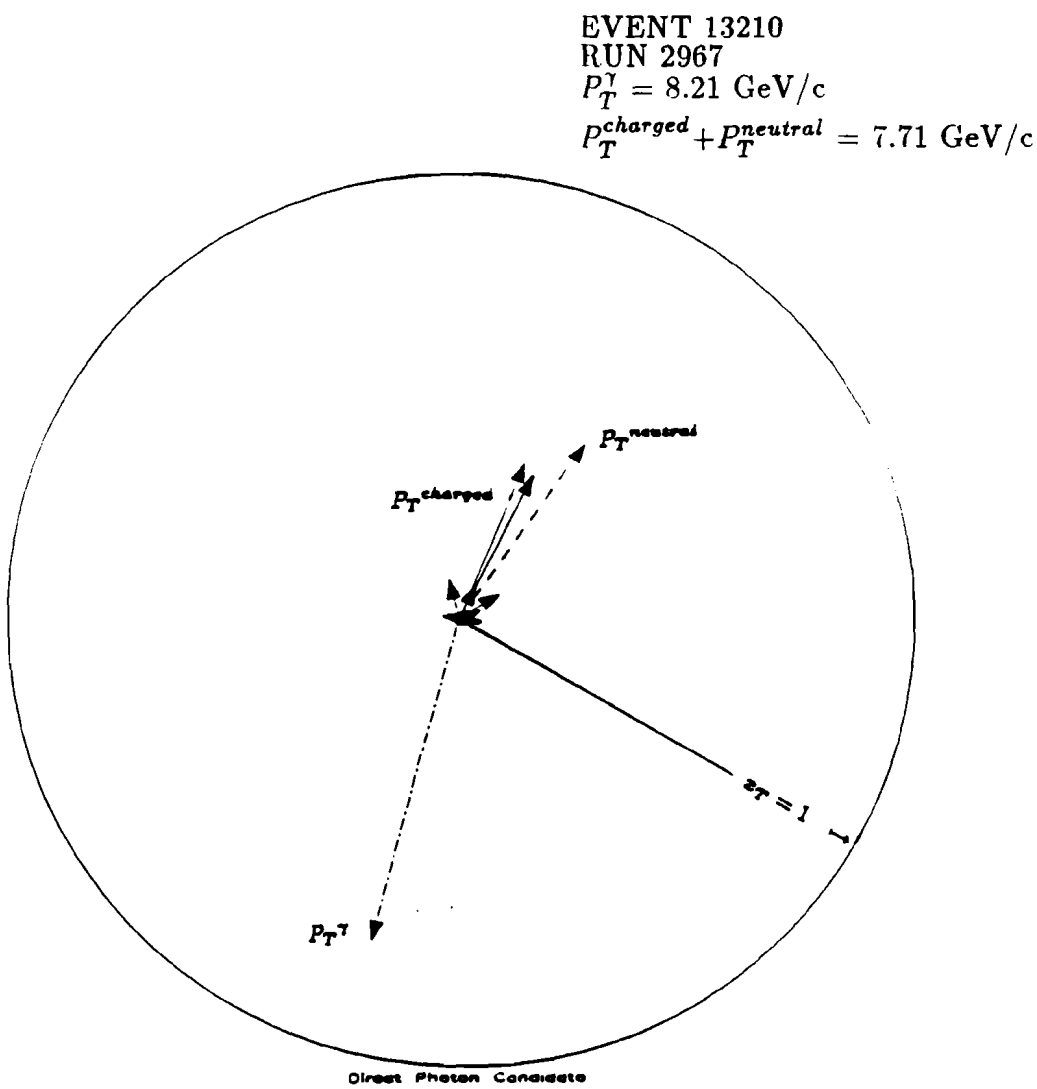

Direct photon candidate $\mapsto$ $P_T{}^{\gamma}$ (dotted-dashed line)

Charged particles $\mapsto$ $P_T{}^{charged}$ (solid line)

Neutral particles $\mapsto$ $P_T{}^{neutral}$ (dashed line)

All P_T vectors (except the $P_T{}^{\gamma}$) have been magnified two times for visual reasons.

Figure 98: An event where particles that survived the cuts described in the text are projected on the p_T plane.

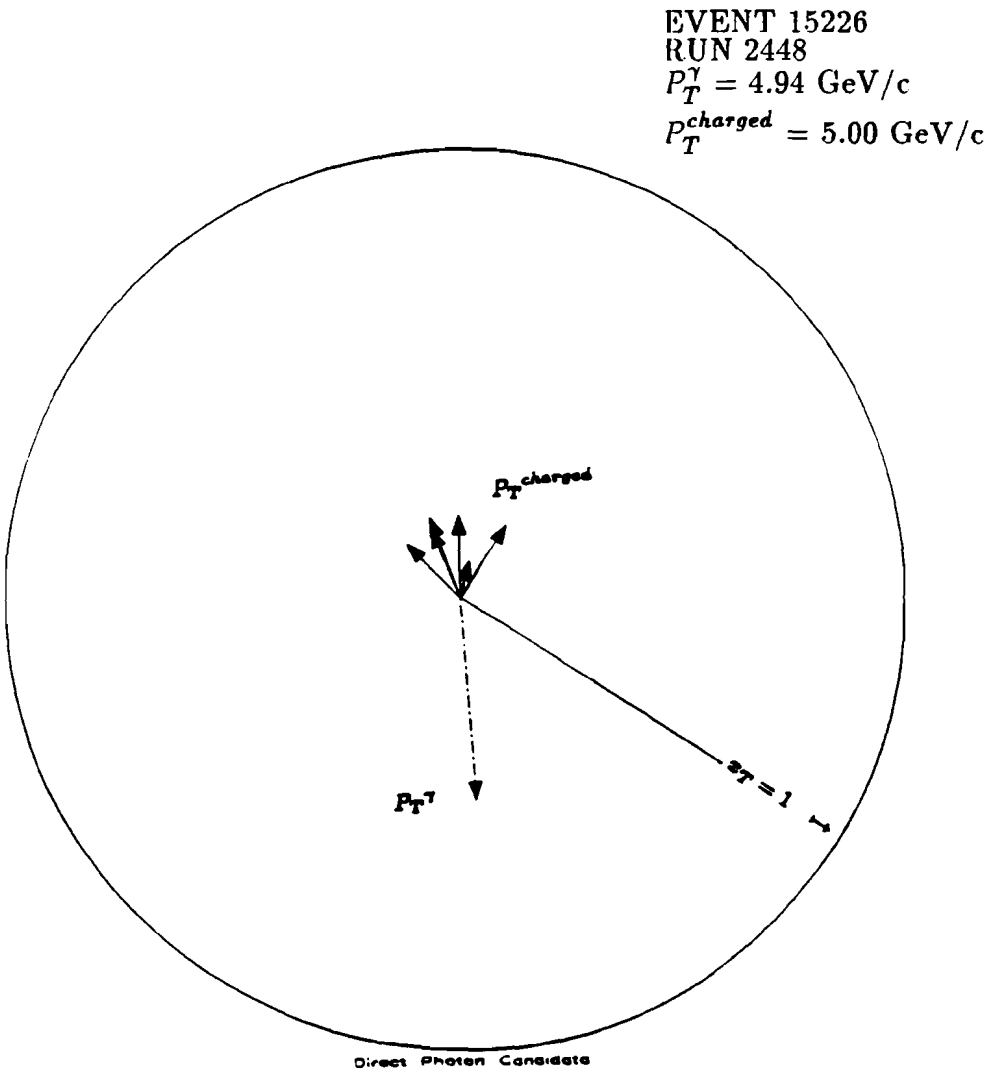

Direct photon candidate $\mapsto$ $P_T{}^{\gamma}$ (dotted line+dashed line)

Charged particles $\mapsto$ $P_T{}^{charged}$ (solid line)

All P_T vectors (except the $P_T{}^{\gamma}$) have been magnified two times for visual reasons.

Figure 99: An event where particles that survived the cuts described in the text are projected on the p_T plane.

p_T plane corresponding to the transverse momentum of the trigger particle, the transverse momenta of the particles associated with the awayside jet, and the low p_T particles. The particle with the maximum p_T in the event is the single gamma candidate and is labeled as $p_T{}^{\gamma}$ and plotted with a dot-dash line. The charged particles are plotted with solid lines and are labeled as $p_T{}^{charged}$. The neutral particles are plotted with the dashed lines and are labeled as $p_T{}^{neutral}$. The radius of the plotted circle corresponds* to $x_T = 1$. The vectors of all particles, except the $p_T{}^{\gamma}$, in Figures 98, and 99 have been magnified two times to make the figure clearer.

6.6. Total p_T

At high p_T, where the k_T effects (i.e., the effects originating from the fact that the partons have an intrinsic transverse momentum relative to the colliding hadrons) become less important, the p_T of the particles recoiling from the high p_T single γ (i.e., the recoiling jet) should balance the $p_T{}^{\gamma}$. This is true since the forward and backward jet particles, which originate from the spectator partons, have the following two characteristics:

a) The average p_T is small.

b) Their directions on the p_T plane are distributed isotropically.

The measurement of the total transverse momentum of the event p_T along the single γ direction is affected by differences in the energy resolution and energy scale for photons and jets, jet acceptance, and the k_T smearing effects. The particles

* $x_T = P^*{}_T/P^*{}_{max} \simeq 2p_T{}^*/\sqrt{s}$. The maximum momentum the photon can carry is $P_T{}^* = \sqrt{s}/2$ which corresponds to $x_T = 1$. Note that $p_T{}^{\gamma}$ is kinematically limited to $\sqrt{s}/2$ since the spectator quarks carry a significant fraction of the momenta of the colliding particles.

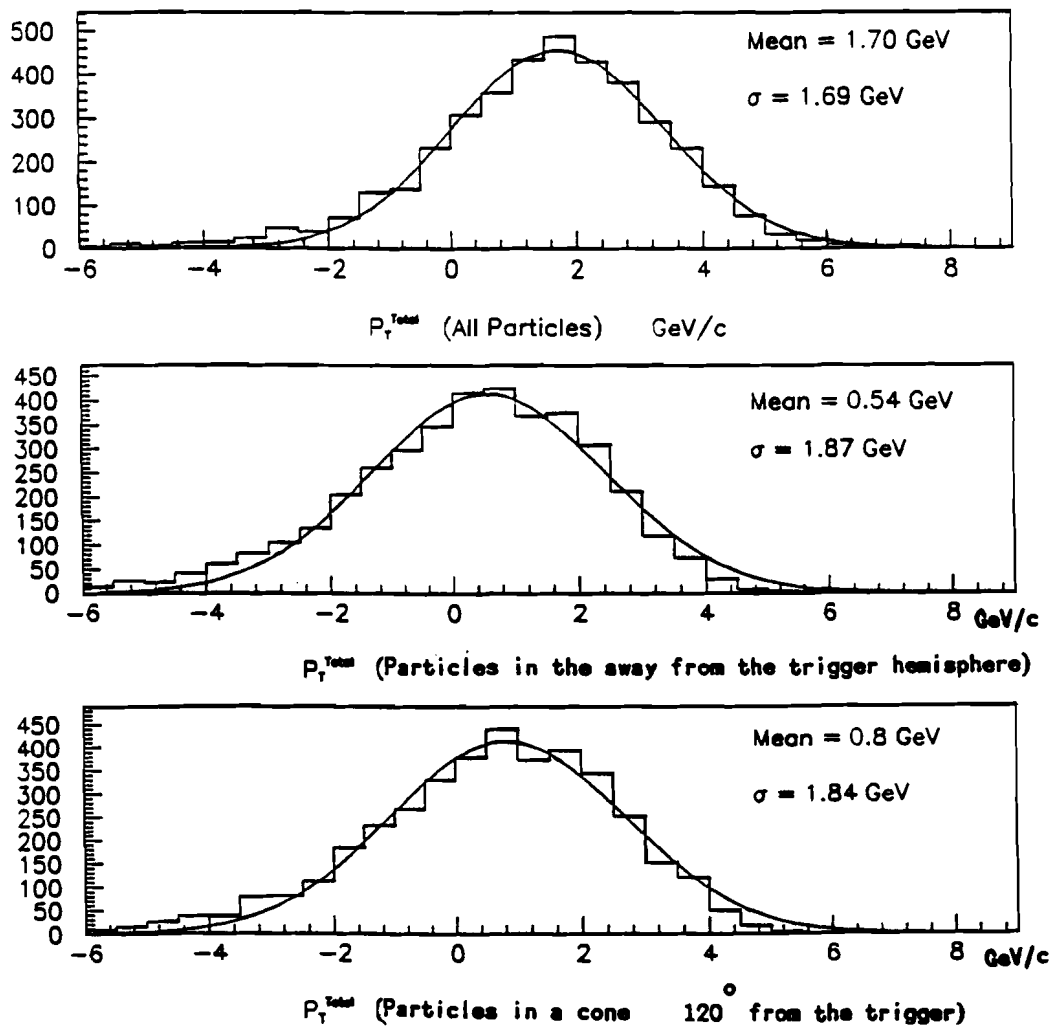

Figure 100: The $p_T{}^{total}$ distribution for all events (i.e., π^0 and single γ triggers with $p_T > 5.0$ GeV/c). Only a fraction of the total data is shown. The distributions have not been corrected for trigger efficiency or detector acceptance.

belonging to the forward jet can be separated (to some extent) from the particles belonging to the awayside jet if a p_T cut is used. This measurement is sensitive to possible systematic errors in the clustering algorithm which assigns the particles to the jet. In this analysis we did not attempt to define the awayside jet. Instead the p_T of all particles in the event was measured. The name assigned to this quantity is "$p_T{}^{total}$" of the event and is defined as follows,

$$p_T{}^{total} = |\mathbf{p_T}{}^{\gamma}| + \sum_{i=1}^{N} \frac{\mathbf{p_T}{}^{i} \cdot \mathbf{p_T}{}^{\gamma}}{|\mathbf{p_T}{}^{\gamma}|}$$

where the summation runs over all particles in the event except the highest p_T photon. Figure 100 (top graph) shows the $p_T{}^{total}$ distribution for all events (i.e., π^0 and single γ triggers with $p_T > 5.0$ GeV/c). The average $p_T{}^{total}$ is 1.70 GeV/c. Figure 100 (middle graph) shows the $p_T{}^{total}$ distribution for all events when we considered only the particles with an azimuthal angle greater than 90 degrees relative to the trigger particle. Figure 100 (bottom graph) shows the $p_T{}^{total}$ distribution for all events when we considered only the particles with an azimuthal angle greater than 120 degrees relative to the trigger particle. Also it was observed that the $p_T{}^{total}$ was higher when the away jet was close to the acceptance boundaries.

Figure 101 (top graph) shows the variations in $p_T{}^{total}$ as a function of the rapidity of the leading particle.* Figure 101 (bottom graph) shows that $p_T{}^{total}$ is independent of the rapidity of the neutral trigger. We define:

$$|\sum_{i=1}^{N} x_e^i| = |\sum_{i=1}^{N} \frac{\mathbf{p_T}{}^{i} \cdot \mathbf{p_T}{}^{\gamma}}{|\mathbf{p_T}{}^{\gamma}|^2}|$$

The $\sum x_e^i$ as a function of the p_T of the trigger is shown in Figure 102 (top

* We assume that the leading particle in the jet is produced along the jet direction.

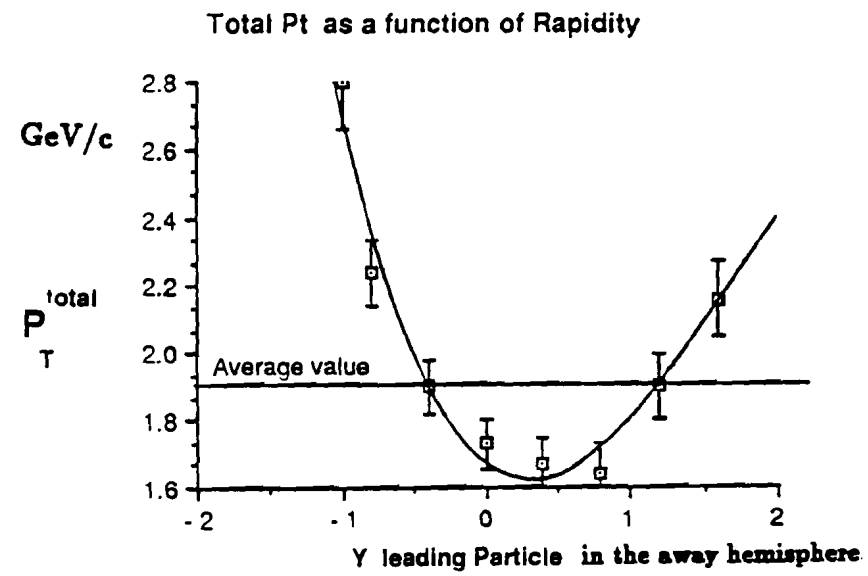

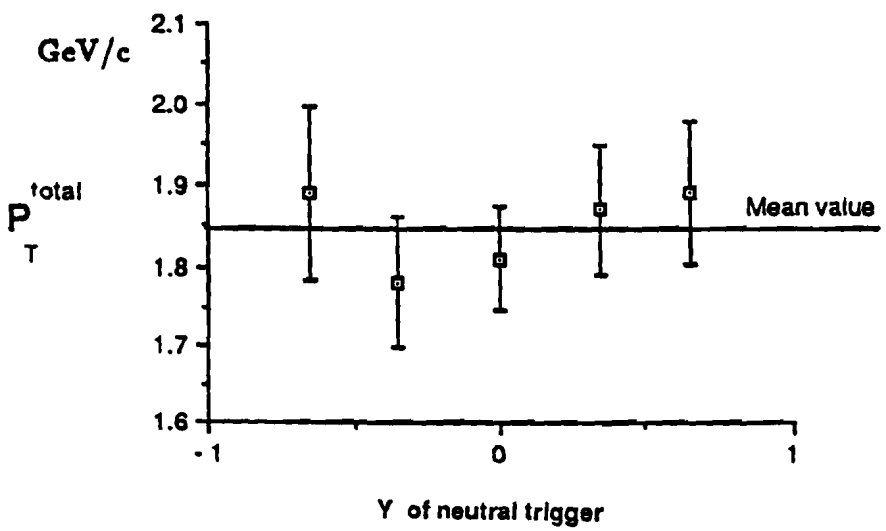

Figure 101: p_T^{total} **as a function of the rapidity.**

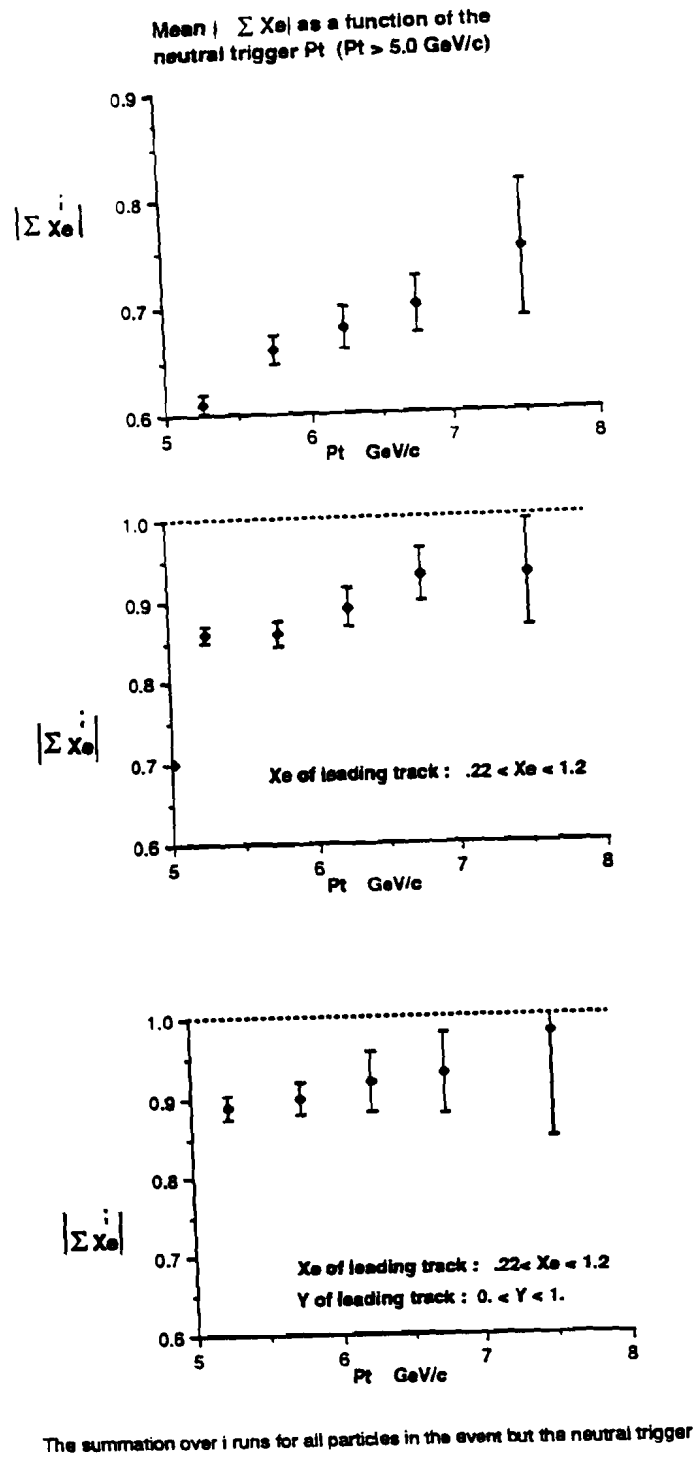

Figure 102: Mean $|\sum x_e|$ as a function of the p_T of the neutral trigger.

graph). This quantity is called x_e and it is introduced in Section 7.4. There is a clear tendency to have events with better p_T balance for higher p_T events. Figure 102 (middle graph) shows the same ratio when the leading charged particle is required to carry at least 22% of the p_T of the neutral trigger. In Figure 102 (bottom graph) the leading particle is also restricted in the forward region. In these cases, where the events are required to have a high p_T leading particle in the awayside, the p_T of the neutral trigger is almost balanced by the p_T of the rest of particles in the event. The last plot in Figure 102 indicates that we can measure about 93% of the transverse momentum of particles in the events with the single photon, provided that we select events where the jet direction points inside the apparatus acceptance. Besides the acceptance losses other losses are expected due to undetected low energy neutral hadrons and γs, and inefficiencies in the pattern recognition for both the charged tracks and the showers reconstructed in the LAC.

The beam particles hit the target with a small incident angle. The beam had an angle relative to the coordinate system. Thus, the beam had a p_T (Figure 103, top graphs). The beam p_T should be taken into account in the measurement of the ${p_T}^{total}$. As seen in the Figure 103 (bottom diagram) the contribution of the beam p_T to the p_T of the single photon is small. For example if we assume that the energy of the single photon is 100 GeV and its measured p_T is 4 GeV/c then the formula of Figure 103 gives for the real p_T of the single photon,

$$ {p_T}^{real} = 4.0 - 100.0 \times 0.001 = 3.9 \text{ GeV/c} $$

where the beam angle is $\Theta^{beam} \sim ({p_T}^{beam})/(P^{beam}) \sim 1.0mr$. The component of the beam p_T in the XZ plane is zero. In conclusion, the effect of the beam p_T on the data is negligible.

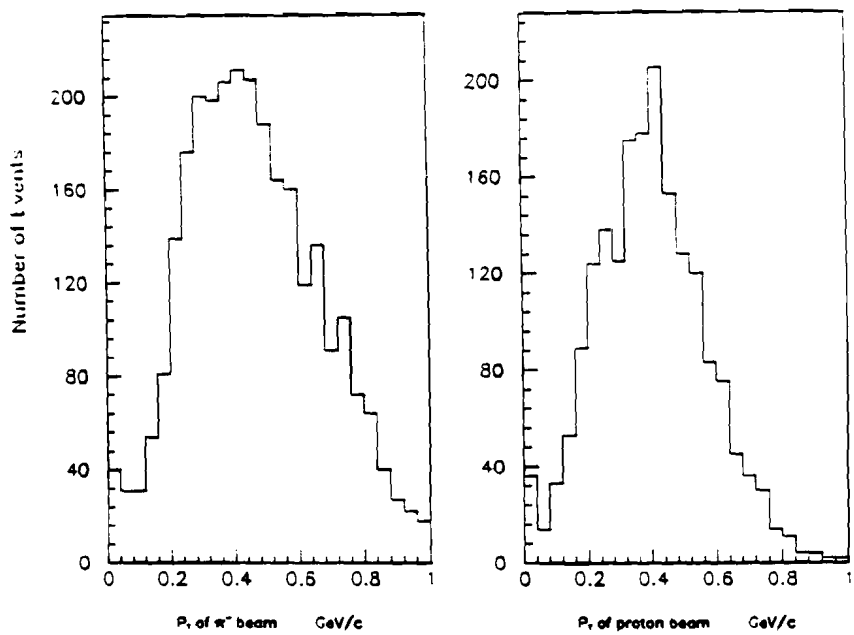

Beam Slope Correction

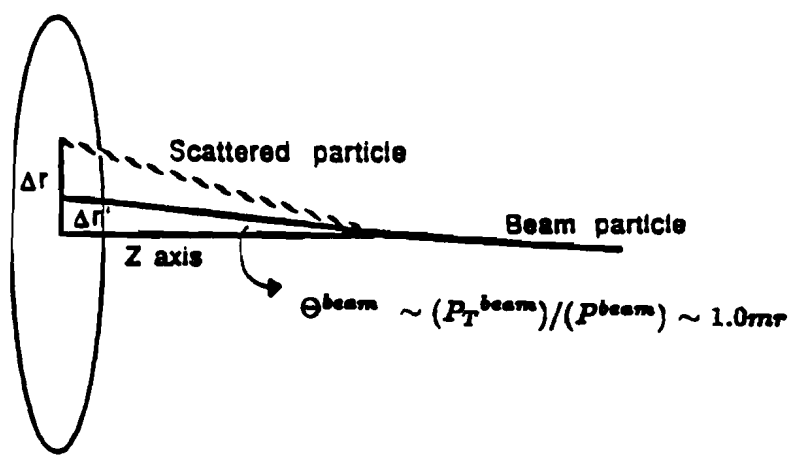

$$P_T = E\left[\frac{\Delta r - \Delta z \tan\theta}{\Delta z}\right] = p_t^{old} - E \tan\theta$$

$$\Delta r' = \Delta z \tan\theta$$

Figure 103: (top): p_T of the beam. (bottom): The beam slope correction calculation.

6.7. The Backgrounds for Direct Photons Due to $\pi^o \rightarrow \gamma\gamma$

The main source of background to the direct photon events arises from the $\gamma\gamma$ decay of π^os in which one of the photons is not detected for one of the following reasons:

1. **Geometry:** Only one photon from $\pi^o \rightarrow \gamma\gamma$ decay hits the effective area of the EMLAC.

2. **Energy threshold:** Because of the energy threshold of the EMLAC, one of the γs is not detected.

3. **Reconstruction:** One of the photons from $\pi^o \rightarrow \gamma\gamma$ decay gets mismatched with another photon (or photons if r and ϕ views are mismatched separately) from the event.

4. **Coalescing:** The two photons are not resolved and therefore misidentified as one, more energetic single photon. This contribution should increase with the energy of π^o since the minimum opening angle is given by $\theta^{min} \sim 2 \cdot m_{\pi^o}/E_{\pi^o}$.

5. **Conversions:** One (or both) of the two π^o photons converts to an e^+e^- pair before it reaches the detector. Background contributions from 1, 2, and 4 were calculated using the Monte Carlo method. The π^o events were generated according to the experimental spectrum using the E-706 Monte Carlo package. The generated events were reconstructed using the same analysis program as the real data.

The single photon background, ${f_\gamma}^{fake}$, was calculated in the following way,

$$ {f_\gamma}^{fake} = {f_\gamma}^{unused} \cdot (1.0 - c) \; + \; c \cdot {f_\gamma}^{All} $$

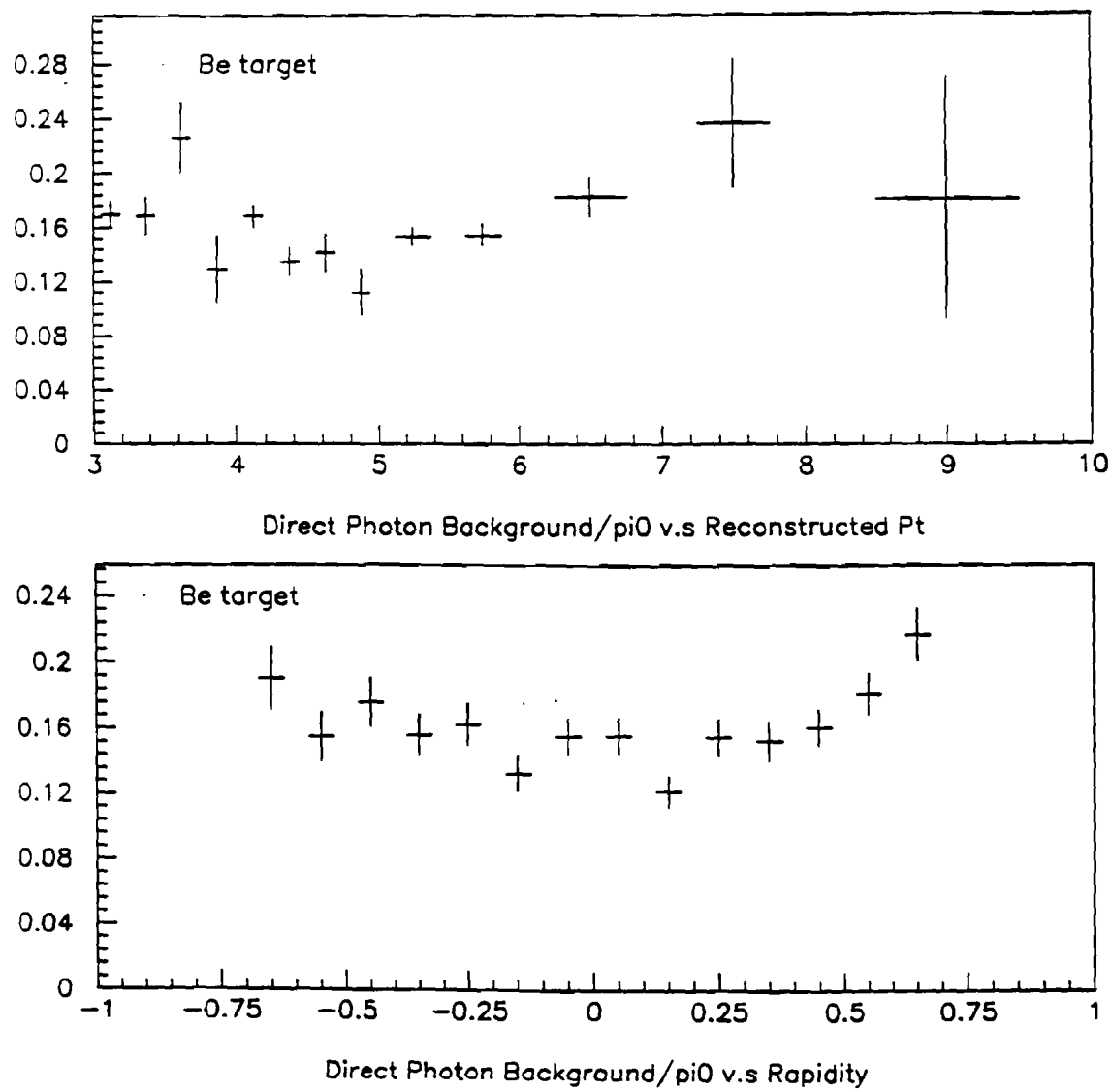

Figure 104: (top): R_{fake} for the negative and positive beam data. The average R_{fake} value for p_T higher than 5.0 GeV/c is 16% for both beam polarities (see text). (bottom): R_{fake} as a function of rapidity.

where ${f_\gamma}^{unused}$ is the p_T distribution of the photons which do not reconstruct as π^os because of the reasons listed above, ${f_\gamma}^{All}$ is the Monte Carlo p_T distribution of all photons due to π^o decays, and c is the probability for photons to convert into an e^+e^- pair in the target. c is equal to 5.6% for the Be target (half of the target is considered) and 16.9% for Cu+Be target (half of the Cu and all of the Be).

The ratio of the fake single photon to π^o is calculated as

$$R_{fake} = \frac{{f_\gamma}^{fake}}{{\pi^o}_{recon}}$$

where ${f_\gamma}^{fake}$ is the number of fake single photons from the generated π^o and ${\pi^o}_{recon}$ is the number of the generated π^os that have been reconstructed. Figure 104 shows R_{fake} for the negative and positive beam data. The average R_{fake} value for p_T higher than 5.0 GeV/c is 16% for both beam polarities.

Once R_{fake} and the experimental π^o spectrum were determined, then the fake single photon yield could be evaluated and subtracted from the experimental single photon distribution,

$${f_\gamma}^{Real} = {f_\gamma}^{exp} - R_{fake} \times {f_{\pi^o}}^{exp}$$

where ${f_{\pi^o}}^{exp}$ and ${f_\gamma}^{exp}$ are the single photon and π^o signals, respectively (calculated in the same p_T bin as R_{fake}). Note that no background subtraction was done in the π^o distribution since the background was negligible.

7. RESULTS AND CONCLUSIONS

All events were grouped into four different categories according to the beam polarity and the type of high p_T particle: a) Single photons, from negative beam data, b) Single photons , from positive beam data, c) π^o events from negative beam data and d) π^o events from positive beam data. Each group was further divided into two subgroups according to the transverse momentum of the trigger particle: (1) 5.0 $< p_T <$ 5.5 GeV/c and (2) 5.5 $< p_T$ GeV/c. These p_T ranges were chosen so that there were adequate statistics in both ranges. The p_T for the trigger particle was restricted to over 5.0 GeV/c because the signal-to-noise ratio for the single photons improved with p_T.

The error-bars shown on all the graphs are statistical only.

7.1. Particle Distributions

The angular distributions of charged and neutral particle multiplicities and p_T densities with respect to the high p_T photon or π^o are shown in Figures (105,106) and (107, 108), respectively. Figures 105 and 106 show the particle density as a function of the difference in the azimuthal angle ($\Delta\phi$) between the particle and the high p_T photon or π^o, for different regions of trigger transverse momentum. Figure 107 and 108 show the average value of $\sum |p_T|_i$ for charged and neutral particles as a function of the azimuthal angle $\Delta\phi$ for different p_T ranges. The asterisk lines in these figures indicate a fit to the particle distributions measured in minimum bias events. Minimum bias events were events taken with the interaction trigger. They had to have at least one reconstructed charged track in the center-of-mass rapidity

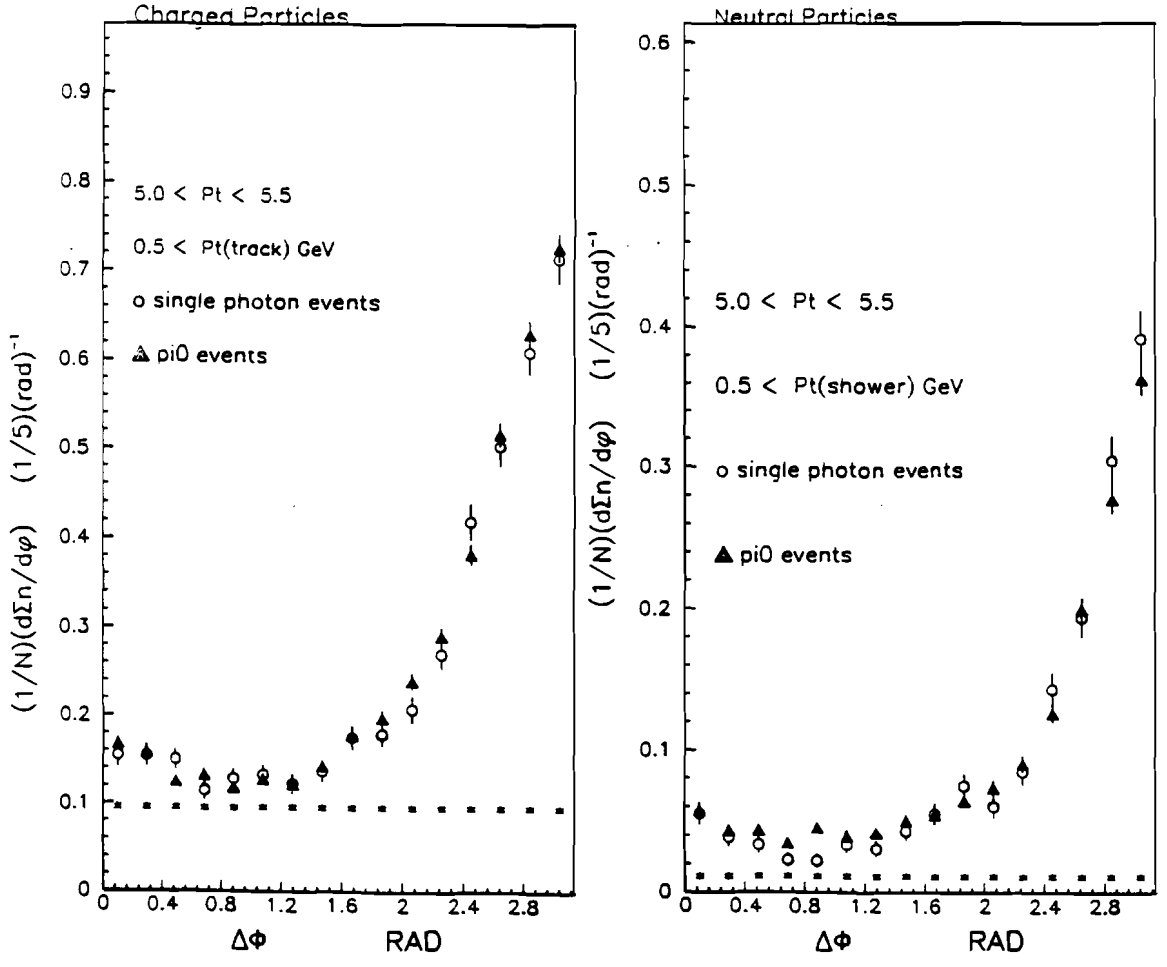

Figure 105: The angular distributions of charged and neutral particle multiplicities with respect to the high p_T photon or π°. Trigger $5.0 < p_T < 5.5$ GeV/c. Only particles with p_T greater than 0.5 GeV/c are counted.

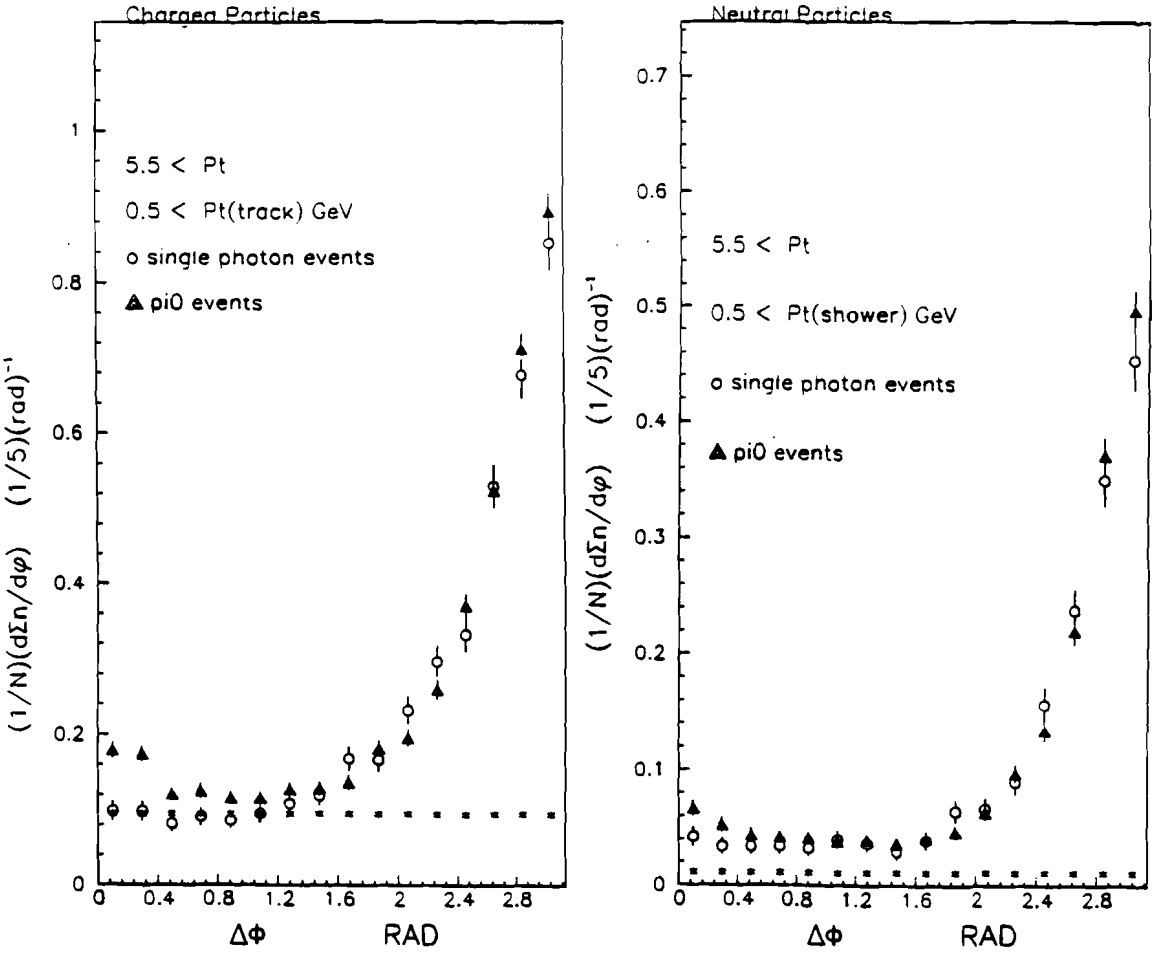

Figure 106: The angular distributions of charged and neutral particle multiplicities with respect to the high p_T photon or π^0. Trigger $5.5 < p_T$ GeV/c. Only particles with p_T greater than 0.5 GeV/c are counted.

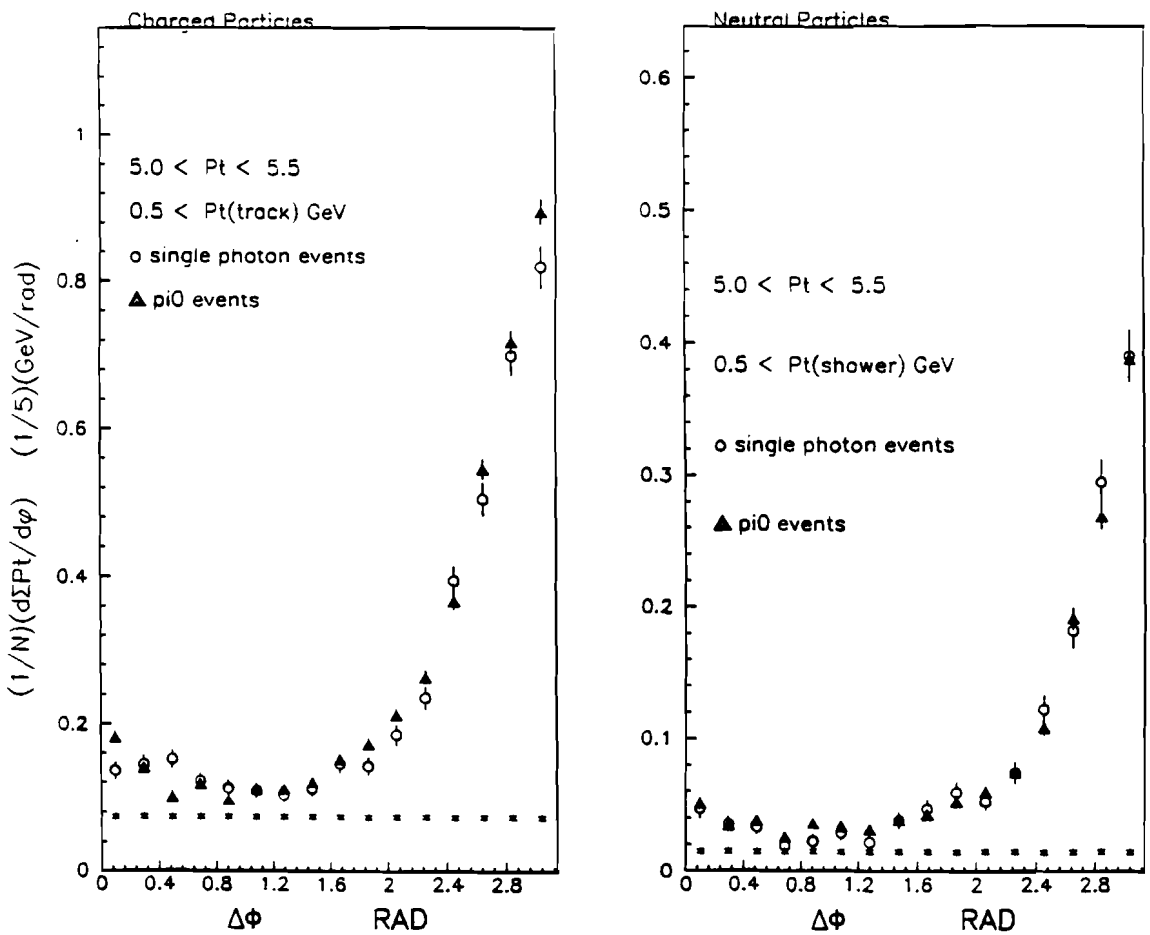

Figure 107: The angular distributions of charged and neutral particle p_T densities with respect to the high p_T photon or π^0. Trigger $5.0 < p_T < 5.5$ GeV/c. Only particles with p_T greater than 0.5 GeV/c are counted.

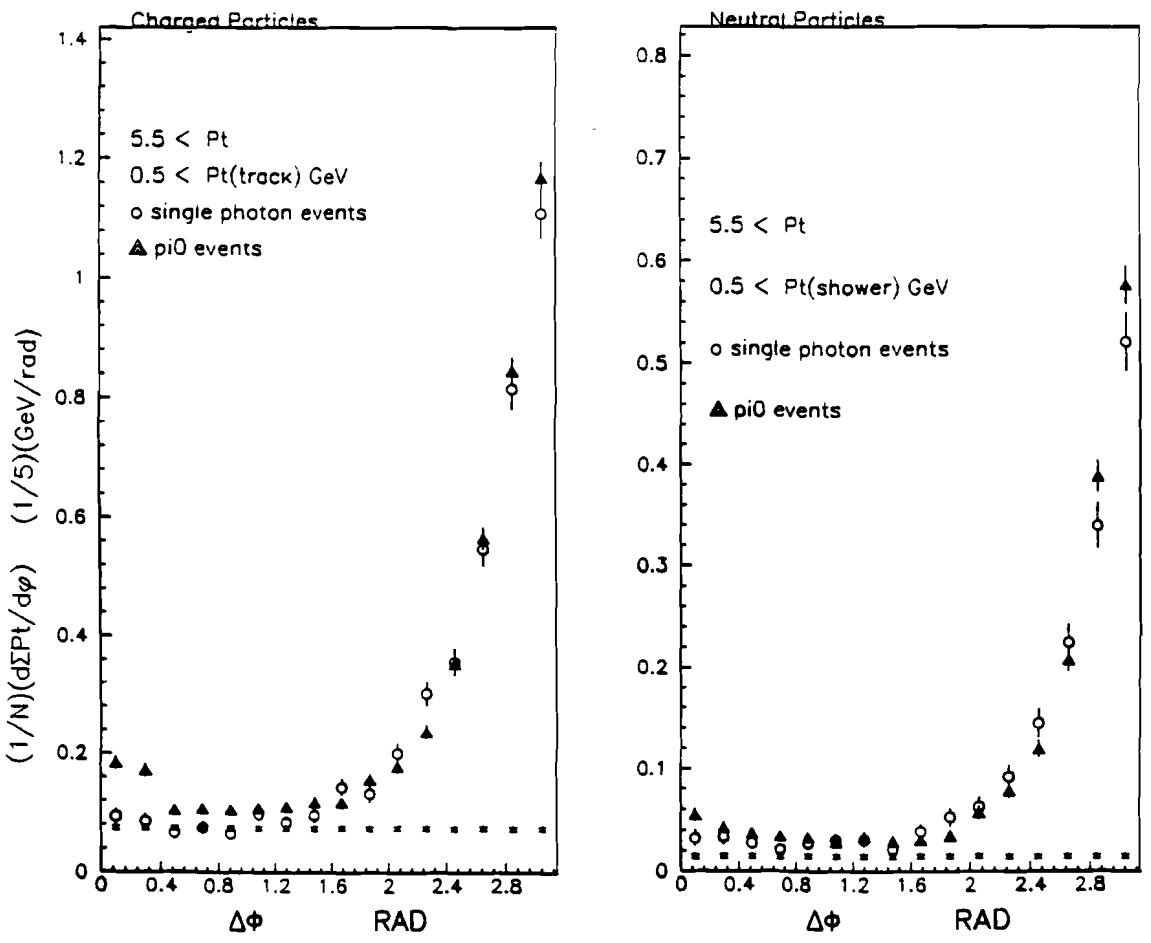

Figure 108: The angular distributions of charged and neutral particle p_T densities with respect to the high p_T photon or π^0. Trigger $5.5 < p_T$ GeV/c. Only particles with p_T greater than 0.5 GeV/c are counted.

interval $|\Delta y| < 1.0$ and the p_T of the leading photon less than 700 MeV/c. The single γ data were corrected for the background contribution from π^o decays. The large peak opposite to the trigger, at $\Delta\phi \sim \pi$ is from the recoiling jet and is very similar for γ and π^o events. In the region $\Delta\phi \sim 0$ there is a clear enhancement in the particle densities over that at $\Delta\phi \sim \pi/3$ for π^o events. This peak near $\Delta\phi \sim 0$ in the π^o events is from the hadrons associated with the π^o. The peak is essentially absent in the case of high p_T γ events. The underlying physics for this is expected to be the following. The π^os are predominantly produced as a fragment of the jet originating from the original quark or gluon, and thus the π^os are frequently accompanied by other particles. The single γs are isolated from other particles when they are produced in the Compton or in the annihilation processes. In bremsstrahlung production, the γ is accompanied by charged and neutral particles. The ratio of bremsstrahlung cross section to the total photon cross section was measured in Reference [22] and calculated in References [17] and [8] for $\sqrt{s}$=63 GeV and $p_T > 5GeV/c$. In the p_T range between 5.0 to 10 GeV/c the contribution of bremsstrahlung component decreases with p_T from 30% to 20%. The consequence of this is that the single γ triggers are more isolated from other particles in the higher p_T interval than the lower one. In the region $\Delta\phi \sim \pi$ the particles recoiling from the π^o have higher density than the particles recoiling from the single photon. The high p_T π^os are produced as a fragment of a jet and do not carry all the p_T of the original parton. Since the q_T of each particle is calculated relatively to the high p_T π^o and not relative to the p_T of the whole "π^o jet", their q_T values are higher relative to the q_T of the particles recoiling from the single photon.

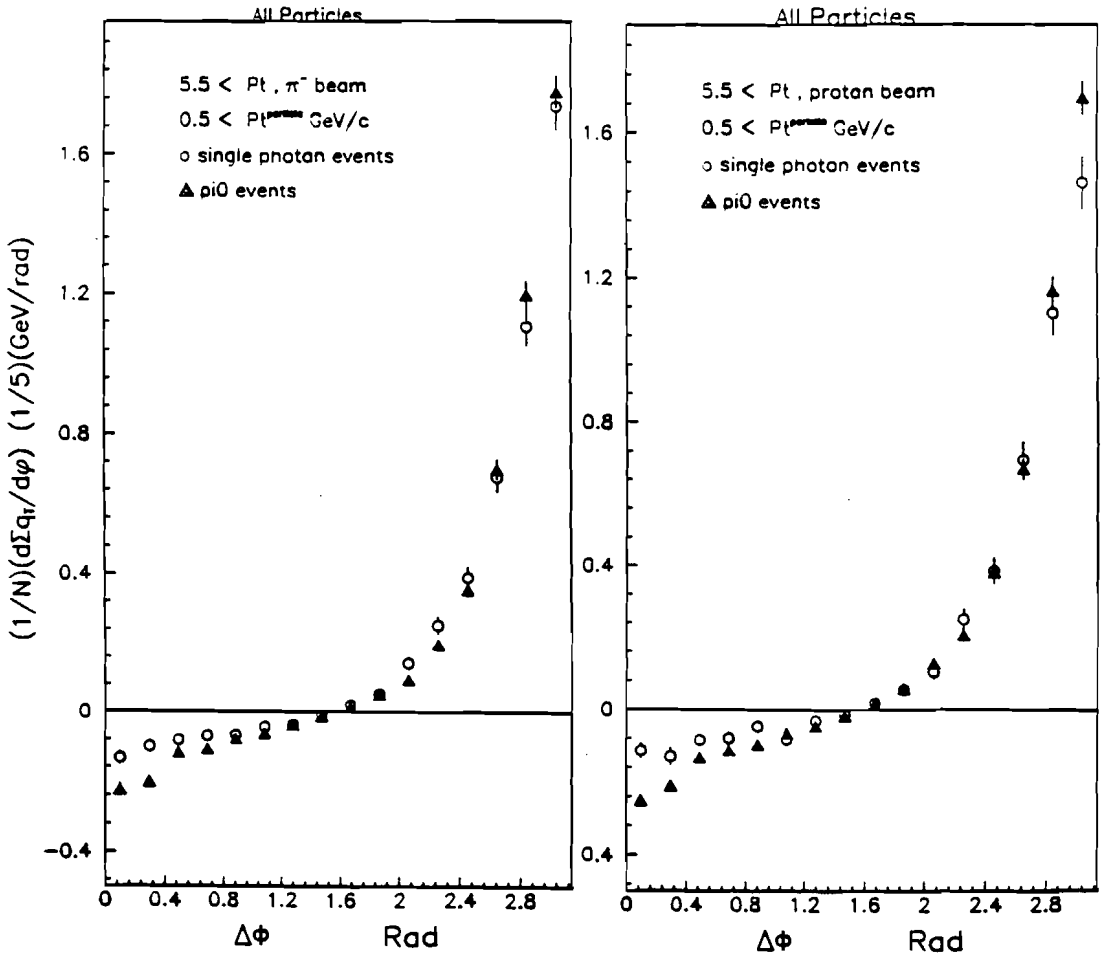

Figure 109: The distribution of the mean value of the sum $\sum |q_T|_i$ for negative beam (left plot) and positive beam (right plot) in intervals of $\Delta\phi$.

Figure 109 shows the distribution of the average value of the sum $\sum q_{T_i}$ for both charged and neutral particles in intervals of $\Delta\phi$ for both beam polarities. q_T is defined as

$$q_T = -\frac{\mathbf{p}_{Th} \cdot \mathbf{p}_{T\gamma}}{|\mathbf{p}_{T\gamma}|} \tag{7.1}$$

where $\mathbf{p}_{T\gamma}$ and $\mathbf{p}_{Th}$ are the transverse momenta of the highest p_T photon (or π^0) and the observed awayside hadron, respectively. Again there is a clear enhancement in -q_T in the region $0 \leq \Delta\phi \leq \pi/3$ for the π^0 events over the single photon events.

Figures 110, and 111 show the particle density and p_T density as a function of the difference in $\Delta\phi$ between all particles and the trigger for different cuts on the particle transverse momentum. Near $\Delta\phi$=0, the particle densities and average p_T accompanying the π^0s are much higher than for single photons and increase with the p_T of the particles in the events.

7.2. Rapidity Correlations

The differences in rapidity, Δy, between the trigger particle and either one or two of the fastest (i.e., the particles with the highest p_Ts) particles on the opposite side are discussed in this section. Only particles with $|x_e| > 0.1$ are used. The number of events is always normalized to the number of single photons.

Figure 112 shows the distribution of $|\Delta y|$ between the rapidity of the trigger particle and the fastest charged track in the event, for ${p_T}^{trig} > 5.0 GeV/c$. The solid line is an estimate of the distribution of $|\Delta y|$ in which there are no correlations between the high p_T photon (or π^0) and the rest of the particles in the event. This,

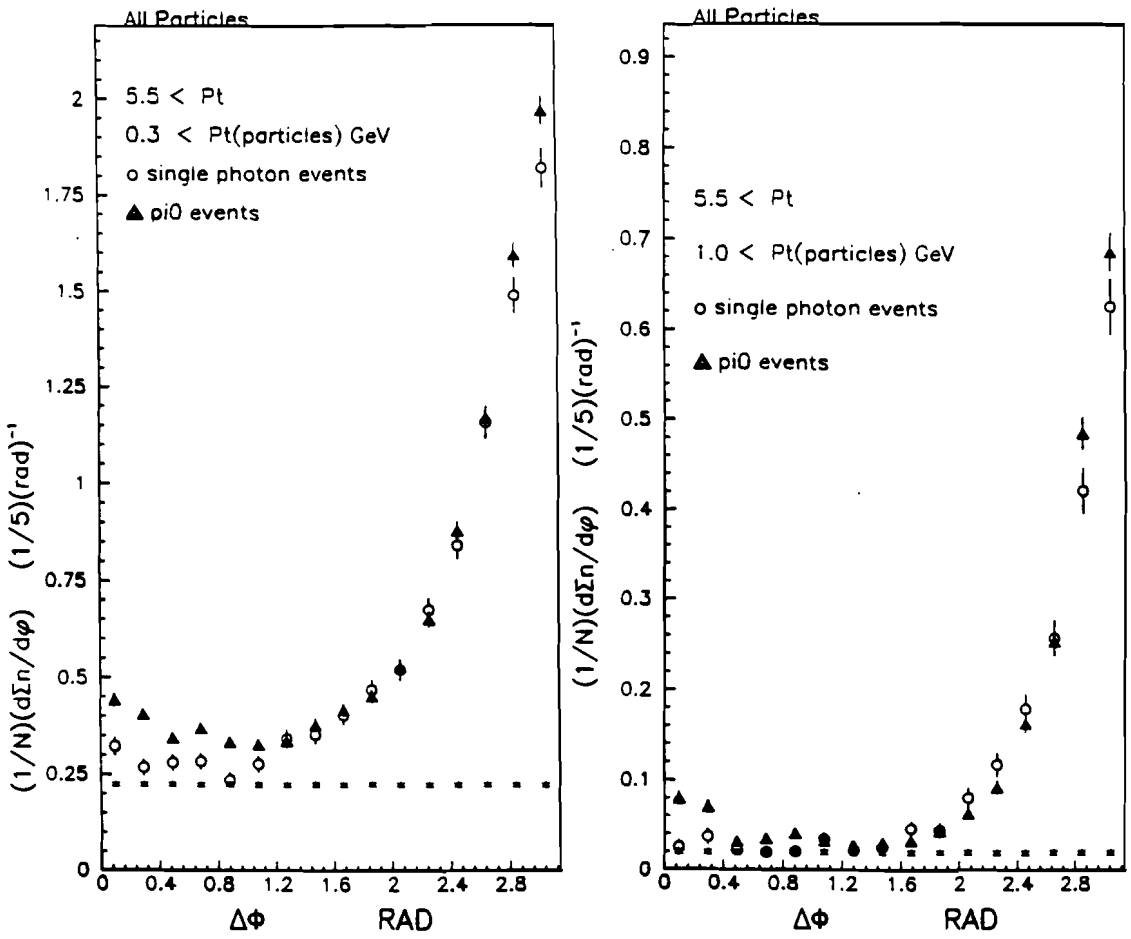

Figure 110: The particle density as a function of the difference in $\Delta\phi$ between the particles and the trigger, for different cuts on the particle transverse momentum.

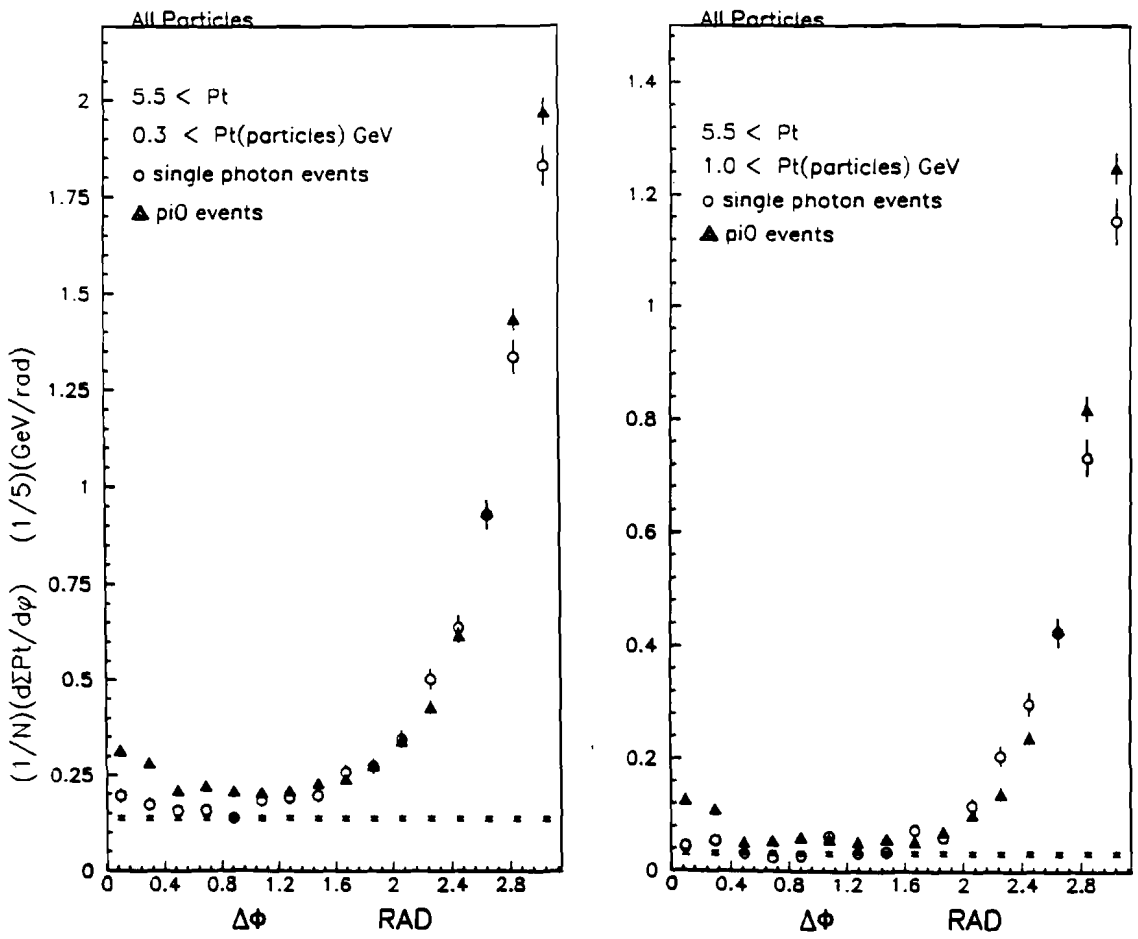

Figure 111: The particle p_T density as a function of the difference in $\Delta\phi$ between the particles and the trigger, for different cuts on the particle transverse momentum.

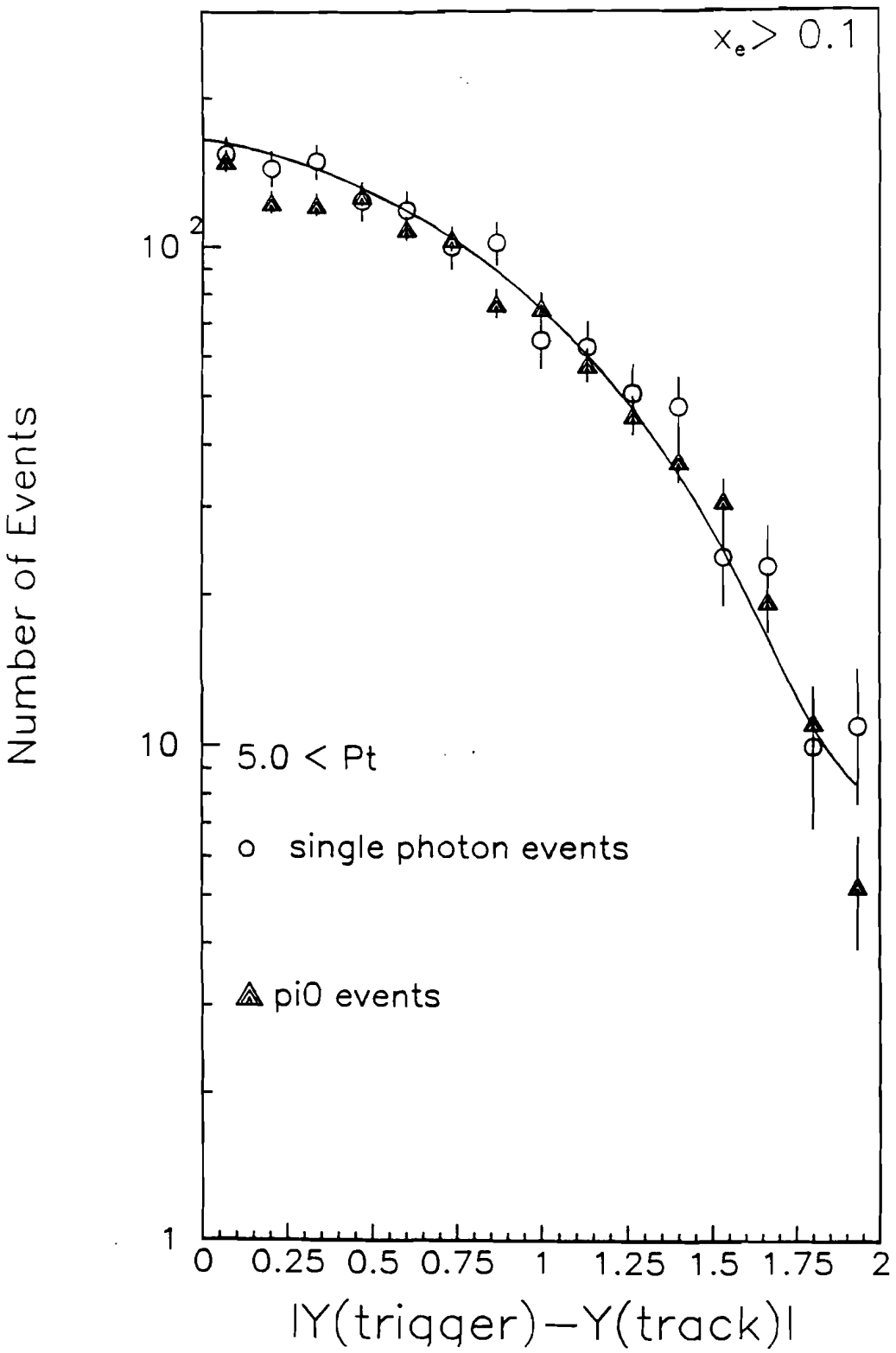

Figure 112: Distribution in $|\Delta y|$, the difference between the rapidity of the trigger particle and the fastest charged track in the event for ${p_T}^{trig} > 5.0 GeV/c$.

solid line, was calculated by taking the rapidity of the high p_T photon (or π^0) and the rapidity of the fastest charged track from different events but otherwise with the same selection criterion as the actual events ("kinematical characteristics"). The distributions obtained are very similar to the solid lines. Assuming that the direction of the recoiling jet is strongly correlated to the direction of the fastest particle, this indicates that the rapidities of the trigger and the recoiling jet are uncorrelated. There is little difference between the distributions for events with single photon and with π^0 triggers. In all figures in this section, the total number of π^0 and photon events are normalized to be equal.

Figure 113 shows the rapidity difference between the two fastest charged tracks opposite to the high p_T photon (or π^0). The method used to calculate the solid line is as before by taking the rapidity of one of the fastest particles from a different event with the same "kinematical characteristics". The excess of events for small rapidity difference, above the uncorrelated distribution (solid line), is attributed to the jet-like structure of the track distribution opposite to the high p_T photon (or π^0). This effect is seen more strongly in the higher p_T region. Again there is little difference between the distributions for events with single photons and with π^0s. Figure 113 (right plot) shows the same distribution as the left plot, but for higher ${p_T}^{trig}$ range.

Figures 114 and 115 show the rapidity difference between the two fastest particles opposite to the neutral trigger, for the same p_T ranges of the trigger for the following two cases:

a) One of the two fastest particles is a neutral hadron (reconstructed in the HALAC and the EMLAC) and the other one is a charged track (Figure 114)

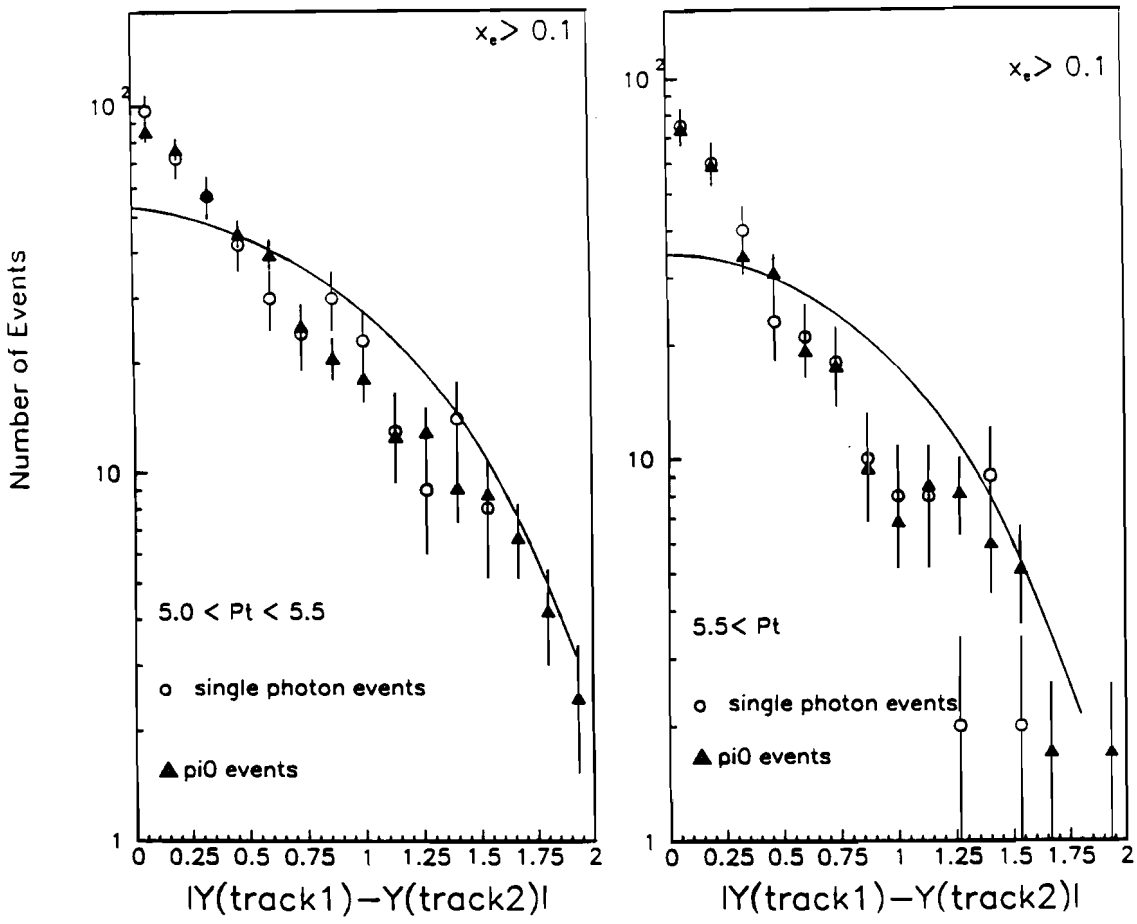

Figure 113: The rapidity difference between the two fastest charged tracks opposite to the high p_T photon (or π°). The π° events are normalized to the number of single photon events.

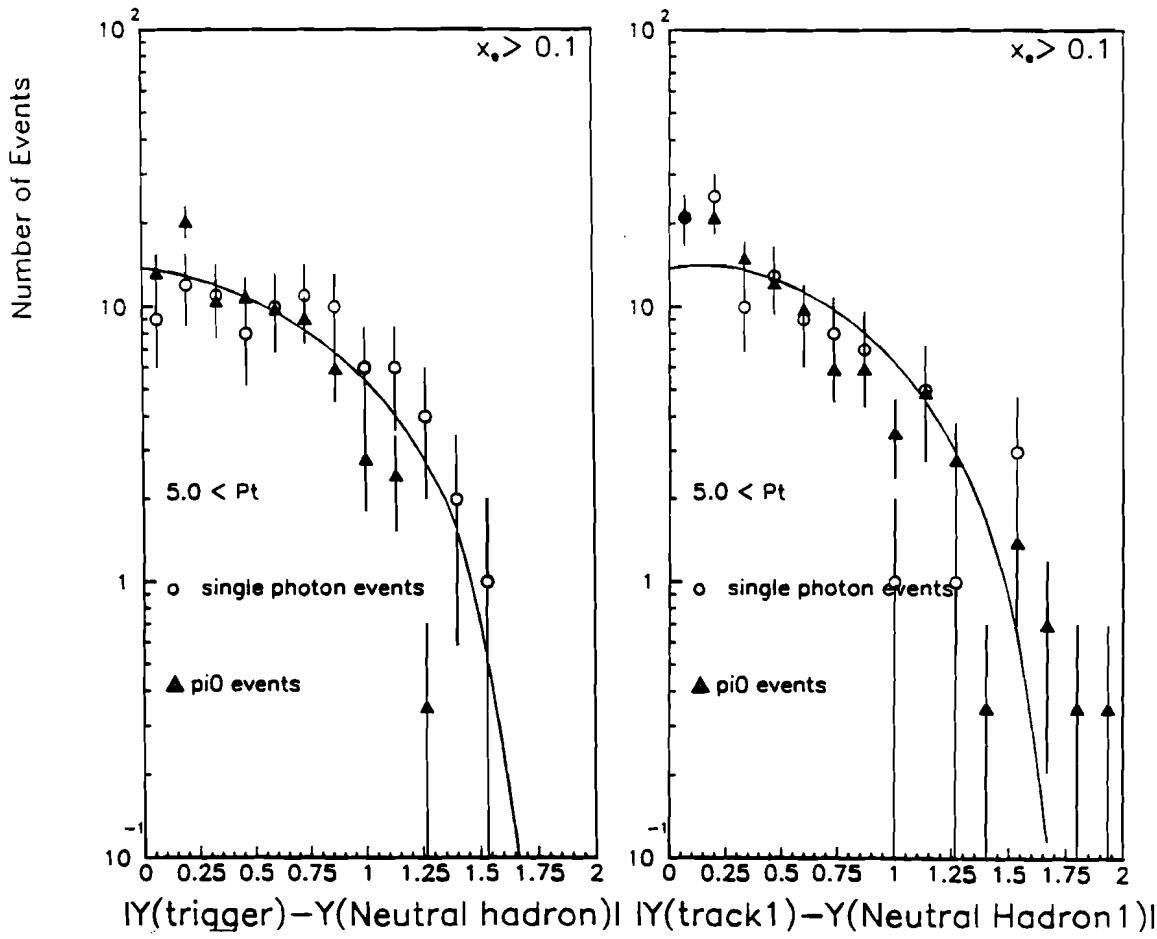

Figure 114: The rapidity difference between the two fastest particles opposite to the neutral trigger, for the same p_T ranges of the trigger when one of the two fastest particles is a neutral hadron (reconstructed in the HALAC and the EMLAC) and the other one is a charged track. The π^0 events are normalized to the number of single photon events.

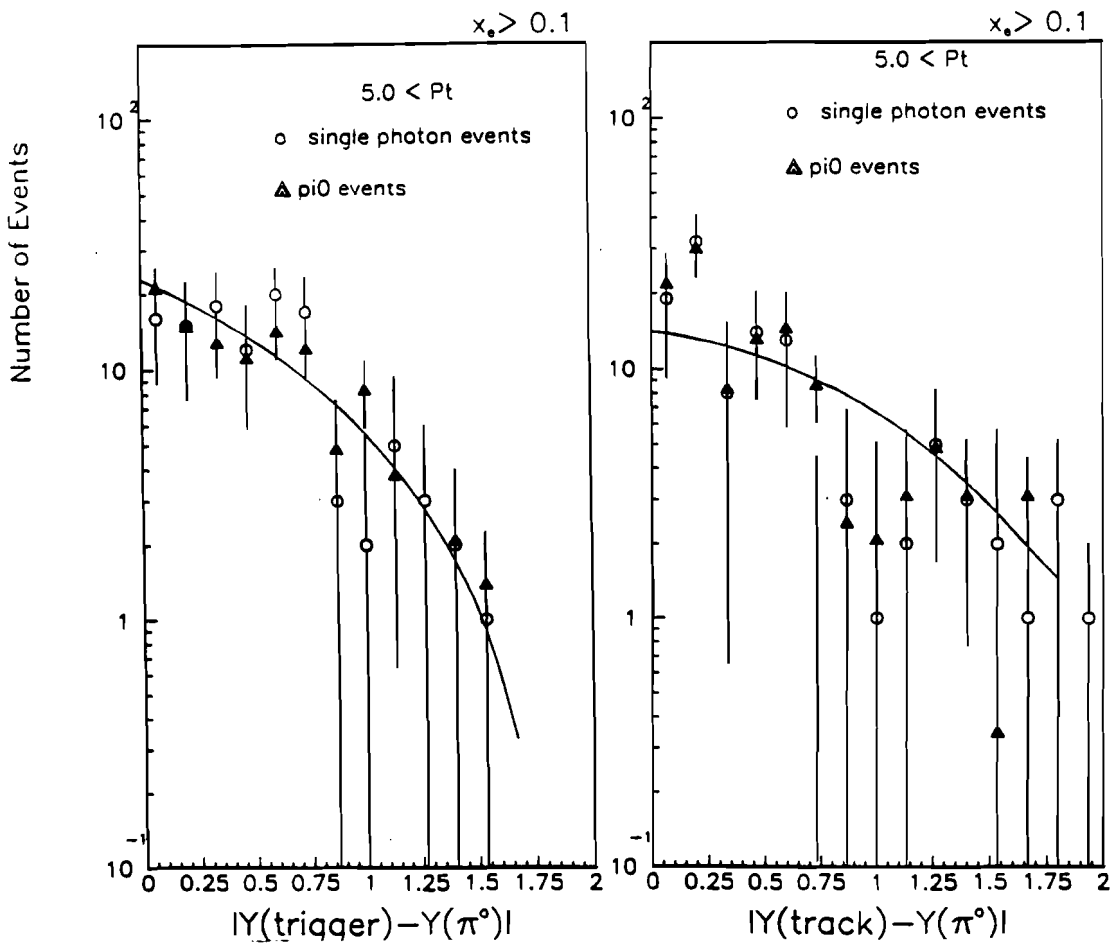

Figure 115: The rapidity difference between the two fastest particles opposite to the neutral trigger, for the same p_T ranges of the trigger when one of the two fastest particles is a π^0 (reconstructed in the EMLAC) and the other one is a charged track. The π^0 events are normalized to the number of single photon events.

b) One of the two fastest particles is a π^o (reconstructed in the EMLAC) and the other one is a charged track (Figure 115) The solid line is drawn as before, by mixing the triggers from different events with the same "kinematical characteristics". Again there is an excess of events for small rapidity difference above the uncorrelated rapidity line. The rapidity distributions of charged particles are consistent with other experiments (Ref. [23]).

Figure 116 shows the distribution of the difference between the rapidity of the high p_T photon (or π^o) and the rapidity of the leading track on the same side with the high p_T photon (i.e., $\Delta\phi < \pi/2$) for four ${p_T}^{track}$ cuts. The solid line is calculated as indicated above, by mixing the high p_T photon (or π^o) from different events. These distributions show some deviations from the uncorrelated distributions shown by the solid lines. In the π^o events the leading track appears to be more strongly correlated with the high p_T π^o than in the single photon events. This effect is more pronounced when the ${p_T}^{track} > 1.0$ GeV/c. This is because the higher p_T cut, on the leading track accompanying the high p_T single photon or π^o, favors the tracks which are part of either the π^o jet or accompany the bremsstrahlung photon and reduces the low p_T tracks which are part of the forward jet. Since the high p_T π^os are produced along with other particles in the same rapidity interval, they are more strongly correlated with the same side leading tracks than the high p_T single photons.

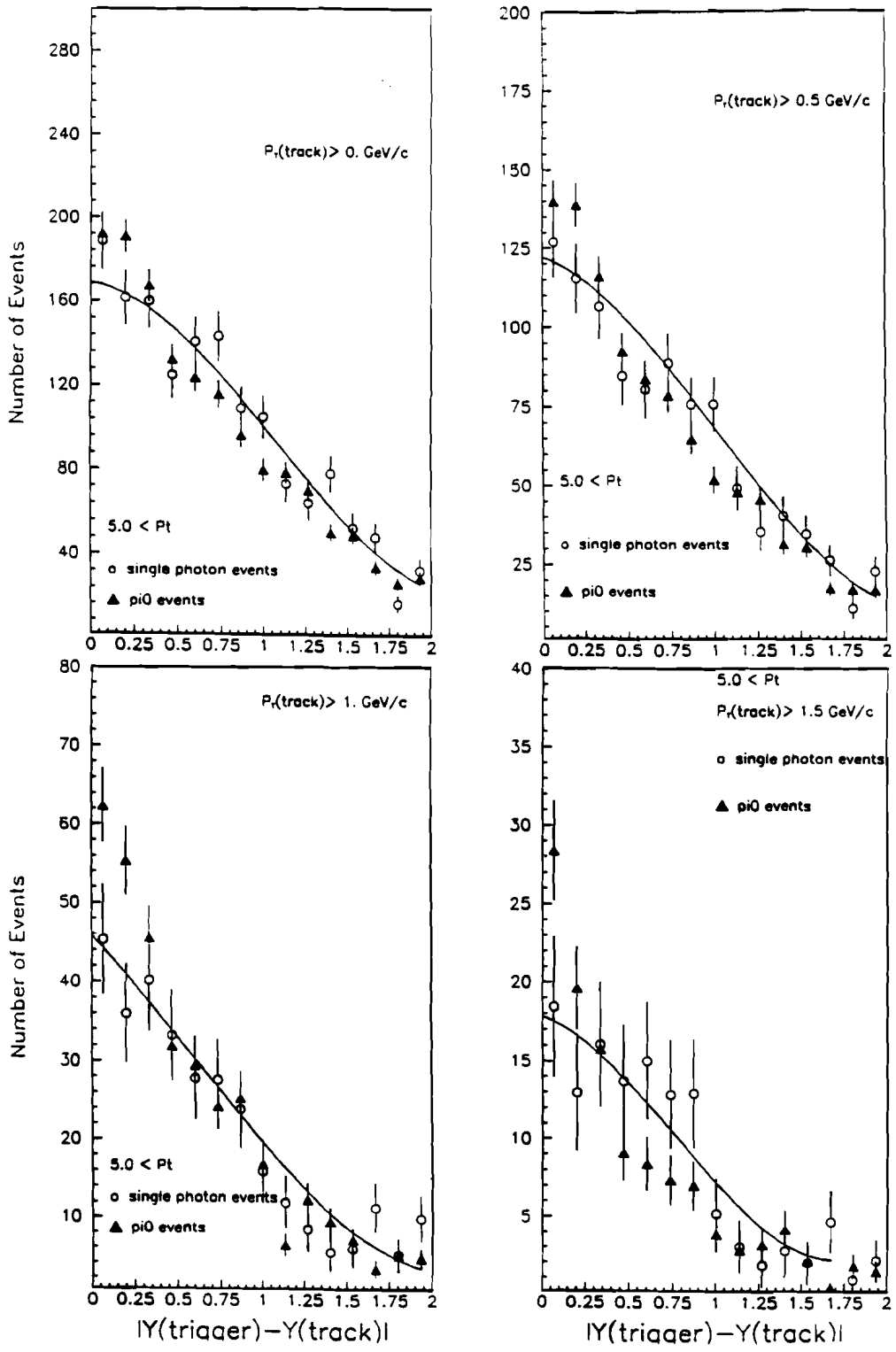

Figure 116: The distribution of the difference between the rapidity of the high p_T photon (or π^0) and the rapidity of the leading track on the same side with the high p_T photon or π^0 (i.e., $\Delta\phi < \pi/2$) for four $p_T{}^{track}$ cuts. The π^0 events are normalized to the number of single photon events.

7.3. Fragmentation Fraction

As stated in Chapter 1 and References [8], [24], [76], [77], [41] and [7], correlations between the trigger photon and the recoiling awayside hadrons in single photon events can yield useful information. In principle, it would be best if the entire awayside jet could be reconstructed and each hadron could then be assigned its respective momentum fraction, z.* In practice, it is often difficult to uniquely assign soft hadrons to a particular jet and an alternative method is used. A useful variable in this instance is x_e defined as[8]

$$x_e = -\frac{\mathbf{p}_{Th} \cdot \mathbf{p}_{T\gamma}}{|\mathbf{p}_{T\gamma}|^2} \tag{7.2}$$

where $\mathbf{p}_{T\gamma}$ and $\mathbf{p}_{Th}$ are the transverse momenta of the trigger photon and the observed awayside hadron, respectively. If the intrinsic transverse momentum of partons and hadron masses are neglected, x_e becomes equal to the usual momentum fraction z. Figure 117 shows the distribution of the mean value of the sum $\sum[x_e]_i$ for both charged and neutral particles in intervals of $\Delta\phi$, for the high p_T single photon and π^o events. In the following, the x_e distributions are studied first for the fastest particle recoiling against the high p_T single photon or π^o, and then for all particles in the event.

A) Leading Particles

Figures 118 and 119 show the x_e distributions of the fastest and second-fastest charged particles for the proton and π^- beam data. The fraction of the transverse

* z is the momentum fraction of the parton carried by a hadron when the parton fragments into the hadron.

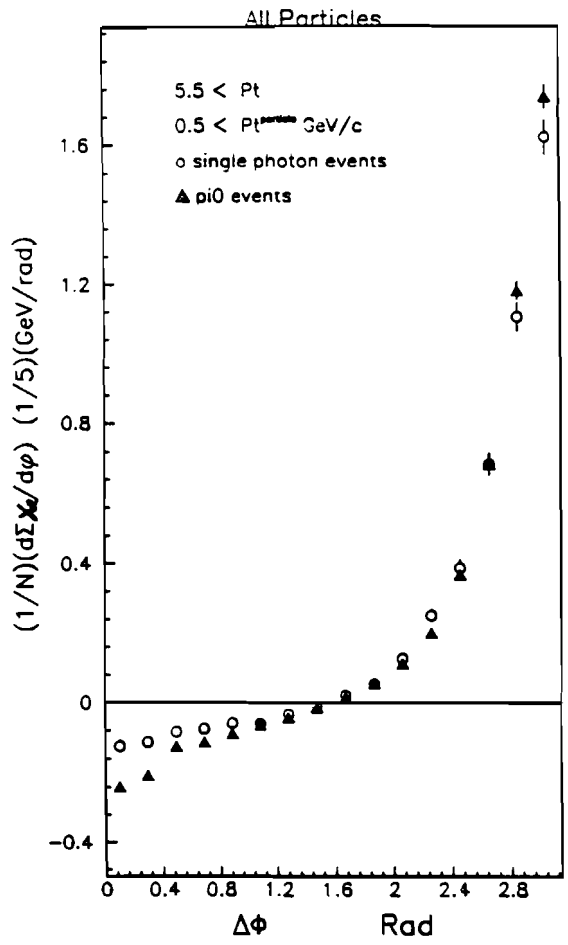

Figure 117: The distribution of the mean value of the sum $\sum[x_e]_i$ for both charged and neutral particles in intervals of $\Delta\phi$, for the high p_T single photon and π° events.

$$x_e = -\frac{\mathbf{P_{Th}} \cdot \mathbf{P_{T\gamma}}}{|\mathbf{P_{T\gamma}}|^2}$$

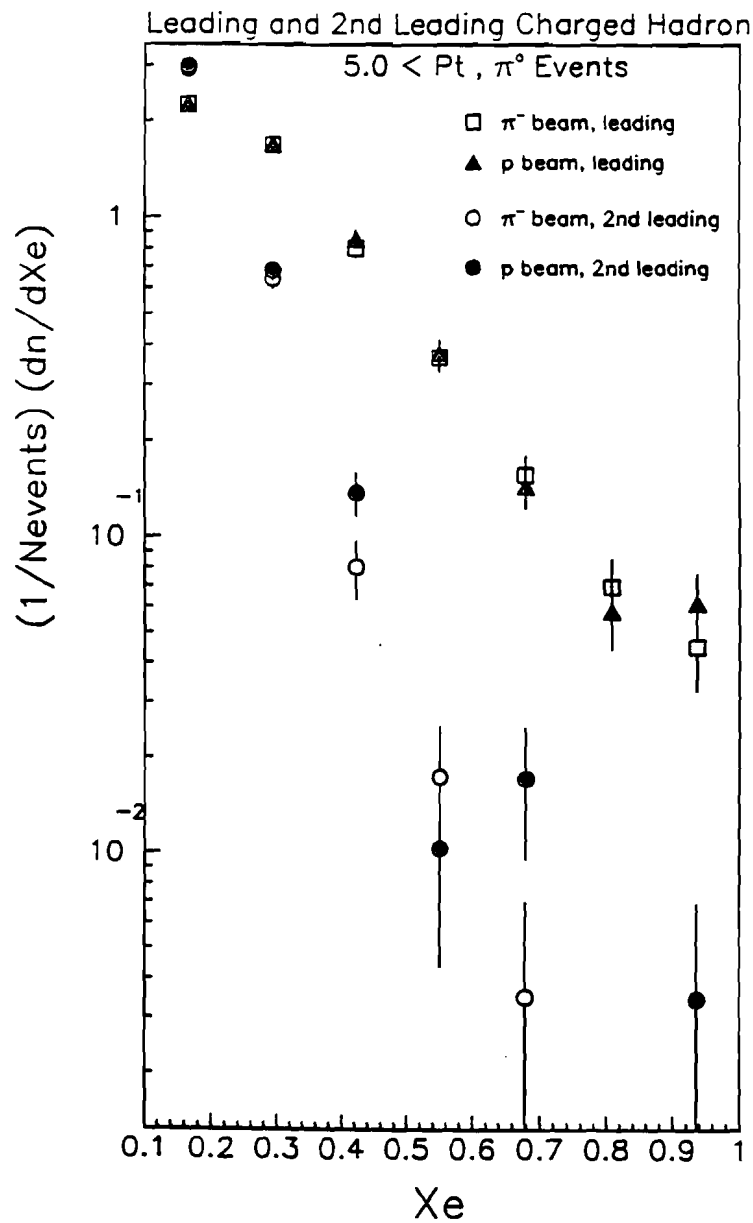

Figure 118: The x_e distributions of the fastest and second-fastest charged particles for the π° data.

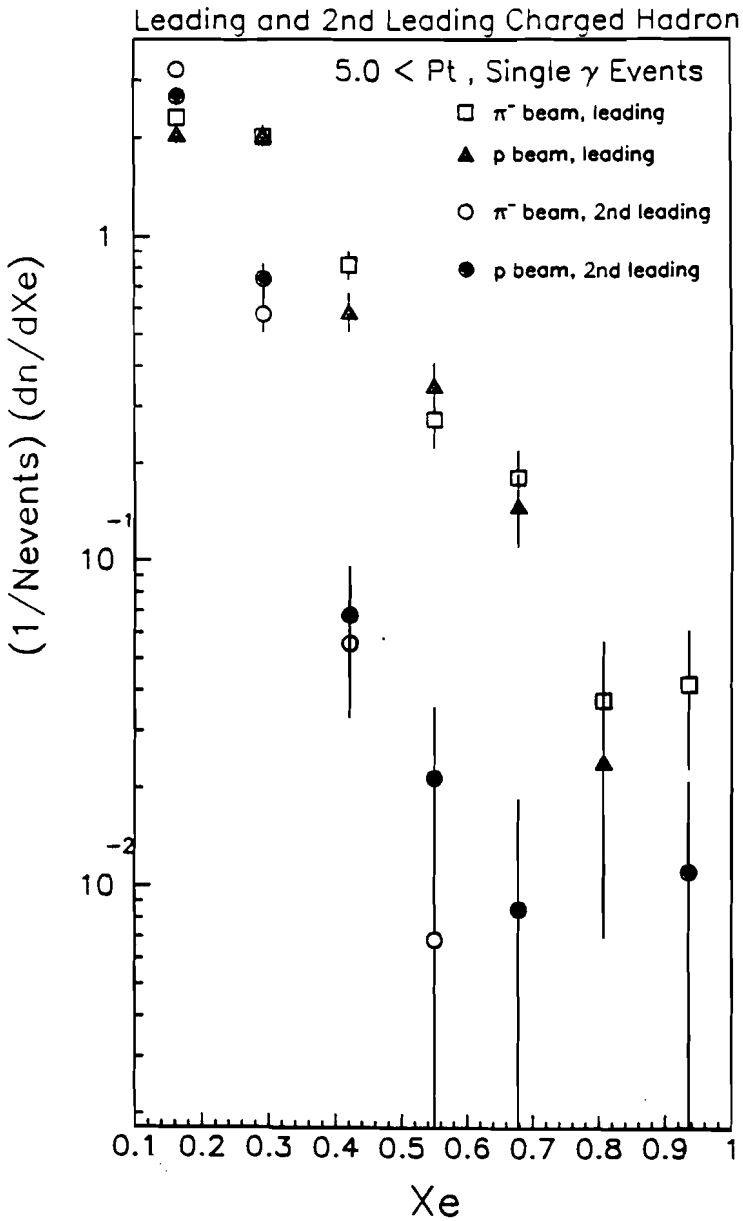

Figure 119: The x_e distributions of the fastest and second-fastest charged particles for the single photon data.

momentum of the high p_T photon or π^0 carried by the fastest and second-fastest charged particles in the region 1.0> x_e >0.1, is shown in Table 14. The errors are statistical.

LEADING PARTICLE	Proton Beam		π^- Beam	
	Single Photon	π^0	Single Photon	π^0
Leading Charged prt. (%)	29±.3	30±.5	30±.7	31±.5
2nd Leading Charged prt. (%)	20±.5	20±.3	19±.8	20±.3

Table 14: Fraction of the momentum of the high p_T photon or π^0 carried by the fastest and second-fastest charged particles.

Figure 120 shows the x_e distribution when the fastest particle other than the trigger, in the event is a neutral hadron ($E^{HAD} \geq 10.0$ GeV in the HALAC). Figure 121 shows the x_e distribution when the fastest particle in the event is a π^0. The x_e distribution of the π^0 was corrected for the background contributions. The measurements have not been corrected for reconstruction inefficiencies and detector acceptances.

B) All Particles

There was an additional cut used for the data presented in this section. It was required that there was at least one charged particle with p_T > 0.5 GeV/c in the hemisphere opposite the high p_T single photon or π^0. The effect of this cut is shown in Table 12. It had a very weak effect only in the lower p_T range. Figure 122 shows the x_e distributions for all particles in the event. Figures 123 and

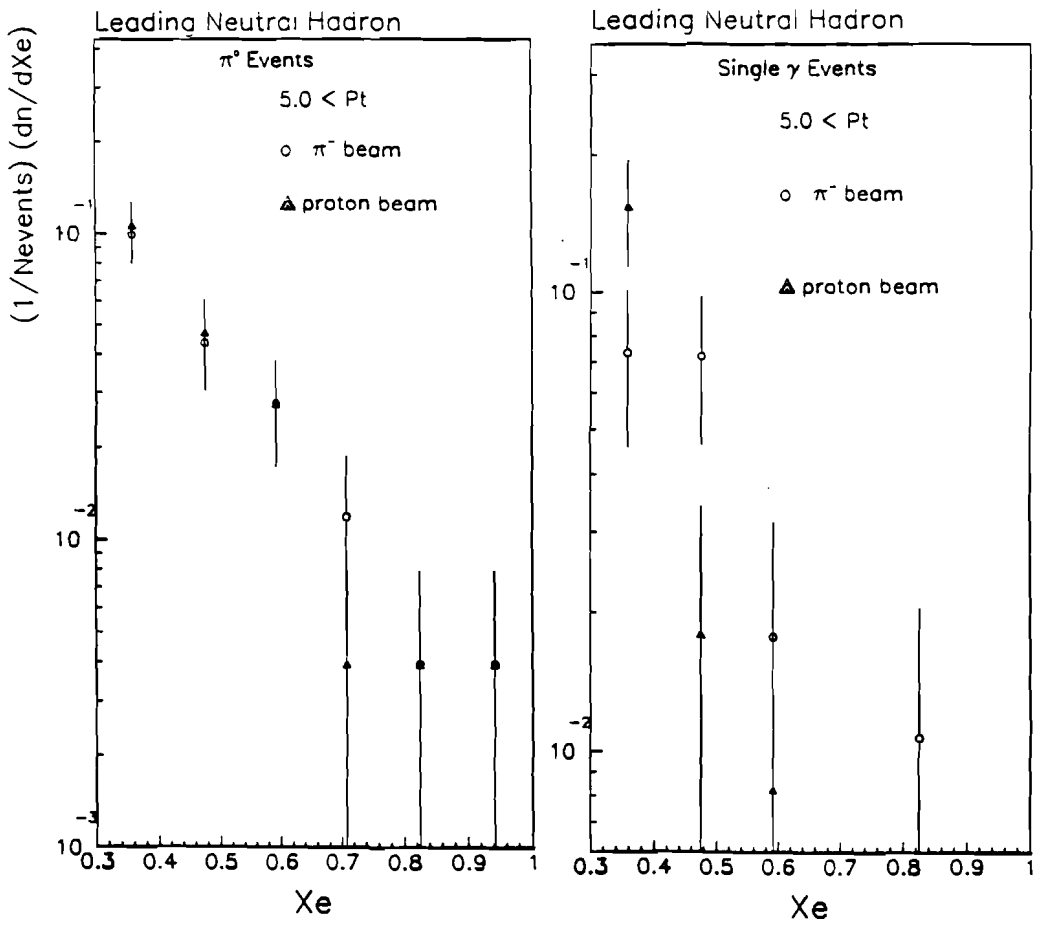

Figure 120: The x_e distribution when the fastest particle in the event is a neutral hadron ($E^{HAD} \geq 10.0$ GeV in the HALAC).

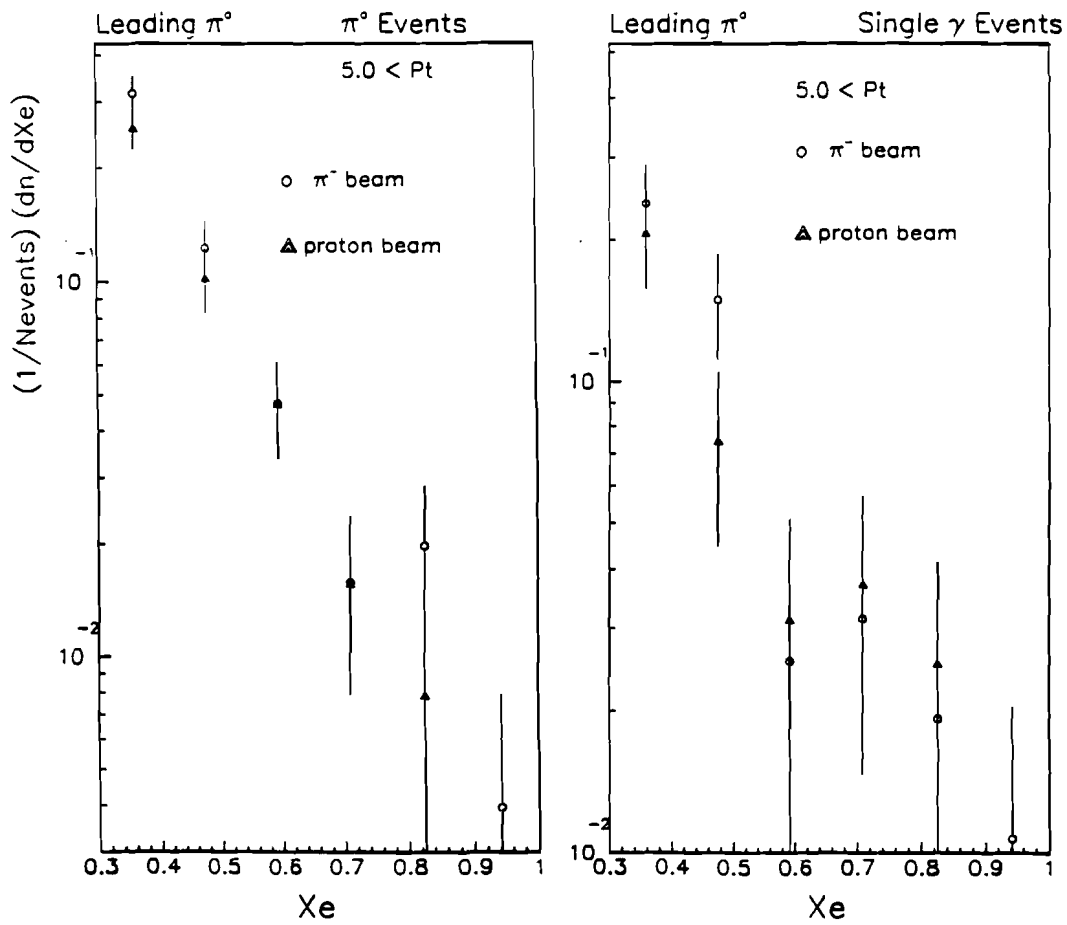

Figure 121: The x_e distribution when the fastest particle in the event is a π°. The x_e distribution of the π° background was subtracted from the x_e distribution of the raw π° signal.

$$x_e = -\frac{\mathbf{P_{Th}} \cdot \mathbf{P_{T\gamma}}}{|\mathbf{P_{T\gamma}}|^2}$$

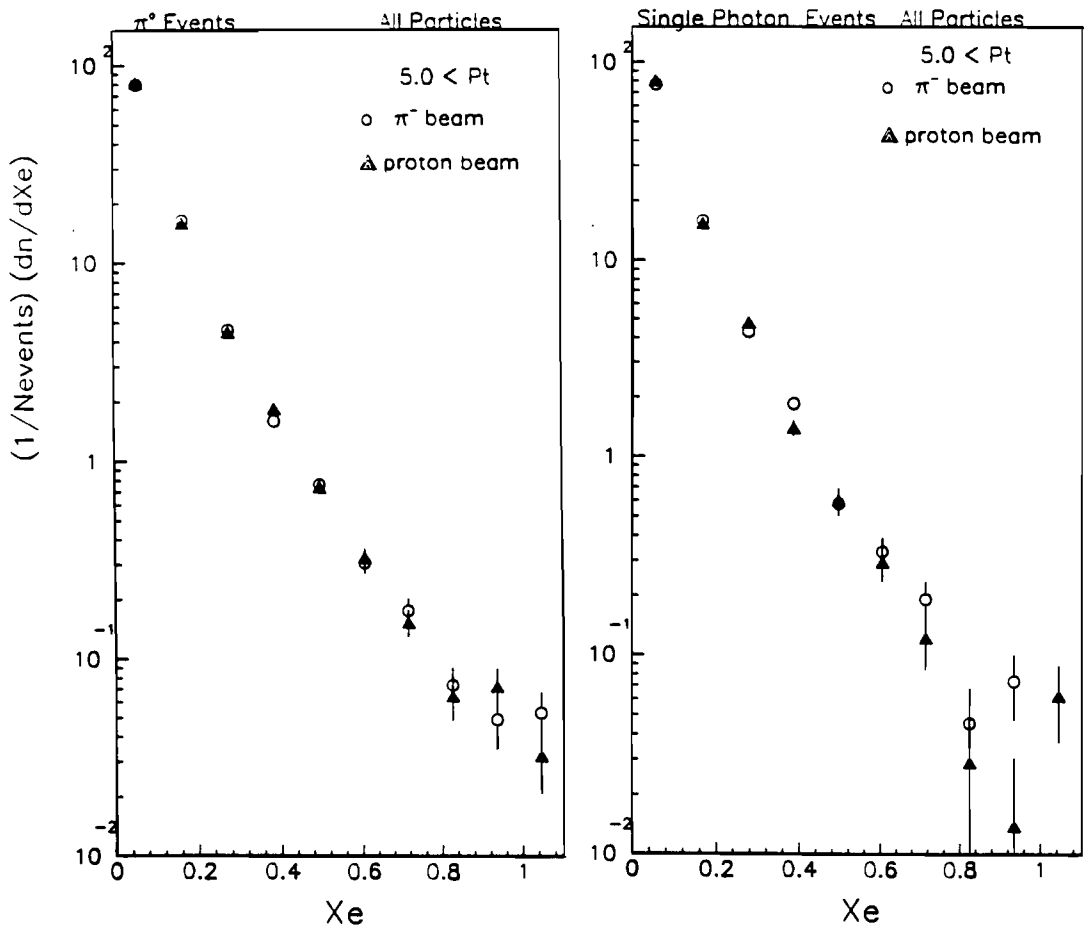

Figure 122: The x_e distributions for all particles in the event for proton/π^- beam and single photon/π° data. p_T (trigger) > 5.0 GeV/c.

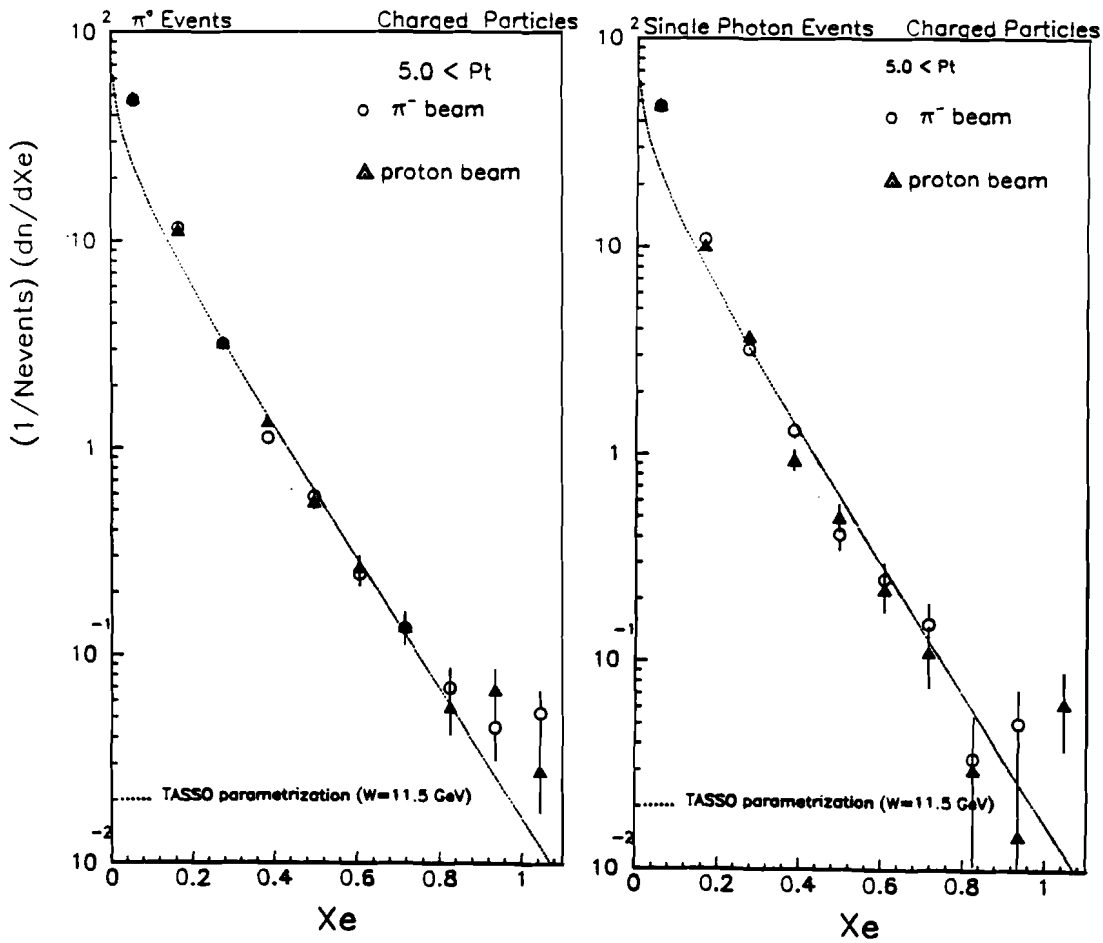

Figure 123: The x_e distributions for the charged particles in the events.

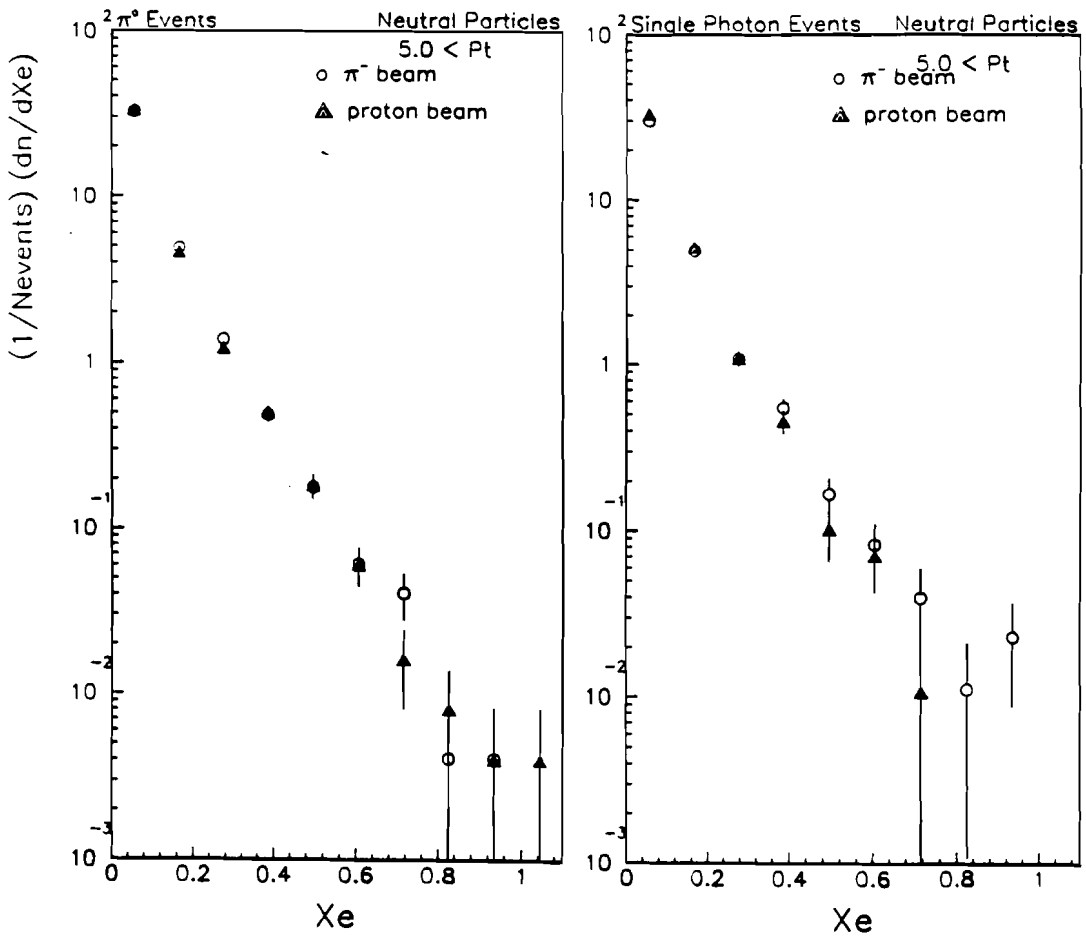

Figure 124: The x_e distributions for the neutral particles in the events.

124 show the x_e distributions for the charged particles and neutral particles in the event. The measurements plotted in Figures 122, and 123 are listed in Tables 15, and 16, respectively.

The data plotted in Figures 122 and 123 are fitted in the interval $0.2 < x_e < 1.1$ to the form

$$D(z) = \frac{ae^{-bz}}{z^c} \tag{7.3}$$

The parameters of the fit are listed in Table 17.

The curve superimposed on Figure 123 is the fragmentation function measured in e^+e^- interactions (see TASSO collaboration Ref. [29]). They measured the normalized differential cross section $1/\sigma_{tot}(d\sigma/dx_{||})$ as a function of $x_{||} = 2p_{||}/W$. $p_{||}$ is the projection of the momentum on the jet axis. $x_{||}$ is equivalent to x_e. The TASSO reported results for W = $\sqrt{s}$ = 14, 22, and 34 GeV. Since W corresponds to the effective mass of the photon - jet system, assuming massless particles and that the energy of the single photon is equal to the energy of the recoiling jet (in the center of mass), W reads:

$$< W > \simeq 2 < p_T > \tag{7.4}$$

It ranges from 10 to 23 GeV in our data and for p_T >5 GeV/c, with an average value of 11.5 GeV, which is the average value of the energy of the parton system in E-706 data. The TASSO experiment gives a parametrization of the fragmentation function as a function of W. The TASSO results, at W = 11.5 GeV, are superimposed on the data in Figure 123. The TASSO data cover the x_e range from .02 to 0.7. The line beyond .7 is an extrapolation of their data. The TASSO results in

Single Photon Events				
All Particles in the Event				
X_e	$D(x_e)$		Statistical error	
	π^- beam	p beam	π^- beam	p beam
.11 - .22	16.14	15.7	.41	.44
.22 - .33	4.38	4.92	.21	.24
.33 - .44	1.88	1.42	.14	.13
.44 - .55	.59	.6	.08	.087
.55 - .66	.34	.28	.06	.059
.66 - .77	.19	.11	.044	.038
.77 - .88	.047	.03	.023	.021

π^o Events				
All Particles in the Event				
X_e	$D(x_e)$		Statistical error	
	π^- beam	p beam	π^- beam	p beam
.11 - .22	16.7	16.3	.26	.26
.22 - .33	4.66	4.56	.14	.14
.33 - .44	1.63	1.87	.083	.088
.44 - .55	.77	.75	.057	.056
.55 - .66	.32	.34	.036	.036
.66 - .77	.17	.16	.027	.025
.77 - .88	.076	.067	.018	.017

Table 15: Fragmentation fraction $D(x_e)$ for $p_T > 5.0$ GeV/c. Both charged and neutral particles are counted.

Single Photon Events				
Charged Particles				
X_e	$D(x_e)$		Statistical error	
	π^- beam	p beam	π^- beam	p beam
.11 - .22	11.18	10.5	.34	.36
.22 - .33	3.31	3.85	.18	.21
.33 - .44	1.35	.98	.12	.11
.44 - .55	.42	.52	.069	.08
.55 - .66	.26	.23	.051	.054
.66 - .77	.15	.12	.04	.038
.77 - .88	.035	.032	.021	.021

π° Events				
Charged Particles				
X_e	$D(x_e)$		Statistical error	
	π^- beam	p beam	π^- beam	p beam
.11 - .22	11.85	11.71	.22	.22
.22 - .33	3.3	3.39	.12	.12
.33 - .44	1.15	1.4	.07	.077
.44 - .55	.6	.58	.05	.05
.55 - .66	.25	.28	.032	.034
.66 - .77	.14	.14	.025	.025
.77 - .88	.072	.059	.017	.016

Table 16: Fragmentation fraction $D(x_e)$ for $p_T > 5.0$ GeV/c. Only charged particles are counted.

$$\textit{Fitted Function} \ : \ D(x_e) \ = \ \frac{a\ e^{-bx_e}}{{x_e}^c}$$

Single Photon Events				
Charged Particles				
Beam	a	b	c	χ^2/DOF
π^-	1.89±.04	4.58±.18	1.4±.02	1.05
proton	10.05±.25	7.12±.2	.65±.025	3.9

π° Events				
Charged Particles				
Beam	a	b	c	χ^2/DOF
π^-	.75±.011	3.25±.06	1.79±.005	.7
proton	1.37±.61	3.92±.66	1.51±.2	.25

Single Photon Events				
All Particles in the Event				
Beam	a	b	c	χ^2/DOF
π^-	1.52±.028	3.91±.15	1.63±.02	1.3
proton	9.83±.21	6.96±.18	.86±.021	1.03

π° Events				
All Particles in the Event				
Beam	a	b	c	χ^2/DOF
π^-	1.65±.02	4.03±.09	1.62±.012	.45
proton	2.16±.85	4.3±.56	1.48±.16	.61

Table 17: Results of the D(x_e) fits. The data in the range $0.1 < x_e < 0.9$ were used in the fit.

the range from .05 to 0.7 are represented by the Equation 7.3 and the parameters in the fit were found to be:

a = 15.0 ± 0.18

b = 6.8 ± 0.14

c = 0.28 ± 0.005

The TASSO results are in good agreement with our data for $x_e > 0.2$. Our x_e distribution does not agree with the TASSO extrapolation in the range $x_e < 0.2$. This is expected because at low x_e values (low p_T) the recoiling jet particles are mixed with particles belonging to the forward or target jets.

7.4. Charge Ratio

In this section the average number of positive and negative charges (denoted by R^+/R^-) in the away hemisphere for high p_T single photons is compared to that in the away hemisphere to the high p_T π^os. The charge of the particles at high x_e values is expected to reflect the charge of the original parton[9],[76],[20]. In the p(Be+Cu) collisions we expect the diagram $ug \rightarrow u\gamma$ to dominate (see Section 2.9) the single photon events. Thus, the overall charge of the recoiling particles from the high p_T photon should reflect the charge of the originating quark, i.e., positive charge. In the π^o events, the overall charge of the away hemisphere should favor the positive charged particles because in the $pBe \rightarrow \pi^o X$ reaction there are more positive quarks than negative ones[8],[78]. In the π^-Be collisions the annihilation diagram starts dominating so that recoiling particles should have no net charge for the single photon events. In the π^o events the overall charge should be zero as expected by quark counting.

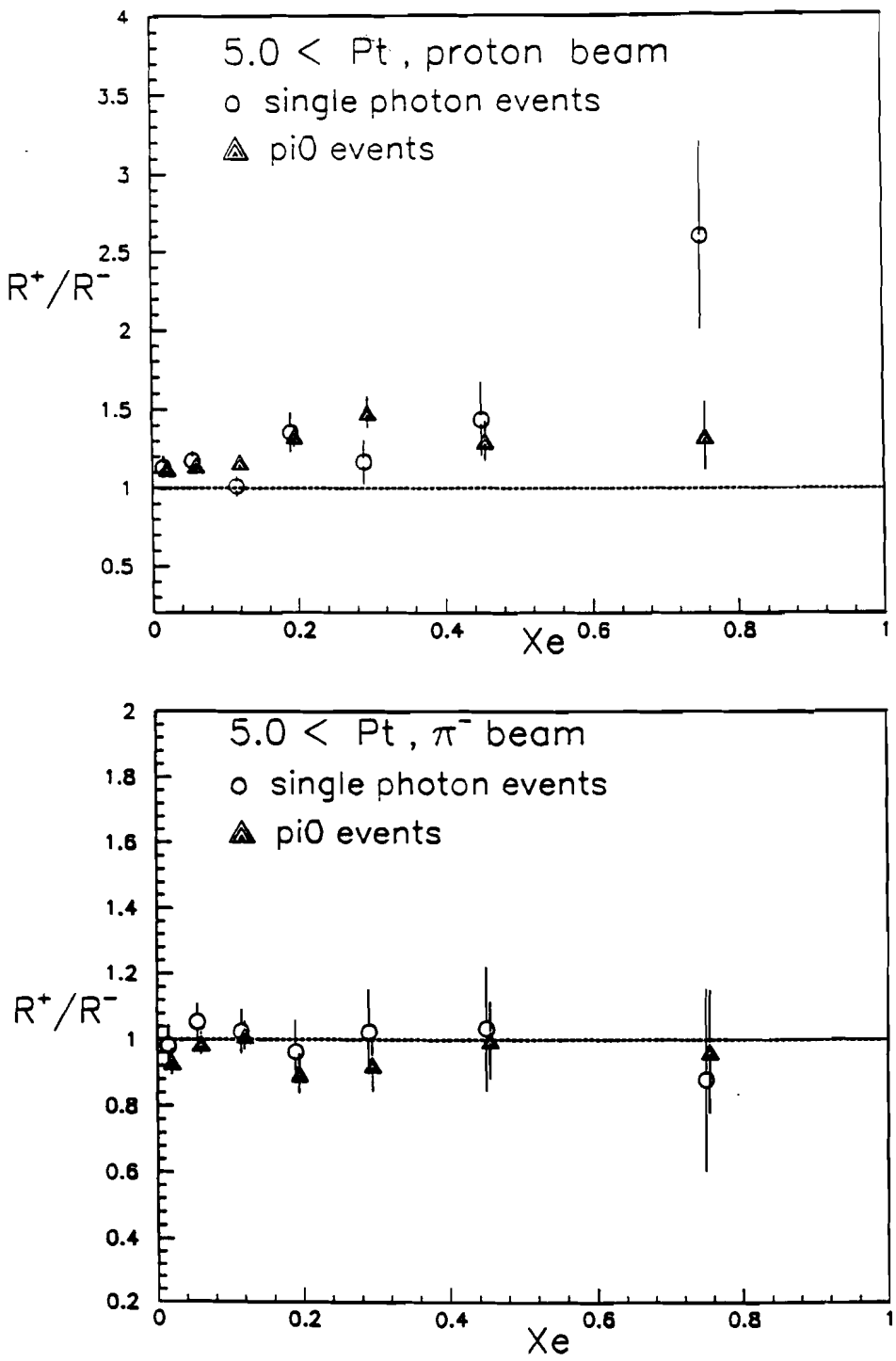

Figure 125: Ratio of the numbers of positive and negative particles as function of x_e. The single photon events are compared with the π° events for the p(Be+Cu) and π^-(Be+Cu) data. The π° background in the single photon events has not been subtracted.

The ratio of the x_e distributions of the positive to that of the negative particles recoiling against the high p_T single photons and π^os is shown in Figure 125 for the p(Be+Cu) and π^-(Be+Cu) data. Only the charged particles within the rapidity interval (-0.7,0.7) and with p_T > 500 MeV/c are plotted. The single photon events have not been corrected for the π^o background. Even though the statistical errors are large the result is consistent with the theoretical predictions and experimental[22],[25] results.

7.5. Discussion

Distributions of charged and neutral particles associated with the high p_T single photons and π^os have been studied. The conclusions are presented below:

(a) Single photon - π^o differences

The azimuthal distributions ($\Delta\phi$) of particle multiplicity, p_T, and q_T demonstrate clearly that π^os are produced along with other particles where as single photons are relatively unaccompanied by other particles. The single photons are more isolated at higher p_T relative to lower p_T. The p_T and q_T densities of particles produced directly opposite to π^os are higher than for single photon. This results from the high p_T π^o carrying a smaller fraction of the p_T in the trigger hemisphere than do the single photons. Again, this observation is consistent with the basic π^o and single photon production mechanisms.

The fact that the single photons are more isolated at higher p_T relative to lower p_T is an indication of the diminishing importance of the photon bremsstrahlung contributions at higher p_T. However, there are two main difficulties in measuring the fraction of the bremsstrahlung contributions. First, it is possible that the

bremsstrahlung events are "contaminated" by π^o events where one of the decay photons is not detected for various reasons. π^os are also a fragment of jets produced from a scattered partons and are also accompanied by other particles. Second, the photons in the bremsstrahlung events may appear isolated from the hadrons in the event as a result of the quark fragmentation process. This can happen because the high p_T bremsstrahlung photon takes a significant fraction of the parent parton's momentum and the accompanying hadrons carry relatively low p_T. Thus it is difficult to isolate these hadrons from the beam or target jets. Another reason lies in the fragmentation process. The fragmentation process will give to the relatively small longitudinal momentum fraction of the hadrons some transverse momentum with respect to the parent parton direction of motion. Thus it is likely that, on the average, there is a significant spatial separation between the bremsstrahlung photon and the associated hadrons.

(b) Jet structure

The demonstration of the jet structure of the particles recoiling against the high p_T photons or π^os is based primarily on the differences in the rapidities between the directions of the high p_T photon or π^o and the two fastest particles on the opposite side. The excess of events for $|\Delta y| < 0.4$ above the uncorrelated distribution is attributed to the jetness of the particle distribution opposite the trigger. The Δy distributions between the high p_T photons or π^os and the accompanying (i.e., the same side) leading charged particle show that the jet - like structure dominates in the trigger hemisphere for the π^o events relative to the single photon ones. This is also evidence that the single photon events have the characteristics of the direct photon production, i.e., they emerge from the parton-parton reaction

directly without been accompanied by a jet.

(c) Fragmentation studies

All fragmentation function distributions are consistent with the parametrizations presented by other experiments. The fragmentation distributions of the charged particles, compared with the ones obtained from the TASSO e^+e^- experiment are found to be in good agreement at the range $0.2 < x_e < 1.0$.

By taking appropriate combinations of beam types and high p_T neutral triggers it is possible to isolate samples of events dominated by jets originating from either gluons or quarks. We expect to see the gluon fragmentation function to be softer than that of the quark. The fragmentation fraction distributions show no significant difference in the particles recoiling from either high p_T single photons or π^os in pBe and π^-Be collisions, within the statistical accuracy.

7.6. Summary

Fermilab experiment E-706 is designed to study high p_T direct photon production and the associated jets from hadronic collisions. E-706 used p, π^+, K^+, π^-, and K^- beams of 530 GeV/c momentum on nuclear targets. The p(Cu+Be) and π^-(Cu+Be) collisions at $\sqrt{s}$ = 31.5 GeV are studied in this thesis. The E-706 apparatus has a large acceptance and excellent sensitivity, -1.0< Y <1.0 for photons, and it reached up to 10.5 GeV/c in single photon p_T. The apparatus consists of a set of silicon strip detectors upstream and downstream of the target, a set of proportional wire chambers downstream of an analysis magnet, a liquid argon calorimeter consisting of an electromagnetic section and a hadronic section, and a forward calorimeter. The first experimental run of E-706, in Feb. 1988, was

completed successfully, and the performance of the various parts of the apparatus have been studied in detail.

Particles produced in association with high transverse momentum single photons and π^0s in hadronic collisions have been measured and their properties are in good agreement with the predictions of the parton model and those of QCD.

REFERENCES

1. R.P. Feynman, Phys. Rev. Lett. 23, 1415(1969).
2. J.D. Bjorken and E.A. Paschos, Phys. Rev. 158, 1975(1969); J.D. Bjorken, Phys. Rev. 179 (1969).
3. S.M. Berman, J.D. Bjorken, J. Kogut, Phys. Rev. D4, 3388(1971).
4. F.W. Busser et al., Phys. Lett. 35, 471(1973); B. Alper et al., Phys. Lett. 44B, 521 (1973).
5. M. Gell Mann, "A Schematic Model of Baryons and Mesons", Phys. Lett. 8, 214(1964); G. Zweig, CERN Preprint TH-492 (1964), unpublished.
6. R.P. Feynman, R.D. Field, G. C. Fox, Nucl. Phys. B128, 1(1977); R.D. Field, R.P. Feynman, Phys. Rev. D15, 2590(1977).
7. T. Ferbel, W. Molzon, Rev. of Modern Phys., 22, 88(1984).
8. "Large Momentum Transfer Production of Direct Photons, Jets, and Particles", J. F. Owens, Rev. Mod. Phys. 59, 465(1987).
9. L. Cormell and J. F. Owens, Phys. Rev. D22, 1609(1980).
10. B. Anderson, G. Gustafson, G. Ingelman, T. Sjostrand, Phys. Reports, 97, 31(1983).
11. "Introduction to High Energy Physics", by D.H. Perkins, Publishing Company: Addison - Wesley.
12. "A Detailed Study of the Proton Structure Functions in Deep Inelastic Muon - Proton Scattering", Nuclear Phys. B259, 189-265(1985).
13. D. W. Duke and J. F. Owens, Phys. Rev. D23, 1671(1981).

14. D. W. Duke, J. F. Owens, Phys. Rev. D30, 49(1984).

15. "Recent results on direct photon production at CERN", presented by E. Lanson (1988).

16. M. Nowak, M. Praszalowicz, Z.Phys. C17, 249(1983).

17. H. Dechansteiter, F. Halzen, D.M. Scott, Phys. Rev. D24, 2856(1981).

18. "Review of Particle Properties", Particle Data Group, 1988.

19. "Applications of Perturbative QCD, R. D. Field", Addison Wesley (1989).

20. "Large p_T Direct Photon Production and Opposite - Side Photon - Hadron Correlations in QCD", A.P. Contogouris, S. Papadopoulos and C. Papavassiliou, Nuclear Physics, B179, 461(1981).

21. "High p_T γ and π^o Production, Inclusive and With a Recoil Hadronic Jet, in pp Collisions at $\sqrt{s} = 63$ GeV", T. Akesson et al., paper submitted to Yadernaya Fizika, CERN - EP/89-88, (1989).

22. T. Akesson et al. Phys. Let., 118B, 178(1982).

23. T. Akesson et al.,Phys. Scripta, 34, 106(1986).

24. "A Comparison of Hadronic Final States in High p_T Direct Photon and π^o Production With Those in e^+e^- Interactions", WA-70 Collaboration, paper submitted to the XIV International Symposium of Lepton - Photon Interactions, 7-12 August 1989, Stanford California.

25. "A study of the Structure of Events Triggered by Direct Photons in π^-p, π^+ and pp Collisions at 280 GeV/c", WA-70 Collaboration (1988).

26. Angelis, A.L.S., et al., Phys. Let., 98B, 115(1981).

27. "Direct Photon Production in $p\bar{p}$ Collisions at $\sqrt{s}$ = 630 GeV", UA2 Collaboration, Z. Phys. C41, 395(1988).

28. "Experimental Evidence for Differences in $< p_T >$ Between Quark and Gluon Jets", JADE Collaboration, Phys. Let., 123B, 460(1983).

29. "Jet Production and Fragmentation in e^+e^- Annihilation at 12-43 GeV, TASSO Collaboration", Z. Phys., 22, 307(1984).

30. "Charged Multiplicity Distributions and Correlations in e^+e^- Annihilation at PETRA Energies", TASSO Collaboration, DESY 89-038, ISSN 0418 - 9833 (1989).

31. "Analysis of the Fragmentation Properties of Quark and Gluon Jets at CERN SPS $p\bar{p}$ Collider", UA1 Collaboration, Nucl. Phys. B276, 253(1986).

32. "Study of High p_T Quark and Gluon Jet Fragmentation", Z. Phys. C Particles and Fields 33, 465(1987).

33. "On the Difference Between Quark and Gluon Jets", H.R. Gerholh, W. Majerotto, Nuovo Cimento, 88A, 74(1985).

34. G. Arnison et al., UA1 Collaboration, Phys. Lett., 136B, 294(1984).

35. G. Arnison et al., UA1 Collaboration, Phys. Lett., 123B, 115(1984).

36. M. Banner et al., UA2 Collaboration, Phys. Lett., 118B, 203(1982).

37. M. Bagnaia et al., UA2 Collaboration, Phys. Lett., 138B, 430(1984).

38. M. Bagnaia et al., UA2 Collaboration, Z. Phys., C20, 117(1983).

39. A. Bernasconi et al., UA-6 Collaboration, paper submitted to Phys. Lett. B, CERN-EP/88-31, (1988).

40. A. Bamberger et al., NA-24 Collaboration, CERN/SPSC/83-3, SPSC/M 344, (1983).

41. "Dijet Production Cross - Section and Fragmentation of Jets Produced in pp Collisions at $\sqrt{s} = 63$ GeV", T. Akesson et al., Z. Phys., C30, 27(1986).

42. F. Halzen, M. Dechanstreiter and D. M. Scott, Phys. Rev., D22, 1617(1980).

43. "Electroproduction of Charged Pions in Quark Fragmentation Region", Phys. Rev. Lett. 41, 1433(1978).

44. "Hadron and Jet Production at Collider Energies in Perturbative QCD", N.G. Antoniou et al., Phys. Lett., 128B, 257(1983).

45. "Multiplicity Distributions in Quark and Gluon Jets", E. D. Malaza, B. R. Webber, Nuclear Phys. B267, 702(1986).

46. W. Baker, E-706-65 Internal memo.

47. W. Desoi, PhD Thesis, unpublished, University of Rochester.

48. S. Mani, E-706- 125, Internal memo.

49. C. Bromberg, E-706-094, Internal memo.

50. F.Lobkowicz, NIM A235, 332(1985).

51. G. Bathow et al., Nucl. Phys. B 20 592(1970).

52. W. J. Willis, V. Radeka, NIM 120, 221(1974).

53. "Simulation of Hadronic Showers by H. Fesefeldt", FNAL Lib. 64,857.

54. D.F. Grawford, H. Messel, Phys. Rev. 128, 352(1962).

55. H.H. Nagel, Z. Phys., 186, 319(1965).

56. E. Longo, I. Sestili, NIM 128, 283(1975).

57. T.A. Gabriel, NIM 150, 145(1978).

58. "On the Energy Resolution of Uranium and Other Hadron Calorimeters" by R. Wigmans, CERN/EF 86-18; "Fluctuations in Calorimetry Measurements" by Ugo Amaldi, Phys. Scripta, 23, 409(1981).

59. T.F. Droedge, K.J. Turner, T.K. Ohska, RABBIT system, FNAL note PIN521/CDF119.

60. Dane Skow, E-706- 157, internal memo.

61. P. Lukens, K. Ruddick, E-706- 141, internal memo.

62. E. Prebys, E-706 internal memo.

63. VAXONLINE, Fermilab Computing Department, Data Acquisition Software Group, Notes: PN252, PN271.2, PN272.2, PN278, PN280. Also 'IEEE transactions on Nuclear Science', NS34 No. 4, 763(1987).

64. J. Engler et al., NIM 133, 521(1976).

65. E.Shibamura et al., NIM 131, 249(1975).

66. J.H. Cobb et al., NIM 158, 93(1979).

67. J. Huston, PhD Thesis, University of Rochester.

68. C.W. Fabjan and T. Ludlam, Ann. Rev. Nucl. Part. Sci., 32, 335(1982).

69. H. Abramowicz et al., NIM 131, 429(1981).

70. J. Huston et al., paper submitted to XXIV International Conference of High Energy Physics.

71. T. Yasuda, private communication and E-706 internal report.

72. R. Brun, M. Goossens, and J. Zoll, ZEBRA, CERN document DD/EE/85-6, CERN program library number Q100.

73. L. deBarbaro, F. Lobkowicz, E-706- 139, internal memo.

74. C. Lirakis, T. Yasuda, E-706 internal report.

75. S. Hossain, E. Pothier, G. Ballocchi, E-706- 130 internal memo.

76. Bair, Engels, Peterson, Z. Phys., C6, 309(1980).

77. P. Aurenche et al., Phys. Let., 169B, 441(1986).

78. O. Benary et al., Z. Phys., C16, 211(1983).